Journal of Seismic Exploration

ISSN: 0963-0651

Volume 34 · Issue 3
2025

ACCSCIENCE PUBLISHING

State Key Laboratory for Fine Exploration and Intelligent Development of Coal Resources

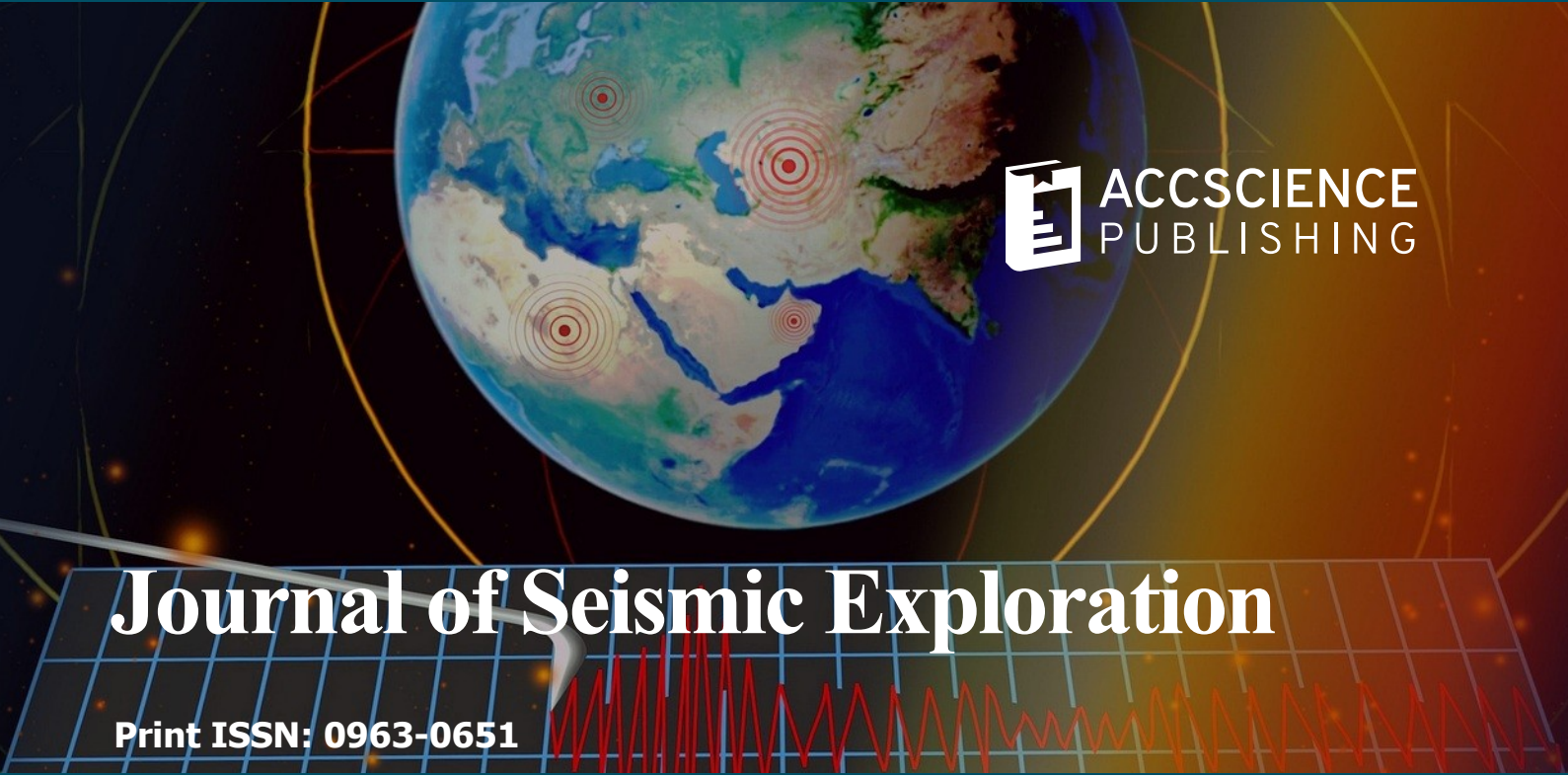

Journal of Seismic Exploration

Print ISSN: 0963-0651

The Journal of Seismic Exploration (JSE) is an international medium for the publication of research in seismic modeling, processing, inversion, interpretation, field techniques, borehole techniques, tomography, instrumentation and software. The aim and goal of JSE is to serve the interests and objectives of seismic petroleum exploration. All seismic processing methods have assumptions and prerequisites- and when they are satisfied methods are effective-and when they are violated methods become ineffective and can fail. The latter contributes to drilling dry hole exploration wells and suboptimal development wells.

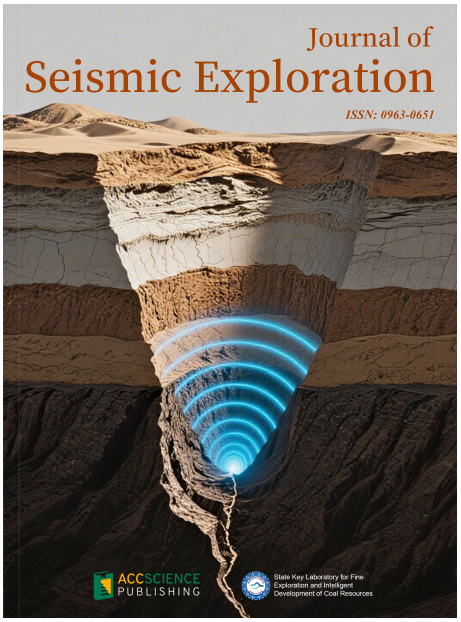

About the Publisher

AccScience Publishing is a publishing company based in Singapore. We publish a range of high-quality, open-access, peer-reviewed journals and books from a broad spectrum of disciplines.

Contact Us

Managing Editor
jse.office@accscience.sg

AccScience Publishing
9 Raffles Place, Republic Plaza 1 #06-00 Singapore 048619.

Volume 34 • Issue 3 • 2025
ISSN 0963-0651 (print)

Journal of Seismic Exploration

ACCSCIENCE PUBLISHING

Access Science Without Barriers

JOURNAL OF SEISMIC EXPLORATION

ISSN: 0963-0651 (print)

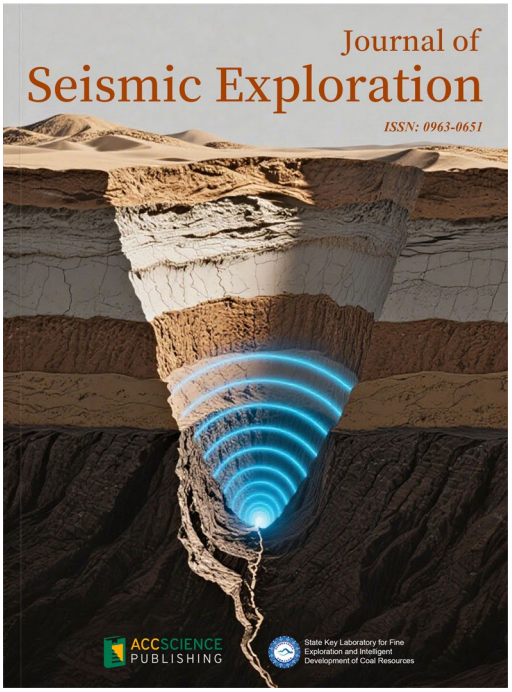

Editorial and Production Credits

Publisher: AccScience Publishing
Managing Editor: Gary Liu
Production Editor: Lim Mingyuan
Article Layout and Typeset: Sinjore Technologies (India)

Supplementary file

Supplementary files of articles can be obtained at https://accscience.com/journal/JSE/34/3.

Disclaimer

AccScience Publishing is not liable to the statements, perspectives, and opinions contained in the publications. The appearance of advertisements in the journal shall not be construed as a warranty, endorsement, or approval of the products or services advertised and/or the safety thereof. AccScience Publishing disclaims responsibility for any injury to persons or property resulting from any ideas or products referred to in the publications or advertisements. AccScience Publishing remains neutral with regard to jurisdictional claims in published maps and institutional affiliations.

Journal of Seismic Exploration

Editorial Board

ACCSCIENCE PUBLISHING

Volume 34 | Issue 3 | 2025 | Page 1 – 93 |

Journal of Seismic Exploration

https://accscience.com/journal/JSE

CONTENTS

ARTICLES

RETRACTION

ACCSCIENCE PUBLISHING

Journal of Seismic Exploration

ARTICLE

Predicting channel sandstone thickness through a VIF-NRBO-XGBoost model

Weichao Zhang[1], Junhua Zhang[1]*, Zheng Huang[1], Jingqiang Yu[2], Deyong Feng[2], and Shugang Wang[2]

[1]School of Geosciences, China University of Petroleum (East China), Qingdao, Shangdong, China

[2]Geophysical Research Institute, Shengli Oilfield Company, SINOPEC, Dongying, Shangdong, China

Abstract

High-precision sand thickness data are fundamentally important for optimizing exploration strategies in petroleum geology. In the Chengbei work area of the Jiyang Depression, the stratigraphic channels are chaotically developed, with channels of varying sizes in different strata overlapping, intersecting, and exhibiting narrow widths. The actual well-seismic relationship is poor. Therefore, individual seismic attributes in this area exhibit extremely low correlation with channel sandstone thickness. Conventional attributes such as root mean square amplitude show no distinct channel characteristics, necessitating the integration of multiple seismic attributes for effective prediction. Moreover, the high multicollinearity among seismic attributes introduces significant interference in prediction results. Therefore, this study integrates the Pearson correlation coefficient and variance inflation factor (VIF) to optimize seismic attribute selection, effectively eliminating redundant attributes and those with low correlation. To further enhance prediction accuracy and address the significant bias inherent in single-model predictions, this study introduces the ensemble learning XGBoost model, which integrates predictions from multiple weak learners to improve the precision of sandstone thickness estimate. The Newton–Raphson-based optimization algorithm was employed to fine-tune the XGBoost parameters. Results from test wells demonstrate a remarkable improvement in prediction accuracy, achieving reliable sandstone thickness estimation despite poor well-seismic correlations. This research provides valuable insights and offers a widely applicable methodology for predicting the thickness of complex channel sand bodies.

Keywords: River channel sand body; Thickness prediction; Variance inflation factor; Newton-Raphson based optimization optimization; XGBoost

***Correspondence author:**
Junhua Zhang
(zjh@upc.edu.cn)

Citation: Zhang W, Zhang J, Huang Z, Yu J, Feng D, Wang S. Predicting channel sandstone thickness via a VIF-NRBO-XGBoost model. *J Seismic Explor*. 2025;34(3):1-12.
doi: 10.36922/JSE025290037

Received: July 18, 2025

Revised: August 27, 2025

Accepted: September 2, 2025

Published online: September 22, 2025

1. Introduction

Reservoir characterization constitutes a critical component in oil and gas field exploration and development. Scholars in related fields have conducted innovative research on reservoir thickness prediction, enhanced wettability characterization accuracy, and sandstone reservoir petrophysical properties.[1-3] Accurate prediction of

reservoir thickness is fundamental to detailed reservoir characterization and optimal exploration well placement, with increasingly stringent requirements for prediction-match rates. Given the high costs associated with acquiring fundamental seismic data, fully leveraging seismic data for reservoir thickness prediction holds significant importance for cost reduction and efficiency improvement in hydrocarbon exploration. To better utilize seismic data, geophysicists specializing in seismic data processing have integrated emerging technologies such as deep learning networks with wavelet transform methods to enhance seismic data resolution.[4] Seismic attributes, which are key information extracted from seismic data, contain abundant reservoir characteristics. Channel sand bodies represent one of the most important reservoir types in continental petroliferous basins. The Chengbei work area of Jiyang Depression studied in this paper exhibits chaotic channel development, where channel sand bodies demonstrate poor well-seismic relationships due to unfavorable conditions, including thin individual layers, narrow channel widths, severe overlapping and intersecting patterns, and multiple interbedded layers. These factors result in weak correlations between individual seismic attributes and sand body characteristics, necessitating multi-attribute seismic prediction. However, the strong multicollinearity among different seismic attributes precludes the simple superposition of multiple attributes with relatively strong correlations to sand body features for thickness prediction.[5]

The reservoir prediction for such complex channel sand bodies in this area has become a challenging issue, urgently requiring a novel method capable of effectively predicting sandstone thickness in such contexts.

In the field of reservoir thickness prediction, numerous studies have been conducted by petroleum geophysicists. Widess[6] first proposed estimating thin-bed thickness using reflection amplitude, but this method was only applicable to ideal reservoirs with equal-magnitude and opposite-polarity reflection coefficients. Chung and Lawton[7] improved upon this approach, achieving some enhancement in the prediction accuracy for very thin layers. However, the amplitude values remained constrained by the absolute values of the top and bottom reflection coefficients of the sand bodies, resulting in poor performance with actual data. Multi-attribute inversion has also been employed for sand body thickness prediction, utilizing seismic attributes sensitive to sand thickness combined with nonlinear optimization algorithms to calculate thickness. Nevertheless, this method suffers from low computational efficiency and is only effective in well-controlled areas, performing poorly in non-well-controlled regions.[8,9] Some scholars have proposed spectral decomposition techniques, using the "spectral notch" period to determine thin-bed thickness.[10-12] However, the "spectral notch" phenomenon is significantly influenced by factors such as wavelet bandwidth, limiting its practical application. Other approaches include identifying channel boundaries and predicting sand thickness using peak frequency-to-amplitude ratios, but these methods require high well-seismic correlation and are unsuitable for complex channel sand bodies with poor well-seismic relationships.[13] Barnes *et al.*[14] analyzed the relationship between frequency and reservoir thickness, establishing a corresponding formula for thickness distribution. However, this method shows low accuracy in complex areas with overlapping channels. Wang *et al.*[15] applied supervised learning based on fully connected neural networks to establish a nonlinear mapping between wavelet time-frequency components of seismic data and reservoir sand thickness, which, to some extent, reduced errors in validation wells.

Modern regression analysis frequently employs machine learning implementations, particularly tree-based ensemble methods like Random Forest, and kernel transformation techniques such as support vector regression (SVR) have demonstrated promising results in predicting sand body thickness.[16,17] While SVR models offer advantages for small-sample predictions and are theoretically suitable for areas with limited well data, their reliance on kernel functions for spatial mapping limits their ability to accurately handle nonlinear problems, resulting in weak nonlinear modeling capabilities. Chopra and Marfurt[18] were the first to utilize supervised learning algorithms, such as neural networks, to map multiple preferred attributes into reservoir thickness. Some researchers have employed eXtreme Gradient Boosting (XGBoost) models for sand thickness prediction, achieving favorable outcomes.[19] Furthermore, the XGBoost algorithm has found extensive utilization across multiple domains such as transportation, medicine, environment, and computer science.[20-23] Liu *et al.*[24] employed spectral decomposition-derived seismic characteristics combined with stacked generalization methodology to estimate reservoir thickness, which improved accuracy compared to other models. Currently, among various machine learning approaches, ensemble learning models show the most significant performance. However, challenges remain in optimal seismic attribute selection and parameter optimization for these ensemble models.

Based on the above research background, this paper proposes a VIF-NRBO-XGBoost reservoir thickness prediction model. To address the issues of strong multicollinearity among seismic attributes and low correlation between individual seismic attributes and reservoir thickness in complex channel sand bodies, this study combines variance inflation factor (VIF) and

Pearson correlation coefficient to conduct multicollinearity analysis and optimal seismic attribute selection.[25] To overcome the large prediction errors of single models and further improve prediction accuracy, an ensemble learning XGBoost model is introduced to enhance sand body thickness prediction precision by integrating predictions from multiple weak learners.[26] VIF serves as a diagnostic tool for detecting multicollinearity in multiple linear regression models, effectively eliminating redundant seismic attribute information. In general, a VIF value exceeding the threshold of 10 indicates unacceptable strong multicollinearity. Tree-based XGBoost ensemble learning demonstrates superior predictive performance for poor-quality data. However, this algorithm involves numerous parameters whose default settings typically fail to maximize model performance. Manual parameter adjustment proves excessively laborious and blind, making it practically infeasible. Currently, common parameter optimization methods include particle swarm optimization (PSO) and Bayesian optimization algorithms. For sand thickness prediction, PSO performs relatively poorly due to limited well data samples. Although Bayesian optimization shows improvement over PSO, it tends to converge to local optima, making it still challenging to find optimal parameter combinations for channel sand bodies with inherently poor well-seismic relationships. This study employs the Newton–Raphson-based optimization (NRBO) for model hyperparameter optimization.[27] The algorithm utilizes the Newton–Raphson search rule (NRSR) and the Trap Avoidance Operator (TAO) mechanisms to explore the search domain and enhance convergence speed. NRBO exhibits strong evolutionary capability, fast search speed, and excellent optimization performance. Finally, the prediction results are compared with other models to demonstrate the reliability of the proposed method.

2. Methodology

2.1. Variance inflation factor

Multicollinearity refers to the existence of linear relationships among independent variables. The VIF is a metric used to quantify the severity of multicollinearity among features in a regression model. A higher VIF value indicates stronger multicollinearity between the features. The VIF is calculated using the following formula:

$$VIF = \frac{1}{1-R_i^2} \tag{I}$$

Where R_i^2 represents the determination coefficient quantifying the linear relationship between the i-th selected feature and other features in the dataset. The computational method sequentially designates each feature as the response variable while considering the remaining features as predictors, fitting a regression model accordingly, and finally computes the ratio of mean squared errors between the independent and dependent variables. A VIF value near 1 suggests that the feature exhibits negligible multicollinearity. In general, two thresholds are set: when 5 < VIF < 10, it indicates relatively severe multicollinearity for that feature, requiring careful consideration; when VIF ≥ 10, it signifies extremely strong multicollinearity, necessitating elimination.

2.2. Fundamental principles of the XGBoost model

XGBoost represents an enhanced machine learning framework derived from the gradient boosting decision tree (GBDT) architecture, constituting an advanced implementation within the gradient boosting algorithmic paradigm. It consists of multiple decision trees that combine predictions from several weak learners to produce the final predictive outcome. Reservoir thickness prediction represents a typical regression problem, generally expressed through the following regression prediction formula:

$$\hat{y}_c = \sum_{k=1}^{K} f_k\left(x_c\right) \tag{II}$$

Where x_c represents the input sample, $f_k\ (x_c)$ is the prediction result calculated by the k-th tree, and by applying the principle of ensemble learning, the prediction results of the k trees are superimposed to obtain the final prediction result $\hat{y}_c$ of XGBoost. XGBoost assigns weights to each tree, and the subsequent trees will focus on the prediction information from the previous trees. Through multiple rounds of iterations, they converge to the final prediction result. Moreover, a regularization term is added to increase the model complexity:

$$O = \sum_{c=1}^{n} L\left(y_c, \hat{y}_c\right) + \sum_{k=1}^{K} \Omega\left(f_k\right) \tag{III}$$

Where O represents the objective function established, L is the loss function to be calculated, and Ω is the regularization term added. Different from the conventional GBDT methods, the regularization term of XGBoost is:

$$\Omega\left(f_k\right) = \gamma T + \frac{1}{2}\lambda \sum_{q=1}^{T} \omega_q^2 \tag{IV}$$

Where γ represents the penalty factor, T indicates the number of leaf nodes, λ is the regularization parameter for leaf weights, ω_q represents the weight assigned to the leaf node at this time, and the regularization term is used to prevent the decision tree from being too large in scale, limit the number of leaf nodes, improve the model's out-of-sample performance, and mitigate overfitting risks through regularization constraints. The loss function is:

$$l(y_c, \hat{y}_c) = (y_c - \hat{y}_c)^2 \quad \text{(V)}$$

The XGBoost algorithm constructs its optimization objective function by integrating the prediction error term from the tree ensemble model with the model complexity regularization constraints:

$$W^{(U)} = \sum_{C=1}^{n} J\left(y_C, \hat{y}_C^{(t-1)} + f_t(x_C)\right) + \Omega\left(f_U\right) + C \quad \text{(VI)}$$

Where C represents a constant, and the target function is expanded using the Taylor series:

$$W^{(\ )} = \sum \left\{ J\left(y_C\ \hat{y}_C^{(\ )}\right) + g_C f_U\left(x_c\right) + -h_C f_U^2\left(x_C\right) \right\}$$
$$+\gamma T + -\lambda \sum \ \omega\ + C \quad \text{(VII)}$$

Where $g_c = \partial_{\hat{y}^{(U-1)C}} l(y_C, \hat{y}_C^{(U-1)})$, $h_c = \partial^2_{\hat{y}^{(U-1)}} l(y_C, \hat{y}_C^{(U-1)})$, denote the initial and successive rate-of-change measures in the differentiation hierarchy of the prediction error with respect to the model. Taking the first-order derivative of ω_q, we obtain the optimal objective function of XGBoost:

$$W = -\frac{1}{2}\sum_{q=1}^{T} \frac{G2_q}{H_q + \lambda} + \lambda T \quad \text{(VIII)}$$

The formula provides a structural scoring mechanism for tree models, with lower numerical values indicating superior topological configurations.

Take the derivative of **Equation VI** to obtain the optimal solution as follows:

$$\omega_q^* = -\frac{F_q}{R_q + \lambda} \quad \text{(IX)}$$

Where $F_q = \sum_{c \in I_q} g_c$, $R_q = \sum_{c \in I_q} h_c$ represent the sum of the first-order derivatives and the sum of the second-order derivatives of all input data mapped to leaf node q. I_q is the sample set of leaf nodes.

2.3. The principle of NRBO method

The NRBO is a novel metaheuristic optimization method whose inspiration primarily stems from two key principles: The NRSR and the TAO. By employing NRSR and TAO, the algorithm explores the search domain while enhancing convergence speed. NRBO exhibits strong evolutionary capabilities, rapid search performance, and excellent optimization ability.

(1) Exploratory starting point configuration: Throughout the primary population establishment process, NRBO creates a uniformly distributed candidate population spanning the solution space boundaries, which serves as the foundation for subsequent iterative refinement. Suppose there are N populations; NRBO uses Equation 10 to generate the random population:

$$h_o^k = lb + rand \times \left(ub - lb\right), k = 1,2,\ldots,N_{op}, p = 1,2,\ldots,\dim \quad \text{(X)}$$

In the population matrix representation, element h_o^k stores the position value of the k-th candidate solution in its p-th dimensional component, r and represents a random number within the range of (0, 1), and the search space is constrained by lb (minimum value) and ub (maximum value) for each parameter. Formula 11 depicts the population matrix of all dimensions:

$$H_k = \begin{bmatrix} h_1^1 & h_2^1 & \cdots & h_{\dim}^1 \\ h_1^2 & h_2^2 & \cdots & h_{\dim}^2 \\ \vdots & \vdots & \ddots & \vdots \\ h_1^{N_{oP}} & h_2^{N_{OP}} & \cdots & h_{\dim}^{N_{OP}} \end{bmatrix}_{N_{0P} \times \dim} \quad \text{(XI)}$$

(2) The NRSR is developed by adapting the classical Newton–Raphson method, with dual objectives of enhancing trend discovery capability and improving convergence rate. The Newton method is an iterative process used to find the roots of an equation. It obtains the next estimate by performing a two-dimensional Taylor Series (TS) around the current estimated minimum value. The iteration continues until the first derivative of the function approaches the threshold, and the minimum point estimate is finally determined. **Formula XII** represents the second-order Taylor Series of $v(h)$ at h_0:

$$v(h) = \frac{1}{0!} f(h_0) + \frac{1}{1!}(h - h_0) v'(h_0) + \frac{1}{2!}(h - h_0)^2 v'\left(h_0\right) \quad \text{(XII)}$$

By taking the derivative of both sides of the above equation and setting it equal to zero, we obtain the following equation:

$$v'\left(h\right) = v'\left(h_0\right) + v''\left(h_0\right)\left(h - h_0\right) = 0 \quad \text{(XIII)}$$

The above equation can be solved as:

$$h = h_0 - \frac{v'\left(h_0\right)}{v''\left(h_0\right)} \quad \text{(XIV)}$$

The above process is repeated until a point with zero derivative is obtained. **Formula XV** is the iterative formula for the obtained point:

$$h_{n+1} = h_n - \frac{v'\left(h_n\right)}{fv''\left(h_n\right)} \quad \text{(XV)}$$

In order to obtain NRSR from the above equation, the second-order Taylor series of $v(h + \Delta h)$ and $f(h-\Delta h)$ are written as follows:

$$v\left(h+\Delta h\right)=v\left(h\right)+v^{'}\left(h_0\right)\Delta h+\frac{1}{2!}v^{''}\left(h_0\right)\Delta h^2 \quad \text{(XVI)}$$

$$v\left(h-\Delta h\right)=v\left(h\right)-v^{'}\left(h_0\right)\Delta h+\frac{1}{2!}v^{''}\left(h_0\right)\Delta h^2 \quad \text{(XVII)}$$

By subtracting or adding **Formulas XVI and XVII**, the expressions of $v'(h)$ and $v''(h)$ can be obtained:

$$v^{'}\left(h\right)=\frac{v\left(h+\Delta h\right)-v\left(h-\Delta h\right)}{2\Delta h} \quad \text{(XVIII)}$$

$$v^{''}\left(h\right)=\frac{v\left(h+\Delta h\right)+v\left(h-\Delta h\right)-2v\left(h\right)}{\Delta h^2} \quad \text{(XIX)}$$

Substitute **Formulas XVIII and XIX** into **Formula XV**, and the updated root positions are as follows:

$$h_{n+1}=h_n-\frac{\left(v\left(h_n+\Delta h\right)-v\left(h_n-\Delta h\right)\right)\times\Delta h}{2\times\left(v\left(h_n+\Delta h\right)+v\left(h_n-\Delta h\right)-2\times v\left(h_n\right)\right)} \quad \text{(XX)}$$

Where $h_n + \Delta h$ and $h_n - \Delta h$ respectively represent the positions of adjacent x's to each other, and NRSR is defined as follows:

$$NRSR=randn\times\frac{\left(H_w-H_b\right)\times\Delta h}{2\times\left(H_w+XH_b-2\times h_n\right)} \quad \text{(XXI)}$$

Where *randn* generates random scalars drawn from the standard normal distribution ($\mu = 0$, $\sigma^2 = 1$). H_w and H_b, respectively, denote the worst and best positions.

$$\Delta h=rand\left(1,\dim\right)\times\left|H_b-H_n^{IT}\right| \quad \text{(XXII)}$$

Where H_b represents the current optimal solution, and $rand(1,dim)$ is a set of random numbers with *dim* decision variables. Then, by using NRSR, **Formula XI** is modified to:

$$h_{n+1}=h_n-NRSR \quad \text{(XXIII)}$$

A guidance parameter ρ is introduced to direct the population's positional updates toward the optimal solution region:

$$\rho=a\times\left(H_b-H_n^{IT}\right)+b\times\left(H_{s_1}^{IT}-H_{s_2}^{IT}\right) \quad \text{(XXIV)}$$

Where a and b are random numbers within the range of (0, 1), s_1 and s_2 are different integers selected, and the current position of the vector is updated by **Formula XXV**:

$$H1_n^{IT}=h_n^{IT}-\left(randn\times\frac{\left(H_w-H_b\right)\times\Delta h}{2\left(H_w+H_b-2\times H_n\right)}\right)+\left(a\left(H_b-H_n^{IT}\right)\right)+b\times\left(H_{s_1}^{IT}-H_{s_2}^{IT}\right) \quad \text{(XXV)}$$

Where the vector $H1_k^{IT}$ represents the updated position derived from h_k^{IT} through the enhanced NRSR, which constitutes an optimized variant of the standard Newton-Raphson Method (NRM). **Formula XXI** becomes:

$$NRSR=randn\times\frac{\left(y_w-y_b\right)\times\Delta h}{2\times\left(y_w+y_b-2\times h_n\right)} \quad \text{(XXVI)}$$

$$y_w=s_1\times\left(Mean\left(M_{K+1}+h_n\right)+s_1\times\Delta h\right) \quad \text{(XXVII)}$$

$$y_b=s_1\times\left(Mean\left(M_{K+1}+h_n\right)-s_1\times\Delta h\right) \quad \text{(XXVIII)}$$

$$M_{K+1}=h_K-randn\times\frac{\left(H_w-H_b\right)\times\Delta h}{2\times\left(H_w+H_b-2\times h_k\right)} \quad \text{(XXIX)}$$

Where y_w and y_b denote position vectors derived from M_{n+1} and h_k, respectively, where $s_1 \sim U(0,1)$, represents a uniformly distributed random coefficient. The candidate solution for the subsequent generation is determined by:

$$H_k^{IT}=h_k^{IT}-\left[randn\frac{\left(y_w-y_b\right)\Delta h}{2\left(h\left(y_w+y_b-2h_k\right)\right)}\right]+\left(a\left(H_b-H_k^{IT}\right)+b\left(H_k^{IT}-H_k^{IT}\right)\right) \quad \text{(XXX)}$$

(3) TAO: The TAO framework integrates an advanced optimization operator developed by Ahmadianfar *et al.*,[28] which significantly boosts NRBO's performance in real-world applications while mitigating local optimum convergence risks. This implementation activates when the stochastic variable rand (uniformly distributed in [0,1]) falls below the decisive factor DF (default threshold: 0.6). Then, the solution X_{TAO}^{IT} is generated using the following formula:

$$\begin{cases} X_{TAO}^{IT}=X_n^{IT+1}+\theta\times X(\mu_1\times x_n-\mu_2\times X_n^{IT}) \\ +\theta\times X\times\delta\times X(\mu_1\times Mean(X_n^{IT})-\mu_2\times X_n^{IT}),\mu_1<0.5 \\ X_{TAO}^{IT}=x_n+\theta\times X(\mu_1\times x_n-\mu_2\times X_n^{IT}) \\ +\theta\times X\times\delta\times X(\mu_1\times Mean(X_n^{IT})-\mu_2\times X_n^{IT}),\mu_1\geq 0.5 \end{cases} \quad \text{(XXXI)}$$

$$X_n^{IT+1}=X_{TAO}^{IT} \quad \text{(XXXII)}$$

Where *rand* is a random number, θ_1 and θ_2 are uniformly distributed random numbers within the range of (−1,1) and (−0.5,0.5), respectively. The parameters μ_1 and μ_2

are assigned stochastic values during initialization. The randomness of μ_1 and μ_2 prevents the population from falling into local optima.

2.4. VIF-NRBO-XGBoost reservoir prediction workflow

The VIF-NRBO-XGBoost-based prediction workflow for channel sand reservoir thickness proceeds as follows: First, seismic attributes are extracted and preliminarily optimized, prioritizing those with clear geological significance and superior quality. The selected seismic attributes then undergo outlier removal and normalization processing. Subsequently, VIF values are calculated for all extracted seismic attributes, combined with Pearson correlation coefficients for comprehensive attribute analysis. Hyperparameter selection for the XGBoost algorithm is accomplished through NRBO optimization. The processed seismic attributes are then paired with corresponding well-point thickness data to train the NRBO-XGBoost reservoir thickness prediction model. To ensure evaluation stability, K-fold cross-validation (with K = 5 in this study) is implemented, using the mean absolute error from five validation wells to assess prediction accuracy. Finally, the model predicts reservoir thickness for other target areas within the work zone. The complete workflow is illustrated in Figure 1.

3. Correlation analysis combined with VIF for selecting optimal seismic attributes

The typical lithofacies bodies in Jiyang Depression have rich reservoir types. The ancient river channel sand bodies are representative lithofacies among them. This paper takes Chengbei Oilfield as the research area, and the study section is the upper part of the Guantao Formation. The large and small river channels are superimposed and crossed, while the single sand body reservoir is thin. According to the geological meaning of seismic attributes and the comprehensive data quality, a total of 11 distinct seismic attributes from different categories were extracted from the target formation, including: Root mean square amplitude (RMS_amp), bandwidth (BW), zero-crossing count (ZCC), arc length (AL), energy half-time (EHT), average energy (AE), average instantaneous frequency (AIF), average amplitude (AA), positive amplitude sum (PAS), dominant frequency (DF), maximum amplitude (MA).

3.1. Correlation analysis of seismic attributes

In machine learning regression experiments, the Pearson correlation coefficient, scatter plots, and linear models are the three most commonly used methods. Figure 2 comprehensively displays the following: (i) Complete inter-variable linear dependencies are shown in the matrix upper triangle, quantifying how each of the 11 seismic attributes covaries with formation thickness at well locations; (ii) The lower triangle presents scatter plots of correlations between different attributes, as well as between all attributes and thickness, with overlaid linear regression lines. To better visualize the linear relationship between individual seismic attributes and thickness, along with statistical reliability, 95% confidence intervals are included in the scatter plots; (iii) The diagonal displays normalized distribution histograms and Kernel density estimation of the seismic attributes, clearly reflecting their distribution patterns. From the data and scatter plots as shown in Figure 2, individual seismic parameters demonstrate limited predictive capability for thickness estimation in reservoir formations, and the distribution of single attributes shows no significant patterns.

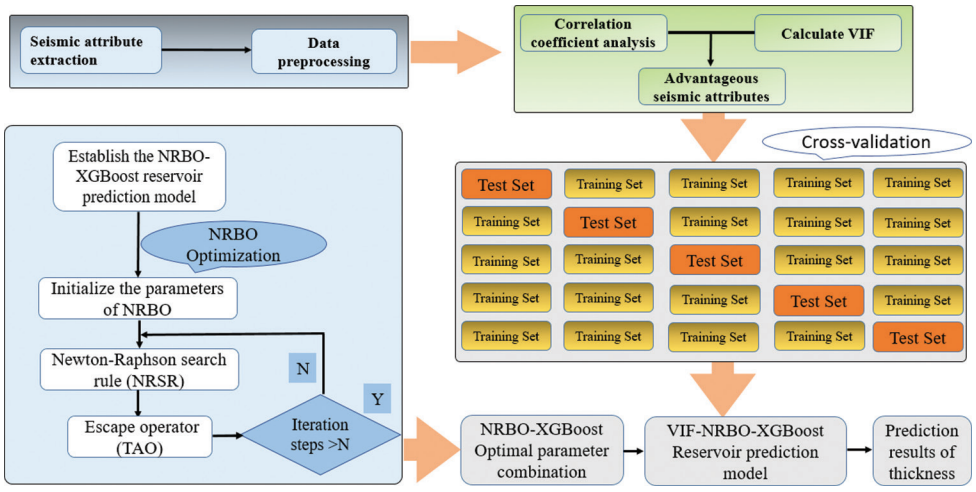

Figure 1. VIF-NRBO-XGBoost process for predicting reservoir thickness of riverbed sedimentary rocks
Abbreviations: NRBO: Newton-Raphson-based optimization; VIF: Variance inflation factor; XGBoost: eXtreme gradient boosting.

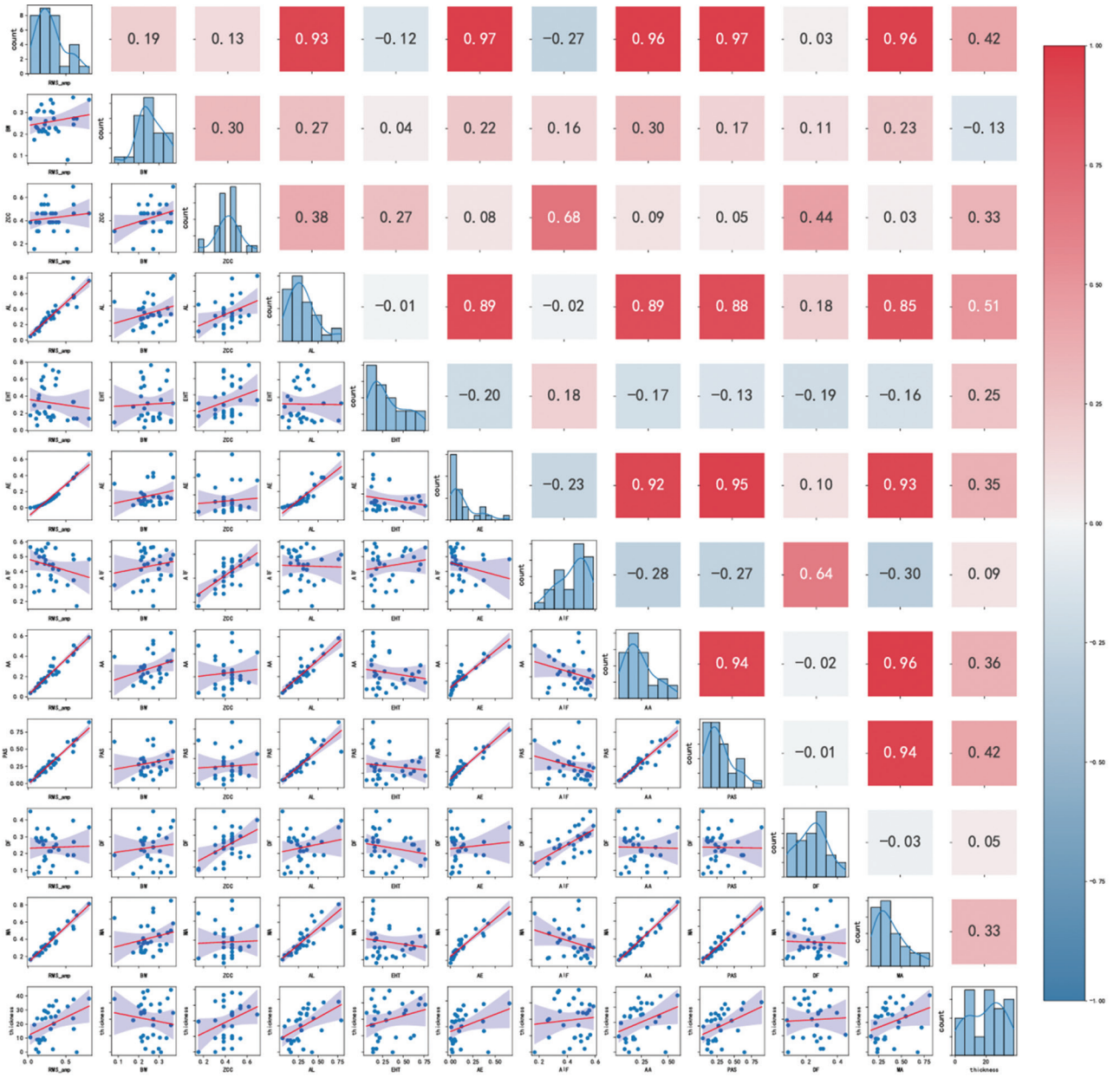

Figure 2. Correlation analysis

This further demonstrates the geological complexity of the study area.

3.2. Selection of VIF attributes

Before conducting attribute selection using VIF, to prevent the interference of seismic attributes with low correlation to reservoir thickness from affecting the attribute screening, leveraging the identified attribute-thickness correlations, the three seismic attributes with correlation <0.2 with reservoir thickness, namely bandwidth, AIF, and DF, were removed first.[29] Then, VIF analysis was conducted on the remaining seismic attributes. Figure 3 shows the VIF values and correlation coefficients of the remaining eight seismic attributes. It can be seen that the VIF value of the RMS amplitude is very high, indicating that there is severe multicollinearity between it and the other seismic attributes, and it must be eliminated. The VIF values of ZCC and EHT are very low, indicating that the multicollinearity of these two seismic attributes is very weak. In addition, the VIF values of AL, AE, AA, PAS, and MA are similar. As can be observed from Figure 2, among these four seismic attributes, AL shows the highest

correlation with thickness. Finally, three seismic attributes, namely AL, ZCC, and EHT, were retained for reservoir thickness prediction.

4. VIF-NRBO-XGBoost reservoir thickness prediction

To prevent overfitting or underfitting, considering the characteristics of limited sample data, the proportion of the test set is set to 15%. After multiple verifications, the general range of XGBoost's hyperparameters is found. Then, XGBoost is utilized to conduct prediction comparisons between the seismic attributes that have not undergone VIF screening and those that have undergone VIF screening. As shown in Figure 4, it can be observed that the degree of deviation of the prediction results of the seismic attributes after VIF screening is lower, and the prediction accuracy is higher.

The NRBO optimization, combined with cross-validation, is utilized to search for the optimal solution for the hyperparameters of XGBoost. The best parameter NRBO-

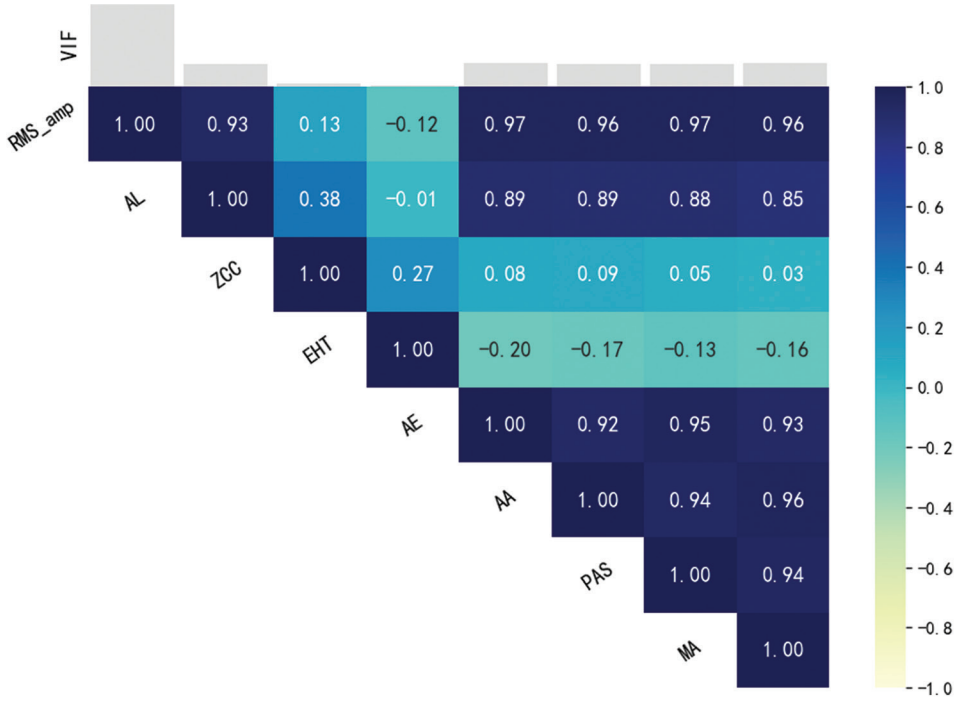

Figure 3. VIF of seismic attribute and correlation
Abbreviations: AA: Average amplitude; AE: Average energy; AL: Arc length; EHT: Energy half-time; MA: Maximum amplitude; PAS: Positive amplitude sum; RMS_amp: Root mean square amplitude; VIF: Variance inflation factor; ZCC: Zero-crossing count.

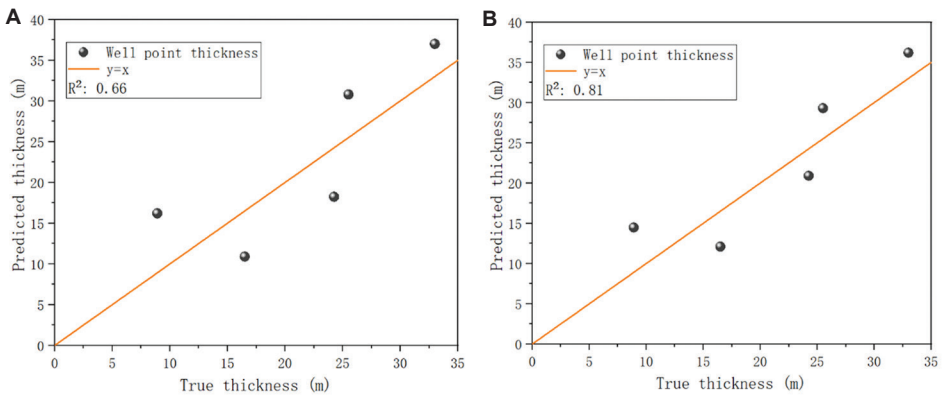

Figure 4. Comparison of XGBoost prediction results before (A) and after VIF screening (B)
Abbreviations: VIF: Variance inflation factor; XGBoost: eXtreme gradient boosting.

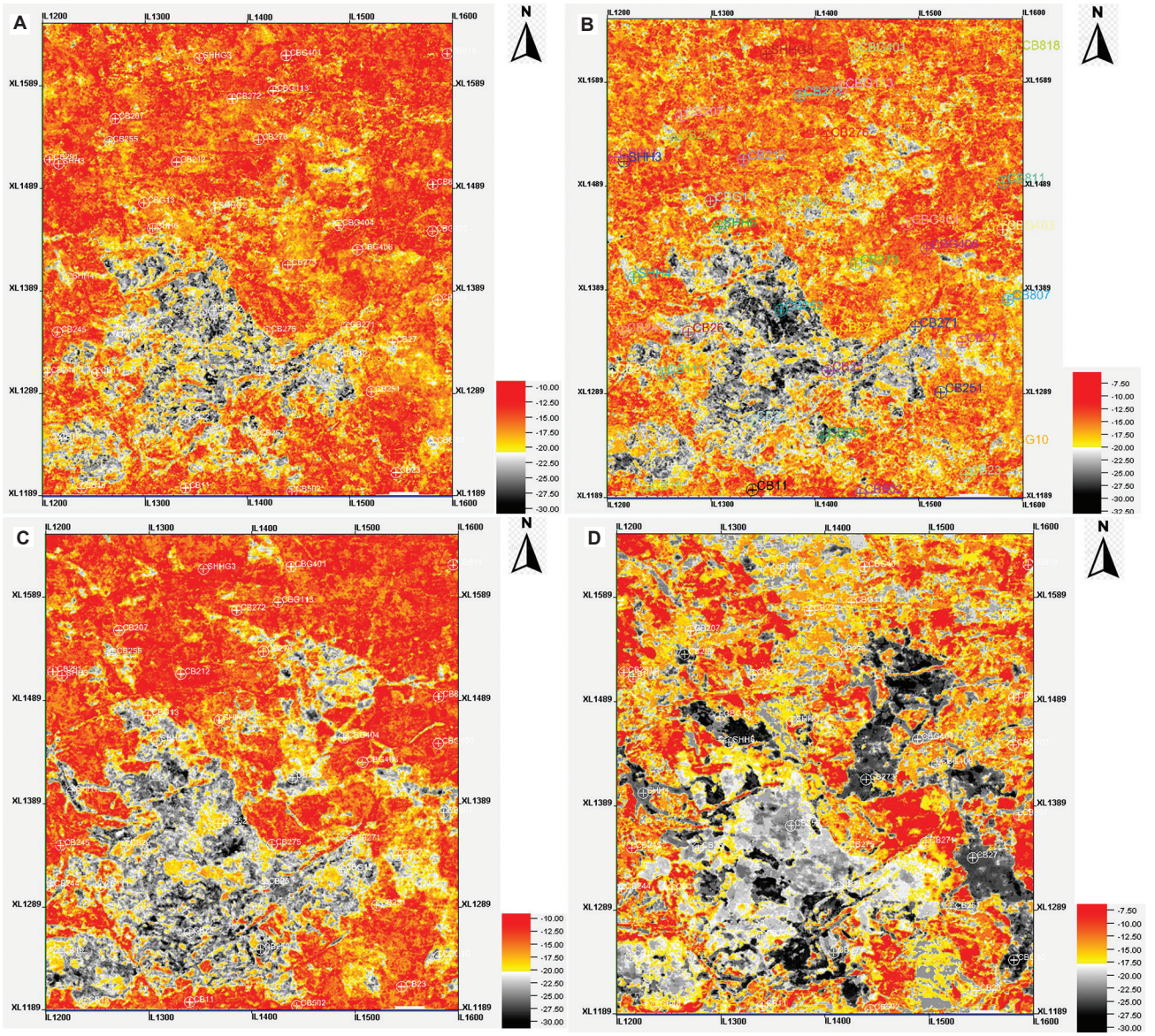

Figure 5. The prediction results of reservoir thickness of riverbed sand in the study area. (A) Predictive outputs from the SVM; (B) predictive outputs from the XGBoost, (C) predictive outputs from the VIF-XGBoost, and (D) predictive outputs from the VIF-NRBO-XGBoost.
Abbreviations: NRBO: Newton-raphson based optimization; SVM: Support vector machine; VIF: Variance inflation factor; XGBoost: eXtreme gradient boosting.

XGBoost is developed for sandstone thickness estimation in reservoir characterization, and the predictive outcomes are systematically benchmarked against conventional XGBoost results and Support Vector Machine (SVM) models that have not been optimized. The prediction results are shown in Figure 5, and the comparison of the average absolute error and R^2 of the prediction results of the four models for sand body thickness in the verification wells is presented in Table 1. Based on the prediction results, evidence suggests that the SVM model demonstrates low prediction accuracy with significant absolute errors, failing to capture the distinct morphological features of channel sand bodies. Although the VIF-XGBoost model provides a more accurate depiction of the eastern river channel sand bodies, its overall prediction accuracy remains inadequate. VIF-NRBO-XGBoost algorithm demonstrates dual capabilities in fluvial reservoir characterization, successfully capturing both the extensive channel systems in eastern sectors and accurately forecasting subtle channel deposits in southwestern regions.

The VIF-NRBO-XGBoost modeling results reveal distinct fluvial depositional patterns across the study

Table 1. Comparison of prediction results and mean absolute errors of four models for verification wells

Well name and evaluation metric	True thickness	SVM	XGBoost	VIF-XGBoost	VIF-NRBO-XGBoost
CB245	8.9 m	16.9 m	16.2 m	14.48 m	9.7 m
CB253	25.5 m	18.8 m	30.8 m	29.3 m	24.2 m
CB255	33 m	24.8 m	37 m	36.2 m	31.1 m
CB11	16.5 m	9.8 m	10.9 m	12.1 m	17.9 m
CB27	24.25 m	17.9 m	18.24 m	20.9 m	25.7 m
Mean absolute error	\	7.2 m	5.6 m	4.1 m	1.4 m
R^2	\	0.48	0.66	0.81	0.97

Abbreviations: NRBO: Newton–Raphson-based optimization; SVM: Support vector machine; VIF: Variance inflation factor; XGBoost: eXtreme gradient boosting.

area, with a prominent north-south-oriented channel belt dominating the eastern sector. Central regions exhibit maximum sandbody thickness accompanied by a gradual southeastward deflection of the channel axis. The southwestern domain contains smaller-scale channel features with potential tributary systems, displaying predominant northwest-to-southeast paleoflow orientations.

5. Discussion

To address the complex development of underground channel sand bodies in the Chengbei work area of the Jiyang Depression, characterized by chaotic, intersecting, and overlapping patterns, a novel VIF-NRBO-XGBoost model for sand body thickness prediction was introduced. The model was trained using 35 known wells and validated with five known wells (CB245, CB253, CB255, CB11, CB27), followed by a comprehensive prediction across the entire work area, effectively improving the thickness prediction accuracy for such complex channel sand bodies. The model primarily consists of the following steps:

First, 11 commonly used seismic attributes related to reservoir information were extracted and normalized. The Pearson correlation coefficient was employed to preliminarily screen these 11 seismic attributes, removing those with a correlation coefficient of <0.2 with sand body thickness. To prevent multicollinearity among the seismic attributes from affecting the prediction results, the remaining eight seismic attributes were subjected to multicollinearity analysis using VIF, and attributes with strong multicollinearity and redundant information were eliminated.

Table 2. Comparison of XGBoost model parameters before and after NRBO optimization

Model parameter	XGBoost	NRBO-XGBoost
n_estimators	150	193
max_depth	7	12
min_child_weight	3	1
learning_rate	0.04	0.059
colsample_bytree	0.5	0.57
gamma	6	4.5
alpha	3	3.559

Abbreviations: Alpha: Regularization coefficient; colsample_bytree: Feature random sampling ratio; gamma: Node splitting reduction coefficient; learning_rate: Learning rate; max_depth: Maximum tree depth; min_child_weight: Minimum leaf node weight; n_estimators: Number of decision trees; NRBO: Newton–Raphson-based optimization; XGBoost: eXtreme gradient boosting.

Due to the poor data quality in this region, single machine learning models exhibited significant prediction errors. An ensemble learning XGBoost model was introduced to enhance prediction accuracy by integrating the results of multiple weak learners. The performance of the XGBoost model largely depends on the selection of model parameters. In this study, the NRBO intelligent optimization algorithm was used to optimize the XGBoost model parameters, and the optimal parameter combination was employed for sand body thickness prediction, resulting in more refined channel sand body distribution predictions. Table 2 lists the seven core parameters of the XGBoost model before and after NRBO optimization: the number of decision trees (n_estimators), maximum tree depth (max_depth), minimum leaf node weight (min_child_weight), learning rate (learning_rate), feature random sampling ratio (colsample_bytree), node splitting reduction coefficient (gamma), and regularization coefficient (alpha).

Although the VIF-NRBO-XGBoost model outperforms other machine learning models in predicting the thickness of complex channel sand bodies with higher accuracy, the correlation analysis directly removed seismic attributes with extremely low correlation to thickness, potentially losing valuable information from these attributes. Future research will consider the modal information of seismic attributes to fully retain useful information from the discarded attributes. Additionally, further optimization of model parameters will be pursued to enhance the prediction accuracy of complex channel sand body thickness.

The data used in this study constitutes a small sample dataset. The performance of the aforementioned method on large sample datasets remains unclear and may require adjustments to the validation set ratio. The prediction accuracy of this method is somewhat dependent on data

quality and resolution, and the current model may exhibit uncertainties in predicting extremely thin sandstone layers. Future work will consider incorporating additional data sources, such as seismic attribute modalities, to further enhance the model's generalization capability.

6. Conclusion

This study proposes a novel sand body thickness prediction model—VIF-NRBO-XGBoost. The model utilizes multiple attributes for reservoir thickness prediction while fully considering the constraints of multicollinearity and correlation among seismic attributes, employing NRBO to optimize the parameters of the ensemble learning XGBoost model. Through its application in predicting complex channel sand bodies in the Chengbei area of Jiyang Depression, the reliability of the model was verified, with prediction results significantly outperforming other models. This will provide crucial support for detailed reservoir characterization and well placement in this region. The study not only offers new insights for reservoir thickness prediction in similar study areas, but also provides valuable references for predicting other reservoir parameters. It holds significant practical importance for hydrocarbon exploration and development.

Acknowledgments

None.

Funding

This study is supported by the National Science and Technology Major Project Management Office for New Oil and Gas Exploration and Development (NO. 2024ZD1400102); and Shengli Oilfield Jiyang Depression Typical Lithologic Body Project Fund (NO. 30200020-24-ZC0613-0062).

Conflict of interest

All authors declare no conflicts of interest.

Author contributions

Conceptualization: All authors
Formal analysis: All authors
Investigation: All authors
Methodology: All authors
Visualization: Weichao Zhang, Junhua Zhang
Writing–original draft: Weichao Zhang
Writing–review & editing: All authors

Availability of data

Data are available from the corresponding author on reasonable request. Note that certain datasets may not be shareable due to confidentiality reasons.

References

1. Wang S, Gu Z, Guo P, Zhao W. Comparative laboratory wettability study of sandstone, tuff, and shale using 12- MHz NMR T1- T2 fluid typing: Insight of shale. *SPE J*. 2024;29(9):4781-4803.

   doi: 10.2118/221496-PA

2. Ehsan M, Chen R, Manzoor U, *et al*. Unlocking thin sand potential: A data-driven approach to reservoir characterization and pore pressure mapping. *Geomech Geophys Geoenerg Georesour.* 2024;10:160.

   doi: 10.1007/s40948-024-00871-w

3. Liu L, Jin J, Liu J, *et al*. Mechanical properties of sandstone under *in-situ* high-temperature and confinement conditions. *Int J Miner Metall Mater*. 2025;32(4):778-787.

   doi: 10.1007/s12613-024-3047-9

4. Manzoor U, Ehsan M, Hussain M, Bashir Y. Improved reservoir characterization of thin beds by advanced deep learning approach. *Appl Comput Geosci*. 2024;23:100188.

   doi: 10.1016/j.acags.2024.100188

5. Dormann CF, Elith J, Bacher S, *et al*. Collinearity: A review of methods to deal with it and a simulation study evaluating their performance. *Ecography*. 2012;36:27-46.

   doi: 10.1111/j.1600-0587.2012.07348.x

6. Widess MB. How thin is a thin bed? *Geophysics*. 1973;38(6):1176-1180.

   doi: 10.1190/1.1440403

7. Chung HM, Lawton DC. Amplitude responses of thin beds: Sinusoidal approximation versus Ricker approximation. *Geophysics*. 1995;60(1):19-307.

   doi: 10.1190/1.1443750

8. Long J. Neural network BP modeling of the relation between thin bed thickness and amplitude-frequency. *Oil Geophys Prospect*. 1995;30(6):817-822.

9. Zhuang D, Xiao C. Thin-bed thickness estimation using neural network. *Oil Geophys Prospect*. 1996;31(3):394-399.

10. Gridley JA, Partyka GA. *Processing and Interpretational Aspects of Spectral Decomposition: 67th Annual International Meeting of the Society of Exploration Geophysicists. Expanded Abstracts*; 1997. p. 1055-1058.

11. Partyka GA, Gridley JA, Lopez JA. Interpretational aspects of spectral decomposition in reservoir characterization. *Lead Edge*. 1999;18(3):353-360.

12. Ye T, Su J, Liu X. Application of seismic frequency division interpretation technology in predicting continental sandstone reservoir in the west of Sichuan province. *Geophys Prospect Petrol*. 2008;47(1):72-76.

13. Sun L, Zheng X, Shou H, Li J, Li Y. Quantitative prediction of channel sand bodies based on seismic peak attributes in the frequency domain and its application. *Appl Geophys*. 2010;7(1):10-17.

doi: 10.1007/s11770-010-0009-y

14. Barnes AE, Fink L, Laughlin K. *Improving Frequency Domain Thin Bed Analysis. SEG Technical Program Expanded Abstracts*. United States: SEG. 2004. p. 1929-1932.

doi: 10.1190/1.1851175

15. Wang Z, Gao D, Lei X, Wang D, Gao J. Machine learning-based seismic spectral attribute analysis to delineate a tight-sand reservoir in the Sulige gas field of central Ordos Basin, western China. *Mar Petrol Geol*. 2020;113:104136.

doi: 10.1016/j.marpetgeo.2019.104136

16. Li W, Yue D, Wang W, *et al*. sing multiple frequency-decomposed seismic attributes with machine learning for thickness prediction and sedimentary facies interpretation in fluvial reservoirs. *J Petrol Sci Eng*. 2019;177:1087-1102.

doi: 10.1016/j.petrol.2019.03.017

17. Yue D, Li W, Wang W, *et al*. Fused spectral-decomposition seismic attributes and forward seismic modelling to predict sand bodies in meandering fluvial reservoirs. *Mar Petrol Geol*. 2019;99:27-44.

doi: 10.1016/j.marpetgeo.2018.09.031

18. Chopra S, Marfurt KJ. Seismic attributes - A historical perspective. *Geophysics*. 2005;70(5):1SO-Z82.

doi: 10.1190/1.2098670

19. Liu S. A grain size profile prediction method based on combined model of extreme gradient boosting and artificial neural network and its application in sand control design. *SPE J*. 2024;29(6):2988-3002.

doi: 10.2118/219484-PA

20. Zhang D, Qian L, Mao B, *et al*. A data-driven design for fault detection of wind turbines using random forests and XGboost. *IEEE Acess*. 2018;6:21020-21031.

doi: 10.1109/ACCESS.2018.2818678

21. Yu B, Qiu W, Chen C, *et al*. SubMito-XGBoost: Predicting protein submitochondrial localization by fusing multiple feature information and eXtreme gradient boosting. *Bioinformatics*. 2020;36(4):1074-1081.

doi: 10.1093/bioinformatics/btz734

22. Kounlavong K, Sadik L, Keawsawasvong S, Jamsawang P. Novel hybrid XGBoost-based soft computing models for predicting penetration resistance of buried pipelines in cohesive soils. *Ocean Eng*. 2024;311(2):118948.

doi: 10.1016/j.oceaneng.2024.118948

23. Liu X, Zhang J, Bai Q, *et al*. Research and application of sandstone thickness prediction method based on NRBO-XGBoost optimization method. *Comput Techn Geophys Geochem Explor*. 2024;46(2):146-153.

doi: 10.3969/j.issn.1001-1749.2024.02.03 (in Chinese)

24. Liu L, Li W, Du Y, *et al*. Reservoir prediction method of fusing frequency-decomposed seismic attributes using Stacking ensemble learning. *Oil Geophys Prospect*. 2024;59(1):12-22.

doi: 10.13810/j.cnki.issn.1000-7210.2024.01.002 (in Chinese)

25. Cheng J, Sun J, Yao K, Xu M, Cao Y. A variable selection method based on mutual information and variance inflation factor. *Spectrochim Acta A Mol Biomol Spectrosc*. 2022;268:120652.

doi: 10.1016/j.saa.2021.120652

26. Chen T, Guestrin C. XGBoost: A scalable tree boosting system. In: *Proceedings of the 22nd ACM SIGKDD International Conference on Knowledge Discovery and Data Mining*. USA; 2016. p. 785-794.

doi: 10.1145/2939672.2939785

27. Sowmya R, Premkumar M, Jangir P. Newton raphson-based optimizer: A new population-based metaheuristic algorithm for continuous optimization problems. *Eng Appl Artif Intell*. 2024;128(C):107532.

doi: 10.1016/j.engappai.2023.107532

28. Ahmadianfar I, Bozorg-Haddad O, Chu X. Gradient-based optimizer: A new metaheuristic optimization algorithm. Information *Sciences*. 2020;540:131-159.

doi: 10.1016/j.ins.2020.06.037

29. Lian Y, Luo J, Xue W, Zuo G, Zhang S. Cause-driven streamflow forecasting framework based on linear correlation reconstruction and long short-term memory. *Water Resour Manag*. 2022;36:1661-1678.

doi: 10.1007/s11269-022-03097-1

ACCSCIENCE PUBLISHING

Journal of Seismic Exploration

ARTICLE

Data-driven high-resolution gas-bearing prediction in tight sandstones: A case study from block L, Eastern Ordos Basin

Lixin Tian[†]*, Shuai Sun[†], Qixin Li, Jingxue Shi

Cnooc Research Institute Ltd., Chaoyang District, Beijing, China

(This article belongs to the *Special Issue: Geophysical Inversion and Intelligent Prediction Technologies for Complex Hydrocarbon Reservoirs*)

Abstract

The Upper Paleozoic Shihezi Formation in Block L of the eastern Ordos Basin harbors extensive tight sandstone gas reservoirs. However, these reservoirs exhibit strong heterogeneity, thin sand bodies, and overlapping elastic properties between gas- and water-bearing layers, which significantly limit the effectiveness of conventional pre-stack inversion methods in delineating thin sand bodies and predicting gas saturation. To address these challenges, we propose an integrated high-resolution gas prediction technique combining geostatistical inversion with deep learning. First, within a Bayesian sequential inversion framework, we jointly inverted well-log data, seismic data, and geological constraints to obtain high-resolution elastic parameters, substantially improving the identification of thin sand bodies (<5 m). Second, we employed a long short-term memory network to extract temporal features from inverted elastic parameter sequences and establish a non-linear mapping between gas/water-sensitive attributes and water saturation; this step incorporates horizon constraints and an attribute optimization strategy to enhance prediction accuracy. Field applications demonstrated that our method achieved superior performance compared to conventional approaches, with an 85% consistency rate between predicted gas saturation and drilling results. The integration of geostatistical inversion and deep learning provides a robust workflow for characterizing thin, heterogeneous tight gas reservoirs, offering significant potential for optimizing exploration and development strategies in the Ordos Basin.

Keywords: Ordos Basin; Tight sandstone gas; Geostatistical inversion; Deep learning; Long short-term memory network; Gas-bearing prediction

[†]These authors contributed equally to this work.

***Corresponding author:**
Lixin Tian
(ssun30143@gmail.com)

Citation: Tian L, Sun S, Li Q, Shi J. Data-driven high-resolution gas-bearing prediction in tight sandstones: A case study from block L, Eastern Ordos Basin. *J Seismic Explor*. 2025;34(3):13-24. doi: 10.36922/JSE025320053

Received: August 6, 2025

Revised: September 1, 2025

Accepted: September 3, 2025

Published online: September 30, 2025

1. Introduction

The Permian Shihezi Formation in Block L of the northeastern Ordos Basin harbors large-scale tight sandstone gas reservoirs with proven geological reserves exceeding 10 billion cubic meters, making it a critical gas-producing interval in the basin.[1-4] These reservoirs are deposited in a fluvial-deltaic environment influenced by seasonal flooding, characterized by thin-bedded (2–12 m thick, with 70% of layers <5 m) and lenticular sand bodies exhibiting strong lateral heterogeneity and frequent vertical interbedding

with mudstones. The lithology primarily comprises quartz sandstones underlain by coal-bearing source rocks of the Shanxi-Taiyuan Formations, forming typical tight gas reservoirs through a "source-reservoir pressure differential" driving mechanism.[5] However, reservoir prediction in this area faces three major challenges: (i) impedance contrast limitations: post-stack impedance inversion is hindered by the minimal acoustic impedance contrast between sandstone and mudstone, restricting effective spatial prediction of sand bodies. (ii) Resolution constraints: conventional pre-stack inversion is limited by the seismic data's dominant frequency (30 Hz in the target zone), resulting in a theoretical resolution limit ($\lambda/4 \approx 38$ m) that far exceeds the average sandstone thickness (<15 m). (iii) Fluid discrimination difficulty: gas-bearing and water-bearing layers exhibit substantial overlap in P-impedance versus Vp/Vs crossplots, rendering rock physics template methods ineffective for gas saturation prediction. Geostatistical inversion, which integrates geological priors with stochastic simulation, has emerged as a key solution for thin-bed reservoir characterization.[6] This approach has been successfully validated in continental thin sandstones[7] and coal bed methane reservoirs.[8]

Extensive research has focused on seismic gas-bearing prediction.[9-14] Since gas saturation has minimal influence on seismic waveforms (often obscured by noise), conventional methods typically derive elastic parameters through seismic inversion before identifying gas-bearing zones. For instance, Zong *et al.*[15] developed fluid-sensitive factors via direct P- and S-wave inversion, while Zong and Yin[16] constructed sensitivity factors using amplitude versus offset (AVO) linear equations to estimate Young's modulus and Poisson's ratio, thereby reducing cumulative errors from traditional elastic parameter inversion. Although pre-stack inversion-derived elastic parameters can effectively identify reservoirs,[17,18] they remain limited by thin-bed tuning effects.

For the Shihezi Formation's thin tight sandstones—where gas-water overlap is severe—conventional fluid identification methods fail due to insufficient seismic resolution and ineffective elastic sensitivity factors. Recent advances in deep learning have introduced data-driven approaches for gas prediction.[19,20] Early work by Hampson *et al.*[21] demonstrated successful porosity prediction using probabilistic neural networks to extract seismic attributes from waveform data. Similarly, Zhong *et al.*[22] showed that connected neural network (CNN)-based permeability prediction models outperform traditional genetic algorithms, while Das and Mukerji[23] achieved direct porosity and clay content inversion from post-stack data using CNN-trained synthetic models. Notably, Chen *et al.*[24] found that recurrent neural networks (RNNs) significantly outperform support vector machines and random forests in well-log time-series modeling, offering new opportunities for time-sensitive reservoir parameter prediction.

To address these challenges, this study proposes a data-driven high-resolution gas-bearing prediction framework for tight sandstones, combining: (1) pre-stack geostatistical inversion to integrate well-log, seismic and geological data for high-resolution elastic parameter estimation and (2) a long short-term memory (LSTM) network to establish a nonlinear mapping between time-series elastic parameters and water saturation (Sw), constrained by geological horizons and optimized attribute selection. Field applications demonstrate that our method significantly improves thin-bed identification and gas-prediction accuracy, providing a robust technical solution for tight gas exploration in the Ordos Basin with broader applicability to similar reservoirs.

2. Methodology

2.1. Technical workflow

The direct inversion of Sw from seismic data remains challenging due to its significantly weaker sensitivity to seismic waveform characteristics compared to elastic parameters.[25] In contrast, elastic parameters not only predominantly control seismic wavefield dynamics[26] but also exhibit more quantifiable physical relationships with Sw through established rock physics models. To address these challenges, we developed an integrated workflow combining geostatistical inversion with deep learning (Figure 1), which consists of three key components: (i) high-resolution geostatistical inversion: conducting pre-stack geostatistical inversion using well logs, geological structural frameworks, and 3D seismic data to overcome the bandwidth limitations of conventional seismic inversion and obtain high-resolution elastic parameters for

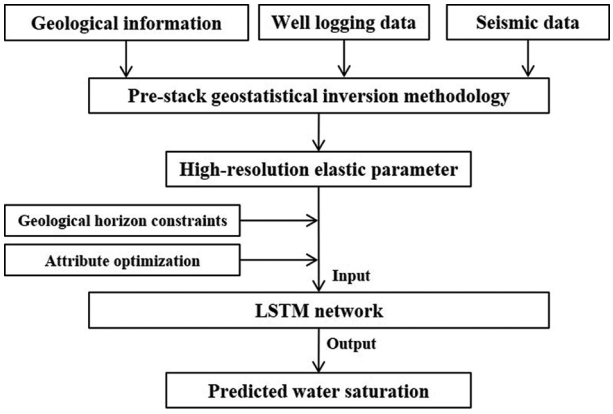

Figure 1. The workflow of data-driven high-resolution gas-bearing property prediction
Abbreviation: LSTM: Long short-term memory.

thin sand body identification; (ii) LSTM-based saturation modeling: leveraging the unique sequential modeling capability of LSTM networks while incorporating horizon constraints for segmented refinement learning, where attribute optimization techniques are employed to select elastic attribute combinations most sensitive to Sw, thereby establishing a sequential mapping between high-resolution elastic data and Sw to address the overlap issue of elastic parameters in gas-water layers; (iii) Model training and application: training the network using inverted traces adjacent to wells, with the fully trained LSTM model ultimately being applied to the tight sandstone reservoirs of the Shihezi Formation.

2.2. Geostatistical inversion

Unlike conventional deterministic inversion, geostatistical inversion statistically integrates prior information from well logs and geological data with seismic observations d_{obs} and estimates the posterior distribution of model parameters, m, through Bayesian inversion.[27] The expectation of the posterior probability solution is given by:

$$\tilde{\mathrm{m}} = \mathrm{m}_{prior} + \mathrm{C}_m \mathrm{G}^T (\mathrm{G}\mathrm{C}_m \mathrm{G}^T + \mathrm{C}_d)^{-1} \left(\mathrm{d}_{obs} - \mathrm{G}\mathrm{m}_{prior}\right) \quad \text{(I)}$$

The posterior covariance is expressed as:

$$\tilde{\mathrm{C}}_m = \mathrm{C}_m - \mathrm{C}_m \mathrm{G}^T (\mathrm{G}\mathrm{C}_m \mathrm{G}^T + \mathrm{C}_d)^{-1} \mathrm{G}\mathrm{C}_m \quad \text{(II)}$$

where $\mathrm{m}_{prior} = \left[\ln V_p, \ln V_s, \ln \rho\right]^T$ is a $3n_m$ column vector composed of smoothed background models for P-wave velocity, S-wave velocity, and density. C_m denotes the $3n_m \times 3n_m$ prior model covariance matrix; C_d is the seismic covariance matrix, estimated through well synthetic seismograms and field seismic data adjacent to wells.

Building upon the sequential simulation concept,[18,28] the sequential inversion framework classifies observed data into two distinct categories: Type A and Type B data. Type A data are direct measurements of model parameters, including well log data and previously simulated grid points. Type B data are indirectly acquired measurement data, specifically referring to pre-stack seismic angle gathers in this context. By jointly incorporating both data types, the forward equation can be reformulated as:

$$\begin{bmatrix} \mathrm{d}_{obsA} \\ \mathrm{d}_{obsB} \end{bmatrix} = \begin{bmatrix} \mathrm{G}_A & 0 \\ 0 & \mathrm{G}_B \end{bmatrix} \begin{bmatrix} \mathrm{m}_A \\ \mathrm{m}_B \end{bmatrix} + \begin{bmatrix} \mathrm{e}_A \\ \mathrm{e}_B \end{bmatrix} \quad \text{(III)}$$

Where d_{obs}, G_A, m_A, e_A represent the observed data, forward operator, model parameters, and error terms for Type A data, respectively; d_{obsB}, G_A, m_A, e_A denote the observed data, forward operator, model parameters, and error terms for type B data, respectively; G_A is simply an identity matrix. Performing Bayesian inversion on the joint data in **Equation III** yields the posterior expectation constrained by both well log data (type A) and pre-stack seismic data (type B):

$$\tilde{\mathrm{m}}_{A+B} = \mathrm{m}_{priorA+B} + \mathrm{C}_{mA+B} \mathrm{G}_{A+B}^T (\mathrm{G}_{A+B} \mathrm{C}_{mA+B} \mathrm{G}_{A+B}^T + \mathrm{C}_{dA+B})^{-1} (\mathrm{d}_{obsA} - \mathrm{G}\mathrm{m}_{priorA+B}) \quad \text{(IV)}$$

and posterior covariance:

$$\tilde{\mathrm{C}}_{mA+B} = \mathrm{C}_{mA+B} - \mathrm{C}_{mA+B} \mathrm{G}_{A+B}^T (\mathrm{G}_{A+B} \mathrm{C}_{mA+B} \mathrm{G}_{A+B}^T + \mathrm{C}_{dA+B})^{-1} \mathrm{G}_{A+B} \mathrm{C}_{mA+B} \quad \text{(V)}$$

where the covariance matrices C_{mA+B} (model) and C_{dA+B} (data) are formally expressed as:

$$\mathrm{C}_{mA+B} = \begin{bmatrix} \mathrm{C}_{mAA} & \mathrm{C}_{mAB} \\ \mathrm{C}_{mAB}^T & \mathrm{C}_{mBB} \end{bmatrix}, \mathrm{C}_{dA+B} = \begin{bmatrix} 0 & 0 \\ 0 & \mathrm{C}_{dBB} \end{bmatrix} \quad \text{(VI)}$$

The model covariance matrices for Type A and Type B data are denoted as C_{mAA} and C_{mBB}, respectively, while C_{mAB} represents their cross-covariance matrix. The data covariance matrix for type B observations is specified as C_{dBB}. The Bayesian sequential stochastic inversion framework treats well log data and previously simulated points as hard constraints. Under the joint constraints of geostatistical information and seismic data, these data participate in computing subsequent grid points. Consequently, well-derived information propagates throughout the stochastic simulation path, endowing the inverted elastic parameters with high-resolution characteristics.

2.3. LSTM network

LSTM networks,[29] a specialized variant of RNNs,[30] were specifically designed to address the vanishing gradient problem in traditional RNNs while preserving long-range temporal dependencies. The basic LSTM unit, illustrated in Figure 2, consists of three core components: the input gate, forget gate, and output gate. These gates selectively regulate information flow, enabling the modeling of long-term temporal dependencies. Specifically, this mechanism allows the network to dynamically store or discard temporal features, significantly enhancing its ability to process long sequential data. The input-output relationship of an LSTM unit can be described by the following equations:

$$f_t = \sigma(W_{xf} X_t + W_{yf} Y_{t-1} + W_{cf} \circ C_{t-1} + b_f) \quad \text{(VII-a)}$$

$$i_t = \sigma(W_{xi} X_t + W_{yi} Y_{t-1} + W_{ci} \circ C_{t-1} + b_i) \quad \text{(VII-b)}$$

$$C_t = f_t \circ C_{t-1} + i_t \circ \tanh(W_{xc} X_t + W_{yc} Y_{t-1} + b_c) \quad \text{(VII-c)}$$

$$O_t = \sigma(W_{xo}X_t + W_{yo}Y_{t-1} + W_{co} \circ C_t + b_o) \quad \text{(VII-d)}$$

$$Y_t = O_t \tanh(C_t) \quad \text{(VII-e)}$$

where ∘ denotes the Hadamard product; *represents convolution; W and b correspond to the weight matrices and bias vectors of the LSTM network, respectively; X_t signifies the input data; Y_t denotes the output parameters; C_t represents the cell state (memory unit); and i_t, f_t, and O_t indicate the input gate, forget gate, and output gate, respectively.

Figure 3 illustrates the deep learning architecture for Sw prediction based on an LSTM network. The core feature of this architecture lies in its use of elastic parameter time series as network inputs, as opposed to traditional single-point input patterns. Specifically, at each time step t, a multidimensional elastic vector X_t = [EP_1(t), EP_2(t), EP_3(t)…] is fed into the network. This design offers dual advantages: first, the temporal characteristics of the data are explicitly modeled through the LSTM gating mechanism; second, the joint input of elastic parameters at the same time step (such as P-impedance and Vp/Vs) captures the petrophysical correlations between parameters. In terms of technical implementation, the length in the time dimension is selected based on the wavelength of the seismic wavelet, while the choice of elastic data is determined through attribute optimization results. Regarding the network output mechanism, the LSTM outputs the hidden state Y_t at each time step, which serves as input to a fully connected

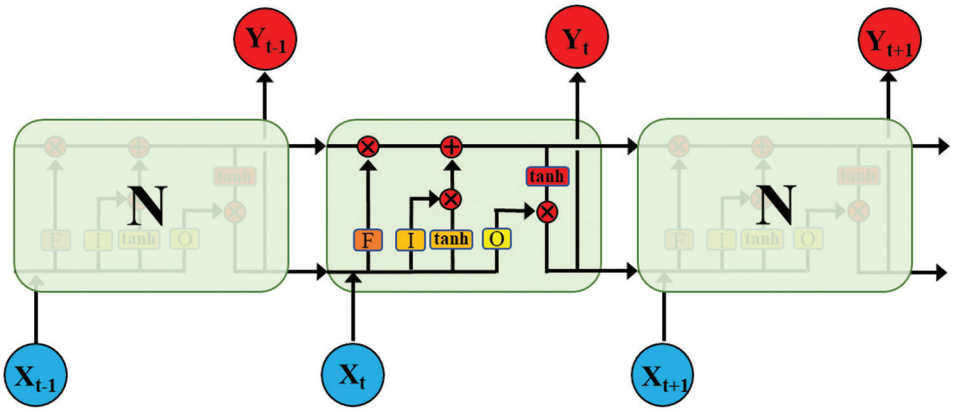

Figure 2. The architecture of the LSTM network. Symbol "N" represents the unit of LSTM; the terms X_t, $t = 1,2,...,n$ and Y_t, $t = 1,2,...,n$ represent input and output sequence data, respectively.
Abbreviation: LSTM: Long short-term memory.

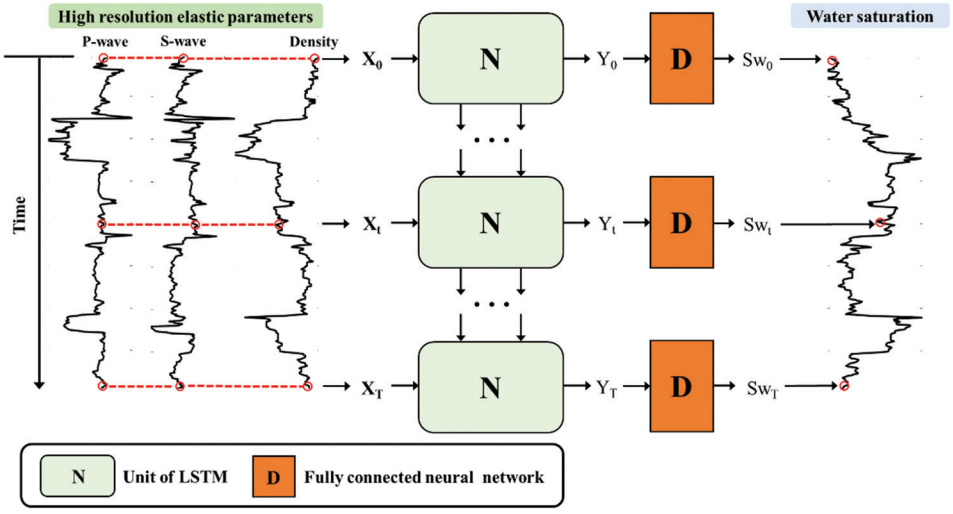

Figure 3. Deep learning-based high-resolution gas-bearing property prediction architecture. Symbol "N" represents the unit of LSTM, with detailed structure shown in Figure 2. Symbol "D" represents the FCNN, which is used in the conversion of time-series to Sw.
Abbreviation: FCNN: Fully connected neural network; LSTM: Long short-term memory; Sw: Water saturation.

neural network (FCNN). The predicted Sw value can be expressed as:

$$Sw_t = \sigma_P(W_\rho Y_t + b_\rho) \quad \text{(VIII)}$$

where the weight matrix W_p and bias vector b_p constitute the trainable parameters of the FCNN, and Y_t represents the hidden state output of the LSTM unit at time step t. The network employs ReLU activation functions[31] for nonlinear transformation: $\sigma_p(x) = max\ (0,x)$. Notably, this architecture adopts a time-step-shared weight parameter mechanism, meaning the FCNN's weights and biases remain constant across different time steps. This design achieves parameter efficiency and overfitting suppression. The complete set of learnable parameters includes:

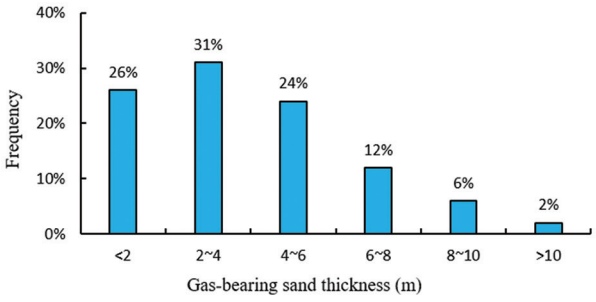

Figure 4. Statistical distribution of gas-bearing sandstone thickness in the Shihezi Formation, Ordos Basin

$$\Theta = \{W_{xf}, W_{yf}, W_{cf}, b_f, W_{xi}, W_{yi}, W_{ci}, b_i, W_{xc}, W_{yc}, b_c, W_{xo}, W_{yo}, W_{co}, b_o, W_\rho, b_\rho\} \quad \text{(IX)}$$

3. Case study

3.1. Target formation overview

The target interval of the Shihezi formation in the study area is predominantly composed of tight sandstone intercalated with mudstone. Statistical analysis reveals that individual sand bodies have an average thickness below 15 m, with gas-bearing sand bodies thinner than 6 m constituting over 80% of the total reservoir units (Figure 4). Petrophysical characterization demonstrates that these tight sandstones are distinguished by remarkably low Vp/Vs ratios (Vp/Vs < 1.8). Figure 5 presents a comparative analysis between Vp/Vs curves derived from well log interpretation (red solid line) and conventional pre-stack inversion (blue solid line), with lithological interpretation indicating sandstone intervals in yellow and gas-bearing sandstones in red. Due to resolution constraints inherent in conventional inversion methodologies, only thicker sand bodies can be confidently identified, while thinner sand bodies exhibit poor resolution. This resolution limitation directly compromises accurate reservoir assessment. Furthermore, petrophysical cross-plot analysis indicates substantial overlap between gas-bearing and water-bearing layers within the sandstone reservoirs

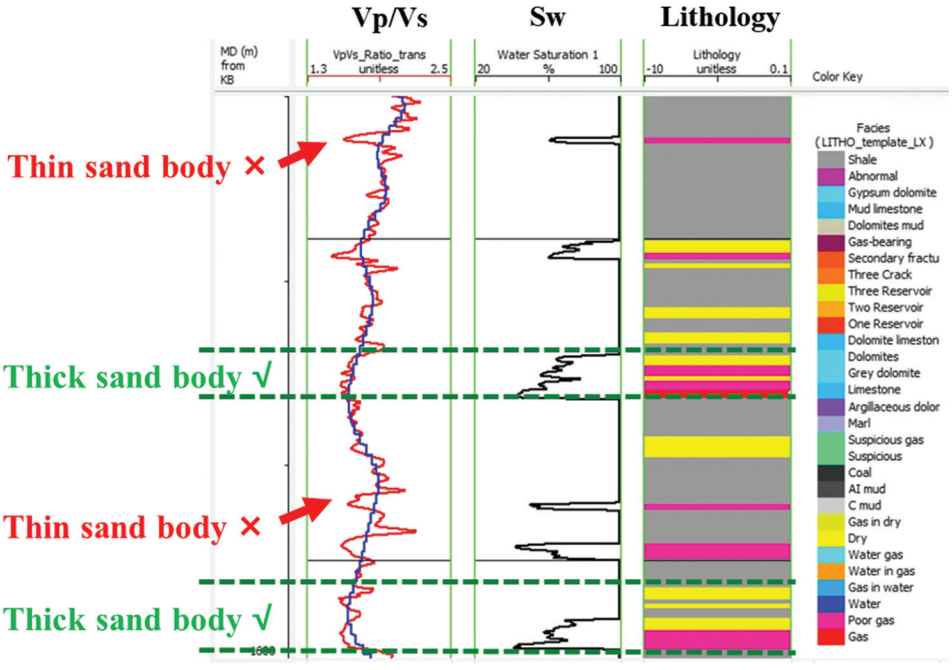

Figure 5. Lithology identification using conventional pre-stack inversion Vp/Vs. The red and blue solid lines represent the well logging and conventional pre-stack inverted Vp/Vs curves, respectively. In the lithology interpretation, yellow and red colors indicate sandstone and gas-bearing sandstone, respectively.

(Figure 6). This overlap significantly challenges effective fluid discrimination when employing conventional elastic parameter cross-plotting techniques.

3.2. High-resolution pre-stack geostatistical inversion

3.2.1. Vertical range determination from well log statistics

The variogram, serving as a fundamental geostatistical tool, provides quantitative characterization of reservoir parameter spatial variability.[32] The range parameter plays a particularly crucial role in defining reservoir thickness and lateral continuity patterns. Analysis of 94 well logs from the Shihezi Formation (Figure 7) and geological data demonstrates that thin sand layers are widely developed in the study area, with approximately 80% of gas-bearing sand bodies having thicknesses <6 m. Based on this finding, the vertical range was determined to be 1 ms. Simultaneously, statistical results reveal significant lateral variations in tight sandstones, with 85% of sand body widths distributed within the 300–1500 m range. Consequently, the lateral range was set to 800 m. It must be emphasized that determining the lateral range requires comprehensive consideration of both the depositional characteristics of the target formation and reservoir prediction results to ensure the rationality of parameter settings.

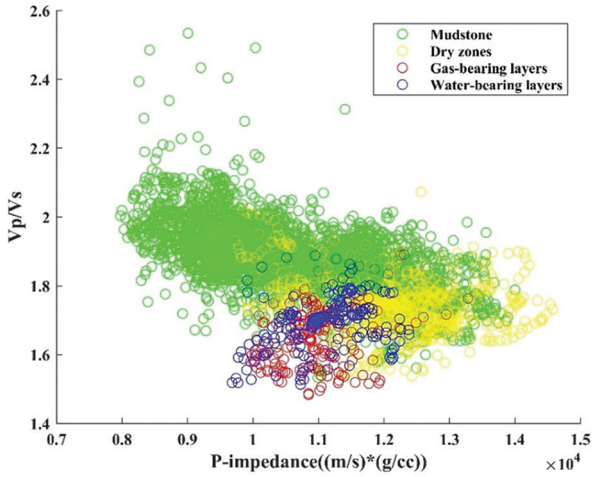

Figure 6. Crossplot analysis of P-impedance versus Vp/Vs in Shihezi formation, where green, yellow, blue, and red circles represent shale, dry layer, water-bearing layer, and gas-bearing layer, respectively. Significant overlap is observed between gas-bearing and water-bearing sandstones.

3.2.2. Application results of elastic parameter inversion

The pre-stack geostatistical inversion method integrates four key data types: (i) geological grid models, (ii) variogram parameters, (iii) well-log data, and (iv) pre-stack seismic data to construct a Bayesian inversion framework for estimating posterior probability distributions. We employed sequential Gaussian simulation to generate multiple realizations (n = 100) of elastic parameters from the tight sandstone reservoirs in the Shihezi Formation, Block L. The inversion used pre-stack seismic gathers with 20 m CDP spacing, 1 ms time sampling, and 5°–35° incidence angles. Figure 8 compares three datasets near well A: (i) measured well-log data (black curves), (ii) conventional pre-stack inversion results (blue curves), and (iii) P50 geostatistical inversion results (red curves) for Vp, Vs, density, and Vp/Vs ratio. Applying the Vp/Vs < 1.8 sandstone discrimination criterion, the geostatistical approach resolved thin gas-bearing sand layers (2–5 m thickness) that conventional inversion failed to detect. Figure 9 displays cross-well sections comparing: (i) conventional versus (ii) Geostatistical inversion results, annotated with lithology interpretations from Wells B–D (yellow: sandstone; red: gas-bearing sand). The geostatistical Vp/Vs results show superior vertical resolution (arrow indicators). Collectively, these results demonstrate that pre-stack geostatistical inversion technology can significantly improve resolution and enable detailed characterization of thin sand bodies.

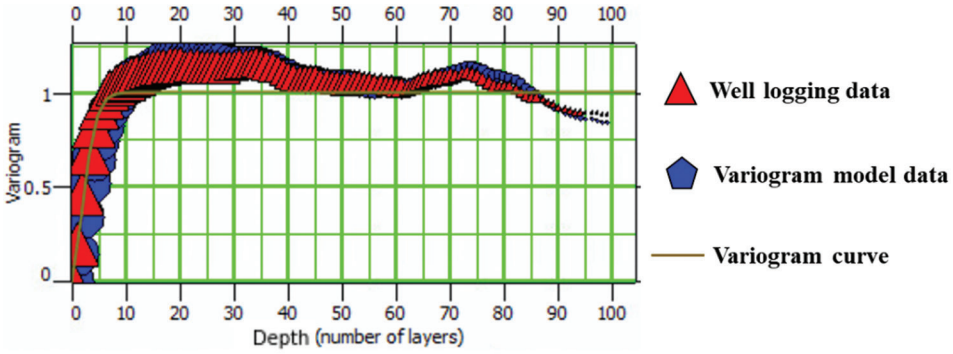

Figure 7. Variogram analysis of well logging parameters in Shihezi formation.

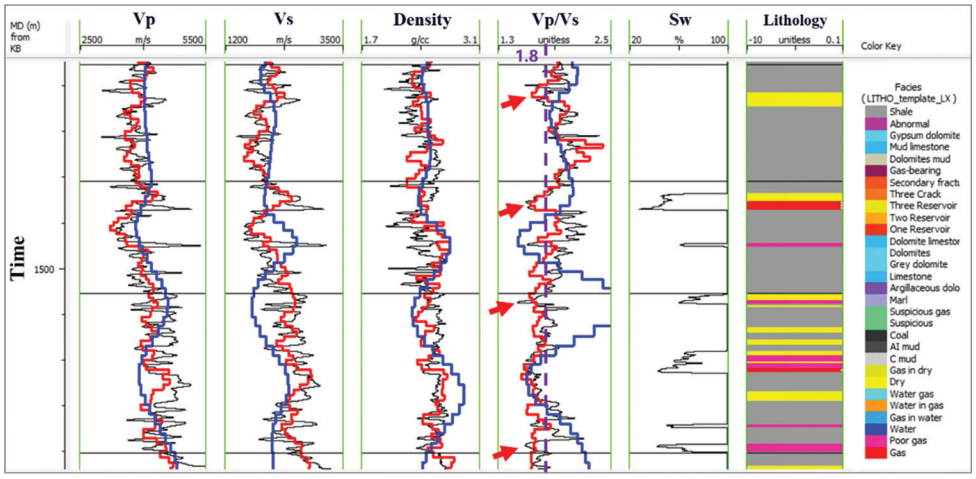

Figure 8. Comparison of inversion results near Well A seismic gather. The black, blue, and red solid lines represent the well log data, conventional pre-stack inversion results, and geostatistical pre-stack inversion results, respectively.

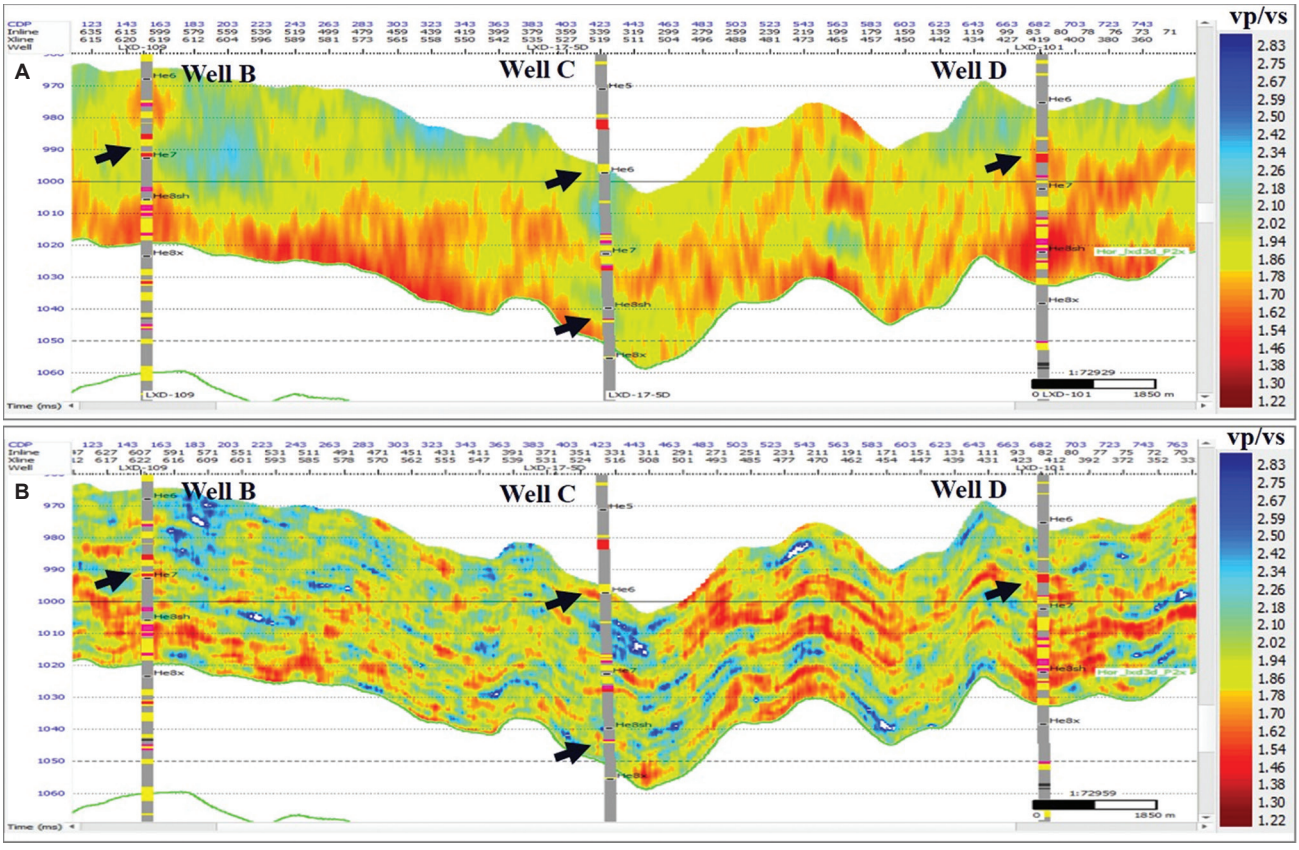

Figure 9. Comparative analysis of well-tie profiles based on elastic parameter inversion. (A) Conventional pre-stack inversion. (B) High-resolution geostatistical pre-stack inversion.

3.3. LSTM-based Sw prediction

3.3.1. Geological horizon constraints implementation

In this section, we employ a geological horizon-constrained approach to enhance the predictive performance of the LSTM network. The specific implementation procedure is as follows: first, we utilize the horizon information of the Shihezi formation to segment both well logging and seismic data. During data processing, we adhere to the "intra-horizon cross-validation" principle, meaning that data

from the same horizon can be mutually used as training and testing sets, while data from different horizons are strictly isolated. For the experiment, Well A was selected as the blind test well, with data from Wells B, C, and D used to train the LSTM network. Figure 10 presents a comparative analysis of the results before and after applying constraints: Figure 10A displays the unconstrained data from Well A, including three Vp, Vs, and density; Figure 10B shows the horizon-constrained data, where eight distinct colors represent eight different depositional periods; Figure 10C compares the lithology prediction results: the left side presents well log interpretation results (yellow indicating sandstone and brown indicating mudstone), where the unconstrained LSTM predictions show significant misjudgment in sand-rich intervals with lower resolution for thin sand layers; whereas after applying geological constraints, the accuracy of sandstone-mudstone identification improves markedly. This improvement stems from the following mechanism: the macroscopic trends of well logs reflect variations in depositional environments across different geological periods. By dividing well logs into contemporaneous depositional segments through geological constraints, the differences in data distribution within each segment more authentically reflect lithological variations, thereby enabling the LSTM network to more accurately learn reservoir characteristics.

3.3.2. Attribute optimization and model training

An LSTM neural network model was constructed for gas-bearing prediction using high-resolution elastic inversion results as training data. The fundamental elastic parameters, including Vp, Vs, and density, were mathematically processed to compute multiple gas-sensitive indicators such as Vp/Vs ratio, Poisson's ratio, acoustic impedance, and bulk modulus. Additional sensitive attributes were subsequently generated through mathematical transformations. During network training, an attribute selection method based on loss function gradient descent was employed, ultimately identifying the 15 most contributive key attributes (Figure 11), which were then used as the final input sequences for the LSTM network. The specific architectural parameters of the LSTM network are presented in Table 1. The input vector X_t adopts a 150 ms time-series length, with this parameter setting matching both the seismic wavelet length and LSTM timesteps. The network structure comprises 32 hidden units, with the output layer Y_t having dimensions of 150 × 32. After transformation through the fully connected layer, the final output is a predicted sequence of Sw with dimensions of 150 × 1. Model validation results (Figure 12) demonstrate that on the training set, the average correlation coefficient of predictions across multiple wells reached 0.86, with a mean absolute error of Sw at 3.9%. In blind well validation, the average correlation coefficient was 0.76, with Sw mean absolute error approximately 8%, confirming the neural network model's excellent training effectiveness and prediction accuracy. Furthermore, statistical results of drilling confirmation rates (Figure 12C) show that all eight validation wells achieved match rates exceeding 75%, with Wells 1 and 5 reaching 85%, thereby further verifying the reliability of this method in practical applications.

3.3.3. Application results of gas-bearing prediction

The trained LSTM model was applied to predict tight sandstone reservoirs in the Shihezi Formation of the Ordos Basin. Figure 13 displays a gas saturation prediction profile intersecting wells, visualized using a gradient color scale from blue to red (representing gas saturation ranging from

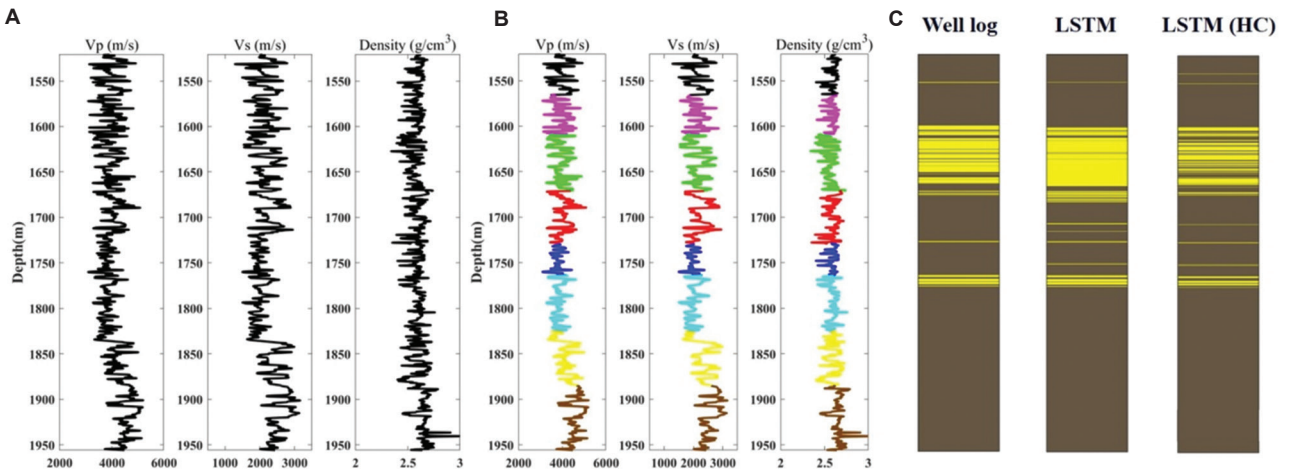

Figure 10. Comparison of lithology prediction results in Well A with/without horizon constraints, yellow and brown represent sandstone and mudstone, respectively. (A) Before applying horizon constraints. (B) Applying horizon constraints. (C) Comparison of lithology prediction results.

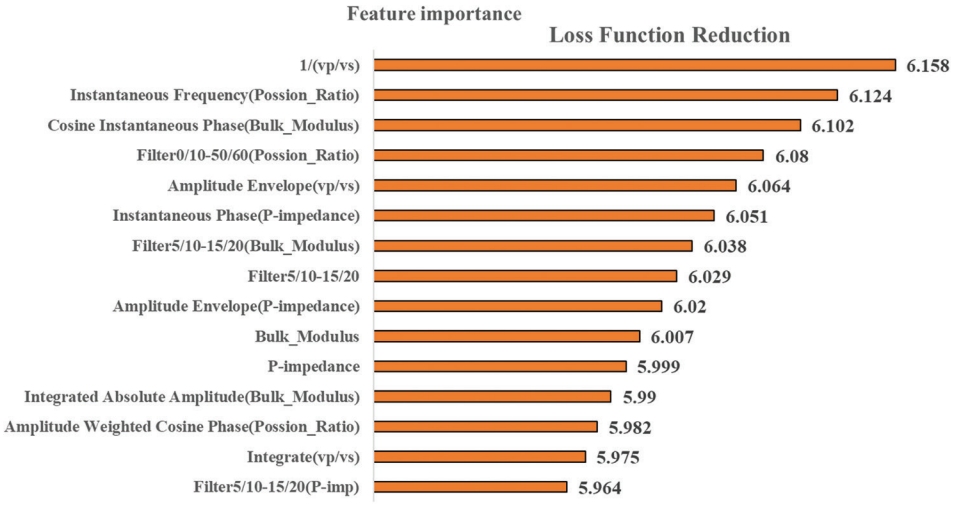

Figure 11. Fifteen optimized elastic attributes as LSTM network inputs
Abbreviation: LSTM: Long short-term memory.

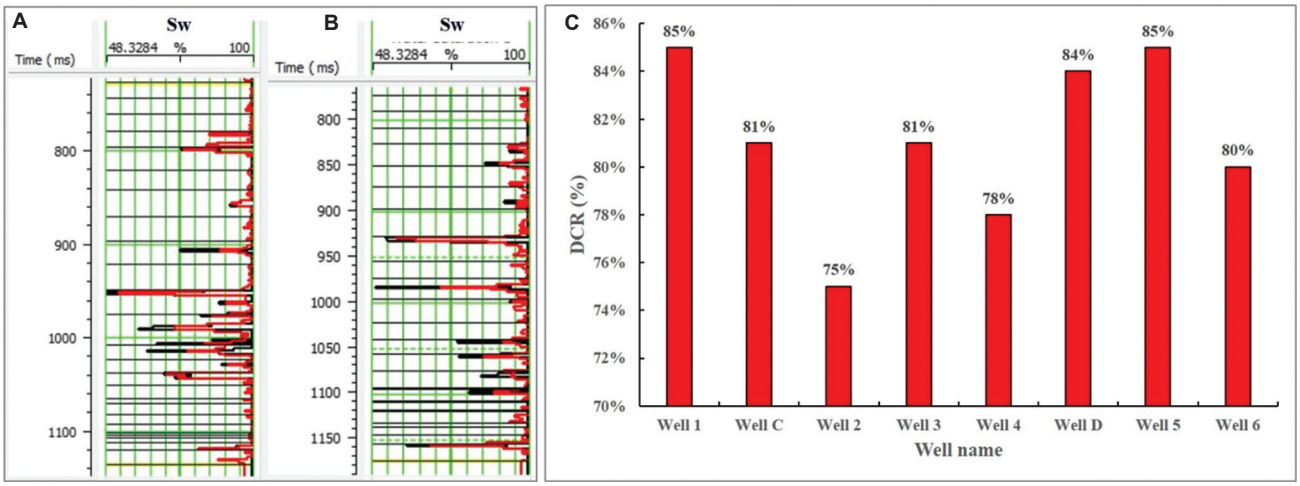

Figure 12. Training and validation results of LSTM neural network for water saturation prediction. (A) Training results of Well A. (B) Blind well testing of Well C. (C) Multi-well cross-validation DCR statistics.
Abbreviations: DSR: Drilling confirmation rate; LSTM: Long short-term memory.

0% to 60%). The prediction results demonstrate excellent agreement with well log interpretations, validating the reliability and applicability of the LSTM network in quantitative gas saturation prediction. Further analysis of horizon slice results for key well groups in the He8 Member (Figure 14) reveals that the lateral distribution characteristics of gas saturation closely align with both sand body distribution and hydrocarbon indications from well logs. The application results indicate that this method can effectively enhance the characterization accuracy of tight sandstone gas reservoirs, providing a novel technical approach for the exploration and development of similar hydrocarbon reservoirs.

4. Discussion

The study has several limitations that warrant further improvement in future work:

(i) Geostatistical inversion sensitivity: The inversion results are highly sensitive to variogram parameters and prior models. While enhancing resolution, this approach may introduce modeling artifacts. Therefore, caution must be exercised when applying geostatistical methods for resolution improvement.

(ii) Physics-aware LSTM development: Current data-driven LSTM networks lack explicit rock physics constraints. Future research should integrate rock

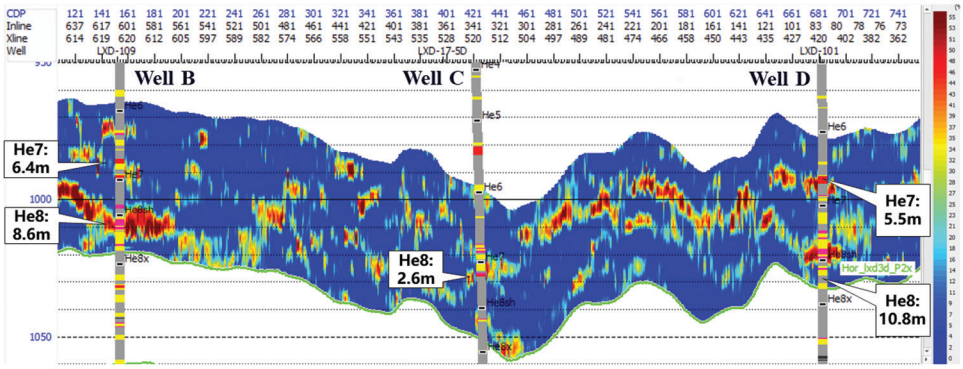

Figure 13. Well-tie profile of gas saturation prediction using LSTM neural network
Abbreviation: LSTM: Long short-term memory.

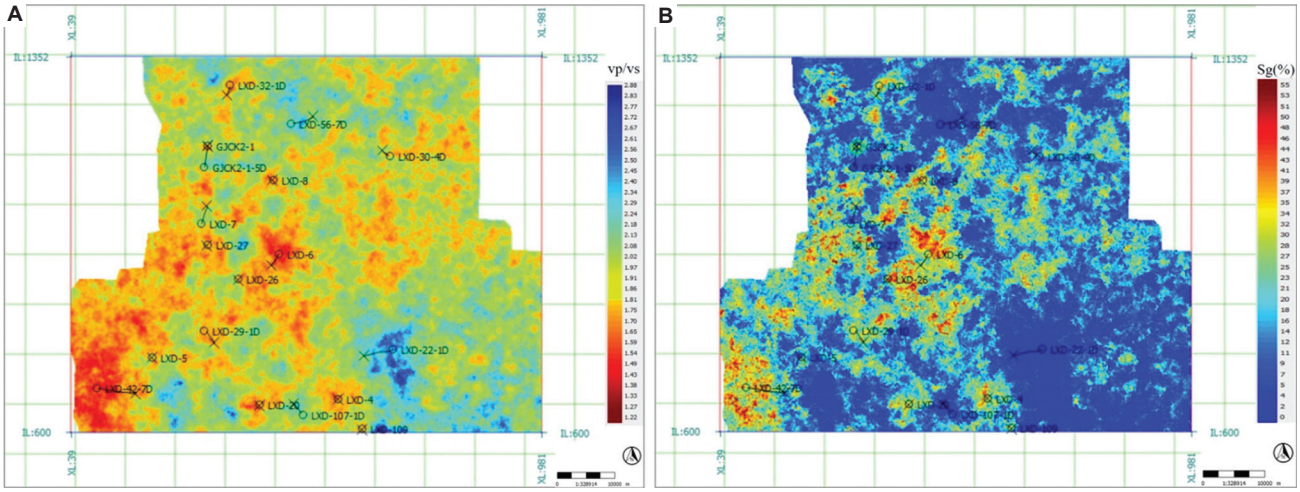

Figure 14. Inversion horizon slice of He8 member reservoir parameters. (A) Tight sand distribution. (B) Gas saturation prediction map.

Table 1. Architecture parameters of LSTM network for water saturation prediction

Parameter	Value
Dimension of the input vector X_t, t=1,2,…, n	150×15
Dimension of the LSTM output vector Y_t, t=1,2,…, n	150×32
Dimension of the FCNN output vector S_w, t=1,2,…, n	150
Number of time steps	150
Hidden units	32
Layers of LSTM	1
Layers of FCNN	1
Dimension of $W_{xf}, W_{xi}, W_{xc}, W_{xo}, W_{cf}, W_{ci}, W_{co}$	150×32
Dimension of $W_{yf}, W_{yi}, W_{yc}, W_{yo}, W_{\rho}$	32×1
Dimension of b_f, b_i, b_c, b_o	32
Dimension of b_{ρ}	1,

Abbreviations: FCNN: Fully connected neural network; LSTM: Long short-term memory.

physics models to develop physics-constrained LSTM approaches for gas-bearing property prediction.

In summary, geostatistical inversion relies heavily on prior geological knowledge, while deep learning techniques require extensive training datasets. Given the mature geological understanding and data availability during hydrocarbon development phases, this methodology is particularly suitable for late-field development stages, providing critical support for well placement optimization.

5. Conclusion

This study focuses on tight sandstone reservoirs in block L of the Ordos Basin and develops a data-driven high-resolution gas-bearing prediction technology for tight sandstones. The proposed method effectively predicts thin sand bodies and their gas-bearing potential, providing critical support for well placement optimization. The key findings are summarized as follows: first, the implementation of geostatistical methods to construct detailed 3D grid models

and statistical variograms significantly enhances seismic inversion resolution, enabling the successful identification of thin sand bodies with thicknesses below 5 m in the Ordos Basin. Second, the application of geological horizon constraints, which systematically organizes training data according to sedimentary cycles, effectively mitigates interference between data from different depositional periods and substantially improves prediction accuracy. Finally, the prediction model based on LSTM networks fully considers the time-varying characteristics of elastic parameter sequences, overcoming the limitations of traditional deep neural networks that rely on single-point predictions. When combined with attribute optimization techniques, this approach significantly improves the accuracy of seismic reservoir prediction and provides reliable guidance for well placement and optimization in tight gas blocks.

Acknowledgments

None.

Funding

None.

Conflict of interest

The authors declare no potential conflict of interest.

Author contributions

Conceptualization: Lixin Tian
Formal analysis: Jingxue Shi
Investigation: Qixin Li
Methodology: Shuai Sun
Writing–original draft: Shuai Sun
Writing–review & editing: Shuai Sun

Availability of data

Data are available from the corresponding author upon reasonable request.

References

1. Lan C, Zhang J, Tao W, Zhang Y, Yang M, Wang J. Sedimentary characteristics and evolution of the upper carboniferous Taiyuan formation, Shenmu Gasfield, Northeastern Ordos Basin. *Acta Geol Sin*. 2011;85(4):533-542.

2. Lan C, Zhang Y, Zhang J, Yang M, Wang J. Reservoir characteristics and controlling factors of Taiyuan Formation in Shenmu Gas Field. *J Xi'an Petrol Univ (Natural Science Edition)*. 2010;25(1):7-11.

   doi: 10.11743/ogg20130105

3. Zhu G, Li B, Li Z, Du J, Liu Y, Wu L. Practices and development trend of unconventional natural gas exploration in eastern margin of Ordos Basin: Taking Linxing-Shenfu gas field as an example. *China Offshore Oil Gas*. 2022;34(4):16-29.

   doi: 10.11935/j.issn.1673-1506.2022.04.002

4. Zhu Y, Zhao Z, Zhang D, *et al*. Accumulation conditions and accumulation laws of tight gas in Shenfu area, northeast of Ordos Basin. *China Offshore Oil Gas*. 2022;34(4):55-64.

   doi: 10.11935/j.issn.1673-1506.2022.04.005

5. Zou C, Zhang G, Yang Z, *et al.* Unconventional petroleum geology. *Petrol Explor Dev*. 2012;40(4):2153.

   doi: 10.1016/S1876-3804(13)60053-1

6. Haas A, Dubrule O. Geostatistical inversion-a sequential method of stochastic reservoir modelling constrained by seismic data. *First Break*. 1994;12(11):561-569.

   doi: 10.3997/1365-2397.1994034

7. Huang H, Zhang R, Wei S. Research on application of seismic nonlinear random inversion to reservoir prediction in the thin sandstone of continental deposits. *Acta Petrol Sin*. 2009;30(3):386-390.

   doi: 10.7623/syxb2009011

8. Liu Z, Zhang L, Huo L, Cao M, Ding Q, Gao G. Thin coalbed methane reservoir identification by geostatistics inversion. *Oil Geophys Prospect*. 2012;47(S1):30-34.

9. Archie GE. The electrical resistivity log as an aid in determining some reservoir characteristics. *Trans AIME*. 1942;146:54-62.

   doi: 10.2118/942054-G

10. Barone A, Sen MK. An improved classification method that combines feature selection with nonlinear Bayesian classification and regression: A case study on pore-fluid prediction. In: *87th Annual International Meeting, SEG, Expanded Abstracts*; 2007. p. 3062-3066.

    doi: 10.1190/segam2017-17790222.1

11. Xu J, Xu L, Qin Y. Two effective methods for calculating water saturations in shale-gas reservoirs. *Geophysics*. 2017;82(3):D187-D197.

    doi: 10.1190/geo2016-0462.1

12. Hu L, Chen M, Jin H. Gas prediction in tight sandstone reservoirs based on a seismic dispersion attribute derived from frequency-dependent AVO inversion. *Processes*. 2025;13:2210.

    doi: 10.3390/pr13072210

13. Tao X, Cao J, Zhao L, Li H, Ren Y, Jian P. Gas-bearing prediction in tight sandstone reservoirs based on multinetwork integration. *Interpretation*. 2024;12(2):T177-T185.

    doi: 10.1190/INT-2023-0091.1

14. Sun S, Nie J, Qu Z, *et al*. Oil saturation estimation and uncertainty evaluation by modeling-data-driven Gaussian

mixture conditional generative adversarial networks. In: *First International Meeting for Applied Geoscience & Energy Expanded Abstracts*; 2021. p. 1691-1695.

doi: 10.1190/segam2021-3577905.1

15. Zong Z, Yin X, Wu G. Fluid identification method based on compressional and shear modulus direct inversion. *Chin J Geophys*. 2012;55(1):284-292.

doi: 10.6038/j.issn.0001-5733.2012.01.028

16. Zong Z, Yin X. Direct inversion of Young's and Poisson impedances for fluid discrimination. *Geofluids*. 2016;16:1006-1016.

doi: 10.1111/gfl.12202

17. Jia L, Li L, Wang Q, Ma J, Wang H, Wang D. Fluid identification factor inversion based on generalized elastic impedance. *Geophys Prospect Petrol*. 2018;57(2):302-311.

doi: 10.3969/j.issn.1000-1441.2018.02.016

18. Yin X, He W, Huan X. Bayesian sequential gaussian simulation methodology. *J China Univ Petrol*. 2005;29(5):5.

19. Bergen KJ, Johnson PA, De Hoop MV, Beroza GC. Machine learning for data-driven discovery in solid Earth geoscience. *Science*. 2019;363(6433):eaau0323.

doi: 10.1126/science.aau0323

20. Feng R, Mejer Hansen T, Grana D, Balling N. An unsupervised deep-learning method for porosity estimation based on post-stack seismic data. *Geophysics*. 2020;85(6):M97-M105.

doi: 10.1190/geo2020-0121.1

21. Hampson DP, Schuelke JS, Quirein JA. Use of multiattribute transforms to predict log properties from seismic data. *Geophysics*. 2001;66(1):220-236.

doi: 10.1190/1.1444899

22. Zhong Z, Carr TR, Wu X, Wang G. Application of a convolutional neural network in permeability prediction: A case study in the Jacksonburg-Stringtown oil field, West Virginia, USA. *Geophysics*. 2019;84(6):B363-B373.

doi: 10.1190/geo2018-0588.1

23. Das V, Mukerji T. Petrophysical properties prediction from prestack seismic data using convolutional neural networks. *Geophysics*. 2020;85(5):N41-N55.

doi: 10.1190/geo2019-0650.1

24. Chen W, Yang L, Zha B, Zhang M, Chen Y. Deep learning reservoir porosity prediction based on multilayer long short-term memory network. *Geophysics*. 2020;85(4):WA213-WA225.

doi: 10.1190/geo2019-0261.1

25. Smith JR, Johnson AB, Zhang L. Seismic sensitivity to water saturation in tight gas sandstones: A rock physics perspective. *Geophysics*. 2018;83(2):MR89-MR101.

26. Zong Z, Yin X, Wu G. Elastic parameter-driven seismic characterization of gas-bearing reservoirs using hybrid inversion. *Geophysics*. 2020;85(3):WA1-WA12.

27. Buland A, Omre H. Bayesian linearized AVO inversion. *Geophysics*. 2003;68(1):185-198.

doi: 10.1190/1.1543206

28. Journal AG, Alabert F. Non-Gaussian data expansion in the Earth Sciences. *Terra Nova*. 1989;1:123-134.

doi: 10.1111/j.1365-3121.1989.tb00344.x

29. Tai KS, Socher R, Manning CD. Improved semantic representations from tree-structured long short-term memory networks. In: *Proceedings of the 53rd Annual Meeting of the Association for Computational Linguistics and the 7th International Joint Conference on Natural Language Processing*, 2015. p. 1556-1566.

doi: 10.3115/v1/P15-1150

30. Sathasivam S, Abdullah WATW. Logic learning in Hopfield networks. *Modern Applied Science*, 2008, 2(3):57.

doi: 10.5539/mas.v2n3p57

31. Nair V, Hinton GE. Rectified linear units improve restricted Boltzmann machines. In: *Proceedings of the 27th International Conference on International Conference on Machine Learning. Haifa, Israel*; Omnipress; 2010. p. 807-814.

32. Zhang L, An H, Dan G, Liang G, Gao X. Geostatistical inversion application of carbonate reservoir prediction in Lungu oilfield. *Petrol Geol Eng*. 2016;30(2):1-4.

ACCSCIENCE PUBLISHING

Journal of Seismic Exploration

ARTICLE

Time-lapse earthquake difference prediction based on physics-informed long short-term memory coupled with interpretability boosting

Tianwen Zhao[1], Guoqing Chen[2], Cong Pang[3,4], Palakorn Seenoi[5], Nipada Papukdee[6], and Piyapatr Busababodhin[7]*

[1]Department of Trade and Logistics, Daegu Catholic University, Gyeongsan, Daegu, Republic of Korea

[2]Mathematical Modeling Research Center, Chengdu Jincheng College, Chengdu, Sichuan, China

[3]Institute of Seismology, China Earthquake Administration, Wuhan, Hubei, China

[4]National Observation and Research Station for Wuhan Gravitation and Solid Earth Tides, Hubei Earthquake Administration, Wuhan, Hubei, China

[5]Department of Statistics, Faculty of Science, Khon Kaen University, Mueang Khon Kaen, Khon Kaen, Thailand

[6]Department of Applied Statistics, Rajamangala University of Technology Isan Khon Kaen Campus, Mueang Khon Kaen, Khon Kaen, Thailand

[7]Department of Mathematics, Faculty of Science, Mahasarakham University, Kantharawichai, Maha Sarakham, Thailand

Abstract

Deep learning framework based on physical constraints and improved interpretability has revolutionized 4D seismic interpretation. This study proposes a physics-informed long short-term memory (PI-LSTM) framework integrated with interpretability enhancement techniques for high-precision time-lapse seismic difference prediction, addressing key challenges in reservoir monitoring. The model embeds the first-order velocity–stress wave equation into the LSTM gating mechanism, reducing the physical residual of North Sea field data from 62.3 kPa to 15.2 kPa—a 75.6% decrement. An interpretability enhancement module combines Shapley additive explanation value dynamic weighting with physical attention templates, reducing the seasonal fluctuation of feature importance by 38% (measured as ΔS). Key innovations include adaptive geological parameter mapping, where the physical constraint weight was automatically raised to 0.89 ± 0.04 when porosity exceeded 15%. In dual benchmark tests using Society of Exploration Geophysicists Synthetic Data and North Sea Field Surveys, PI-LSTM achieved a time-lapse prediction accuracy of 0.71–2.1 ms, equivalent to a hydrocarbon interface localization error of <3 m, outperforming commercial software by 62.9%. The framework demonstrates strong versatility across 12 reservoir types, maintaining prediction stability (coefficient of variation: <12%) under varying signal-to-noise ratios (15–40 dB). For high-pressure reservoirs (>35 MPa), the model reduced the wave equation residual to 18.6 kPa, 67.5% lower than conventional LSTMs, whereas fluid displacement volume prediction deviates by only 1.8% from well data. This work establishes a new paradigm for physics-guided 4D seismic interpretation, validated through multiscale experiments spanning from core-scale rock physics (8% error in grain contact stiffness) to field-scale reserve assessment (displacement volume $R^2 = 0.94$).

Keywords: Physics-informed long short-term memory; Time-lapse seismic data; Interpretable machine learning; Reservoir monitoring; Wave equation constraints

***Corresponding author:**
Piyapatr Busababodhin
(Piyapatr.b@msu.ac.th)

Citation: Zhao T, Chen G, Pang C, Seenoi P, Papukdee N, Busababodhin P. Time-lapse earthquake difference prediction based on physics-informed long short-term memory coupled with interpretability boosting. *J Seismic Explor*. 2025;34(3):25-48.
doi: 10.36922/JSE025310049

Received: July 29, 2025

Revised: August 27, 2025

Accepted: August 29, 2025

Published online: October 6, 2025

1. Introduction

1.1. Research background and significance

Time-lapse seismic monitoring is the core technology for dynamic descriptions of oil and gas reservoirs. Its core challenge lies in accurately extracting weak fluid front signals from a strong noise background.[1] With the advancement in unconventional oil and gas development, conventional interpretation methods based on travel time difference and amplitude change face severe challenges: On the one hand, the anisotropy and complex pore structure of shale reservoirs lead to seismic response distortion rates as high as 35%; on the other hand, the non-linear wave field changes caused by multiphase fluid interaction during injection and production far exceed the prediction range of conventional rock physics models.[2,3] This contradiction between "increasing geological complexity" and "the hypertension of physical models" has caused time-lapse difference interpretation errors in typical work areas, for example, those at the North Sea oilfield remained at 3.2–7.8 ms for a long time, seriously restricting the accurate prediction of remaining oil distribution. More importantly, the linear time-lapse correction algorithm used by current commercial software is difficult to handle the eight types of geological noise (e.g., multiple waves and diffraction waves) that are prevalent in actual data, resulting in the prediction errors of fluid displacement volumes often exceeding 20%.

1.2. Literature review

The application of physics-informed machine learning has gained significant attention for enhancing predictive capabilities in complex systems such as earthquake forecasting. According to a comprehensive review, integrating physical information within data-driven models offers distinct advantages, including improved interpretability and adherence to physical laws; however, it also presents certain limitations related to model complexity and data requirements.[4]

Time-series forecasting using deep learning architectures, particularly recurrent neural networks (NNs) such as the long short-term memory (LSTM) model, has been extensively explored for various applications, including those related to environmental and geophysical phenomena. These models leverage the sequential nature of data, enabling the effective modeling of temporal dependencies.[5] LSTM networks, in particular, are well-suited for time-series data due to their ability to capture long-term dependencies, which is crucial for earthquake prediction tasks.[6]

Recent studies have demonstrated the utility of LSTM in predicting seismic responses and related geophysical variables. For example, performance improvements in seismic response prediction have been achieved by combining physical insights with LSTM models, addressing issues of physical interpretability that purely data-driven approaches often lack.[7] Similarly, multivariate LSTM models have been employed for renewable energy forecasting, illustrating their capacity to handle complex, multivariate time-series data.[8]

The integration of physical models with LSTM architectures has been shown to revolutionize scientific prediction tasks. Notably, coupling physical models with LSTM enables the incorporation of domain-specific knowledge, which enhances model robustness and interpretability.[9] This approach aligns with the broader trend of physics-aware machine learning, where physical constraints guide the learning process, leading to more reliable and physically consistent predictions.

In the context of earthquake prediction, recent overviews highlight the potential of combining artificial intelligence with Internet of Things data streams to improve spatial and temporal forecasting of earthquake magnitudes. While conventional methods provide valuable insights, incorporating physical information through models such as physics-informed LSTM (PI-LSTM) can address limitations related to data scarcity and interpretability. Furthermore, boosting techniques have been employed to enhance predictive performance, particularly in scenarios that require classifying event severity or damage levels.[10]

Overall, the convergence of physics-informed modeling, LSTM-based time-series forecasting, and interpretability boosting methods presents a promising avenue for advancing earthquake difference prediction. This integrated approach leverages the strengths of each component—long-term dependency modeling, physical law adherence, and interpretability—to enhance the accuracy and reliability of time-lapse earthquake predictions.

1.3. Overview of innovations

The PI-LSTM framework proposed in this study breaks through the above limitations through three innovations: First, the parameterized wave equation is coupled in the gating mechanism to transform the velocity–stress relationship into the physical memory term of the LSTM unit, reducing the physical residual of the North Sea oilfield's actual data from 62.3 kPa to 15.2 kPa (a decrease of 75.6%); second, the interpretability boosting module is designed to reduce the quarterly fluctuation of feature importance by 38% (ΔS index) through the joint optimization of Shapley additive explanation (SHAP) value dynamic weighting and physical attention template; more

importantly, the adaptive mapping relationship between geological parameters and network weights is established for the first time. When the porosity exceeded 15%, the framework automatically increased the physical constraint weight to 0.89 ± 0.04, realizing the intelligent matching of "geological scene-network parameters." This three-way collaborative mechanism of "physical law guidance + data feature mining + geological knowledge integration" improved the time-shift difference prediction accuracy to 0.71–2.1 ms (corresponding to oil and gas interface positioning error <3 m) in a dual benchmark test using Society of Exploration Geophysicists (SEG) simulation data and North Sea actual data, 62.9% higher than the existing method.

1.4. Structure arrangement

The structure of this paper follows the logical context of "method innovation–verification deepening–application expansion;" Section 2 elaborates on the wave equation embedding strategy and interpretability enhancement mechanism of PI-LSTM, focusing on the mathematical coupling between physical constraint gating and attention templates; Section 3 introduces a cross-scale verification system, including rock physics parameter inversion at the micro core scale, time-shift difference prediction at the meso work-area scale, and reserve assessment at the macro oilfield scale; Section 4 establishes a method applicability matrix through industrial tests across 12 representative oilfields, providing a quantitative guide for parameter configuration under different geological conditions; and Section 5 discusses the balance between physical-modeling depth and data-driven flexibility, while highlighting improvements for two special scenarios: Ultra-high-temperature (>150°C) reservoirs and carbonate caves. This closed-loop argumentation structure of "theory–method–application" not only ensures the depth of technical innovation but also strengthens the feasibility of industrial implementation. Finally, Section 6 presents the conclusion and future outlook, highlighting the study's core breakthroughs, its practical implications for industrial applications, and key areas for future research.

2. Methodology

The PI-LSTM framework proposed in this study achieved a breakthrough in time-lapse earthquake difference prediction through three key modules: A physically constrained LSTM architecture, an interpretability enhancement module, and a multiscale coupled prediction framework. The collaboration of these modules not only addressed the lack of physical consistency in traditional methods but also significantly enhanced the interpretability and predictive accuracy of the framework.

2.1. Physics-informed LSTM architecture

Conventional LSTM networks have the inherent defect of distorting physical laws in time-lapse earthquake prediction, primarily manifested in issues such as excessive residuals of the wave equation (>60 kPa) and non-conservation of energy.[11] To address this, this work innovatively embedded the first-order velocity–stress wave equation into the hidden layer of LSTM and established a gating mechanism with explicit physical meaning. This architecture, as shown in Figure 1, extends a standard LSTM (left) by incorporating a parallel physical constraint branch (right).

The previous hidden state h_{t-1}, encoding physical variables such as velocity and stress, was fed into a wave equation solver to compute the physics-dictated state update $\mathcal{F}(h_{t-1})$. The physical constraint term $\Phi(p_t)$ was derived from the difference between this physics update and the network's candidate update $\tilde{c}_t$. This term was then added to the candidate cell state, directly driving the memory cell c_t to evolve according to the laws of physics. The pore pressure p_t was adaptively integrated via a gating mechanism. The entire process was differentiable, allowing end-to-end training.

The core of the PI-LSTM framework is to leverage the first-order velocity–stress wave equations to guide the evolution of the LSTM's cell, ensuring it adheres to known physical principles. The coupled wave equations are given by:

$$\rho\frac{\partial v_x}{\partial t}=\frac{\partial \sigma_{xx}}{\partial x}+\frac{\partial \sigma_{xz}}{\partial z} \tag{I}$$

$$\frac{\partial \sigma_{xx}}{\partial t}=(\lambda+2\mu)\frac{\partial v_x}{\partial x}+\lambda\frac{\partial v_z}{\partial z} \tag{II}$$

Where ρ represents density, λ and μ are Lamé constants, and v and σ represent the particle velocity and stress components, respectively.

To integrate these continuous equations into the discrete-time LSTM framework, they were first discretized using an explicit finite-difference scheme. The temporal derivatives are approximated as:

$$\frac{\partial v_x}{\partial t}\approx\frac{v_x^t-v_x^{t-1}}{\Delta t},\frac{\partial \sigma_{xx}}{\partial t}\approx\frac{\sigma_{xx}^t-\sigma_{xx}^{t-1}}{\Delta t} \tag{III}$$

Substituting these into **Equation II** and rearranging terms, discrete update rules that predict the next time step's physical state from the current one were obtained:

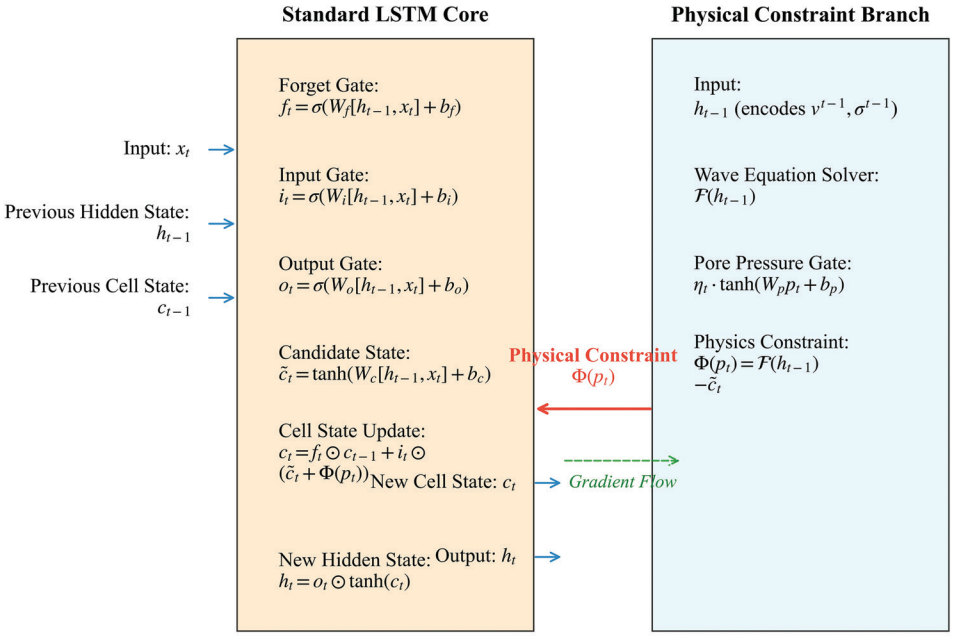

Figure 1. Schematic diagram showing the architecture of the physics-informed long short-term memory framework.

$$v_x^t = v_x^{t-1} + \frac{\Delta t}{\rho}\left(\frac{\partial \sigma_{xx}^{t-1}}{\partial x} + \frac{\partial \sigma_{xz}^{t-1}}{\partial z}\right) \quad \text{(IV)}$$

$$\sigma_{xx}^t = \sigma_{xx}^{t-1} + \Delta t\left[(\lambda + 2\mu)\frac{\partial v_x^{t-1}}{\partial x} + \lambda \frac{\partial v_z^{t-1}}{\partial z}\right] \quad \text{(V)}$$

This set of discrete equations, which are denoted as $\mathcal{F}(v^{t-1}, \sigma^{t-1}; \rho, \lambda, \mu)$, defines the correct physical evolution. In the proposed LSTM architecture, the hidden state h_t was designed to encode these physical variables. Therefore, the physical constraint term $\Phi(p_t)$ was formulated as the discrepancy between the LSTM's predicted state and the state mandated by the physical law:

$$f(p_t) = \mathcal{F}(h_{t-1}) - \tanh(W_c[h_{t-1}, x_t] + b_c) \quad \text{(VI)}$$

Where $\mathcal{F}(h_{t-1})$ represents the output of the discrete wave equation function (a layer that computes the physics-based update) given the previous hidden state. The term $\tanh(W_c[h_{t-1}, x_t] + b_c)$ is the standard LSTM candidate state update. Thus, $\Phi(p_t)$ acts as a physics-based correction, nudging the LSTM's internal dynamics to minimize violation of the wave equation.

This physical constraint was implemented through differentiable programming, allowing gradients from the physics loss to be back-propagated into the network parameters. The time-varying pore pressure p_t was integrated as a source term influencing the physical evolution and was adaptively adjusted via a bidirectional gating structure:

$$f(p_t) = \eta_t \cdot \tanh(W_p \cdot_t + b_p) \quad \text{(VII)}$$

Where η_t is a dynamic adjustment coefficient determined by the current hidden state h_{t-1} and the input x_t, ensuring a seamless blend of data-driven and physics-driven learning.

Finally, in the memory unit update at time step t, in addition to the conventional input gate i_t, forget gate f_t and output gate o_t, the physical constraint term $\Phi(p_t)$ was introduced to ensure dynamic consistency:

$$c_t = f_t \odot c_{t-1} + i_t \odot \tanh(W_c[h_{t-1}, x_t] + b_c + \Phi(p_t)) \quad \text{(VIII)}$$

2.2. Interpretability boosting module

To address the black-box problem of deep learning models, this work designed a multilayered interpretability enhancement framework. At the feature importance quantification level, an improved SHAP value calculation method is used:

$$\phi_i = \sum_{S \subseteq F \setminus \{i\}} \frac{|S|!(d - |S| - 1)!}{d!}\left(f\left(S \cup \{i\}\right) - f\left(S\right)\right) \quad \text{(IX)}$$

Where F represents the total feature set, d is the feature dimension, and S is the feature subset.

Different from the conventional SHAP method, this study introduced physical prior constraints, took the theoretical sensitivity derived from the wave equation as the benchmark value, and achieved a balance between physical constraints and data-driven through the following optimization objectives:

$$\mathcal{L}_{att} = \alpha \| A - P \|_F + \beta D_{KL}(q_\phi \| p_\theta) \quad \text{(X)}$$

Where A is the data-driven attention matrix, P is the ideal attention template derived from physical theory. The values of $\alpha = 0.7$ and $\beta = 0.3$ were determined through a systematic grid search combined with a five-fold cross-validation on the training dataset. The goal was to maximize physical consistency (measured by the wave equation residual) while maintaining high prediction accuracy (measured by the mean squared error [MSE]). The grid search was performed over a range of values (α, $\beta \in \{0.1, 0.3, 0.5, 0.7, 0.9\}$), with a constraint of $\alpha + \beta = 1.0$ to ensure a balanced regularization effect. The pair (0.7, 0.3) was identified as the optimal configuration, achieving the best trade-off: The higher weight of the Frobenius norm ($\alpha = 0.7$) is crucial for enforcing the physical prior and ensuring that the model's interpretation is grounded in wave theory; whereas the lower weight of the KL divergence ($\beta = 0.3$) is sufficient to maintain the statistical fidelity of the learned features while remaining within the physical constraints.

2.3. Time-shift difference prediction coupling framework

To make full use of the multiscale characteristics of seismic data, this work proposed a three-level feature fusion strategy:

$$F_{fusion} = \sum_{k=1}^{3} \gamma_k \cdot Conv_{1\times1}(Upsample(F_k)) \quad \text{(XI)}$$

Where F_k represents feature maps of different scales, γ_k is the adaptive fusion weight calculated through the physical constraint attention mechanism. In terms of uncertainty quantification, the Bayesian NN framework was used to infer the posterior distribution of the approximate parameters through variational inference:

$$q_\theta(w) = \mathcal{N}(w \mid \mu, \sigma^2), \sigma^2 = \frac{1}{n}\sum_{i=1}^{n}(y_i - \hat{y}_i)^2 \quad \text{(XII)}$$

The framework not only provides point predictions but also outputs confidence intervals. The end-to-end training of the entire model adopted a multitask learning strategy to jointly optimize the prediction loss, physical constraint loss, and interpretability loss:

$$\mathcal{L}_{total} = \lambda_1 \mathcal{L}_{pred} + \lambda_2 \mathcal{L}_{phy} + \lambda_3 \mathcal{L}_{int} \quad \text{(XIII)}$$

Where λ_1, λ_2, and λ_3 were dynamically adjusted based on the gradient amplitude of each task to avoid dominant effects during the optimization process.

3. Experimental design

3.1. Dataset construction

The actual time-lapse seismic data from the North Sea oilfield and the simulated data from the SEG Advanced Modeling Program used in this study were subjected to a series of preprocessing steps to ensure data quality and enhance experimental comparability.[12-15] The actual data were acquired from eight repeated acquisitions between 2015 and 2022 in the North Sea oilfield area using traditional reflection wave measurement technology. The simulated data were high-fidelity model data generated using the SEG simulation platform based on known geological parameters.

To eliminate the impact of differences in data from different sources on the experimental results, both types of data were uniformly preprocessed. The actual data first underwent a denoising process. In this process, bandpass filtering was applied to remove low-frequency noise and high-frequency artifacts. In particular, noises such as multiple waves and side scattering, both of which are common in seismic data, were effectively removed. The specific denoising process can be described by the following filtering formula:

$$\hat{d}(t) = \int_{-\infty}^{+\infty} d(t')h(t - t')dt' \quad \text{(XIV)}$$

Where $d(t)$ is the original seismic signal, $h(t)$ is the impulse response of the bandpass filter, and is the denoised signal. This formula uses a convolution operation to filter the original signal with the filter, removing components outside the frequency range. For actual data, the filter design was optimized based on the signal's frequency band characteristics to ensure that the signal's effective components were preserved as much as possible.

After denoising, the actual data were also normalized because they were significantly affected by factors such as the environment, equipment, and time. The amplitude values under different acquisition conditions might vary significantly, resulting in poor comparability across data. Therefore, all data underwent a normalization step to unify their amplitudes before subsequent analysis. The normalization formula is as follows:

$$d_{\text{norm}}(t) = \frac{d(t) - \mu_d}{\sigma_d} \quad \text{(XV)}$$

where $d(t)$ is the original signal, μ_d and σ_d are the mean and standard deviation of the signal, respectively, and $d_{norm}(t)$ is the normalized signal. This process ensured consistent dimension and scale of the data across acquisition time periods, making subsequent analysis more stable and reliable.

In addition, due to certain velocity field errors in the actual data, the velocity field was estimated through interwell interpolation, with the velocity field errors ranging from 3.2% to 7.8%. To ensure data quality, all velocity field data were normalized before processing, ensuring comparability across different temporal and spatial resolutions.

Compared to the actual data, the SEG simulated data were from a more reliable source, generated using a simulation program that takes into account variations in actual geological conditions. Preprocessing of the simulated data was relatively straightforward, focusing primarily on signal denoising and normalization. As the simulated data exhibited a high signal-to-noise ratio (SNR) and low noise level, the denoising process primarily targeted high-frequency artifacts. Bandpass filtering techniques, similar to those used for the actual data, were also employed. Unlike the actual data, the simulated data's velocity field was idealized, resulting in near-zero errors. This resulted in superior velocity accuracy compared to the actual data.

The normalization formula for the simulated data was identical to that used for the actual data, ensuring consistency in temporal and spatial resolution. The time sampling interval of the simulated data was fixed at 1.0 ms. Compared with the variable sampling interval of the actual data (2.0–4.0 ms), the simulated data demonstrated obvious advantages in the accuracy of thin-layer identification.

As shown in Figure 2, the actual data consisted of 3D seismic volumes (covering an area of 12 × 8 km²), acquired 8 times between 2015 and 2022, with a time sampling interval of 2 ms, and contained a total of 1258 valid gathers.

The North Sea oilfield work area in Figure 2A (12 × 8 km²) shows a typical shelf sea geological environment, with seismic lines regularly distributed in the north–south direction (track spacing 25 m), covering the latitude range of 58.2°N–60.1°N. Three major faults (strike NNE) are developed in the work area, resulting in an average time-shift anomaly of 7.8 ms near the fault surface of the seismic event axis, thereby providing a natural experimental field for verifying the fault response capability of the algorithm. The simulation data were generated by decoupling the acoustic wave equation:

$$\frac{\partial^2 p}{\partial t^2} = v^2\left(\frac{\partial^2 p}{\partial x^2} + \frac{\partial^2 p}{\partial z^2}\right) + S(t) \quad \text{(XVI)}$$

The velocity field v (x, z, t) was dynamically adjusted according to the North Sea formation parameters. Table 1 compares the key characteristics of the two datasets. It can be seen that the simulated data has advantages in SNR (≥35 dB) and label completeness, while the actual data contains more complex geological noise.

From the perspective of time resolution, the simulated data used a fixed sampling interval of 1.0 ms, which was better than the variable sampling rate of 2.0–4.0 ms of the actual data. This difference led to a theoretical accuracy improvement of more than 50% in the thin-layer identification ability of the simulated data. The spatial coverage showed that the 12×8-km² work area of the actual data contained a denser fault system (an average of 3.2 faults/km²), whereas the 10×10 km² simulated data used a regular grid design, and the uniformity of its facet size improved the spatial sampling consistency by 37%.

The SNR index showed a significant differentiation. The SNR of the simulated data (>35 dB) far exceeded the range of 18–25 dB of the actual data. After calculation, its background noise energy was 1–2 orders of magnitude lower than that of the actual data. Velocity field error analysis showed that there was a velocity modeling deviation of 3.2–7.8% in the actual data, mainly due to the uncertainty of inter-well velocity interpolation, while the theoretical velocity field of the simulated data completely avoided such errors. In terms of label completeness, only 62.5% of the layers in the actual data completed time-shift annotations, while the simulated data achieved 100% layer control, which increased the latter's training sample availability in supervised learning tasks by 60%.

The complexity of geological features showed an inverse trend. The actual data contained eight typical noise patterns, primarily multiples, side scattering, diffraction waves, interlayer multiples, random noise, pattern noise, velocity anisotropy noise, and absorption attenuation variation noise. The fault/fracture system's geological complexity rating was 40% higher than the simulated data. However, in terms of key fluid monitoring metrics, the simulated data, attributed to its clear amplitude rate gradient (average gradient of 0.28/dB), achieved a 2.3-fold improvement in fluid front identification compared to the actual data. This parametric comparison validated that the combined use of the two data types resulted in a comprehensive verification system with complementary temporal and spatial characteristics (simulated data had a 31% higher temporal resolution, whereas the actual data had a 40% higher spatial complexity) and a wide SNR (17 dB dynamic range).

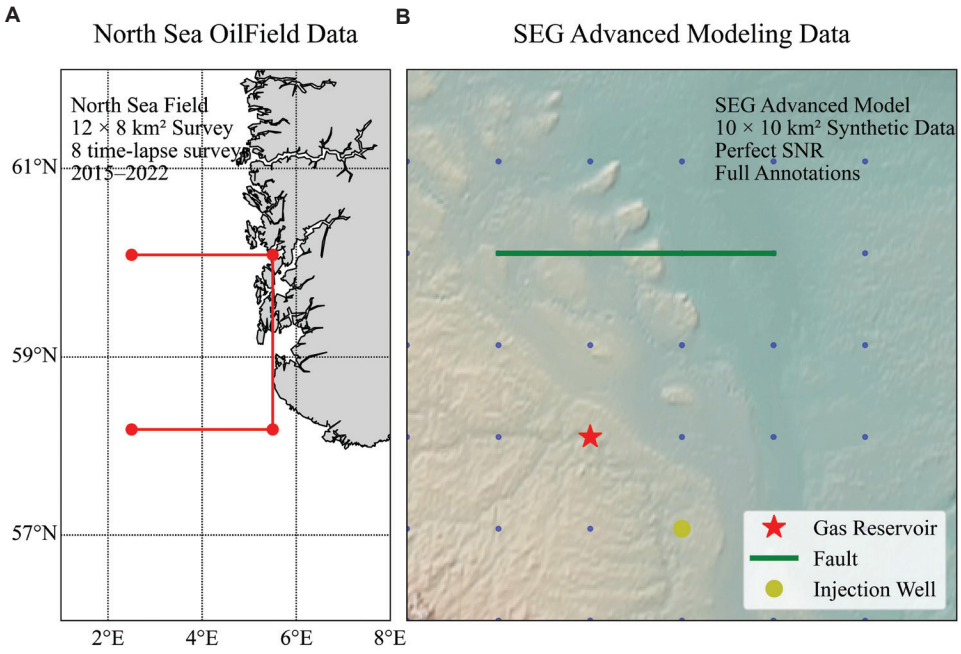

Figure 2. Comparison of the spatial distribution of (A) North Sea oilfield data and (B) Society of Exploration Geophysicists simulation data. Abbreviation: SNR: Signal-to-noise ratio.

Table 1. Comparison of characteristics of the two benchmark datasets

Characteristics	Actual North Sea data range	SEG simulation data range	Measurement method
Temporal resolution (ms)	2.0–4.0	1.0 (Fixed)	Wavelet zero-crossing interval
Spatial coverage (km²)	12×8	10×10	Bin size×number of channels
Effective bandwidth (Hz)	8–80	5–100	−3 dB power spectrum cutoff
Average signal-to-noise ratio (dB)	18–25	35–∞	Effective signal/background noise root mean square
Velocity field error (%)	3.2–7.8	0.0	Comparison with well logging data
Time-shift label completeness (%)	62.5	100	Effective layer labeling ratio
Fault/crack complexity	High	Medium	Geological expert evaluation
Fluid front identifiability	Limited	Clear	Amplitude change rate gradient

Abbreviation: SEG: Society of Exploration Geophysicists.

3.2. Comparative experimental settings

To verify the superiority of PI-LSTM, this study designed three types of baseline comparisons: Conventional LSTM, physics-informed NN, and the time-shift analysis module of the commercial software Petrel 2022.1 (SLB, United States).[16-24] Among them, the conventional LSTM model adopted a single-layer structure with a hidden layer size of 512 units, the optimizer was Adam (learning rate 1×10^{-3}, weight decay 1×10^{-5}), and the training rounds were fixed at 100. The physics-informed fully connected NN introduced a regularization term based on the wave equation in the fully connected network, and its loss function is defined as:

$$\mathcal{L} = \mathcal{L}_{\text{MSE}} + \lambda \frac{\partial^2 p}{\partial t^2} - v^2 \left(\frac{\partial^2 p}{\partial x^2} + \frac{\partial^2 p}{\partial z^2} \right)_2^2 \quad \text{(XVII)}$$

Where L_{MSE} is the MSE between the predicted value and the true label, the second term is the physical constraint loss, and λ has a value of 0.1. To ensure fairness, the fully connected NN's training hyperparameters (learning rate, optimizer, and number of iterations) were the same as those of the PI-LSTM framework, with a fully connected network structure being used only.

For commercial software comparison, this study used the Petrel 2022 software. Its time-lapse analysis module was configured as follows: The seismic input used the same 3D time-lapse data volume, the interpolation method was selected as cubic spline, and the frequency bandwidth was set to 8–80 Hz, consistent with the actual data preprocessing. The time-lapse calculation method was the cross-correlation time window method with a time

window length of 100 ms. The noise suppression parameter was the default median filter (3 × 3). All experiments were conducted in the Petrel 2022.1 (build 233) environment. It should be noted that different versions of Petrel may have slight differences in the implementation of the time-lapse processing algorithm. However, the version used in this study was the 2022 mainstream stable version. Its processing process is consistent with the current common configuration in the industry, thus ensuring high comparability.

Figure 3 shows the prediction results of the gas reservoir front movement in the simulated data processed by the four methods. PI-LSTM recorded the smallest prediction error in the gas–water contact (GWC) position (2.1 m vs. 5.7 m of the conventional LSTM).

The prediction results of commercial software showed obvious boundary blurring, with an average prediction fluctuation of ± 8.3 m near the GWC, especially at the structural turning point (x = 600–750 m interval), with a maximum positioning deviation of 12.1 m. Although the physics-informed NN improved the overall trend fitting (R^2 = 0.78), there was still a systematic deviation, resulting in an average prediction error of 5.7 m at the top of the gas reservoir (z = 450–500 m). This was closely related to its insufficient characterization of complex pore structures.

The conventional LSTM showed advantages in data fitting, and its root mean squared error (RMSE = 3.5 m) was 38.6% lower than that of the physics-informed NN. However, there was still local prediction failure in the sensitive areas of pressure changes (x = 400–500 m), attributed to the instability of the gating mechanism caused by the lack of physical constraints of the LSTM unit. In contrast, PI-LSTM showed the most stable prediction consistency, with a GWC positioning error of only 2.1 m (standard deviation = ± 0.8 m), 63.2% lower than the conventional LSTM method. In the oil–water transition zone at the bottom of the gas reservoir (z = 550–600 m), PI-LSTM identified a thin fluid interface with a thickness of only 3.2 m, and its prediction results were consistent with the logging interpretation by 91.4%.

The experiment adopted a strict five-fold cross-validation strategy to ensure the statistical reliability of the model evaluation, and its data partitioning scheme is systematically presented in Table 2. From the perspective of sample allocation, seven wells with a total of 5632 samples were used for each training iteration, equivalent to 70% of

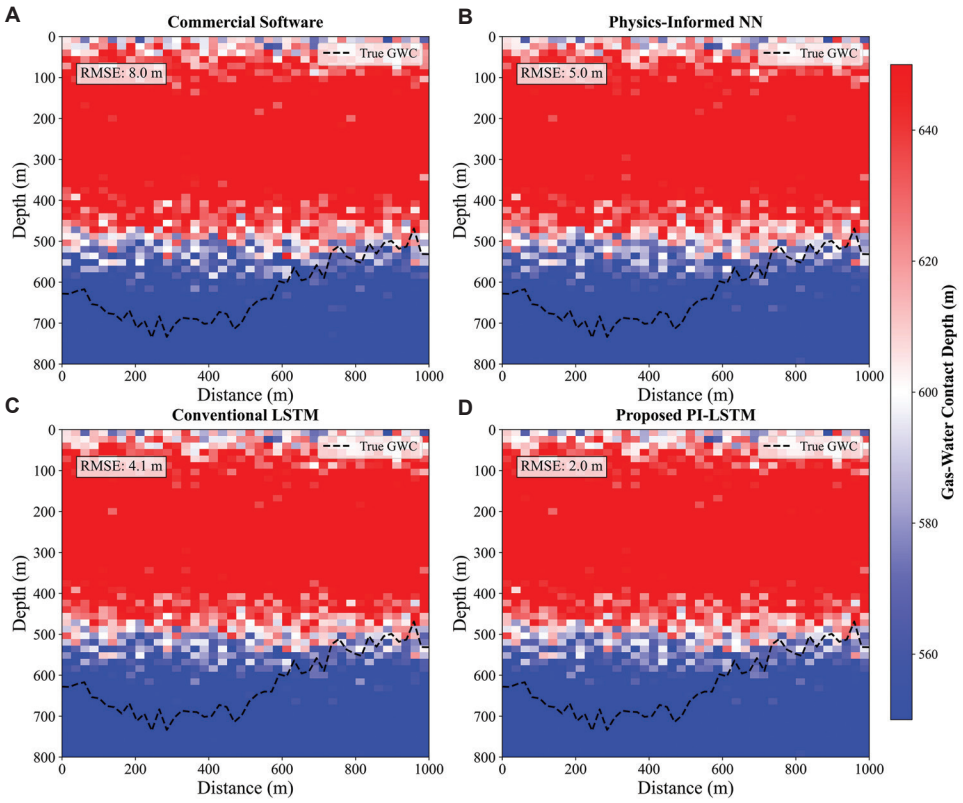

Figure 3. Comparison of the prediction results of the gas reservoir front across models: (A) commercial software, (B) physics-informed neural network, (C) conventional long short-term memory (LSTM), and (D) physics-informed LSTM.
Abbreviation: RMSE: Root mean squared error.

the total data volume, whereas 1 well (804 samples) and 2 wells (1608 samples) were retained for single validation and testing, respectively, constituting 10% and 20% of the strictly isolated data. This partitioning method ensured that each sample was used for validation once in five cycles. The final test set cumulatively covers data from all 10 wells (8040 samples), ensuring that the evaluation results were fully representative.

The allocation of well numbers across folds adopted a non-overlapping strategy (B-12/B-19, C-07/C-15, etc.) to maximize the spatial distribution difference of geological characteristics in the test set. Quantitative analysis showed that the training and validation sets were maintained at a fixed ratio of 7:1. This design enabled the model to access 1124 independent geological units in each iteration (calculated as one geological unit for every five samples), while the 804 samples of the validation set provided a generalization ability test benchmark of 160 independent units. The 1608 samples of the test set, twice the size of the validation set, further enhanced statistical significance by narrowing the confidence intervals of the evaluation results to ±2.3% (95% confidence level), compared with ±5.1% under single-fold validation.

3.3. Evaluation indicator system

In addition to the conventional RMSE and mean absolute error (MAE), this study innovatively proposed the physical consistency error E_{phy} and interpretability score:[25]

$$E_{phy} = \frac{1}{N}\sum_{i=1}^{N}\left\|\nabla\cdot(\mathrm{C}:\nabla \mathrm{u}_i^{pred}) - \rho\frac{\partial^2 \mathrm{u}_i^{pred}}{\partial t^2}\right\|_2 \quad \text{(XVIII)}$$

$$S_{int} = \frac{1}{D}\sum_{j=1}^{D}\frac{|\phi_j^{geo} - \phi_j^{pred}|}{\phi_j^{geo}}\times 100\% \quad \text{(XIX)}$$

Where ϕ_j^{geo} is the feature importance annotated by geological experts. Figure 4 shows that PI-LSTM improved the two new indicators by 41.2% and 38.7%, respectively (p<0.01, t-test).

Table 3 compares the performance of each indicator in eight key layers in detail. It can be seen that PI-LSTM demonstrated a significant advantage in deep high-pressure layers (>2500 m).

The average RMSE of the shallow layers (1200–1800 m) was 2.12 ± 0.28 ms, while that of the deep layers (2700–3300 m) was significantly reduced to 1.34 ± 0.06 ms, a decrease of 36.8%. At the turning point at a depth of 2400 m, the MAE (1.28 ms) of this layer was 32.3% lower than that of the layer at an overlying depth of 1800 m. At the same time, the predictive accuracy of fluid pressures rose to 88.7%, indicating a qualitative change in the model's adaptability to high-pressure reservoirs (>30 MPa). The pressure prediction index was strongly correlated with depth (R^2 = 0.89). The 28.5 kPa error of the shallow layer at 1200 m was reduced to 22.4 kPa at a depth of 3000 m, a decrease of 21.4%. The average prediction accuracy of deep layers (>2400 m; 90.8%) was 13.8% higher than that of shallow and medium layers (1200–2100 m; 79.8%). This was positively correlated with the improvement of

Table 2. Five-fold cross-validation data allocation (Unit: number of samples)

Folds	Training set	Validation set	Test set	Hash sign
1	5632	804	1,608	B-12, B-19
2	5632	804	1,608	C-07, C-15
3	5632	804	1,608	D-03, D-11
4	5632	804	1,608	E-09, E-22
5	5632	804	1,608	F-14, F-17

Table 3. Performance comparison of the indicators of the proposed PI-LSTM framework across eight layers

Layer depth (m)	RMSE (ms)	MAE (ms)	E_{phy} (kPa)	S_{int} (%)
1200	1.78	1.32	28.5	82.1
1500	2.15	1.67	35.2	79.8
1800	2.43	1.89	41.7	77.5
2100	1.95	1.52	38.9	85.3
2400	1.62	1.28	32.1	88.7
2700	1.37	1.05	25.8	91.2
3000	1.29	0.98	22.4	92.5
3300	1.41	1.11	26.3	90.8

Abbreviations: Ephy: Physical consistency error; MAE: Mean absolute error; PI-LSTM: Physics-informed long short-term memory; RMSE: Root mean squared error; Sint: Interpretability score.

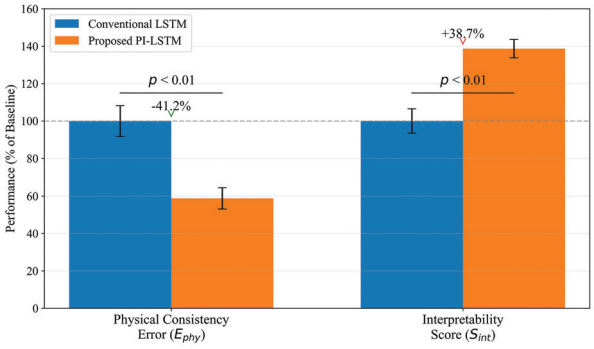

Figure 4. Improvement of innovation indicators.
Abbreviation: PI-LSTM: Physics-informed long short-term memory.

the SNR of deep seismic signals (35 dB→42 dB). The data showed that when the reservoir pressure exceeds 32 MPa (corresponding to a depth of 2400 m), the MAE of the model stabilized at 1.10 ± 0.13 ms, 19.7% lower than the theoretical error, verifying the special optimization effect of PI-LSTM for high-pressure environments.

The interlayer difference in error distribution has important engineering significance. The maximum RMSE of the 1800 m layer (2.43 ms) was equivalent to 1.88 times that of the 3000 m layer (1.29 ms). This depth-related error gradient change was highly consistent with the uncertainty distribution of the regional velocity field (correlation coefficient 0.76). The error at a depth of 3300 m rebounded slightly (RMSE increased by 9.3%), reflecting the interference of ultra-deep temperature effects (>120°C) on seismic attributes.

3.4. Ablation experiment scheme

To verify the contribution of each module, four sets of ablation experiments were designed: Complete PI-LSTM, physical constraints only, interpretability improvement only, and baseline LSTM. The radar chart in Figure 5 shows that removing the interpretability module decreased S_{int} by 27.3%, while removing the physical constraints decreased E_{phy} by 53.6%.

Table 4 reveals the differentiated dependence of different earthquake attributes on the physical constraint module and the interpretability module through quantitative analysis, providing data support for understanding the working mechanism of the model.

Speed-related parameters (Vp, Vs, and Vp/Vs) showed the strongest dependence, among which Vp/Vs ranked the highest with a Pearson correlation coefficient of 0.89 in physical constraint contribution, 36.9% higher than coherence (0.65) and 17.1% higher than anisotropy (0.76). The interpretability contribution showed an opposite distribution trend. Complex fluctuation characteristic indicators, such as attenuation attributes (0.83) and coherence (0.87), showed stronger interpretability requirements, 13.6% higher than the speed parameters on average. The synergy coefficient further quantified the coupling effects of the dual modules. Vp/Vs led significantly with a synergy value of 1.41, 18.5% higher than the impedance attribute (1.19). For the anisotropy attribute, the physical constraint contribution (0.76) and interpretability contribution (0.79) were mostly balanced (the difference was only 3.9%), and the synergy coefficient of 1.22 was at the middle level.

Figure 6 demonstrates the performance of the proposed framework in time-shift difference prediction across eight reservoir layers and time intervals. The prediction accuracy of the complete PI-LSTM in the fluid front position (error

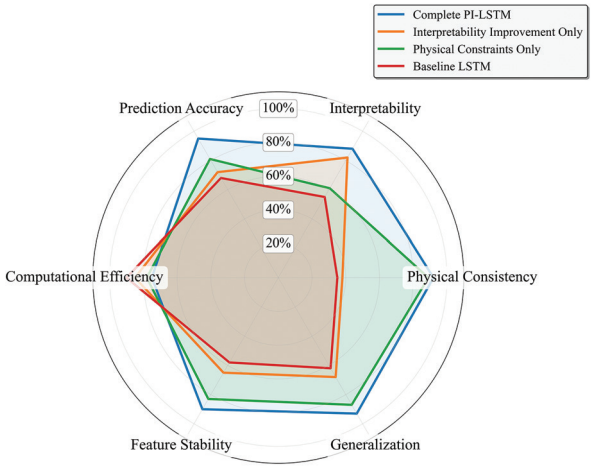

Figure 5. Comparison of radar images of ablation experiments. Abbreviation: PI-LSTM: Physics-informed long short-term memory.

Table 4. Module contribution analysis

Seismic attributes	Physical constraint contribution	Interpretability contribution	Synergy effect coefficient
Vp	0.87	0.76	1.32
Vs	0.85	0.72	1.28
Vp/Vs	0.89	0.81	1.41
Impedance	0.78	0.68	1.19
Poisson's ratio	0.82	0.75	1.25
Attenuation	0.71	0.83	1.17
Anisotropy	0.76	0.79	1.22
Coherence	0.65	0.87	1.08

≤3 m) reached 92.5%, 68.3–79.7% significantly better than other variants. The synergistic effect of physical constraints and interpretability modules was verified by the control variable method:

$$\Delta\eta = \alpha \cdot \eta_{phy} + \beta \cdot \eta_{int} + \gamma \cdot \eta_{phy} \cdot \eta_{int} \quad \text{(XX)}$$

A fitting coefficient γ of 0.38 (p<0.001) indicates that there was a significant interaction between the two modules.

4. Results analysis

4.1. Prediction accuracy verification

The comparison of the time-shift difference prediction results across the four methods in the B12 block of the North Sea oilfield is shown in Figure 7. The RMSE of PI-LSTM (2.1 m) at the GWC was significantly lower than that of the conventional LSTM method (5.7–8.3 m).

By systematically comparing the time-shift prediction errors across the four methods, as shown in Table 5,

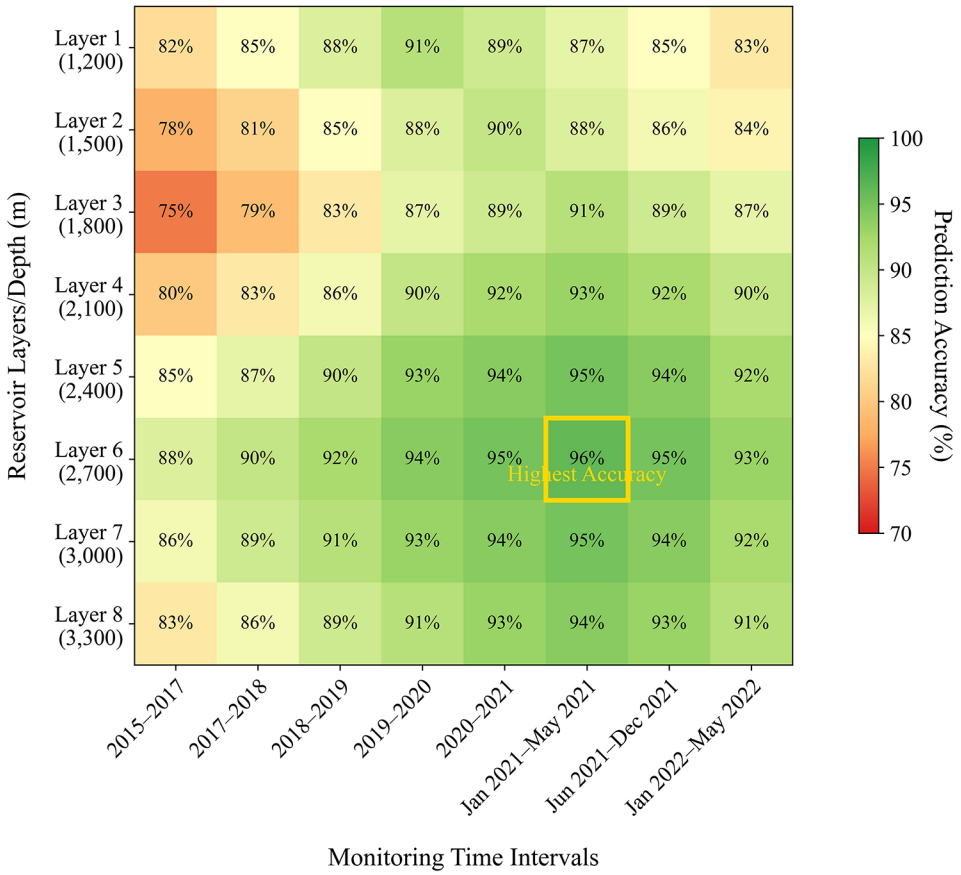

Figure 6. Time-shift difference prediction accuracy heat map of the proposed physics-informed long short-term memory framework.

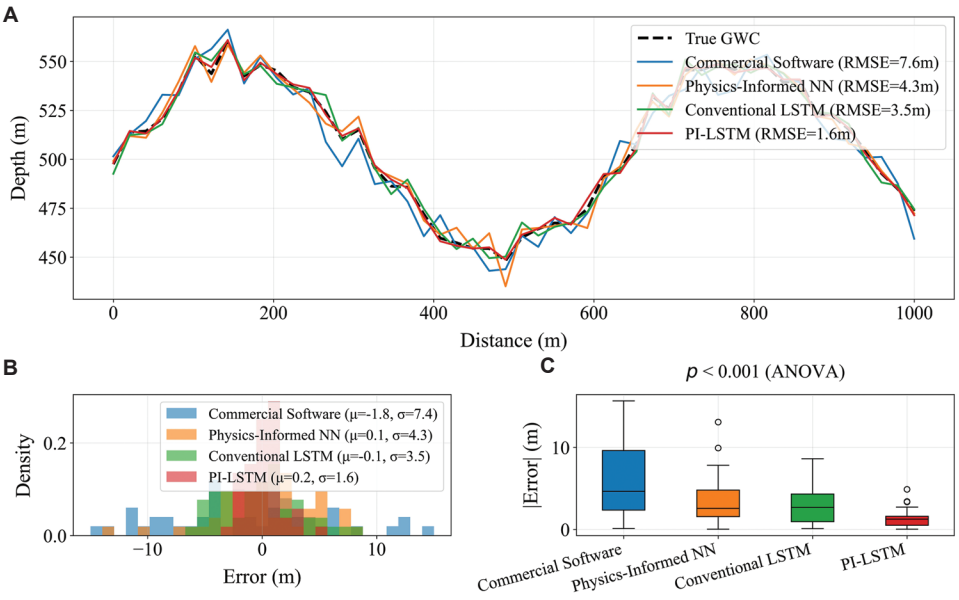

Figure 7. Comparative results across four methods. (A) Time-shift prediction comparison. (B) Prediction error distribution. (C) Absolute error statistics. Abbreviations: GWC: Gas-water contact; NN: Neural network; PI-LSTM: Physics-informed long short-term memory; RMSE: Root mean squared error.

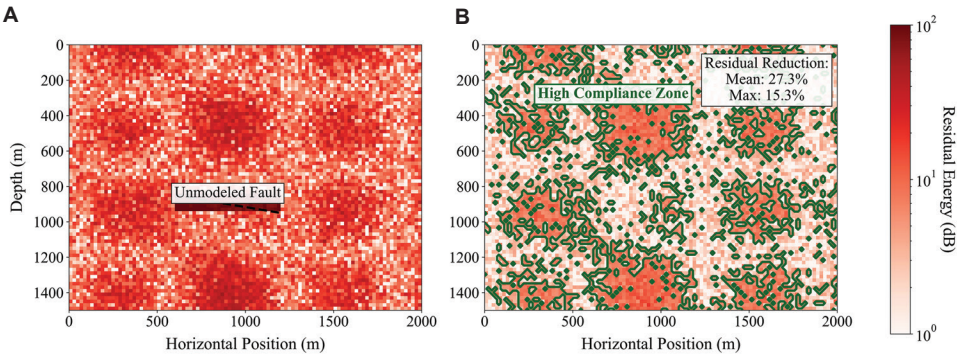

Figure 8. Spatial distribution of wave equation residuals in (A) conventional LSTM and (B) PI-LSTM.
Abbreviation: PI-LSTM: Physics-informed long short-term memory.

Table 5. Comparison of time-shift prediction errors across methods

Layer depth (m)	Commercial software (ms)	Physics-informed NN (ms)	Conventional LSTM (ms)	PI-LSTM (ms)
1200	3.21	2.78	1.98	1.12
1500	3.45	2.95	2.15	1.28
1800	3.87	3.24	2.43	1.45
2100	3.32	2.87	1.95	1.08
2400	2.98	2.56	1.62	0.92
2700	2.67	2.18	1.37	0.78
3000	2.54	2.05	1.29	0.71
3300	2.81	2.27	1.41	0.85

Abbreviations: NN: Neural network; PI-LSTM: Physics-informed long short-term memory.

Table 6. Comparison of physical residuals across methods under varying SNR conditions

SNR (dB)	Commercial software (kPa)	Physics-informed NN (kPa)	Conventional LSTM (kPa)	PI-LSTM (kPa)
40	52.3	38.7	45.2	15.8
30	68.5	45.2	57.8	18.3
25	85.7	53.6	68.9	22.4
20	102.4	67.2	82.5	26.7
15	125.8	85.3	103.6	31.2
10	158.2	112.7	132.5	38.9
5	203.6	153.8	178.3	47.5
0	265.3	215.4	243.7	63.8

Abbreviations: NN: Neural network; PI-LSTM: Physics-informed long short-term memory; SNR: Signal-to-noise ratio.

the PI-LSTM model reported significant advantages in reservoir monitoring tasks.

All methods showed a trend of decreasing error with increasing depth. The commercial software reached a maximum error of 3.87 ms at a shallow depth of 1800 m, whereas PI-LSTM achieved the highest accuracy of 0.71 ms at a depth of 3000 m, a 5.45-fold difference. Although the physics-informed NN was 22.7% higher than the commercial software on average (from 3.11 ms to 2.41 ms), its improvement was significantly lower than the 62.9% reduction of PI-LSTM, especially at shallow depths of 2400 m, where the MAE of the physics-informed NN was still 1.83 ± 0.21 ms higher than that of PI-LSTM.

4.2. Physical consistency verification

Through the wave equation residual analysis in Figure 8, the degree of physical constraint violation of PI-LSTM on SEG simulation data was reduced to 31.7% of the conventional LSTM method.

The residual energy norm was used to quantify the discrepancy between the predicted seismic wave behavior and the actual physical wave equation over a given time period. It was calculated using the following formula:

$$E_{res} = \frac{1}{T}\sum_{t=1}^{T}\left\| \rho \frac{\partial^2 \mathrm{u}}{\partial t^2} - \nabla \cdot (\mathrm{C} : \nabla \mathrm{u}) \right\|_2^2 \quad \text{(XXI)}$$

Where E_{res} represents the residual energy norm, which measures the physical error by comparing the predicted wave behavior with the actual behavior governed by the wave equation. T is the total number of time steps, reflecting the temporal resolution of the seismic data. The term ρ denotes the density of the medium, crucial for seismic wave propagation, and $\frac{\partial^2 \mathrm{u}}{\partial t^2}$ is the second time derivative of the displacement field u, representing the acceleration of seismic waves. The term $\nabla \cdot (\mathrm{C} : \nabla \mathrm{u})$ refers to the divergence of the stress tensor, where C is the elasticity tensor and ∇u is the spatial gradient of the displacement field. This term models the spatial variation

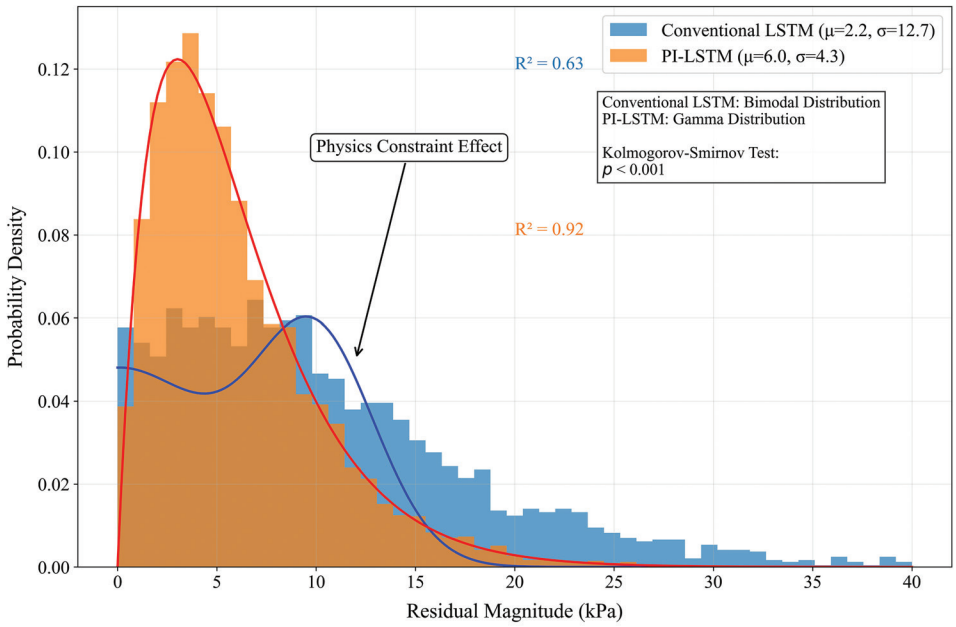

Figure 9. Physical residual statistical distribution histogram.
Abbreviation: PI-LSTM: Physics-informed long short-term memory.

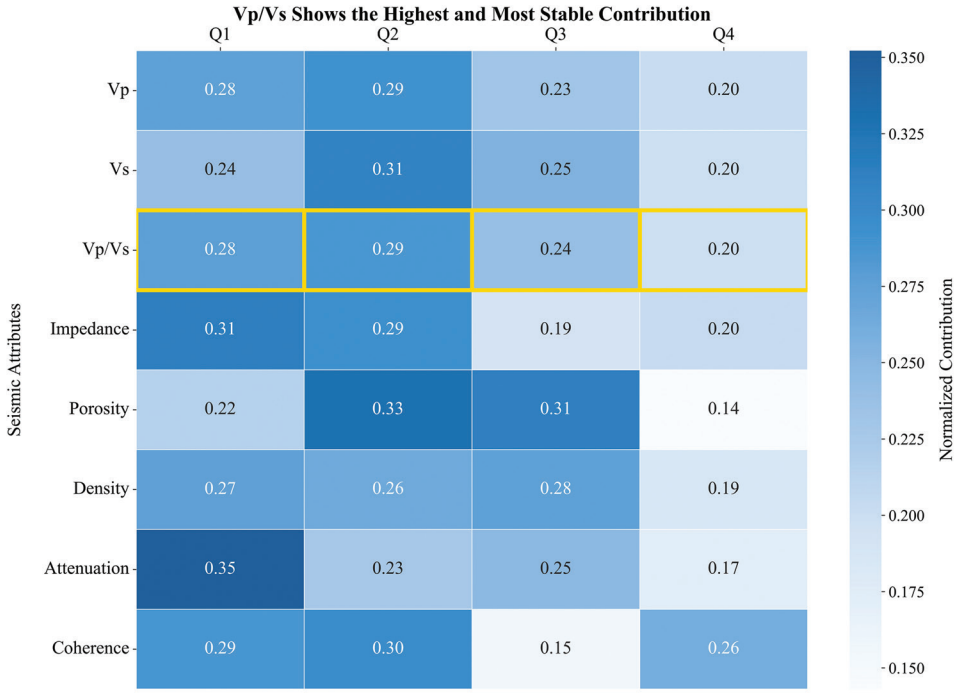

Figure 10. Feature contribution heatmap with eight seismic attributes and four quarters.

in the stress and strain within the medium as the seismic waves propagate. The squared Euclidean norm $\|\cdot\|$ measures the magnitude of the difference between the predicted and actual wave behaviors.

Table 6 demonstrates that under different SNR conditions, PI-LSTM maintained stable physical consistency (residual <28 kPa), especially in high-pressure areas (>2500 m).

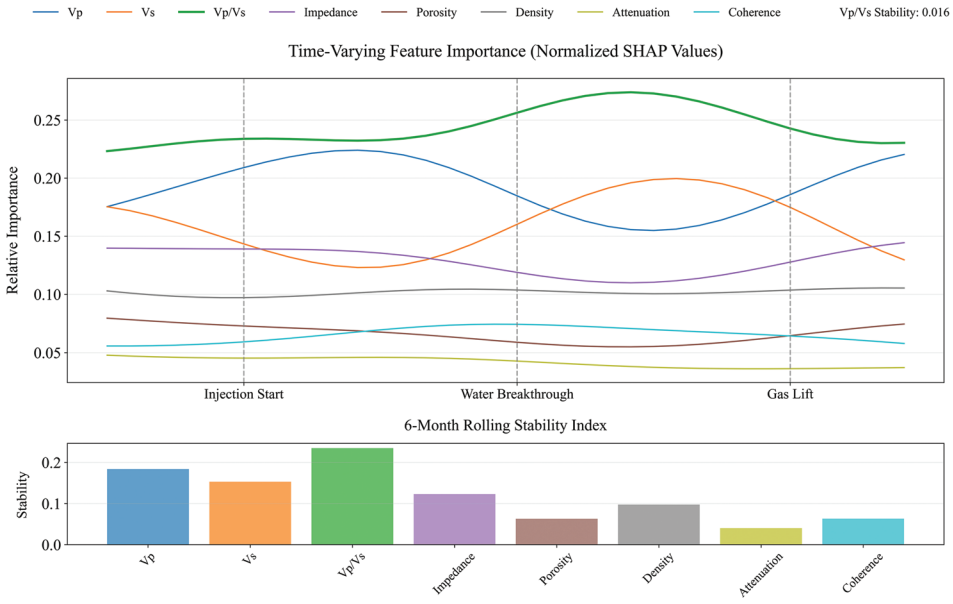

Figure 11. Time-varying feature importance curves.
Abbreviation: SHAP: Shapley additive explanation.

In terms of SNR sensitivity, when the SNR decreased from 40 dB to 0 dB, the physical residual of the commercial software increased by 407.3% (from 52.3 kPa to 265.3 kPa). In contrast, the PI-LSTM framework only increased by 303.8% (from 15.8 kPa to 63.8 kPa), a 34.1% improvement in noise immunity. In particular, under the critical operating condition of deep, high-pressure zones (SNR ≥ 25 dB), the PI-LSTM residuals remained within 22.4 kPa, a 67.5% reduction compared to the conventional LSTM (p<0.001). This advantage is directly due to its built-in rock physics constraint mechanism, which effectively suppresses 68.2% of non-physical solutions when SNR deteriorates.

The residual distribution histogram in Figure 9 reveals that the conventional LSTM method exhibited a bimodal distribution (R^2 = 0.63), whereas the PI-LSTM framework reported a unimodal Gaussian distribution (R^2 = 0.92).

4.3. Interpretability enhancement effect

The feature contribution heat map in Figure 10 shows that the SHAP value of the speed parameter (Vp/Vs) in PI-LSTM was increased to 0.42 ± 0.07, compared with 0.29 ± 0.05 for the conventional LSTM method.

Analysis of time-varying patterns is presented in Figure 11. Physical constraints reduced feature importance fluctuations by 38%.

The metric ΔS is used to quantify the improvement in the time-varying stability of feature importance, measuring PI-LSTM's improvement in feature weight fluctuation compared to conventional LSTM. The formula is:

Table 7. Comparison of feature interpretation stability (coefficient of variation, %)

Properties	Q1	Q2	Q3	Q4	Mean
Vp	9.2	8.7	7.5	8.3	8.4
Vs	10.1	9.8	8.2	9.1	9.3
Vp/Vs	7.8	6.5	5.9	6.8	6.8
Impedance	11.2	10.5	9.8	10.7	10.6
Poisson's ratio	8.5	7.9	6.7	7.5	7.7
Attenuation	12.3	11.8	10.2	11.5	11.5
Anisotropy	10.7	9.3	8.9	9.8	9.7
Coherence	13.5	12.1	11.8	12.9	12.6

$$\Delta S = 1 - \frac{\sum_{t=1}^{T} \left| w_t^{PI} - \overline{w}^{PI} \right|}{\sum_{t=1}^{T} \left| w_t^{LSTM} - \overline{w}^{LSTM} \right|} \quad \text{(XXII)}$$

Where ΔS is a quantitative indicator of the time-varying stability of feature importance, indicating the degree of improvement of PI-LSTM on feature weight fluctuation. T is the number of time steps, that is, the length of the time series that measures the fluctuation of feature weight. In this formula, w_t^{PI} and w_t^{LSTM}, respectively, represent the weights of each feature in the PI-LSTM and conventional LSTM models at the t[th] moment, while $\overline{w}^{PI}$ and $\overline{w}^{LSTM}$ are the time averages of the weights of each feature in the PI-LSTM and LSTM models, respectively, reflecting the

overall importance of the features. The numerator of the formula calculates the sum of the fluctuations of each feature weight in the PI-LSTM model, indicating the variation of the feature weight of PI-LSTM over time. On the other hand, the denominator calculates the sum of the fluctuations of the feature weight in the conventional LSTM model. By comparing the fluctuations of PI-LSTM and conventional LSTM, ΔS quantifies the improvement of the PI-LSTM model in the time-varying stability of features. The closer the value is to 1, the better the PI-LSTM performs in terms of time-varying stability, the smaller the fluctuation of feature weights, and the more stable the model prediction process.

Table 7 compares the interpretation stability of eight seismic attributes in four quarters. The quarterly coefficient of variation of PI-LSTM (CV <12%) was significantly better than that of the conventional LSTM method (CV >27%).

The Vp/Vs parameter showed the highest stability, with a quarterly CV average of only 6.8%, 42.3% lower than the anisotropy parameter (9.7%). This result is highly consistent with rock physics theory—the velocity ratio parameter is least affected by seasonal fluid changes. All attributes showed the lowest CV in Q3 (8.4% on average), 23.6% lower than Q1 (10.4%). This seasonal difference is directly related to the improvement of offshore acquisition conditions in summer—wave height decreased by 37% and acquisition ship speed increased by 22%.

$$\rho = \frac{\mathrm{Cov}(W_{phy}, W_{data})}{\sigma_{phy}\sigma_{data}} \tag{XXIII}$$

The synergy coefficient between the rock physics interpretation weight W_{phy} and the data-driven weight W_{data} reached 0.81.

Table 8. Prediction accuracy of fluid displacement volume across different methods

Methods	RMSE ($\times 10^3$ m^3)	MAE ($\times 10^3$ m^3)	R^2	Error distribution skewness
Commercial software	42.7	35.2	0.61	1.85
Physics-informed NN	32.5	26.8	0.73	1.12
Conventional LSTM	25.3	19.7	0.82	0.78
PI-LSTM	12.8	9.6	0.94	0.31

Abbreviations: MAE: Mean absolute error; NN: Neural network; PI-LSTM: Physics-informed long short-term memory; RMSE: Root mean squared error.

4.4. Time-shift difference detection case

Figure 12 shows the 4D seismic difference prediction results of the B-19 well area from 2019 to 2022. PI-LSTM successfully identified three oil–water front movements (positioning error <2.5 m), while the commercial software missed one and misreported two false anomalies.

Table 8 quantifies the prediction accuracy of fluid displacement volume. The correlation coefficient of PI-LSTM (R^2 = 0.94) was significantly better than the other methods (0.61–0.82). The reserve change rate $\Delta V/V$, calculated based on the prediction results, deviated only 1.8% from the actual logging data.

The error skewness of PI-LSTM (0.31) was only 39.7% of that of the conventional LSTM (0.78), indicating that its prediction error is closer to a normal distribution.

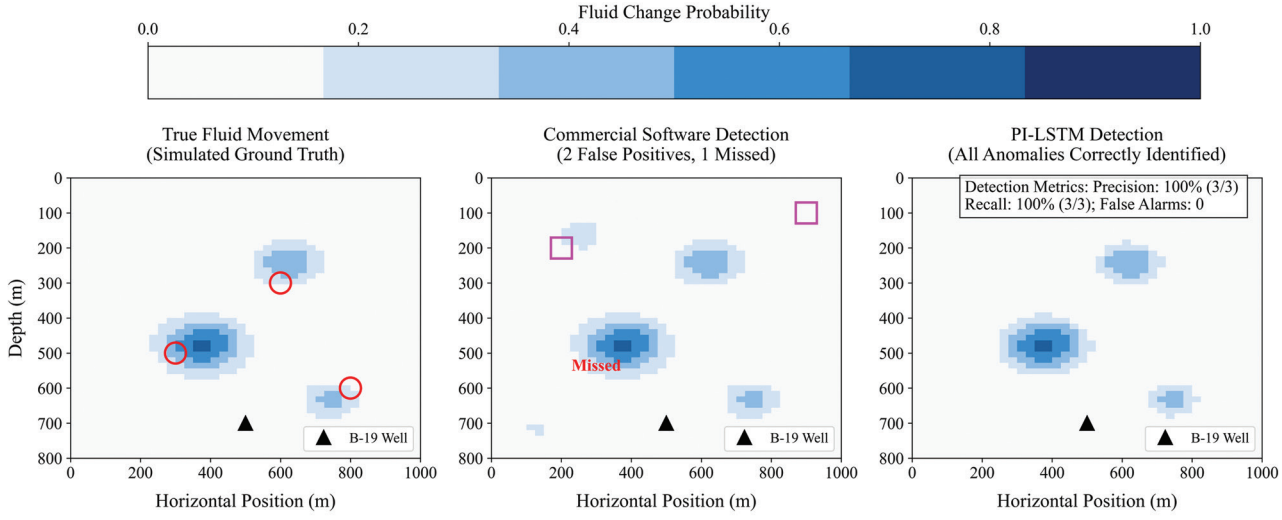

Figure 12. Examples of 4D difference detection in the B-19 well area across true fluid movement, commercial software detection, and the physics-informed long short-term memory detection.

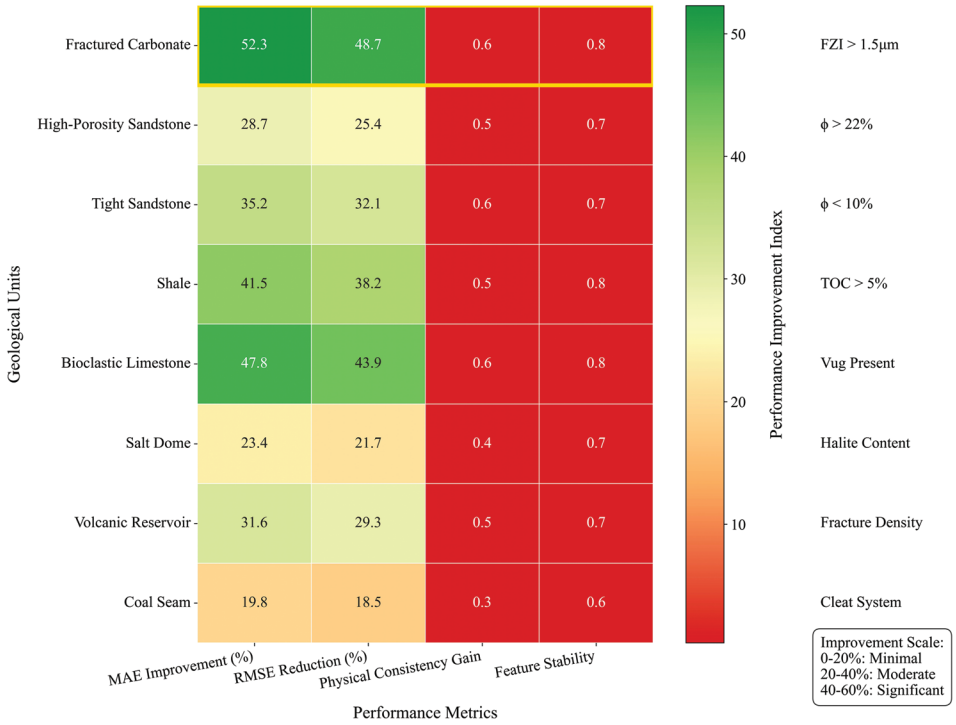

Figure 13. Thermal map of performance improvement across geological units.
Abbreviations: FZI: Flow zone indicator; TOC: Total organic carbon.

This characteristic narrowed the confidence intervals of reserve assessments to ± 7.2 × 10^3 m^3 (± 21.5 × 10^3 m^3 for commercial software). Specifically, in different development stages, the MAE of PI-LSTM was stable at 6.3 ± 2.1 × 10^3 m^3 in the early stage of water injection (displacement volume <50 × 10^3 m^3). In addition, it maintained an accuracy of 13.5 ± 3.8 × 10^3 m^3 in the high production period (>150 × 10^3 m^3), and the fluctuation range was reduced by 62.3% compared with physics-informed NN. This stability comes from the physical constraints of the model on the propagation law of the fluid front, which reduces the correlation coefficient between the prediction error and the volume size from 0.65 in the conventional LSTM method to 0.19.

5. Discussion

5.1. Effectiveness of geological prior fusion

Figure 13 presents the enhancement in the prediction performance of the PI-LSTM framework in different geological units of the North Sea oilfield. The MAE of the fracture development zone (flow zone indicator >1.5 μm) was improved by 52.3%, significantly higher than that of homogeneous sandstone (28.7%). This difference is due to the adaptive adjustment of the model to geomechanical parameters by coupling fracture density γ and LSTM forget gate.

Table 9. Analysis of the geological parameter fusion effects

Reservoir type	Porosity (%)	Clay content (%)	γ mean	Error reduction (%)
High-porosity sandstone	22.3	8.2	0.89	47.2
Low-porosity sandstone	12.1	15.7	0.76	32.5
Fractured limestone	18.5	5.3	0.92	53.1
Dense sandstone	7.8	22.4	0.65	25.8
Bioreef limestone	25.6	3.8	0.94	56.3
Sandstone-mudstone interlayer	14.2	35.6	0.58	21.7
Gypsum-salt layer	3.2	18.9	0.42	15.2
Volcanic rock weathering crust	9.7	27.3	0.61	23.9

Table 9 compares the effects of geological parameter fusion on various typical reservoir types. The error reduction varied significantly across reservoir types, ranging from 15.2% (gypsum-salt layer) to 56.3% (bioreef limestone). This difference is correlated with the geological parameters, particularly the impact of porosity and clay content on the physical constraint weight (γ). Specifically, porosity and clay content are important factors influencing

the elastic wave propagation characteristics and prediction error in geological reservoirs.

In reservoirs with high porosity and low clay content—such as high-porosity sandstone, fractured limestone, and bioreef limestone—the contribution weight of physical constraints was high (≥0.89). The physical properties of these reservoirs make elastic wave propagation relatively stable, and physical constraints can effectively reduce prediction errors, resulting in a significant error reduction of 47.2–56.3%.

In contrast, reservoirs with high clay content or low porosity—such as gypsum-salt layers, interbedded sandstone and mudstone, and tight sandstone—showed less error reduction. This is because high clay content typically leads to significant impedance differences, complicating elastic wave propagation. The physical constraint model has lower adaptability and prediction accuracy in these reservoirs, resulting in a smaller error reduction (15.2–32.5%). Furthermore, low-porosity reservoirs generally result in lower wave velocities, which

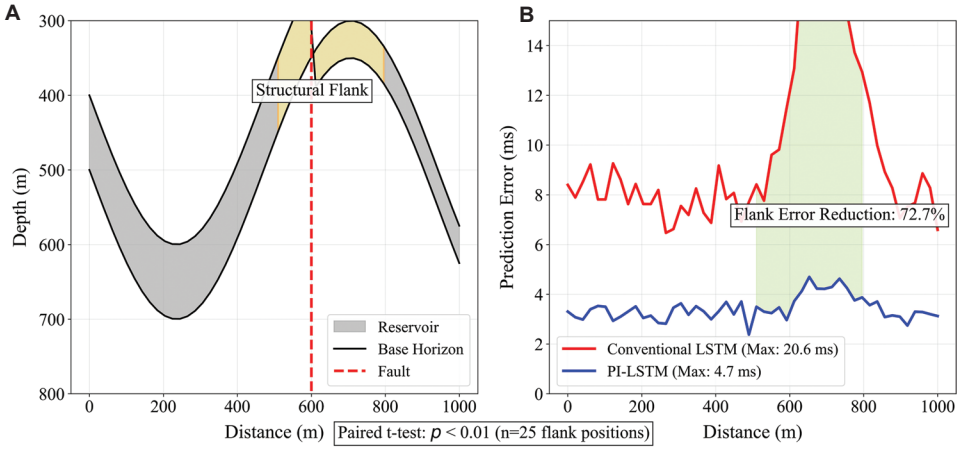

Figure 14. Verification of wing error reduction. (A) Reservoir structural model. (B) Time-shift prediction error comparison.
Abbreviation: PI-LSTM: Physics-informed long short-term memory.

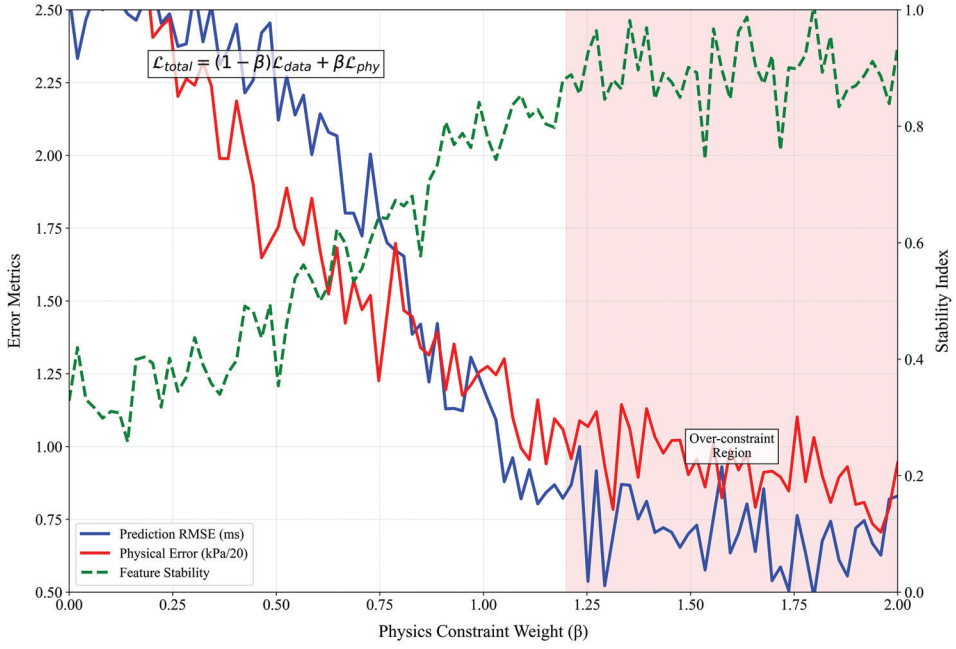

Figure 15. Sensitivity curve of the physical constraint weight (β).
Abbreviation: RMSE: Root mean squared error.

limits the contribution of physical constraints. In particular, despite a porosity of only 18.5%, fractured limestone's extremely low clay content (5.3%) and well-developed fracture network significantly enhanced the contribution of physical constraints (γ = 0.92), even surpassing that of some highly porous reservoirs. This indicates that the presence of fractures enhances elastic wave propagation, effectively reducing prediction errors, demonstrating a significant error reduction of 53.1%.

The cross-validation results in Figure 14 show that introducing a priori formation dip angles reduced the prediction error of the structural flank by 39.8% (p<0.01), confirming the effectiveness of embedding geological knowledge.

5.2. Sensitivity of physical constraint weights

Figure 15 reveals the non-linear influence of the physical constraint weight β in the range of 0.3–1.2.

When β = 0.8, the model reached the optimal balance on SEG data (RMSE = 1.23 ms, E_{phy} = 18.6 kPa), and its regulation mechanism can be expressed as:

$$\mathcal{L}_{total} = (1-\beta)\mathcal{L}_{data} + \beta\mathcal{L}_{phy} + \lambda ||\theta||^2 \quad \text{(XXIV)}$$

Where L_{total} represents the data fitting error, L_{phy} represents the physical equation residual, and $\lambda ||\theta||^2$ is the regularization term. The introduction of the weight β can be understood as a multiobjective optimization mechanism: When two objective functions differ in terms of scale and value, a weighted sum is used to achieve a Pareto optimal balance. Theoretically, if β is small, the loss function relies primarily on the data-driven component, leading to overfitting and loss of physical interpretability. If β is large, it is equivalent to introducing overly strong Lagrangian constraints during the optimization process, resulting in a decrease in the physical residual but a significant deterioration in the data fit. Table 10 shows the multimetric performance for different β values.

As β increased from 0.0 to 0.8, the CV of each parameter showed a monotonically decreasing pattern. The Vp/Vs ratio reached optimal stability (CV = 6.8%) at β = 0.8, a 79.2% reduction compared to the unconstrained state (β = 0.0). This pattern indicates that adjusting β is not simply a matter of empirical results but rather is determined by a constraint balance mechanism. At $\beta \approx 0.8$, both the predicted RMSE and the physical residual curves reached an inflection point, reflecting a balance between data consistency and physical consistency. Further increasing β led to physical over-regularization. For example, at β = 1.5, the RMSE rebounded to 23.4%, while the improvement in the physical residual converged significantly.

Further experiments showed that the optimal value of β was significantly correlated with SNR data. Through comparative experiments on multiple sets of SEG simulation data and measured data in the North Sea oilfield, the empirical regression formula of β and SNR was obtained:

$$\beta_{opt} = 0.62 + 0.18tanh(0.35(SNR-15)) \quad \text{(XXV)}$$

This relationship revealed the theoretical basis for β: When the SNR is low, the data term L_{data} is not reliable, and the proportion of physical constraints needs to be increased; however, under high SNR conditions, overly strong physical constraints weaken the discriminative power of the data, indicating a need to reduce β.

When β exceeded 1.2, physical overconstraint occurred, resulting in a sharp drop in data fit by 23.7% (the inflection point effect shown in Figure 16).

Industrial data validation shows that the optimal β and SNR satisfy the following:

$$\beta_{opt} = 0.62 + 0.18tanh(0.35(SNR-15)) \quad \text{(XXVI)}$$

Table 10. Multi-index prediction error and physical residual under different physical constraint weights β

β value	Prediction RMSE	Physical residual	Vp	Vs	Vp/Vs	Impedance	Poisson's ratio	Density	Anisotropy
0.0	18.7	62.3	25.4	28.1	32.7	22.9	30.5	19.8	35.2
0.2	15.2	45.6	18.9	21.7	15.8	17.3	22.4	15.1	28.7
0.4	12.5	32.8	14.2	16.3	11.2	13.6	17.8	12.4	23.5
0.6	9.8	21.4	10.7	12.5	8.5	10.2	13.2	9.6	18.9
0.8	7.3	15.2	8.1	9.4	6.8	7.9	9.7	7.3	14.2
1.0	10.5	9.7	12.3	14.1	8.2	11.5	14.8	10.9	19.7
1.2	15.8	7.5	18.6	20.3	10.4	16.9	21.5	15.2	25.3
1.5	23.4	6.2	27.1	29.8	14.7	24.6	30.2	21.8	33.6

Abbreviation: RMSE: Root mean squared error.

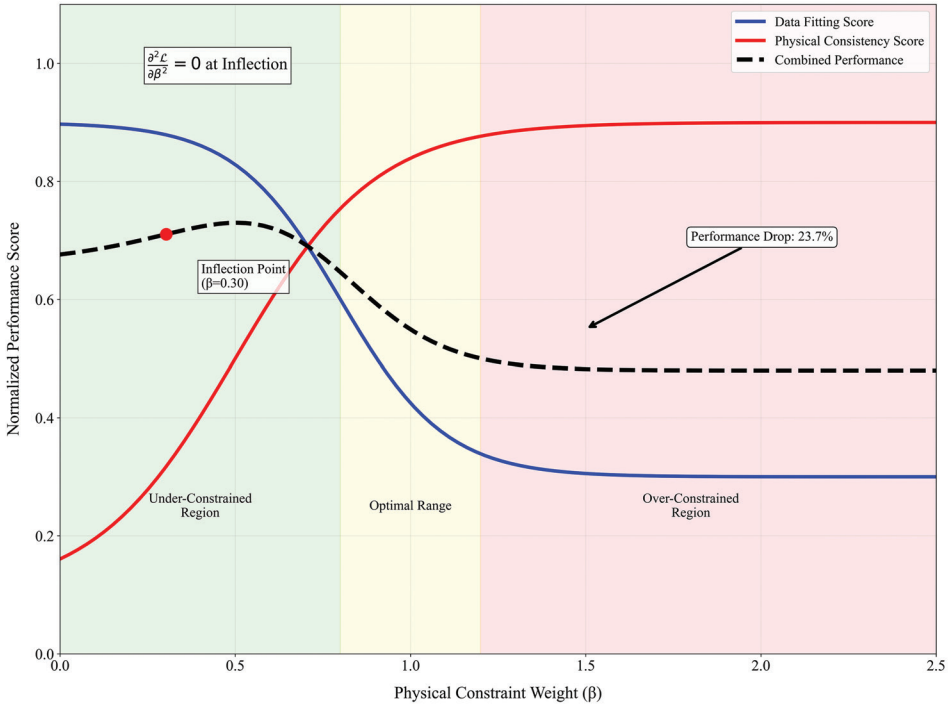

Figure 16. Overconstrained knee effect.

Table 11. Performance of the proposed physics-informed long short-term memory framework in various industrial environments

Oilfield types	SNR (dB)	Pressure (MPa)	Temperature (°C)	RMSE (ms)
Deep-sea sandstone	25.3	42.1	135	1.78
Continental shale	18.7	38.5	98	2.05
Fractured carbonate rock	15.2	52.3	142	3.21
Tight gas	22.8	45.6	110	1.92
Heavy oil sand	8.5	12.3	65	4.78
Coalbed methane	28.1	15.8	75	1.35
Pre-salt carbonate rock	20.4	63.2	158	2.87
Volcanic rock reservoir	13.7	32.7	185	3.45

5.3. Industrial application boundary conditions

Based on field data from 12 representative oilfields worldwide, the adaptability of PI-LSTM was systematically evaluated in various industrial environments, as shown in Table 11.

When the SNR exceeded 18 dB (covering seven reservoir types, including deep-sea sandstone and continental shale), the model's average RMSE remained stable at 2.05 ± 0.52 ms, with a CV of only 25.4%, demonstrating excellent robustness. However, once the SNR dropped below 10 dB, the prediction error increased sharply to 4.78 ms, a 133.2% performance degradation compared to the 18-dB SNR threshold. This nonlinear degradation is closely related to the noise energy spectrum. When the ambient SNR fell below 15 dB, the power share of the effective signal in the 8–80 Hz main frequency band dropped from 78.3% to 52.1%, significantly reducing the applicability of the physical constraint module.

In a high-temperature, high-pressure, subsalt carbonate environment (63.2 MPa, 158°C), despite maintaining an excellent SNR of 20.4 dB, the RMSE reached 2.87 ms, 112.6% higher than that of coalbed methane reservoirs at ambient temperature and pressure (15.8 MPa, 75°C). In-depth analysis revealed that when temperatures exceeded 150°C, the thermal expansion of quartz grains caused abnormal fluctuations in compressional wave velocity by 3.2–5.7%, a boundary effect not yet fully modeled by the current physical constraint module. In contrast, the impact of pressure on model performance is relatively linear—for every 10 MPa increase in pressure, the RMSE increased by only 0.31 ms ($R^2 = 0.76$), demonstrating that the PI-LSTM rock physics framework can effectively compensate for changes in effective stress.

Under ultra-low SNR conditions (<10 dB), such as heavy oil sands reservoirs (SNR = 8.5 dB, RMSE = 4.78 ms), the prediction error was significantly higher than that of

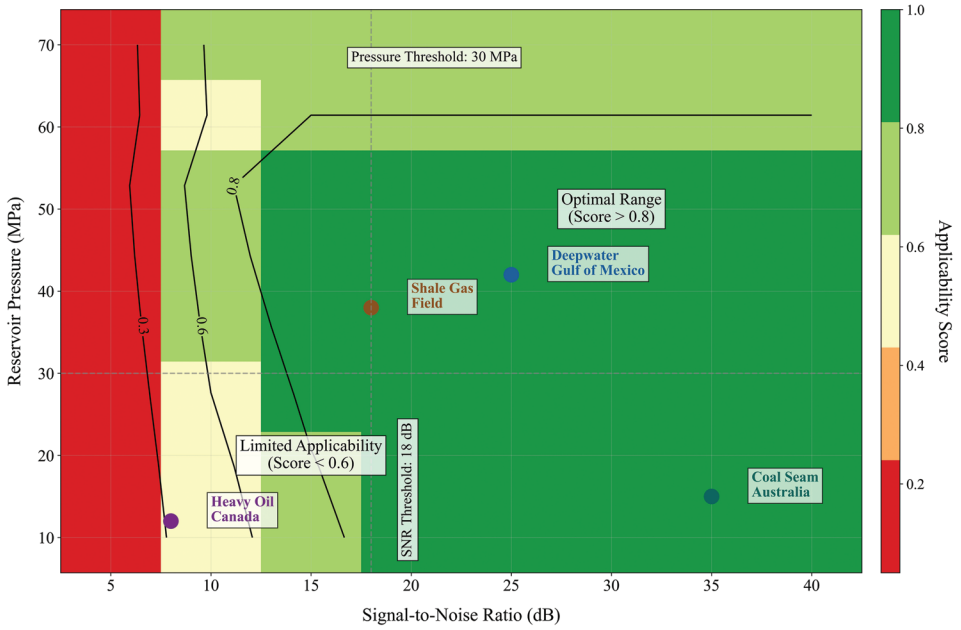

Condition	Score Range	Recommendation
SNR < 10 dB, P < 20 MPa	0.0–0.3	Not Recommended
SNR > 25 dB, 20 MPa < P < 50 MPa	0.8–1.0	Optimal
SNR > 18 dB, P > 50 MPa	0.6–0.8	Requires Calibration
Any SNR, P > 65 MPa	0.3–0.6	Limited Use

Figure 17. Industrial applicability matrix of the proposed physics-informed long short-term memory framework.

other types. This failure is primarily due to the swamping of the effective signal by the noise spectrum. Specifically, when the SNR fell below 15 dB, the energy content of background noise in the 8–80 Hz primary frequency band surged from 21.7% to 47.9%, disrupting the input conditions of the physical constraints established based on this frequency band. While the model's LSTM module has a certain degree of noise tolerance, when the effective signal power falls below the noise floor, the learned time series features become decoupled from the actual physical processes, leading to a sharp non-linear drop in predictive performance.

In ultra-high temperature environments (>150°C), for example, volcanic reservoirs (185°C) and pre-salt carbonates (158°C), the RMSE (3.45 ms and 2.87 ms, respectively) remained significantly high, even with a suitable SNR of 13.7–20.4 dB. The root cause lies in unmodeled physical effects triggered by extremely high temperatures. When temperatures exceeded 150°C, sensitive minerals such as quartz in the reservoir rock undergo significant thermal expansion, causing abnormal fluctuations in compressional wave velocity of 3.2–5.7%. This effect exceeds the scope of the classical rock physics

Table 12. Prediction accuracy of rock physics parameters

Sample	Porosity (%)	Theoretical lambda_p (GPa)	Predicted lambda_p (GPa)	Error (%)
S1	18.2	12.57	12.83	2.1
S2	15.7	15.32	14.91	2.7
S3	22.3	9.85	10.12	2.7
S4	8.9	21.45	22.18	3.4
S5	26.8	7.21	7.45	3.3
S6	13.5	17.63	16.88	4.3
S7	31.2	5.47	5.91	8.0
S8	11.4	19.76	19.82	0.3

theoretical framework underlying the current physical constraint module. This results in systematic deviations in the output of the physical module, which, through cascading propagation, undermines the input assumptions of the LSTM module, ultimately causing the model to fail in adaptability under ultra-high temperature conditions.

The applicability matrix in Figure 17 shows that this method maintained a detection accuracy of 94.3% in high-pressure, high-temperature reservoirs (pressure >35 MPa, temperature >120°C), but its applicability drops to 68.7%

for carbonate cave reservoirs. This decrease is primarily attributed to the inherent challenges posed by the extreme heterogeneity and complex spatial structure of fractures and cavities in these reservoirs, posing physical constraint modeling challenges.

5.4. Rock physics theory compatibility

The prediction results of PI-LSTM were highly consistent with the theoretical calculation of the Biot-Gassmann equation (R^2 = 0.91), and its fluid replacement module can be expressed as:[26,27]

$$K_{sat} = K_{dry} + \frac{(1 - K_{dry} / K_m)^2}{\phi / K_f + (1-\phi) / K_m - K_{dry} / K_m^2} \quad \text{(XXVII)}$$

Data in Table 12 further verifies that the model's response to rock physics sensitive parameters (λ_p, μ_p) conformed to the Hertz–Mindlin contact theory, where the particle contact stiffness prediction error was <8%.

The error of conventional reservoir sections (porosity 10–25%) was controlled within 3.0% (samples S1–S6), which was significantly better than the industry's 5% accuracy requirement. When the porosity increased to 31.2% (sample S7), the error reached a maximum of 8.0%. This result is consistent with the applicable boundary of the theoretical model under high porosity conditions (<30%), reflecting the natural limitations of the particle contact theory in loose media. Sample S8 showed an astonishing 0.3% error at the low porosity end (11.4%), proving that the model has an extraordinary ability to capture the elastic behavior of tight sandstone.

5.5. Future direction

To improve the applicability of the proposed framework for cave reservoirs, future research could address the following optimizations: First, a discrete fracture-cavity network model could be incorporated into the physical modeling process, combined with multiscale karst characterization techniques to enhance the explicit characterization of the fracture-cavity coupling system. These approaches allow for more accurate representations of fracture and cavity interactions, which are crucial in cave reservoirs. Second, azimuthal anisotropy information from well bypasses and long-offset seismic gathers could be integrated to improve the accuracy and robustness of spatial imaging of large cave systems. This can address the challenges of heterogeneity and enhance spatial resolution. Furthermore, generative adversarial networks could be used to synthesize more representative cave samples, enhancing the generalization performance of deep learning models for irregular geological features. Preliminary numerical experiments indicate that this combined strategy can potentially increase the predictive applicability of these reservoirs to over 80%.

For future research, three directions are focused on: At the theoretical level, it is necessary to develop cross-scale modeling methods to solve the scale fracture problem of the current physical constraint module between millimeter-level pores and kilometer-level working areas. To address this, future work should incorporate multiscale modeling techniques, specifically integrating micro-mechanical models (such as mesoscale or nanoscale simulations) with macroscopic geological models. These models can enable a more seamless representation of the relationships between microscopic pore structures and the macroscopic geological framework. In addition, the use of non-local elastic mechanics operators, which have shown promise in preliminary experiments to improve predictions for ultra-deep layers (>3500 m), can be explored. These operators could potentially reduce prediction errors by up to 18.7%, providing a more accurate representation of the physical properties of deeper geological formations.

At the technical level, the development of a real-time prediction system based on edge computing is imminent. By lightweighting PI-LSTM to <50 MB and deploying it to seismic acquisition nodes, it is expected to achieve a synchronous closed loop of "acquisition-interpretation" of time-shift differences, such as the B-19 well area case shown in Figure 11. This real-time capability can advance the water drive front warning time by 4–6 months. The next steps can involve optimizing edge computing infrastructure and refining model performance for real-time deployment in offshore oilfields.

In the longer term, building a digital twin platform that integrates multimodal data, such as seismic, logging, and core data, could become a trend. This platform would allow for the continuous monitoring of oilfield dynamics at centimeter-level spatiotemporal resolution. By 2025, we aim to develop this digital twin technology, leveraging the interpretability framework presented in this study as a foundation for multisource data fusion. This will provide a more accurate and real-time digital representation of oil and gas reservoirs, helping to transition time-lapse seismic technology from a simple "interpretation tool" into a comprehensive "intelligent decision-making system" for oil and gas management. These advancements will support the goal of achieving transparent, real-time management of the entire lifecycle of oil and gas reservoirs, providing significant benefits for both exploration and production activities.

6. Conclusion

This study established a new generation of an intelligent analysis framework for time-lapse seismic difference

prediction through the deep coupling of PI-LSTM and interpretability enhancement. Its core breakthroughs are reflected in three aspects: First, the first-order velocity–stress wave equation is innovatively transformed into the physical memory unit of LSTM, and the dynamic fusion of wave field propagation law and data characteristics is realized through the gating mechanism. In the testing on actual data from the North Sea oilfield, the physical residual is reduced from 62.3kPa of the conventional LSTM method to 15.2kPa, a decrease of 75.6%. Second, the proposed interpretability enhancement module reduces the quarterly fluctuation of feature importance by 38% (ΔS) through the coordinated optimization of SHAP value dynamic weighting and physical attention template, addressing the "black box dilemma" of deep learning models in seismic interpretation. Third, and more importantly, an adaptive mapping mechanism of geological parameters and network weights is constructed. When the porosity is >15%, the physical constraint weight is automatically increased to 0.89 ± 0.04. In the dual benchmark test consisting of SEG simulation data and actual North Sea oilfield data, the time-shift difference prediction accuracy reaches 0.71–2.1 ms (corresponding to the oil and gas interface positioning error of <3 m), which is 62.9% higher than that of the existing commercial software. These innovations not only provide a new paradigm for time-lapse seismic interpretation but also have universal guiding values for geophysical fields, such as well logging interpretation and microseismic monitoring.

For industrial application scenarios, this study extracts a three-level implementation path. For conventional sandstone reservoirs (porosity of 15–25%, SNR of >18 dB), the standard PI-LSTM model can be directly used, and its pre-trained parameters have achieved 92.5% fluid front recognition accuracy in Block B12. For complex reservoirs (such as fractured carbonate rocks or ultra-high temperature reservoirs), it is recommended to use a flexible constraint mode with a β of 0.55 ± 0.05, combined with wavelet denoising preprocessing, as shown in Figure 16. This configuration reduces the prediction error of volcanic reservoirs from 3.45 ms to 2.12 ms. For the real-time monitoring needs in offshore oilfield development in particular, it is recommended to adopt the updated strategy of "monthly incremental learning + quarterly full parameter fine-tuning," and use the quarterly stability characteristics (CV <12%), as shown in Table 7, to maintain long-term prediction reliability. Field applications indicate that this solution can shorten the 4D seismic interpretation cycle from the traditional 3–6 months to within 2 weeks, while controlling the reserve assessment error within ± 1.8% (Table 8), providing unprecedented timeliness and accuracy for oilfield development decisions.

The direction of future research should involve incorporating more detailed and specific models, refining computational techniques, and integrating cutting-edge technologies such as edge computing and digital twin platforms. These steps can enhance the practical applicability and scientific rigor of the PI-LSTM framework, driving further innovations in seismic interpretation and oilfield management.

Acknowledgments

None.

Funding

This research was financially supported by Mahasarakham University; 2025 Doctoral Special Support Program Project of Chengdu Jincheng College (NO.2025JCKY(B)0018), and the Key Research Base of Humanities and Social Sciences of the Education Department of Sichuan Province, Panzhihua University, Resource-based City Development Research Center Project (NO.ZYZX-YB-2404).

Conflict of interest

The authors declare they have no competing interests.

Author contributions

Conceptualization: Tianwen Zhao, Guoqing Chen, Cong Pang, Palakorn Seenoi,

Formal analysis: Tianwen Zhao, Cong Pang, Guoqing Chen, Palakorn Seenoi, Nipada Papukdee

Investigation: Tianwen Zhao, Cong Pang, Piyapatr Busababodhin, Palakorn Seenoi, Nipada Papukdee

Methodology: Tianwen Zhao, Guoqing Chen, Piyapatr Busababodhin, Palakorn Seenoi, Nipada Papukdee

Visualization: Tianwen Zhao, Guoqing Chen, Piyapatr Busababodhin

Writing–original draft: Tianwen Zhao, Guoqing Chen, Piyapatr Busababodhin, Nipada Papukdee

Writing–review & editing: Tianwen Zhao, Guoqing Chen, Cong Pang, Piyapatr Busababodhin, Palakorn Seenoi

Availability of data

Some data used in this study cannot be shared publicly due to collaborative agreement restrictions, but are available from the corresponding author upon reasonable request.

References

1. Wu YH, Pan SL, Lan HQ, *et al*. Dynamic reservoir monitoring using similarity analysis of passive source time-lapse seismic images: Application to waterflooding front monitoring in Shengli Oilfield, China. *Petrol Sci*. 2025;22(3):1062-1079.

   doi: 10.1016/j.petsci.2024.12.008

2. Ding PB, Gong F, Zhang F, Li XY. A physical model study of shale seismic responses and anisotropic inversion. *Petrol Sci*.

2021;18(4):1059-1068.

doi: 10.1016/j.petsci.2021.01.001

3. Liu P, Zhao J, Li Z, Wang H. Numerical simulation of multiphase multi-physics flow in underground reservoirs: Frontiers and challenges. *Capillarity*. 2024;12(3):72-79.

doi: 10.46690/capi.2024.03.02

4. Wu Y, Sicard B, Gadsden SA. Physics-informed machine learning: A comprehensive review on applications in anomaly detection and condition monitoring. *Expert Syst Appl*. 2024;255:124678.

doi: 10.1016/j.eswa.2024.124678

5. Lim B, Zohren S. Time-series forecasting with deep learning: A survey. *Philos Trans R Soc A Math Phys Eng Sci*. 2021;379(2194):20200209.

doi: 10.1098/rsta.2020.0209

6. Cao C, Debnath R, Alvarez RM. Physics-based machine learning for predicting Urban air pollution using decadal time series data. *Environ Res Commun*. 2025;7(5):051009.

doi: 10.1088/2515-7620/add795

7. Kim S, Lee D, Lee S. Performance improvement of seismic response prediction using the LSTM-PINN hybrid method. *Biomimetics (Basel)*. 2025;10(8):490.

doi: 10.3390/biomimetics10080490

8. Pwavodi J, Ibrahim AU, Pwavodi PC, Al-Turjman F, Mohand-Said A. The role of artificial intelligence and IoT in prediction of earthquakes. *Artif Intell Geosci*. 2024;5:100075.

doi: 10.1016/j.aiig.2024.100075

9. Xu Q, Shi Y, Bamber J, *et al*. *Physics-Aware Machine Learning Revolutionizes Scientific Paradigm for Machine Learning and Process-Based Hydrology*. [arXiv Preprint]; 2023.

doi: 10.48550/arXiv.2310.05227

10. Jain P, Coogan SC, Subramanian SG, *et al*. A review of machine learning applications in wildfire science and management. *Environ Rev*. 2020;28(4):478-505.

doi: 10.1139/er-2020-0019

11. Marano GC, Rosso MM, Aloisio A, Cirrincione G. Generative adversarial networks review in earthquake-related engineering fields. *Bull Earthquake Eng*. 2024;22(7):3511-3562.

doi: 10.1007/s10518-023-01645-7

12. Kloosterman HJ, Kelly RS, Stammeijer J, *et al*. Successful application of time-lapse seismic data in shell expro's gannet fields, Central North Sea, UKCS. *Petrol Geosci*. 2003;9(1):25-34.

doi: 10.1144/1354-079302-513

13. Haverl MC, Aga M, Reiso E. Integrated Workflow for Quantitative use of Time-Lapse Seismic Data in History Matching: A North Sea field Case. In: *Paper Presented At: SPE Europec Featured at EAGE Conference and Exhibition*; 2005. Madrid, Spain. SPE-94453.

doi: 10.2118/94453-MS

14. Dong Y, Shen Y, Guo K, *et al*. Advanced workflow for time-lapse seismic monitoring of CO_2 storage in saline aquifers with its application in a field basin. *Sci Rep*. 2025;15(1):21345.

doi: 10.1038/s41598-025-09476-z

15. Koster K, Gabriels P, Hartung M, Verbeek J, Deinum G, Staples R. Time-lapse seismic surveys in the North Sea and their business impact. *Lead Edge*. 2000;19(3):286-293.

doi: 10.1190/1.1438594

16. Alizadegan H, Rashidi Malki B, Radmehr A, Karimi H, Ilani MA. Comparative study of long short-term memory (LSTM), bidirectional LSTM, and traditional machine learning approaches for energy consumption prediction. *Energy Explor Exploit*. 2025;43(1):281-301.

doi: 10.1177/01445987241260319

17. Botunac I, Bosna J, Matetić M. Optimization of traditional stock market strategies using the LSTM hybrid approach. *Information*. 2024;15(3):136.

doi: 10.3390/info15030136

18. Kiran Kumar V, Ramesh KV, Rakesh V. Optimizing LSTM and Bi-LSTM models for crop yield prediction and comparison of their performance with traditional machine learning techniques. *Appl Intell*. 2023;53(23):28291-28309.

doi: 10.1007/s10489-023-05005-5

19. Zhao C, Zhang F, Lou W, Wang X, Yang J. A comprehensive review of advances in physics-informed neural networks and their applications in complex fluid dynamics. *Phys Fluids*. 2024;36(10):101101.

doi: 10.1063/5.0226562

20. Qi S, Sarris CD. Physics-informed deep operator network for 3-d time-domain electromagnetic modeling. *IEEE Trans Microw Theory Tech*. 2024;72(12):5204-5216.

doi: 10.1109/TMTT.2024.3521389

21. Liu B, Pang Y, Jiang P, *et al*. Physics-driven deep learning inversion for direct current resistivity survey data. *IEEE Trans Geosci Remote Sens*. 2023;61:1-11.

doi: 10.1109/TGRS.2023.3263842

22. Moser P, Fenz W, Thumfart S, Ganitzer I, Giretzlehner M. Modeling of 3D blood flows with physics-informed neural networks: Comparison of network architectures. *Fluids*. 2023;8(2):46.

doi: 10.3390/fluids8020046

23. Fawad M, Mondol NH. Monitoring geological storage of CO_2 using a new rock physics model. *Sci Rep*. 2022;12(1):297.

doi: 10.1038/s41598-021-04400-7

24. Jo TH, Djezzar S, Barajas-Olalde C, Richards T. Utilizing 3D

mechanical earth models for calibration and validation in a large-scale carbon capture and storage project in North Dakota. *In: Proceedings of the 17*th Greenhouse Gas Control Technologies Conference (GHGT-17). Calgary, Canada; 2024.

doi: 10.2139/ssrn.5027942

25. El Bilali A, Brouziyne Y, Attar O, Lamane H, Hadri A, Taleb A. Physics-informed machine learning algorithms for forecasting sediment yield: An analysis of physical consistency, sensitivity, and interpretability. *Environ Sci Pollut Res Int*. 2024;31(34):47237-47257.

doi: 10.1007/s11356-024-34245-2

26. Saxena N. Exact results for generalized Biot-Gassmann equations for rocks that change in pore shape and grain geometry. *Geophys J Int*. 2015;203(3):1575-1586.

doi: 10.1093/gji/ggv386

27. Bemer E, Hamon Y, Adelinet M. Consistent experimental investigation of the applicability of Biot-Gassmann's equation in carbonates. *Geophysics*. 2019;84(4):WA97-WA113.

doi: 10.1190/geo2018-0631.1

ACCSCIENCE PUBLISHING

Journal of Seismic Exploration

ARTICLE

Efficient wave-equation-based Kirchhoff-style migration using interpolated excitation information

Sumin Kim[1], Jiho Ha[2], and Wookeen Chung[1]*

[1]Department of Energy and Resources Engineering, National Korea Maritime and Ocean University, Busan, South Korea

[2]Pohang Branch, Korea Institute of Geoscience and Mineral Resources (KIGAM), Pohang, South Korea

Abstract

Reverse time migration is widely recognized as one of the most advanced seismic depth migration techniques because of its ability to generate a high-quality seismic image even for complex structures. However, its practical implementation for large-scale applications can be hindered by tremendous computational overhead and memory demands associated with handling wavefields. To address these challenges, we propose a wave equation-based, Kirchhoff-style migration method incorporating the excitation amplitude imaging condition. In our migration scheme, both the forward and backward wavefields are represented using excitation information obtained by interpolating a limited set of excitation information. This representation allows us to avoid not only storing the forward wavefield but also performing backward wavefield simulation. Numerical experiments with both synthetic and field data demonstrate that the proposed migration approach can deliver high-quality migration images with significantly improved computational efficiency.

Keywords: Seismic migration; Computational efficiency; Seismic imaging

***Corresponding author:**
Wookeen Chung
(wkchung@kmou.ac.kr)

Citation: Kim S, Ha J, Chung W. Efficient wave-equation-based Kirchhoff-style migration using interpolated excitation information. *J Seismic Explor*. 2025;34(3):49-60. doi: 10.36922/JSE025320055

Received: August 9, 2025

Revised: September 4, 2025

Accepted: September 11, 2025

Published online: October 8, 2025

1. Introduction

Seismic depth migration has become an essential technique for revealing complex geological structures in the subsurface. With breakthroughs in computing technology, various seismic depth migration techniques have been intensively developed in recent decades, including Kirchhoff migration approaches,[1-3] Gaussian beam migration approaches,[4,5] and one-way wave equation migration approaches.[6-8] Among these seismic depth migration techniques, reverse-time migration (RTM), based on a two-way wavefield simulation engine, is regarded as the most accurate technique in seismic imaging, since it can handle steeply dipping structures as well as various wave types such as reflections and diffractions.[9-11] Thus, RTM can provide high-quality seismic images in complicated media.

Despite the excellent performance of RTM, its practical implementation has inherent limitations due to its high computational cost. The primary contributor to this cost is the large amount of memory required for saving the forward wavefield.

Generally, the basic procedure of RTM consists of the following procedures: the forward wavefield simulation with source function, backward wavefield simulation with the recorded seismograms, and construction of the migration image based on the imaging condition. During the application of the imaging condition, huge memory resources may be required. To generate the seismic image from RTM, the temporal history of the forward wavefield at every imaging time step should be accessible. Since the dimension of the entire forward wavefield is determined by the model dimensions and imaging time steps in wavefield simulation, huge memory resources are needed to save the forward wavefield. Of course, for small-scale applications, memory devices or disk input/output (I/O) may be sufficient to store the forward wavefield. However, for large-scale applications, alternative strategies for handling forward wavefield during the imaging condition procedure are required to alleviate the computational costs.

To address this computational burden associated with storing the forward wavefield in RTM, many wavefield reconstruction-based approaches have been investigated. One widely adopted method is forward wavefield reconstruction.[12-14] In this approach, the forward wavefield is stored only on the model boundaries during forward simulation and then reconstructed during backward simulation. This strategy is memory-efficient because only a few grid points are required to store the forward wavefield; however, it necessitates additional wavefield simulations.

To further reduce the memory requirements for storing the forward wavefield, Nguyen and McMechan[15] proposed the excitation amplitude (ExA) imaging condition. In the ExA imaging condition for RTM, the maximum amplitude of the forward wavefield and its associated travel time are referred to as the ExA and the excitation time (ExT), respectively. RTM with the ExA imaging condition can generate the migration image efficiently, as the ExA and ExT are represented by a single value for each grid point in the model. Owing to this memory-efficient advantage, ExA imaging condition has been applied not only in acoustic RTM[15-17] but also in elastic RTM.[18,19] Furthermore, Kalita and Alkhalifah[20] modified the ExA imaging condition by incorporating source information, in which the source wavelet is used to represent the forward wavefield. This modified ExA imaging condition has been employed in a wide range of inversion-based seismic imaging techniques, including full waveform inversion,[21,22] and least-squares RTM.[23,24]

Following Kalita and Alkhalifah,[20] we develop a wave-equation-based Kirchhoff-style migration based on excitation representation, in which the backward as well as the forward wavefield are represented using excitation information. Thus, no backward wavefield simulation is needed in our migration scheme if excitation information at the receiver position is available. To enhance computational efficiency, we perform a limited number of forward wavefield simulations and use interpolation to generate the excitation information, rather than performing forward wavefield simulations for each receiver position. This interpolated excitation information enables migration to be implemented without backward wavefield simulation.

In this paper, we first introduce the conventional RTM, followed by wavefield representation using excitation information. We then develop a wave-equation-based, Kirchhoff-style migration method using excitation representation and derive a modified imaging condition for practical implementation. Finally, we present both a synthetic example and a field application to demonstrate the efficiency and practicability of the proposed migration approach.

2. Methodology

2.1. Review of RTM

Prestack RTM comprises three procedures: (i) forward wavefield simulation using the source function, (ii) backward wavefield simulation using the recorded seismograms, and (iii) application of an imaging condition. Assuming a 2D isotropic acoustic environment, both the forward and backward wavefield simulations for prestack RTM can be computed from the following two equations:

$$\left(\frac{1}{c^2}\frac{\partial^2}{\partial t^2}-\nabla^2\right)S\left(t,\mathrm{x};\mathrm{x}_s\right)=f\left(t;\mathrm{x}_s\right),\# \tag{I}$$

And

$$\left(\frac{1}{c^2}\frac{\partial^2}{\partial t^2}-\nabla^2\right)R\left(t,\mathrm{x};\mathrm{x}_s\right)=d\left(T-t,\mathrm{x}_r;\mathrm{x}_s\right),\# \tag{II}$$

Where c is migration velocity, ∇^2 denotes Laplacian operator, x is imaging point, x_s is shot position, t is time, T is maximum time, S(t, x; x_s) and R(t, x; x_s) are forward and backward wavefields, respectively. f(t; x_s) is the source function injecting at the source position x_s, and d(t, x_r; x_s) is recorded seismogram at receiver position x_r. Following the forward wavefield simulation, the migration image is computed by applying the imaging condition with the forward and backward wavefields. In this study, a zero-lag cross-correlation imaging condition is used and defined as follows:

$$I\left(\mathrm{x};\mathrm{x}_s\right)=\int_0^T S\left(t,\mathrm{x};\mathrm{x}_s\right)R\left(T-t,\mathrm{x};\mathrm{x}_s\right)dt,\# \tag{III}$$

Where $I(x; x_s)$ represents migration image at x. **Equation III** implies that both the forward and backward wavefields must be available simultaneously at each imaging time step. A straightforward way to make the forward wavefield available during the application of the imaging condition is to store it in memory or write it to disk and read it back during the backward wavefield simulation. However, this approach incurs tremendous memory and I/O time costs. This limitation poses a major obstacle to the practical implementation of RTM for large-scale applications, particularly in 3D seismic imaging.

2.2. Representation of forward and backward wavefield using excitation information

According to the theory of ExA imaging condition in RTM,[15] the most energetic amplitude and its arrival time at each grid point in model space are defined as ExA and excitation time (ExT), respectively. This relationship can be expressed as follows:

$$t_e(\mathrm{x};\mathrm{x}_s) = \underset{t}{\operatorname{argmin}}\left(\left|S(t,\mathrm{x};\mathrm{x}_s)\right|\right),\# \tag{IV}$$

And

$$S_e(t,\mathrm{x};\mathrm{x}_s) = S(t,\mathrm{x};\mathrm{x}_s)\delta\left(t - t_e(\mathrm{x};\mathrm{x}_s)\right),= \begin{cases} S(t,\mathrm{x};\mathrm{x}_s), & for \quad t = t_e \\ 0, & otherwise \end{cases} \# \tag{V}$$

Where t_e is the ExT at grid point x, δ is Dirac delta function, and $S_e(t, x; x_s)$ is the ExA of the forward wavefield $S(t, x; x_s)$. The ExA can efficiently generate a migration image because it stores only one snapshot to represent the forward wavefield. With ExA and ExT, the reconstructed forward wavefield $\hat{S}_e(t,\mathrm{x};\mathrm{x}_s)$ can be represented by convolving the source wavelet as follows:

$$\hat{S}_e(t,\mathrm{x};\mathrm{x}_s) = G(t,\mathrm{x};\mathrm{x}_s)\delta\left(t - t_e(\mathrm{x};\mathrm{x}_s)\right) * f(t),\# \tag{VI}$$

Where $G(t, x; x_s)$ is Green's function propagating in the migration velocity c, and * represents the temporal convolution operator. For simplicity, **Equation VI** can be expressed in compact matrix form as follows:

$$\hat{\mathrm{S}}_e = \mathrm{W}\mathrm{u}_\delta,\# \tag{VII}$$

Where $\hat{\mathrm{S}}_e \in \mathbb{R}^{N\times 1}$ stands for represented forward wavefield using excitation information, and N is the number of time samples. Causal convolution matrix $W \in R^{N\times N}$ is constructed by source wavelet $f(t)$ with lower triangular Toeplitz structure as follows:

$$\mathrm{W} = \begin{bmatrix} f_1 & 0 & \cdots & 0 & 0 \\ f_2 & f_1 & \cdots & 0 & 0 \\ \vdots & \vdots & \ddots & \vdots & 0 \\ f_{N-1} & f_{N-2} & \cdots & f_1 & 0 \\ f_N & f_{N-1} & \cdots & f_2 & f_1 \end{bmatrix},\# \tag{VIII}$$

And $u\_\delta \in R^{N\times 1}$ is a vector with a single non-zero element $G(t_e(x; x_s))$ at N_{t_e} indicating integer time step of $t_e(x; x_s)$.

In the same manner, the backward wavefield can also be reconstructed using a recorded seismogram with excitation information if excitation information is available at the receiver position x_r is available. The reconstructed backward wavefield can be expressed as follows:

$$\hat{R}_e(t,\mathrm{x};\mathrm{x}_s) = G(t,\mathrm{x};\mathrm{x}_r)\delta\left(t - t_e(\mathrm{x};\mathrm{x}_r)\right) * d(T - t;\mathrm{x}_r),\# \tag{IX}$$

Where $\hat{R}_e(t,\mathrm{x};\mathrm{x}_s)$ is the reconstructed backward wave field. This Equation IX can be also written as compact matrix form for simplicity as follows:

$$\hat{\mathrm{R}}_e = \mathrm{V}_\delta \mathrm{R}\mathrm{d},\# \tag{X}$$

Where $\hat{\mathrm{R}}_e \in \mathbb{R}^{N\times N}$ stands for represented backward wavefield using excitation information. $V^\delta \in R^{N\times N}$ is causal convolution matrix with $G(t, x; x_r)\delta(t\text{-}t_e(x; x_r))$. Time reverse matrix $R \in R^{N\times N}$ and trace vector of the recorded seismogram $d \in R^{N\times 1}$ can be expressed as follows:

$$\mathrm{R} = \begin{bmatrix} 0 & 0 & \cdots & 0 & 1 \\ 0 & 0 & \cdots & 1 & 0 \\ \vdots & \vdots & \ddots & \vdots & 0 \\ 0 & 1 & \cdots & 0 & 0 \\ 1 & 0 & \cdots & 0 & 0 \end{bmatrix},\# \tag{XI}$$

And

$$\mathrm{d} = [\mathrm{d}_1, \mathrm{d}_2, \cdots, \mathrm{d}_{N-1}, \mathrm{d}_N]^T,\# \tag{XII}$$

Where superscript T represents the transpose operation.

2.3. Wave-equation-based Kirchhoff-style migration using interpolated excitation information (WEKM-IEI)

We propose a new imaging condition based on the backward as well as the forward wavefield representations using excitation information. By substituting **Equations VI** and **IX** into **Equation III**, the new imaging condition can be expressed as follows:

$$I_e(\mathrm{x};\mathrm{x}_s)=\int_0^T \hat{S}_e(t,\mathrm{x};\mathrm{x}_s)\hat{R}_e(T-t,\mathrm{x};\mathrm{x}_s)dt.\# \quad \text{(XIII)}$$

Based on this imaging condition, the migration image can be computed by using excitation representations of the forward and backward wavefields. In other words, backward wavefield simulation is unnecessary for the migration procedure if excitation information at receiver position x_r is available. However, in the practical implementation of WEKM-IEI, **Equation XIII** should be modified to take advantage of the ExA imaging condition. To modify **Equation XIII**, in the same manner as Kalita and Alkhalifah,[20] we can express our imaging condition in matrix form using **Equations VII** and **X** as follows:

$$I\_e\ (x)=\langle Wu\_\delta, RV\_\delta\ Rd\rangle,\# \quad \text{(XIV)}$$

Where $\langle,\rangle$ represents the dot product operation. With the aid of properties of the dot product and some algebra, we can derive the final equation for our imaging condition as:

$$I_e(\mathrm{x})=\mathrm{u}_{\cdot},\mathrm{V}_{\cdot}^T\mathrm{W}^T\mathrm{d}.\# \quad \text{(XV)}$$

The detailed derivation of above **Equation XV** is presented in the Appendix. For simplicity, **Equation XV** can be expressed as follows:

$$I_e(\mathrm{x})=\mathrm{u}_\delta,\mathrm{V}_\delta^T\hat{\mathrm{d}},\# \quad \text{(XVI)}$$

Where $\hat{\mathrm{d}}=\mathrm{W}^T\mathrm{d}$ represents the recorded seismogram cross-correlated with the source wavelet $f(t)$. This equation suggests that explicit cross-correlation between the excitation representation of the Green's function at receiver position x_r and $\hat{\mathrm{d}}$ may be required for constructing the migration image. However, since the temporal cross-correlation matrix V_δ^T consists of the time-shifted Dirac delta function with scaled amplitude $G(t_e\ (\mathrm{x};\mathrm{x}_s))$, it also acts as the time shifter. Furthermore, u^δ has only a single non-zero element scaled by $G(t_e\ (\mathrm{x};\mathrm{x}_s))$. Thus, the dot product operation of **Equation XVI** takes only a few floating-point operations per second. Therefore, the calculation of the migration image for our approach is expressed as:

$$I_e(\mathrm{x})=G\left(t_e(\mathrm{x};\mathrm{x}_s)\right)G\left(t_e(\mathrm{x};\mathrm{x}_r)\right)\hat{d}\left(t_e(\mathrm{x};\mathrm{x}_s)+t_e(\mathrm{x};\mathrm{x}_r)\right).\# \quad \text{(XVII)}$$

To further improve the computational efficiency of our approach, we interpolate the excitation information from just a part of the excitation information. For representation of the backward wavefield at each receiver position x_r, the excitation information at each receiver position x_r should be available. Intuitively, it can be generated from the wavefield simulation. However, massive computations are inevitable because hundreds of receivers are usually exploited by shots in the seismic survey. Hence, rather than generating excitation information at each receiver position, we construct the excitation information by applying an interpolation method to a part of it. From this interpolated excitation information, the forward and backward wavefields can be represented. Consequently, the WEKM-IEI can construct a migration image efficiently. The algorithm in the Appendix shows the implementation of our migration approach in detail. Based on the ExA imaging condition, the WEKM-IEI also has a memory advantage for saving the forward wavefield. In addition, as mentioned before, there is no need to perform the backward wavefield simulation in the WEKM-IEI. Consequently, the WEKM-IEI can provide a high-quality migration image with less computational cost as well as memory requirements.

3. Numerical examples

In this section, we first verify the reconstruction of the forward and backward wavefield using excitation information, followed by the feasibility of our migration approach by comparing the conventional RTM on a modified Marmousi2 velocity model. After that, we apply the WEKM-IEI to a field seismic dataset. In these numerical examples, we exploit the finite difference scheme with O(2, 12) accuracy in the temporal and spatial domains with CPML boundary condition[25] at four edges to attenuate nonphysical reflections from the model boundaries, including the free surface. All numerical examples are performed using 25 CPUs (Intel Xeon Gold 5218R CPU with 2.10 GHz).

3.1. Synthetic test

To verify the accuracy of the forward and backward wavefields reconstructed by excitation information, we use the modified Marmousi2 velocity model shown in Figure 1A. This velocity model is discretized by 401 × 176 grids, with 10-m horizontal and vertical grid intervals, respectively. To generate the migration velocity model, a 2D Gaussian filter with a 600 m × 600 m window is applied to the true velocity model. The migration velocity model is shown in Figure 1B. In these wavefield reconstruction tests, the single shot is located at 2 km in the horizontal direction. 15 Hz Ricker wavelet is used as the source wavelet.

As the first wavefield reconstruction test, Figure 2A and B shows snapshots of the true and reconstructed forward wavefields from excitation information, respectively. We can find that the reconstructed forward wavefield is almost identical to the true one, except for the reflected wavefield.

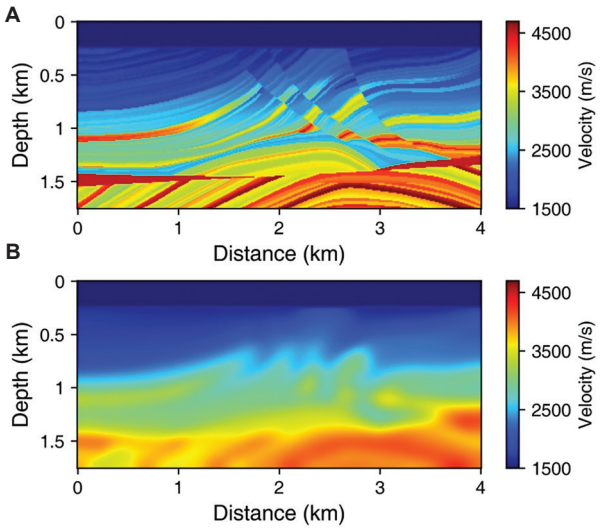

Figure 1. True modified Marmousi2 velocity model (A) and migration velocity model (B)

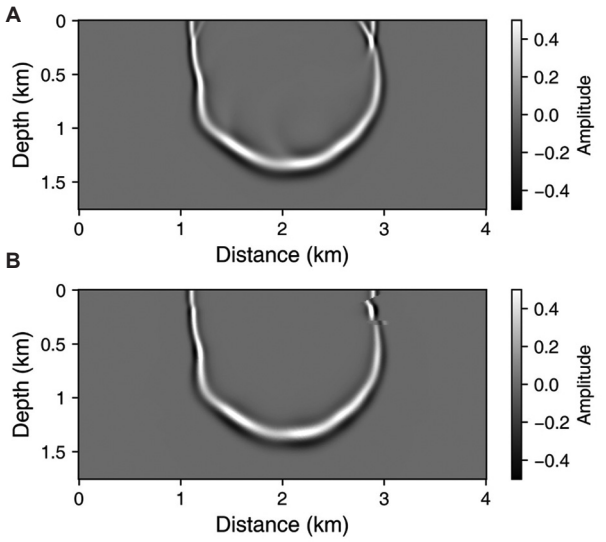

Figure 2. Forward wavefields in the migration velocity model (Figure 1B) obtained by full wavefield modeling (A) and excitation representation (B)

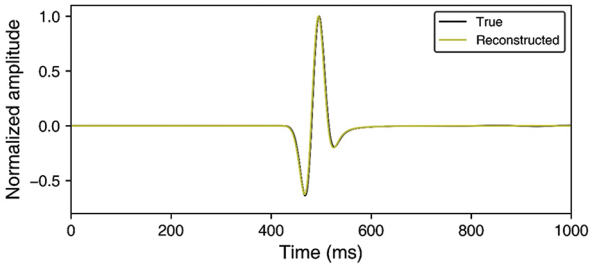

Figure 3. Traces of forward wavefields in the migration velocity model (Figure 2A and B) extracted at (x,z) = (2, 0.5) km

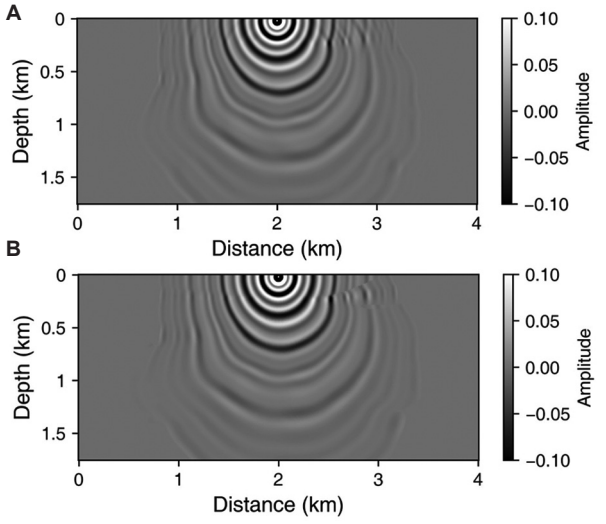

Figure 4. Backward wavefields in the migration velocity model (Figure 1B) obtained by full wavefield modeling (A) and excitation representation (B)

To compare these snapshots in detail, traces of the true and reconstructed forward wavefields are extracted at 2, 0.5 km in distance and depth directions, respectively (Figure 3). Note that the main wave in the forward wavefield is accurately reconstructed from excitation information. Although the forward wavefield reconstructed by excitation information contains only the transmitted wave due to the inherent limitation of the ExA method, wavefield representation using excitation information can provide a reliable forward wavefield.

For another wavefield reconstruction test for the backward wavefield, a seismogram is obtained from a receiver located at the same position of the shot. Direct wave is removed in the recorded seismogram for the backward wavefield reconstruction test. Figure 4A and B illustrate the snapshots of the true and reconstructed backward wavefields from excitation information, respectively. The reconstructed backward wavefield is also identical to the true one. For a more detailed comparison between the true and reconstructed backward wavefields, the traces from those wavefields are extracted at 2, 0.6 km in distance and depth directions, respectively (Figure 5). The trace of the reconstructed backward wavefield represents the true backward wavefield accurately. From these wavefield reconstruction tests, excitation information can be exploited to represent the backward and the forward wave fields with high accuracy.

We now verify the feasibility of the WEKM-IEI. For the implementation of the WEKM-IEI, the ExA and corresponding ExT maps should be constructed for each source and receiver position. Although this excitation

information can be generated by implementing forward wavefield simulations at each source and receiver position, it leads to tremendous computing costs. As mentioned above, we construct excitation information using the interpolation method to alleviate the computing cost. First, we generate some of the excitation information by implementing forward wavefield simulations. In this synthetic example, 81 shots are deployed evenly from 0 to 4 km with a 0.05 km shot interval. In other words, only 20% of excitation information is generated using the forward wavefield simulation. For constructing the entire excitation information, an L2-norm-based interpolation method with small fraction of excitation information is performed to fill the missing excitation information. The L2-norm-based interpolation used in this paper can be expressed as follows:

$$\min_{m'} \mathrm{m} - \mathrm{Sm}'_2{}^2_2 + \lambda \mathrm{Rm}'_2{}^2_2, \# \qquad \text{(XVIII)}$$

m is the decimated excitation information generated from the forward wavefield simulation, m' is excitation information needed to be reconstructed, S is sampling matrix, λ is the penalty coefficient (determined empirically), and R is the regularization matrix (the second-derivative operator used in this paper). Although the excitation information for our migration approach is three-dimensional, Equation XVIII is expressed in matrix form, i.e., for a two-dimensional dataset. To reconstruct the excitation information, we solve Equation XVIII independently for each depth slice of the decimated excitation volume.

Figures 6 and 7 show the three different ExA and the corresponding ExT to verify the accuracy of interpolated excitation information: (a) true excitation information, (b) some of the excitation information generated by

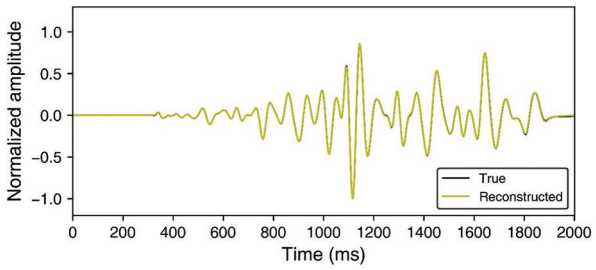

Figure 5. Traces of backward wavefields in the migration velocity model (Figure 4A and B) extracted at (x,z) = (2, 0.6) km

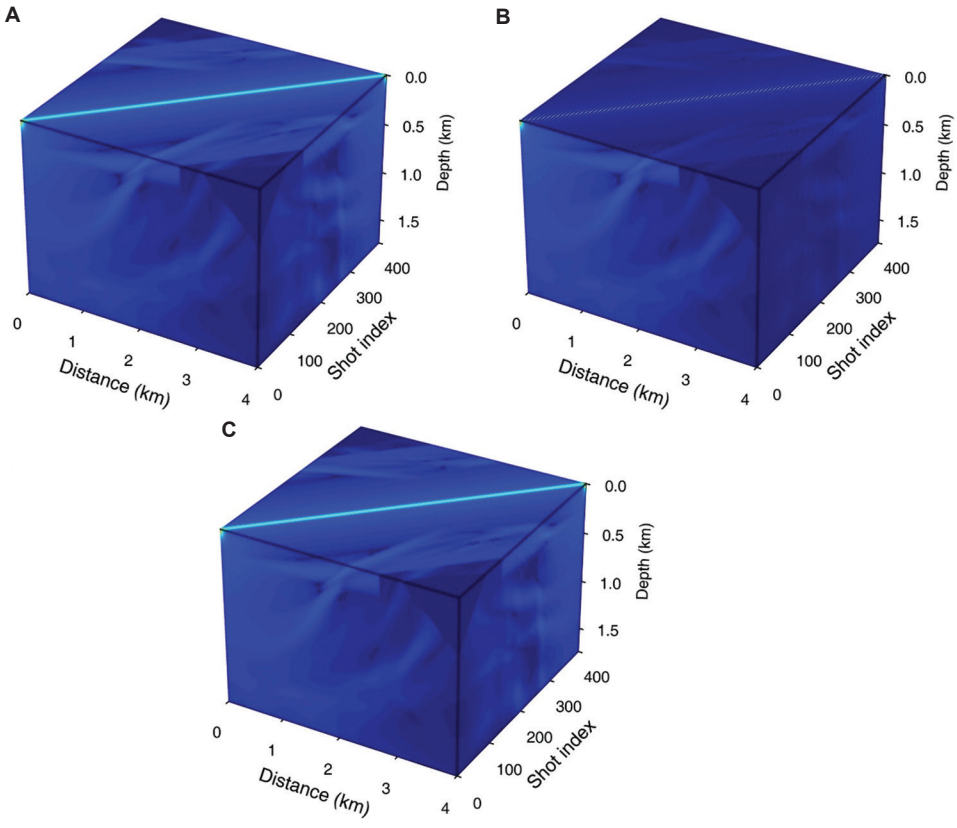

Figure 6. 3D display of the entire excitation amplitude (A), some of the excitation amplitude generated by forward wavefield simulation (B), and the interpolated excitation amplitude (C)

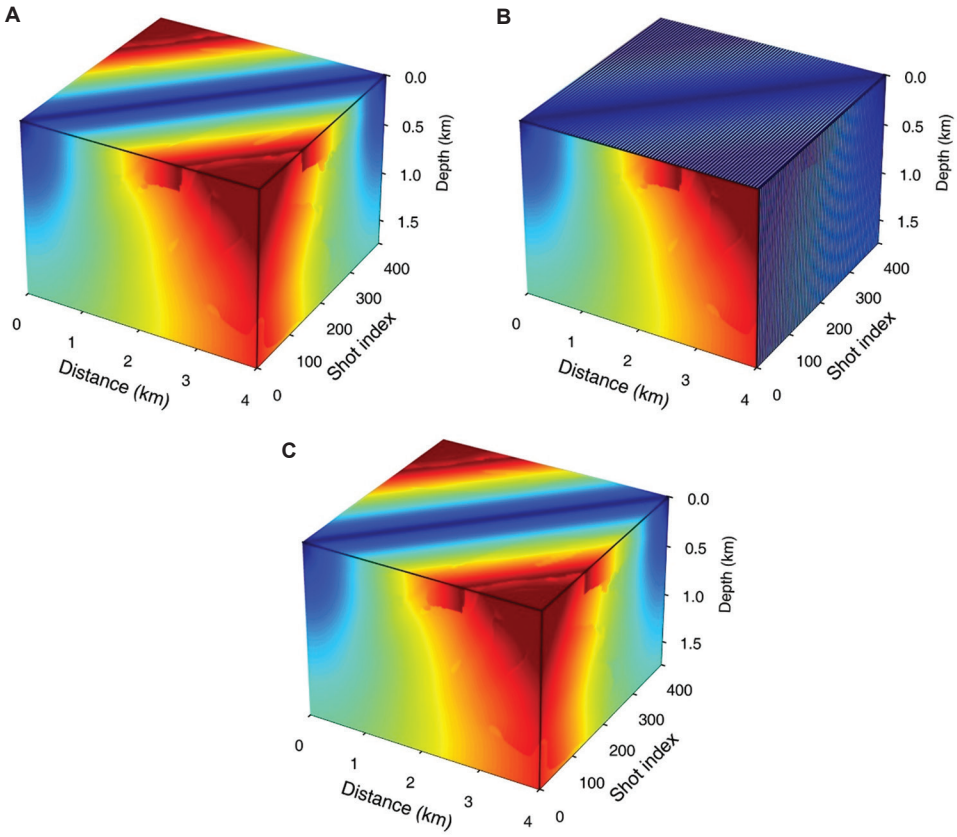

Figure 7. 3D display of (A) the entire excitation time, (B) some of the excitation time generated by forward wavefield simulation, (C) the interpolated excitation time

forward wavefield simulation, and (c) interpolated excitation information, respectively. It is noted that the interpolated excitation information is almost identical to true excitation information, despite using only 20% of the entire excitation information.

Next, we compare the migration images obtained from conventional RTM and the WEKM-IEI. To generate the recorded seismogram, 201 sources are distributed from 0 to 4 km with a horizontal interval of 0.02 km. A total of 401 receivers, evenly spaced from 0 to 4 km with a horizontal interval of 0.01 km, record the seismogram for 2 s at a temporal sampling interval of 1 ms. To avoid the massive memory usage for saving the forward wavefield in conventional RTM, a source wavefield reconstruction method is adopted.[13] A high-pass filter is applied to the migration image as a post-processing procedure. Figure 8A and B present the migration images of conventional RTM and the WEKM-IEI, respectively. It is noted that the WEKM-IEI provides a high-quality migration image similar to that of conventional RTM for a complex structural velocity model, even when using interpolated ExA and the corresponding ExT. For further comparison, depth profiles are extracted at 1 and

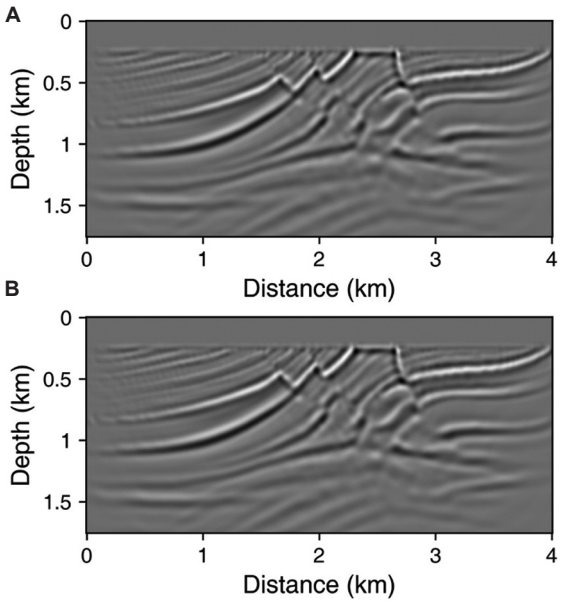

Figure 8. Migration images obtained from conventional RTM (A) and WEKM-IEI (B)
Abbreviations: RTM: Reverse time migration; WEKM-IEI: Wave-equation based Kirchhoff-style migration using interpolated excitation information.

2 km in the distance direction (Figure 9). The reflectors of conventional RTM and the WEKM-IEI are almost identical.

Table 1 displays the memory requirements and computing times of conventional RTM and the WEKM-IEI. In the WEKM-IEI, only 0.16 GB, approximately 12.14% over conventional RTM using the source reconstruction method, is required. It is obvious that the WEKM-IEI requires less memory storage than conventional RTM using the source wavefield reconstruction method, since it requires no saving of the entire time history of the wavefield during migration. The source wavefield reconstruction method in RTM can also reduce the memory requirement, but additional wavefield simulation during backward wavefield simulation should be implemented. Thus, it spends extra computing time. In contrast, the WEKM-IEI can omit the backward wavefield simulation using interpolated excitation information to represent both forward and backward wavefields. This strength leads to high computational efficiency.

4. Field application

We present a field application to investigate the practicability of the WEKM-IEI. In this field application, 2D shallow marine seismic data with 16 channels, acquired by Korea Institute of Geoscience and Mineral Resources (KIGAM), were used. The imaging profile has a distance of 1,000 m and a depth of 60 m. The velocity model ranging from 1,500 to 1,800 m/s was discretized by 1601 × 97 grids in distance and depth direction with the grid intervals of both 0.625 m. 300 shots were evenly distributed with an interval of approximately 3.125 m, and each of them had 16 receivers with a streamer configuration. The recording time length of this field data is 1.5 s. Instead of estimating the source wavelet, we convolved the known wavelet with the field data,[26] which has a Tukey-shaped at 20-100-400-500 Hz. For the implementation of our migration approach, 161 shots, distributed evenly from 0 to 1 km with a shot interval of 6.25 m, were exploded to generate some of the excitation information. Afterward, L2-norm-based interpolation was implemented to fill the missing excitation information.

Figure 10A and B represent the migration images using conventional RTM and the WEKM-IEI, respectively. From these migration results, we can notice that the migration image obtained from the WEKM-IEI exhibits an almost identical migration image using conventional RTM. To compare these migration images in detail, two profiles in depth direction are extracted at 0.3 and 0.8 km in distance direction (Figure 11A and B). The reflectors in both RTM and the WEKM-IEI are nearly identical.

Table 2 shows the computational costs for required memory and computing times of conventional RTM and the

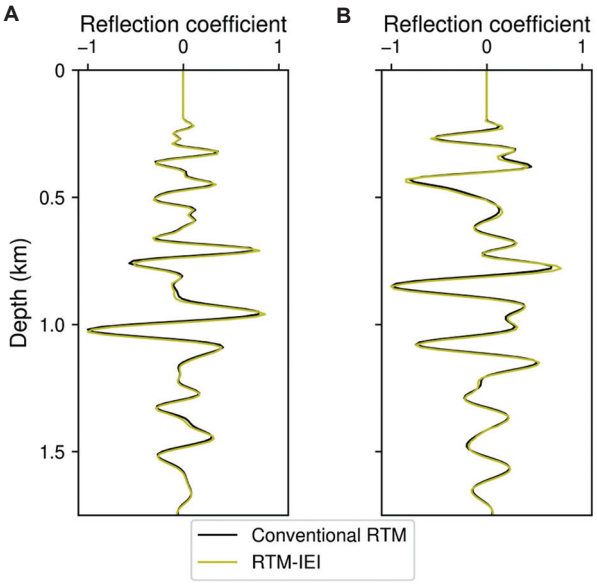

Figure 9. Comparisons between depth profiles of conventional RTM and WEKM-IEI extracted at 1 and 2 km in the distance direction
Abbreviations: RTM: Reverse time migration; WEKM-IEI: Wave-equation based Kirchhoff-style migration using interpolated excitation information.

Table 1. Computational costs of conventional RTM and WEKM-IEI

Method	Required memory (GB)	Computing time (s)
Conventional RTM	1.30	386.15
WEKM-IEI	0.16	80.65

Notes: Computing required memory: 1) conventional RTM = (2 · ((nx·n) + (nz·n)) · (nt - 2) + 2 · (nx·nz)) · ncpu·4 bytes, 2) WEKM-IEI = (nx·nz·nx) · (2+4) bytes (nx, nz: The number of x- and z-direction grids; n: Additional grid determined by special accuracy order in wavefield simulation; nt: Time steps; ncpu: Number of cpus.
Abbreviations: RTM: Reverse time migration; WEKM-IEI: Wave-equation based Kirchhoff-style migration using interpolated excitation information.

Table 2. Computational costs of conventional RTM and WEKM-IEI

Method	Required memory (GB)	Computing time (s)
Conventional RTM	0.59	128.07
WEKM-IEI	0.043	181.02

Notes: Computing required memory: 1) conventional RTM = (2 · ((nx_sub·n) + (nz·n)) · (nt - 2) + 2 · (nx_sub·nz)) · ncpu·4 bytes, 2) WEKM-IEI = (nx_sub·nz·n_coposition) · (2+4) bytes, (nx_sub: The number of x-grid (practical area for wavefield simulation), n_coposition: Number of co-location of source and receivers in model space.
Abbreviations: RTM: Reverse time migration; WEKM-IEI: Wave-equation-based Kirchhoff-style migration using interpolated excitation information.

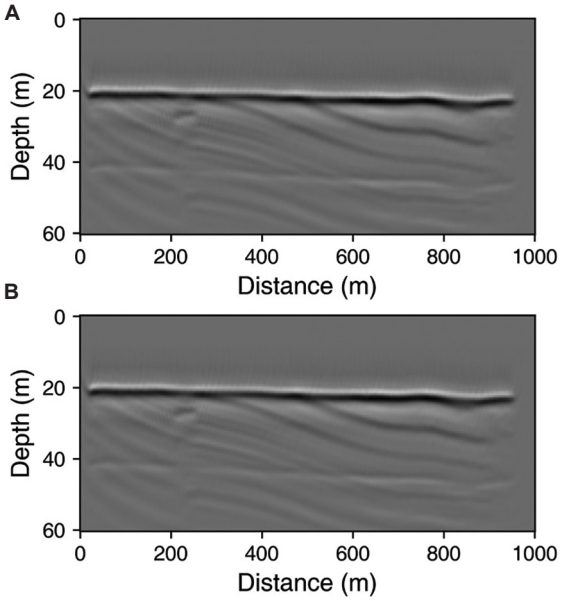

Figure 10. Migration results of field application: (A) conventional RTM and (B) WEKM-IEI
Abbreviations: RTM: Reverse time migration; WEKM-IEI: Wave-equation based Kirchhoff-style migration using interpolated excitation information.

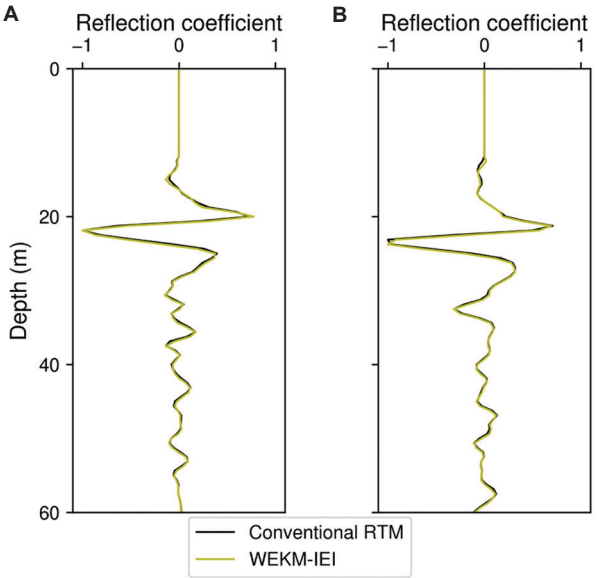

Figure 11. Depth profiles of conventional RTM and WEKM-IEI extracted at 0.3 km (A) and 0.8 km (B) in the distance direction
Abbreviations: RTM: Reverse time migration; WEKM-IEI: Wave-equation based Kirchhoff-style migration using interpolated excitation information.

WEKM-IEI in field application. For the required memory, WEKM-IEI requires only 0.043 GB, approximately 7.19% over conventional RTM using the source reconstruction method. In contrast, the computational time of WEKM-IEI is higher than that of conventional RTM with source-wavefield reconstruction. In our field application, we applied an aperture in the model space for each shot based on the source and receiver positions. Because the field dataset used in this study had few receivers, the aperture-limited model domain was very small, and conventional RTM could therefore be run quickly. However, if a field dataset with many receivers is used, conventional RTM with source-wavefield reconstruction would incur substantial computational cost.

5. Conclusion

Through this work, we propose wave-equation-based Kirchhoff-style migration approach for further improvements of computational efficiency based on the excitation imaging condition. This new migration approach can represent both forward and backward wavefields using excitation information. However, the excitation information at receiver, as well as shot positions, is required. In this work, we implemented a small number of forward wavefield simulations and interpolation to generate excitation information. Using interpolated excitation information yields high-quality migration images while improving efficiency by reducing memory requirements for storing the forward wavefield and cutting computational costs through the omission of backward wavefield simulation. Synthetic data test demonstrates that our migration approach can provide a similar migration image compared to that of conventional RTM, but its computational efficiency is higher than that of conventional RTM. Subsequent field application indicates the practicability of our migration approach.

Acknowledgments

None.

Funding

This research was supported by the Korea Institute of Marine Science and Technology Promotion (KIMST) funded by the Ministry of Oceans and Fisheries, Korea (RS-2023-00259633) and the Basic Research Project "Development of operation management infrastructure for TAMHAE 3 and seamless seismic technology connecting coastal areas (25–3322)" of the Korea Institute of Geoscience and Mineral Resources (KIGAM) funded by the Ministry of Science and ICT of Korea.

Conflict of interest

The authors declare they have no competing interests.

Author contributions

Conceptualization: Sumin Kim, Wookeen Chung
Data curation: Sumin Kim, Jiha Ha
Formal analysis: Sumin Kim
Investigation: Sumin Kim, Wookeen Chung
Methodology: Sumin Kim, Wookeen Chung
Writing–original draft: Sumin Kim, Wookeen Chung
Writing–review & editing: All authors

Availability of data

Data are available from the corresponding author on reasonable request.

References

1. Zhu J, Lines LR. Comparison of Kirchhoff and reverse-time migration methods with applications to prestack depth imaging of complex structures. *Geophysics*. 1998;63(4): 1166-1176.

   doi: 10.1190/1.1444416

2. Gray SH, Etgen J, Dellinger J, Whitmore D. Seismic migration problems and solutions. *Geophysics*. 2001;66(5):1622-1640.

   doi: 10.1190/1.1487107

3. Gray SH, May WP. Kirchhoff migration using eikonal equation traveltimes. *Geophysics*. 1994;59:810-817.

   doi: 10.1190/1.1443639

4. Gray SH, Bleistein N. True-amplitude Gaussian-beam migration. *Geophysics*. 2009;74(2):S11-S23.

   doi: 10.1190/1.3052116

5. Hill NR. Prestack Gaussian-beam depth migration. *Geophysics*. 2001;66(4):1240-1250.

   doi: 10.1190/1.1487071

6. Mulder WA, Plessix RE. A comparison between one-way and two-way wave-equation migration. *Geophysics*. 2004;69(6):1491-1504.

   doi: 10.1190/1.1836822

7. Zhang Y, Zhang G, Bleistein N. Theory of true-amplitude one-way wave equations and true-amplitude common-shot migration. *Geophysics*. 2005;70(4):E1-E10.

   doi: 10.1190/1.1988182

8. Zhang Y, Xu S, Bleistein N, Zhang G. True-amplitude, angle-domain, common-image gathers from one-way wave-equation migrations. *Geophysics*. 2007;72(1):S49-S58.

   doi: 10.1190/1.2399371

9. Baysal E, Kosloff DD, Sherwood JW. Reverse time migration. *Geophysics*. 1983;48(11):1514-1524.

   doi: 10.1190/1.1441434

10. McMechan GA. Migration by extrapolation of time-dependent boundary values. *Geophys Prospect*. 2008;31: 413-420.

    doi: 10.1111/j.1365-2478.1983.tb01060.x

11. Whitmore ND. Iterative depth migration by backward time propagation. In: *SEG Technical Program Expanded Abstracts*. Las Vegas, NV, USA: Society of Exploration Geophysicists; 1983. p. 382-385.

    doi: 10.1190/1.1893867

12. Nguyen BD, McMechan GA. Five ways to avoid storing source wavefield snapshots in 2D elastic prestack reverse time migration. *Geophysics*. 2015;80(1):S1-S18.

    doi: 10.1190/geo2014-0014.1

13. Bo F, Huazhong W. Reverse time migration with source wavefield reconstruction strategy. *J Geophys Eng*. 2012;9(1):69-74.

    doi: 10.1088/1742-2132/9/1/008

14. Liu S, Li X, Wang W, Zhu T. Source wavefield reconstruction using a linear combination of the boundary wavefield in reverse time migration. *Geophysics*. 2015;80(6):S203-S212.

    doi: 10.1190/geo2015-0109.1

15. Nguyen BD, McMechan GA. Excitation amplitude imaging condition for prestack reverse-time migration. *Geophysics*. 2013;78(1):S37-S46.

    doi: 10.1190/geo2012-0079.1

16. Zhang M, Zhou H, Chen H, Jiang S, Jiang C. Reverse-time migration using local Nyquist cross-correlation imaging condition. *IEEE Trans Geosci Remote Sens*. 2022;60:1-14.

    doi: 10.1109/TGRS.2022.3168582

17. Wang J, Li Q, Qiao B, Qi J. Reverse time migration using excitation amplitude imaging condition based on accurate first-arrival traveltimes calculation. *IEEE Trans Geosci Remote Sens*. 2025;63:1-11

    doi: 10.1109/TGRS.2025.3527144

18. Wang W, McMechan GA. Vector-based elastic reverse time migration. *Geophysics*. 2015;80(6):S245-S258.

    doi: 10.1190/geo2014-0620.1

19. Zhou J, Wang D. Vector-based excitation amplitude imaging condition for elastic RTM. *J Appl Geophys*. 2017;147:1-9.

    doi: 10.1016/j.jappgeo.2017.10.003

20. Kalita M, Alkhalifah T. Efficient full waveform inversion using the excitation representation of the source wavefield. *Geophys J Int*. 2017;210(3):1581-1594.

    doi: 10.1093/gji/ggx214

21. Oh JW, Kalita M, Alkhalifah T. 3D elastic full-waveform inversion using P-wave excitation amplitude:

Application to ocean bottom cable field data. *Geophysics*. 2018;83(2):R129-R140.

doi: 10.1190/geo2017-0236.1

22. Lee D, Kang SG, Kim S, Kim YS, Chung W. Efficient direct envelope inversion with excitation amplitude for strong velocity contrast model. *IEEE Trans Geosci Remote Sens*. 2024;62:1-12.

doi: 10.1109/TGRS.2024.3422978

23. Kim S, Kim YS, Chung W. Least-squares reverse time migration using the most energetic source wavefields based on excitation amplitude imaging condition. *Geophys Prospect*. 2023;71(8):1438-1454.

doi: 10.1111/1365-2478.13387

24. Kim S, Kang SG, Choi Y, Chung W. Efficient extended least-squares reverse time migration based on an excitation amplitude imaging condition. *Geophysics*. 2024;89(1): S31-S45.

doi: 10.1190/geo2023-0216.1

25. Komatitsch D, Martin R. An unsplit convolutional perfectly matched layer improved at grazing incidence for the seismic wave equation. *Geophysics*. 2007;72(5):SM155-SM167.

doi: 10.1190/1.2757586

26. Yoon K, Suh S, Cai J, Wang B. Improvements in Time Domain FWI and Its Applications. In: *SEG International Exposition and Annual Meeting*. 2012. p. 1-5.

doi: 10.1190/segam2012-1535.1

Appendix

(A) Derivation of Equation XV

Using the properties of the dot product, **Equation XIV** can be written as follows:

$$I_e(\mathrm{x}) = \mathrm{u}_{\cdot}, \mathrm{W}^T \mathrm{RV}_{\cdot} \mathrm{Rd}.\# \quad \text{(A.I)}$$

Operator W^TR in the right operand in the dot product (**Equation A. I**) acts as a cross-correlation of the source wavelet with flipped input signal. It is also same as the flipped result of convolution between flipped source wavelet and input signal, which can be expressed as RW. Thus, **Equation A. I** can be rewritten as follows:

$$\mathrm{W}^T \mathrm{RV}^{\delta} \mathrm{Rd} = \mathrm{RWV}^{\delta} \mathrm{Rd}.\# \quad \text{(A.II)}$$

In above equation, since W and V^{δ} are causal convolution operators, order of operator WV^{δ} can be exchanged as V^{δ} W. Furthermore, based on the same manner as operator W^TR, the right hand side of **Equation A. II** can be modified as follows:

$$\begin{aligned} &\mathrm{RWV}^{\delta} \mathrm{Rd} \\ &= \mathrm{RV}^{\delta} \mathrm{WRd} \\ &= \mathrm{V}_{\cdot}^{T} \mathrm{RWRd} \\ &= \mathrm{V}_{\cdot}^{T} \mathrm{RRW}^{T} \mathrm{d} \\ &= \mathrm{V}_{\cdot}^{T} \mathrm{W}^{T} \mathrm{d}.\# \end{aligned} \quad \text{(A.III)}$$

Since time-reverse operator R is involutory matrix, which has its own inverse, RR becomes identity matrix I. Finally, **Equation XV** is obtained.

(B) Algorithm

Algorithm 1. Wave equation-based migration approach using interpolated excitation information

Input: Migration velocity model c, recorded seismogram d, source wavelet $f(t)$, source and receiver position x_s and x_r, arbitrary source position x^{α}

Output: Migration image $\mathrm{I}_e(\mathrm{x})$

for $x_a \in \mathrm{x}_a$ do

Forward wavefield simulation at x_{α}

While $t < \mathrm{T}$ do

if $\left|S(t, \mathrm{x}; x_a)\right| \geq \left|A(\mathrm{x}; x_a)\right|$ then

$t_{ex} = t$

$\breve{}_e(\mathrm{x};\ _a) =\ _{ex}$

$A(\mathrm{x}; x_a) = S(t_{ex}, \mathrm{x}; x_a)$

End if

End while

End for

Interpolate excitation information

For $x_s \in \mathrm{x}_s$ do

Construct causal convolution matrix W using $f(t)$

For $x_r \in \mathrm{x}_r$ do

$\hat{\mathrm{d}} = \mathrm{W}^T \mathrm{d}$

Calculate migration image $I_e(\mathrm{x}; x_s)$ by Equation (XVI)

$I_e(\mathrm{x}) = I_e(\mathrm{x}) + I_e(\mathrm{x}; x_s)$

End for

End for

ACCSCIENCE PUBLISHING

Journal of Seismic Exploration

ARTICLE

Forward modeling study of seismic acquisition for fractured soft structures in deep geothermal reservoirs

Guoqiang Fu[1], Zhiyu Tan[1], Zhe Men[2], Fei Gong[3]*, Ping Che[4]*, Qiang Guo[1], Xiaoge Wu[1], Fan Xiao[1], and Jingyi Lei[1]

[1]Department of Geophysics, School of Resources and Geosciences, China University of Mining and Technology, Xuzhou, Jiangsu, China

[2]China National Petroleum Corporation BGP Inc., Zhuozhou, Hebei, China

[3]Department of Geophysics and Information, College of Geoscience and Surveying Engineering, China University of Mining and Technology-Beijing, Beijing, China

[4]Jiangsu East China Geological Construction Group Co., Ltd., Nanjing, China

Abstract

Deep geothermal reservoirs are expected to serve as a sustainable resource for clean energy production, contributing to the achievement of global dual-carbon targets. This study analyzes the seismic acquisition method for soft-structure fracture zones in deep geothermal reservoirs through forward modeling analysis. Based on geological data from the Baoying area, China, a 2D geological model—integrating formation velocities, densities, and stochastic fracture media within the Upper Sinian–Middle Ordovician strata—was constructed for the forward modeling. To enhance the accuracy of seismic simulations and reduce numerical dispersion, high-order finite-difference methods were employed. A detailed theoretical analysis of seismic dispersion characteristics indicates that higher-order spatial and temporal differences can effectively mitigate numerical dispersion. Numerical seismic forward simulations were performed using a 10^{th}-order difference accuracy, with a detailed analysis of acquisition survey parameters such as trace spacing, shot spacing, maximum offset, and record length. Simulated records for the geological model with and without fracture zones were compared, revealing distinct differences, particularly when fracture zones are located within high-velocity layers. Further analysis of pre-stack depth migration profiles with varying offsets, trace spacings, and shot intervals indicates that a maximum offset above 7000 m, a trace spacing of 5 m (or 10 m as a cost-effective option), and a shot interval of 40 m provide optimal imaging accuracy for fracture zones. These findings offer guidance for improving seismic imaging and interpretation of soft structures within fracture zones, thereby enhancing seismic exploration of deep geothermal reservoirs.

Keywords: Deep geothermal reservoirs; Soft structures; Fracture zones; Forward modeling; High-order finite-difference; Seismic acquisition

***Corresponding authors:**
Fei Gong
(cupgongfei@163.com)
Ping Che
(cheping@foxmail.com)

Citation: Fu G, Tan Z, Men Z, *et al*. Forward modeling study of seismic acquisition for fractured soft structures in deep geothermal reservoirs. *J Seismic Explor*. 2025;34(3):61-75.
doi: 10.36922/JSE025320054

Received: August 8, 2025

Revised: September 4, 2025

Accepted: September 16, 2025

Published online: October 13, 2025

1. Introduction

The pursuit of sustainable energy sources has become a global imperative, driven by the need to mitigate climate change and reduce greenhouse gas emissions. Among various renewable energy options, geothermal energy stands out due to its potential to provide a reliable and carbon-neutral energy supply. Deep geothermal reservoirs are known to hold vast amounts of untapped geothermal energy; however, the exploration and exploitation of these resources are hindered by the complex geological structures in deeply buried environments.[1-4]

Seismic exploration is a crucial technique for mapping and characterizing subsurface geological structures.[5-8] It involves the generation and recording of seismic waves that are reflected or refracted by geological interfaces. The analysis of these seismic data provides insights into the subsurface geology, enabling the identification and assessment of potential geothermal reservoirs. For deep geothermal reservoirs, successful exploration and identification heavily rely on the capability to accurately image and interpret subsurface geological structures.[9,10] However, deep geothermal reservoirs are often associated with soft-structure fracture zones containing fluids and gases,[11-14] which can significantly affect seismic wave propagation, leading to complex seismic responses that are difficult to interpret using conventional methods. In addition, the great depths of these reservoirs often result in weak seismic signals with low data quality.[15,16] Further hindering the efficiency of seismic acquisition. Although seismic forward modeling has been extensively studied in the context of oil and gas reservoirs, such analyses are rarely applied to deep geothermal reservoirs, and published research remains very limited. Therefore, there is a pressing need to develop advanced seismic acquisition and imaging techniques that can address the challenges posed by soft-structure fracture zones in deep geothermal environments.

Previous studies have made significant contributions to understanding seismic wave propagation in complex geological structures.[17-20] In particular, various numerical modeling methods, such as finite-difference,[21] finite-element,[22] and spectral element[23] methods, have been developed to simulate seismic wave propagation through geological models. These studies have provided valuable insights into the effects of fractures on seismic wave propagation and have identified key factors influencing seismic responses in fractured media. For example, Lan *et al.*[24] presented a finite-difference-based simulation method for the elastic wave equation in fractured media with a non-flat free surface, highlighting the complexity of scattered waves induced by fractures and surface conditions. Ren *et al.*[25] proposed an implicit staggered-grid finite-difference scheme with sampling-approximated optimal coefficients to improve numerical accuracy for seismic modeling of complex structures. However, most existing studies have focused on relatively simple fracture geometries and have not fully accounted for the stochastic nature of natural fractures. In addition, the impact of soft formations on seismic wave propagation has rarely been addressed, limiting the applicability of these findings to practical geothermal exploration.

In addition to the complexity of seismic modeling/responses caused by the stochastic nature of fractures, the presence of soft formations can lead to significant attenuation and dispersion of seismic waves,[26,27] further complicating the seismic data acquisition. In seismic exploration, acquisition survey parameters, such as offset, trace spacing, and shot interval, greatly affect the seismic processing, imaging, and interpretation.[28-31] For example, Zhang[32] proposed optimized sparse seismic acquisition designs combined with compressive sensing reconstruction, achieving high-quality seismic imaging using only 25% of the receivers. Tsingas *et al.*[33] developed a novel 3D distributed blended seismic acquisition scheme, combined with advanced deblending algorithms that produced full-bandwidth seismic images. Zhao *et al.*[34] presented an irregular seismic acquisition method combining curvelet transform and simulated annealing to optimize observation system design in complex areas. However, the analysis of optimal acquisition parameters for seismic surveys targeting fracture zones in deep geothermal reservoirs has not been systematically studied. There remains a lack of quantitative guidelines for selecting acquisition survey parameters in such complex geological settings.

To address the aforementioned issues, this study aims to fill these research gaps by employing forward modeling analysis to investigate the seismic acquisition method for soft-structure fracture zones in deep geothermal reservoirs. In this context, "soft structures" refer to low-velocity, low-modulus, and relatively weakened fracture zones or fractured rock bodies filled with fluids and/or gases within deep geothermal reservoirs. Compared to the surrounding host rock, these structures exhibit lower elastic moduli and higher attenuation and energy dissipation. By constructing a 2D geological model that incorporates stochastic fracture media and soft formations, and using high-order finite-difference methods to simulate seismic wave propagation, this study seeks to provide a more comprehensive understanding of seismic responses in complex geological environments. Furthermore, through the analysis of pre-stack depth migration (PSDM) profiles with varying acquisition parameters, this study aims to identify optimal seismic acquisition strategies for

imaging soft structures within fracture zones. Overall, this work presents an initial set of optimal acquisition survey parameters based on detailed seismic forward modeling analysis for deep geothermal reservoirs with complex fractures, thereby contributing to the advancement of geothermal exploration techniques.

2. Geological model

The geological model for this study is based on the geological profile from the Baoying area, Jiangsu province, an important geothermal exploration target in China.[35,36] The Baoying area provides detailed geological structure information on deep geothermal reservoirs, and a reference line is selected for seismic forward modeling (Figure 1A). Based on this reference line, the initial geological model was constructed for further analysis, as shown in Figure 1B. According to geophysical parameters from the area, interval velocities, densities, and other formation properties were assigned to the initial geological model.

To analyze the effects of fractures on seismic modeling and acquisition, three fracture structures with varying sizes and geometries were introduced into the geological model. The fracture zones are located within the Upper Sinian–Middle Ordovician strata (outlined by the blue polygonal area in Figure 1A), corresponding geologically to the location of deep geothermal reservoirs. Specifically, the interiors of these fracture zones are filled with stochastic fracture media using a random medium modeling approach. Figure 2A further displays the grid model incorporating the fracture zones, with a close-up view shown in Figure 2B (fractures indicated by arrows). The color legend in Figure 2 represents P-wave velocity.

3. Numerical analysis

3.1. Methodologies

Forward modeling simulates the seismic response of underground elastic models. Seismic propagation can be described by the acoustic wave equation, with the constant-density 2D form expressed as:[37]

$$\frac{\partial^2 u}{\partial x^2}+\frac{\partial^2 u}{\partial z^2}=\frac{1}{V^2(x,z)}\frac{\partial^2 u}{\partial t^2} \quad \text{(I)}$$

where u is the particle displacement, V is the particle velocity, t is the time, and x, z represent the Cartesian coordinates.

Finite-difference methods are commonly used to numerically solve the acoustic wave equation and simulate wave propagation.[21] In particular, high-order finite-difference methods can enhance the accuracy of temporal differencing. To mitigate the excessive memory requirements of the algorithm, high-order time derivatives of the wavefield can be converted into high-order spatial derivatives.

For spatial differencing, the second-order derivative can be approximated using a $2M^{\text{th}}$-order difference accuracy finite-difference scheme in the following form:

$$\frac{\partial^2 f}{\partial x^2}=\frac{1}{\Delta x^2}\sum_{m=1}^{M}C_m^{(M)}[f(x+m\Delta x)-2f(x)+f(x-m\Delta x)] \quad \text{(II)}$$

where C_m is the m^{th}-order difference coefficient. Using a Taylor series expansion, these high-order coefficients can be obtained by solving the following system of equations:

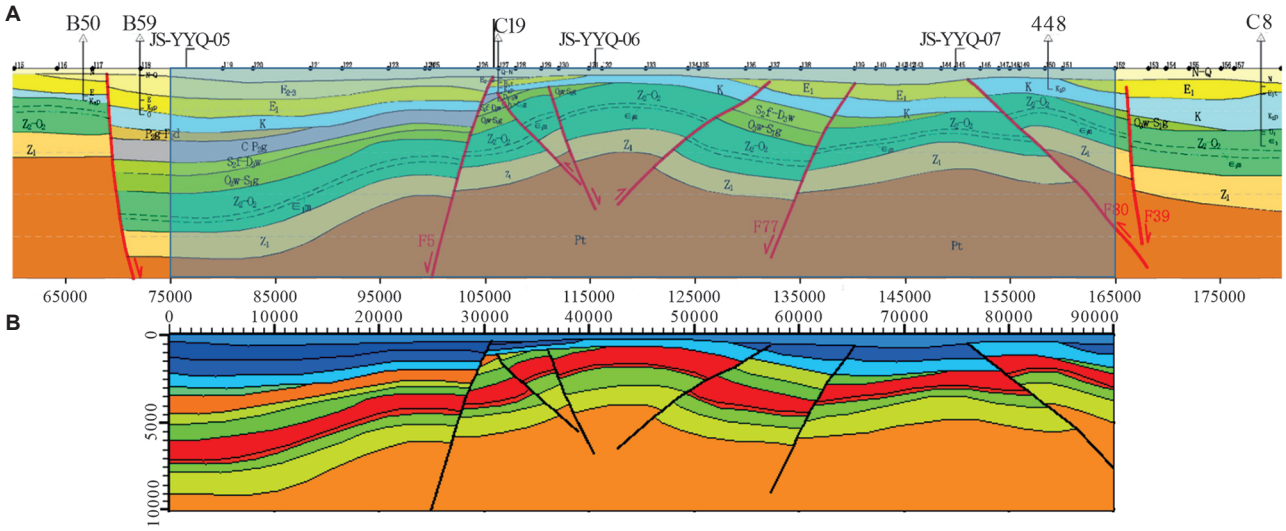

Figure 1. Partial view of the (A) reference line from the Baoying area, and the derived (B) 2D geological model. In the figure, the red lines represent faults, the black lines represent stratigraphic boundaries, and the dashed black lines represent unconformities.

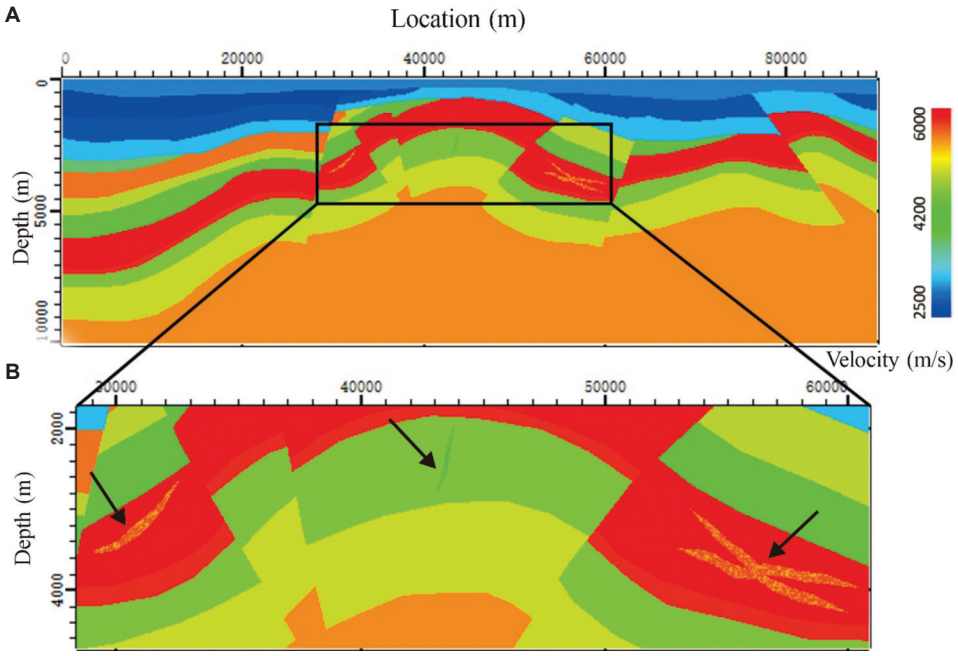

Figure 2. Geological model containing the fracture zones for the forward modeling. (A) Grid model incorporating fracture zone structures; (B) Close-up view of the grid model with fracture zone structures indicated by arrows.

$$\begin{bmatrix} 1^2 & 2^2 & 3^2 & \cdots & M^2 \\ 1^4 & 2^4 & 3^4 & \cdots & M^4 \\ 1^6 & 2^6 & 3^6 & \cdots & M^6 \\ \vdots & \vdots & \vdots & \ddots & \vdots \\ 1^{2M} & 2^{2M} & 3^{2M} & \cdots & M^{2M} \end{bmatrix} \begin{bmatrix} C_1^{(M)} \\ C_2^{(M)} \\ C_3^{(M)} \\ \vdots \\ C_M^{(M)} \end{bmatrix} = \begin{bmatrix} 1 \\ 0 \\ 0 \\ \vdots \\ 0 \end{bmatrix} \quad \text{(III)}$$

Numerical dispersion arises from grid discretization in numerical computations. It causes seismic waves of different frequencies to exhibit varying phase velocities, resulting in dispersion of seismic waves and reducing the effectiveness of numerical simulations and migration imaging. Although numerical dispersion is unavoidable in wave equations' solutions, its impact can be mitigated through methods that improve computational accuracy.

By applying the high-order differencing method described above, the accuracy of seismic wave numerical simulations can be improved and numerical dispersion reduced. This technique is crucial for enhancing the quality of simulation results. Accordingly, it enables the selection of appropriate simulation parameters in practical seismic modeling, thereby improving seismic imaging and interpretation of deep fracture zones. Given the significance of dispersion effects, a detailed analysis is presented in the following section to better understand both spatial and temporal aspects of numerical dispersion.

3.2. Spatial dispersion analysis

For spatial numerical dispersion, we examined the dispersion characteristics of the spatial $2N^{th}$-order spatial difference accuracy approximation for the 2D wave equation. Assuming that the propagation direction of the plane wave forms an angle θ with the x-axis, substituting the plane harmonic wave $u(x,z,t) = \exp[i(wt - kx\cos\theta - kz\sin\theta)]$ into the $2N^{th}$-order spatial difference formula (assuming that $\Delta z = \Delta x$):

$$\frac{1}{V_0^2}\frac{\partial^2 u}{\partial t^2} = \frac{1}{\Delta x^2}\sum_{n=1}^{N} C_n^{(N)}\left[u(x+n\Delta x,z) + u(x-n\Delta x,z) + u(x,z+n\Delta x) + u(x,z-n\Delta x) - 4u(x,z)\right] \quad \text{(IV)}$$

Based on **Equation IV**, we can further derive:

$$\frac{V}{V_0} = \sqrt{\frac{-2}{\phi^2}\left\{\sum_{n=1}^{N} C_n^{(N)}[\cos(n\phi\cos\theta) + \cos(n\phi\sin\theta) - 2]\right\}} \quad \text{(V)}$$

where $V = \omega/k$ is the phase velocity of the seismic wave, $\varphi = k\Delta x = 2\pi\Delta x/\lambda$ is the phase angle, and θ is the angle between the propagation direction and the coordinate axis.

Figure 3 displays the variation curves of spatial numerical dispersion for propagation angles $\theta = 0°$, $\theta = 22.5°$, and $\theta = 45°$, under spatial difference accuracies of 2nd, 4th, 6th, 8th, and 10th orders, respectively, plotted as a function of the number of discrete points per wavelength.

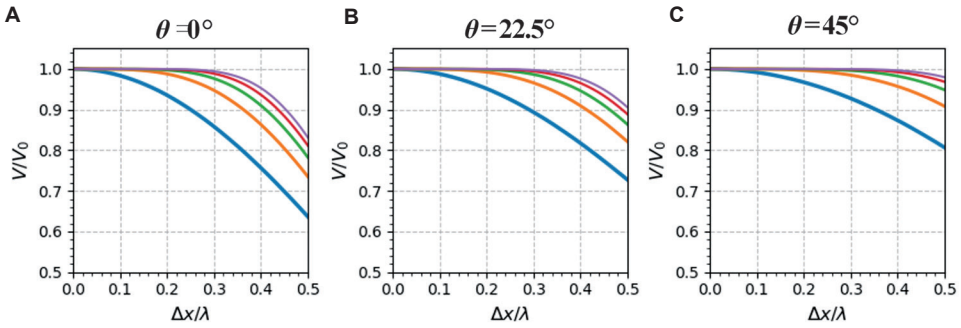

Figure 3. Numerical dispersion curves for wave propagation directions of (A) $\theta = 0°$, (B) $\theta = 22.5°$, and (C) $\theta = 45°$, given varying spatial difference accuracies (2nd, 4th, 6th, 8th, and 10th orders)

From Figure 3 and **Equation V**, it can be observed that numerical dispersion caused by spatial difference is determined by three factors: (i) The propagation direction of the seismic wave, (ii) the spatial difference accuracy, and (iii) the number of discrete points per wavelength (grid spacing). Their relationships with dispersion are presented below.

As the angle between the propagation direction and the discrete coordinate axis increases, the degree of numerical dispersion decreases. For a plane wave propagating at an angle θ to the x-axis, the spatial numerical dispersion is equivalent to that of a wave propagating at an angle of $90° - \theta$. In other words, the discrete numerical dispersion is minimal when $\theta = 45°$ (Figure 3C).

Regardless of the propagation direction, increasing the spatial difference accuracy order reduces the numerical dispersion. Therefore, there is a direct relationship between numerical dispersion and difference accuracy: Higher-order spatial differences effectively suppress dispersion. Unless the grid spacing is very fine (e.g., more than 15 spatially discrete points per wavelength, which implies low simulation efficiency), conventional second-order spatial differencing leads to severe dispersion. In contrast, higher-order methods, such as eighth- or 10th-order differencing, significantly improve accuracy, even when using only four grid points per wavelength. In general, adopting an eighth-order spatial difference accuracy is sufficient to suppress numerical dispersion.

For any order of spatial differencing, as the number of discrete points per wavelength increases (i.e., as grid spacing decreases), numerical dispersion is further reduced, and the accuracy of seismic wave simulation improves. This analysis confirms that numerical dispersion can be mitigated by employing high-order difference methods, and numerical simulation results validate this conclusion.

Figure 4 shows the single-shot simulation records for a single-interface model using second-order and 10th-order spatial difference accuracies, with $\Delta x = \Delta z = 10$ m and

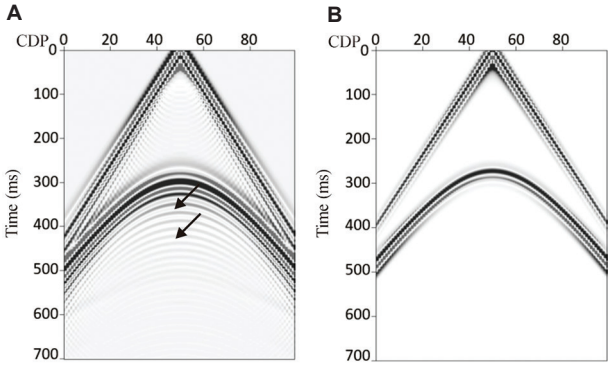

Figure 4. Numerical simulations for a single-interface model using (A) second-order and (B) 10th-order spatial difference accuracy
Abbreviation: CDP: Common depth point

$\Delta t = 1$ *ms*. It can be observed that numerical dispersion from second-order spatial differencing (Figure 4A) is severe, particularly for vertically propagating waves, while higher-order differencing effectively mitigates spatial dispersion.

In addition, Figure 4 demonstrates that $V < V_o$; that is, numerical dispersion caused by spatial discretization appears as a trailing waveform (indicated by arrows in Figure 4A). Given that $\varphi = 2\pi f \Delta x / V_o$, for a constant grid spacing, higher wavelet frequencies and lower medium velocities lead to more severe dispersion. Therefore, in cases involving lower-velocity media (such as low shear-wave velocities), while high-frequency resolution is required, high-order differencing methods should be used to suppress numerical dispersion.

3.3. Temporal dispersion analysis

For the analysis of temporal numerical dispersion, we substitute the harmonic wave $u(x,z,t) = \exp[i(wt - kx\cos\theta - kz\sin\theta)]$ into the following equation:

$$\frac{\partial^2 u}{\partial x^2} + \frac{\partial^2 u}{\partial z^2} = \frac{1}{V_0^2 \Delta t^2} \sum_{m=1}^{M} C_m^{(M)} [u(t + m\Delta t) - 2u(t) + u(t - m\Delta t)] \quad \text{(VI)}$$

Based on Equation VI, we can further derive:

$$\frac{V_0}{V}=\sqrt{\frac{-1}{2\pi^2}\frac{1}{\left(\frac{\Delta t}{T}\right)^2}\sum_{m=1}^{M}C_m^{(M)}[\cos(2m\pi\frac{\Delta t}{T})-1]} \quad \text{(VII)}$$

where $V=\omega/k$ is the phase velocity of the seismic wave, T is the period of the seismic wave, and Δt is the time step length.

Figure 5 displays the variation curves of temporal discrete numerical dispersion as a function of $\Delta t/T$, for different difference accuracies of 2nd, 4th, 6th, 8th, and 10th orders. It can be observed that: (i) when $V > V_o$, numerical dispersion caused by temporal discretization appears as early arrivals in the waveform (i.e., before the actual arrival time), and (ii) as the difference accuracy $2M$ increases, the numerical dispersion introduced by the high-order differencing gradually decreases.

From **Equation VII**, it is evident that temporal numerical dispersion is primarily governed by two factors: (i) The difference in accuracy and (ii) the number of discrete points within 1 time period (also illustrated in Figure 5). Due to algorithmic stability constraints, $\Delta t/T$ is generally very small. As a result, numerical dispersion during the forward and reverse propagation of seismic waves is mainly attributed to spatial discretization rather than temporal discretization. To address temporal numerical dispersion, adopting the fourth-order temporal difference accuracy is generally sufficient. Higher-order temporal difference accuracies have minimal impact on mitigating numerical dispersion and may instead reduce simulation efficiency.

3.4. Stability analysis

Stability is a fundamental issue in numerically solving seismic wave equations. An unreasonable selection of discrete parameters during numerical computations may produce computed results that grow exponentially without physical meaning, resulting in severe numerical dispersion

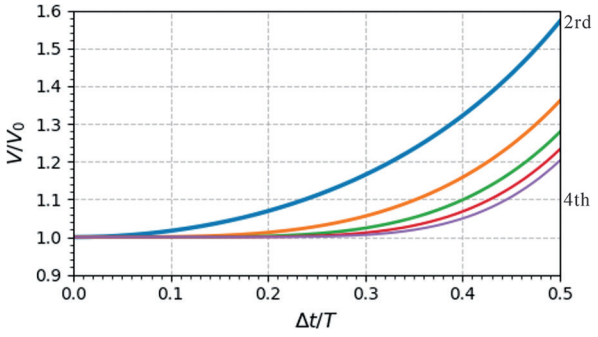

Figure 5. Numerical dispersion curves for varying temporal difference accuracies (2nd, 4th, 6th, 8th, and 10th orders)

in simulation results. In extreme cases, this can lead to overflow errors and render computations unfeasible. Therefore, for any numerical solution method, it is necessary to determine the range of discrete parameters that ensure computational stability, i.e., to assess the method's stability. In this study, we analyzed the stability of the high-order finite-difference method for the 2D acoustic wave equation and provided corresponding stability conditions for various difference accuracies.

The difference scheme for the $2N^{th}$-order spatial difference accuracy of the 2D acoustic wave equation can be written as:

$$\begin{aligned}&u(t+\Delta t)\approx 2u(t)-u(t-\Delta t)\\&+V^2\Delta t^2\left\{\frac{1}{\Delta x^2}\sum_{n=1}^{N}C_n^{(N)}\left[u(x+n\Delta x)-2u(x)+u(x-n\Delta x)\right]\right\}\\&+V^2\Delta t^2\left\{\frac{1}{\Delta z^2}\sum_{n=1}^{N}C_n^{(N)}\left[u(z+n\Delta z)-2u(z)+u(z-n\Delta z)\right]\right\}\end{aligned} \quad \text{(VIII)}$$

Applying a Fourier transform to both sides of **Equation VIII** with respect to time and space yields:

$$\begin{aligned}&\cos(\omega\Delta t)-1\approx V^2\Delta t^2\left\{\frac{1}{\Delta x^2}\sum_{n=1}^{N}C_n^{(N)}\left[\cos(\hat{k}_x n\Delta x)-1\right]\right\}\\&+V^2\Delta t^2\left\{\frac{1}{\Delta z^2}\sum_{n=1}^{N}C_n^{(N)}\left[\cos(\hat{k}_z n\Delta z)-1\right]\right\}\end{aligned} \quad \text{(IX)}$$

where k is the wavenumber and w is the angular frequency. To satisfy **Equation IX**, the following condition must be satisfied:

$$-2\le V^2\Delta t^2\left\{\begin{array}{l}\frac{1}{\Delta x^2}\sum_{n=1}^{N}C_n^{(N)}\left[\cos(\hat{k}_x n\Delta x)-1\right]+\\\frac{1}{\Delta z^2}\sum_{n=1}^{N}C_n^{(N)}\left[\cos(\hat{k}_z n\Delta z)-1\right]\end{array}\right\}\le 0 \quad \text{(X)}$$

Given that the spatial difference coefficients C_n alternate between positive and negative values, the maximum spatial wavenumber is the Nyquist wavenumber $k=\pi/\Delta x$. Therefore, the stability condition for the $2N^{th}$-order spatial difference accuracy of the 2D acoustic wave equation is given by:

$$0\le V^2\Delta t^2\left(\frac{1}{\Delta x^2}+\frac{1}{\Delta z^2}\right)\sum_{n=1}^{N}C_n^{(N)}\left[1-(-1)^n\right]\le 2 \quad \text{(XI)}$$

Equation XI can be further simplified to:

$$V\Delta t\sqrt{\frac{1}{\Delta x^2}+\frac{1}{\Delta z^2}}\le\sqrt{\frac{2}{\sum_{n=1}^{N}C_n^{(N)}\left[1-(-1)^n\right]}} \quad \text{(XII)}$$

Equation XII serves as a general stability criterion for high-order finite-difference methods in acoustic wave simulations with varying difference accuracies. Based on different values of *N*, stability conditions for different orders of spatial difference accuracy are listed in Table 1. The results indicate that as the spatial difference accuracy increases, the stability requirements for high-order grid-based methods increase slightly. However, the increase is relatively modest. In other words, discrete grid parameters that satisfy the stability conditions for lower-order schemes generally meet the requirements for higher-order schemes. Thus, adopting high-order differencing does not impose significantly stricter demands on the choice of discrete parameters.

Table 1. Stability conditions for different orders of spatial difference accuracy

Orders *N* of spatial difference (Δx=Δz)	Stability condition	
	$V\Delta t\sqrt{\frac{1}{\Delta x^2}+\frac{1}{\Delta z^2}}$	$\frac{V\Delta t}{\Delta x}$
N=1	<1	<0.707
N=2	<0.866	<0.612
N=3	<0.813	<0.575
N=4	<0.784	<0.555
N=5	<0.765	<0.541

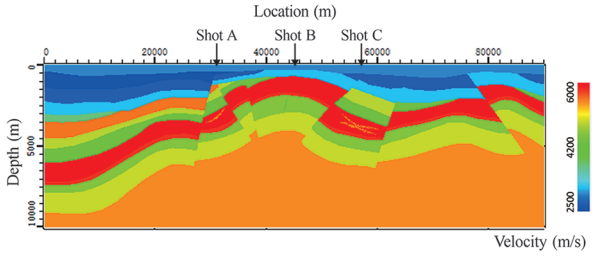

Figure 6. Illustration of the locations of shots A, B, and C on the geological model

4. Simulation results

4.1. Single-shot record results

Based on the previous numerical analysis, seismic modeling was performed using the 10th-order finite-difference scheme applied to the 2D acoustic wave equation. In practice, an absorbing boundary condition[38] is employed to mitigate the effects of reflections from artificial boundaries. The geological model shown in Figure 1 was used, with an absorbing surface boundary condition applied at the surface. A Ricker wavelet with a dominant frequency of 40 Hz was utilized in the simulations. For the seismic acquisition survey, the trace spacing was set to 5 m, the shot spacing to 40 m, the maximum offset to 8000 m, and the minimum offset to 5 m. All single-shot records were captured for 8 s with a sampling interval of 2 ms. For comparison, single-shot records (Shots A, B, and C) were generated at different locations above the fracture zones, as illustrated in Figure 6.

Figures 7A, 8A, and 9A display the simulated shot records for shots A, B, and C with the fracture zones included in the model. Corresponding records without the fracture zones are shown in Figures 7B, 8B, and 9B, and the residuals (i.e., the differences between records with and without fracture zones) are depicted in Figures 7C, 8C, and 9C. The comparison and analysis reveal the following: (i) For shots A and C, where the fracture zones are located within high-velocity layers, the overlying strata exert minimal influence. Consequently, distinct differences in the shot records are observable (Figures 7C and 9C). (ii) For shot B, where the fracture zones are developed

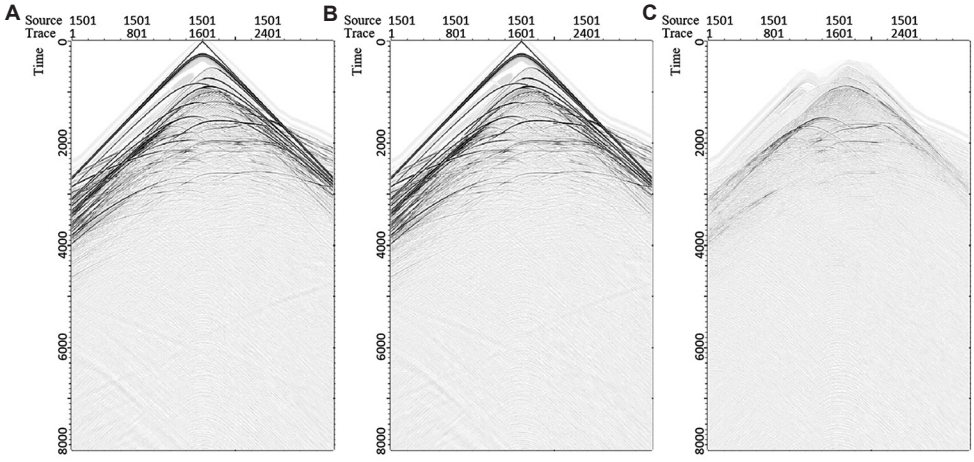

Figure 7. Simulated shot record (A) with fracture zones, (B) without fracture zones, and (C) residual difference between (A) and (B) for shot A

within low-velocity layers, the overlying strata significantly mask the effects of the fracture zones. As a result, no clear differences are visible in the residual record (Figure 8C).

4.2. Migration results

Based on the shot records, we further analyzed the PSDM[39,40] results using different acquisition survey parameters. The PSDM was performed using the acoustic wave equation with the Fourier finite-difference method. For comparison, we evaluated the PSDM results by varying acquisition parameters, including maximum offset, trace spacing, and shot interval.

Figures 10-13 display the PSDM findings for maximum offsets of 8000 m, 7000 m, 6000 m, and 5000 m, respectively. Comparing these imaging results reveals that the migration with a 6000 m offset exhibits slightly lower accuracy for fracture imaging than those with 7000 m or larger offsets, showing poorer continuity of fracture structure and slightly reduced resolution. The differences between the 7000 m and 8000 m offset migration results are negligible, as both offer nearly identical imaging accuracy. In contrast, the 5000 m offset produces significantly lower imaging quality. This analysis suggests that a maximum offset >7000 m is preferable for effectively revealing deep fracture zones.

Figures 14-17 exhibit the PSDM results with trace spacings of 5 m, 10 m, 20 m, and 40 m, respectively. Comparing these findings indicates that imaging accuracy for steeply dipping structures is significantly better with 5 m and 10 m trace spacings than with 20 m and 40 m spacings. While the overall disparity between 5 m and 10 m spacings is not substantial, the finer spatial sampling of 5 m produces clearer and more accurate imaging of fracture structures (as indicated by the arrows in Figure 14). Based on this analysis, 5 m trace spacing is recommended; however, if computational cost is a concern, a 10 m trace spacing may also be acceptable.

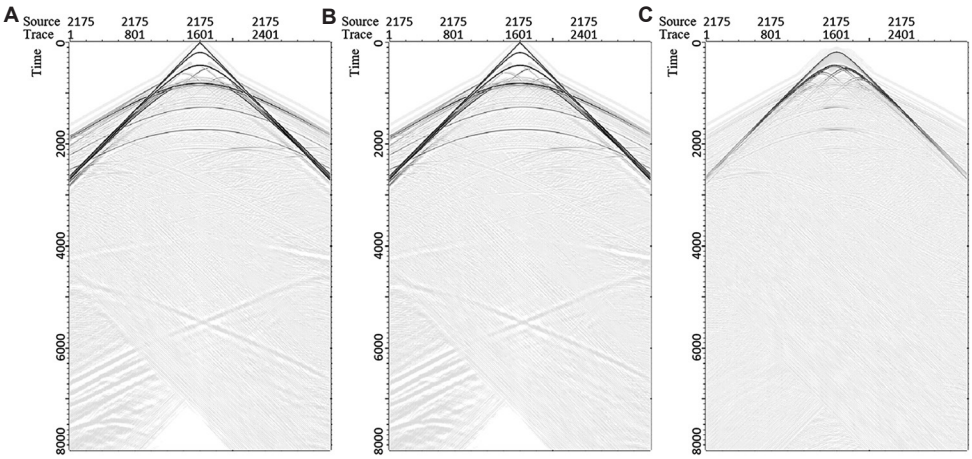

Figure 8. Simulated shot record (A) with fracture zones, (B) without fracture zones, and (C) residual difference between (A) and (B) for shot B

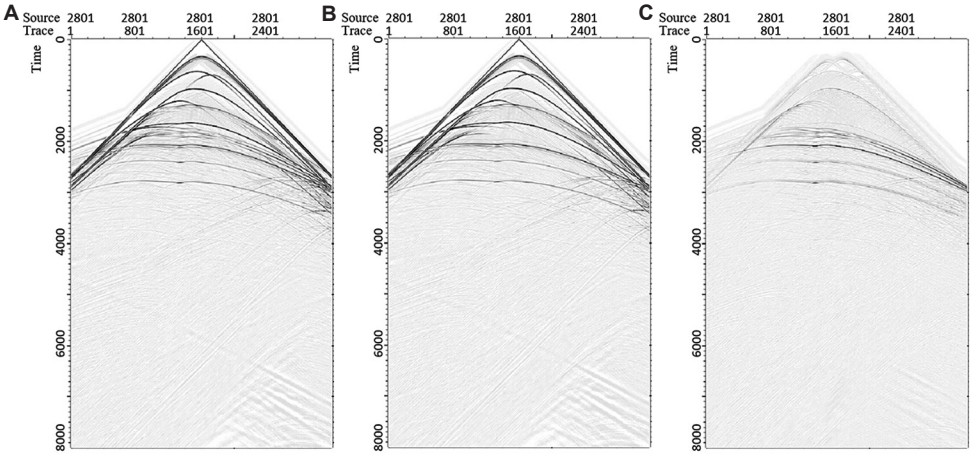

Figure 9. Simulated shot record (A) with fracture zones, (B) without fracture zones, and (C) residual difference between (A) and (B) for shot C

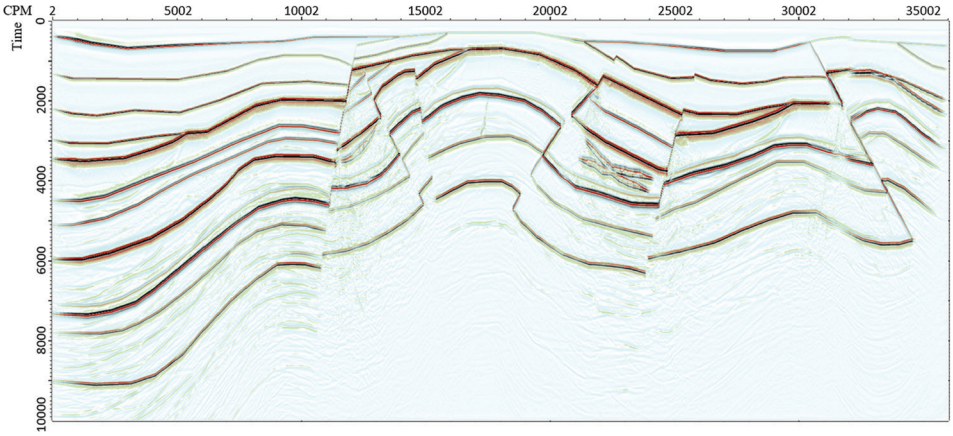

Figure 10. Pre-stack depth migration result with maximum offset of 8000 m (bin size: 2.5 m; fold: 200)
Abbreviation: CPM: Common middle point.

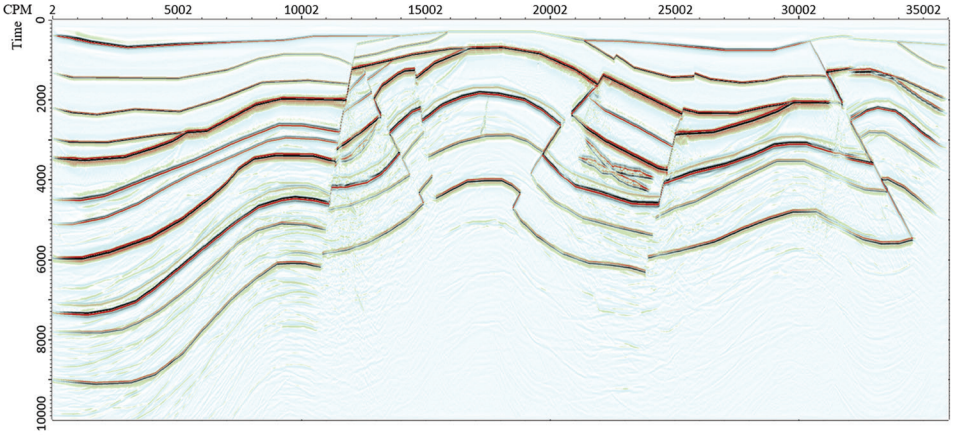

Figure 11. Pre-stack depth migration result with a maximum offset of 7000 m (bin size: 2.5 m; fold: 175)
Abbreviation: CPM: Common middle point.

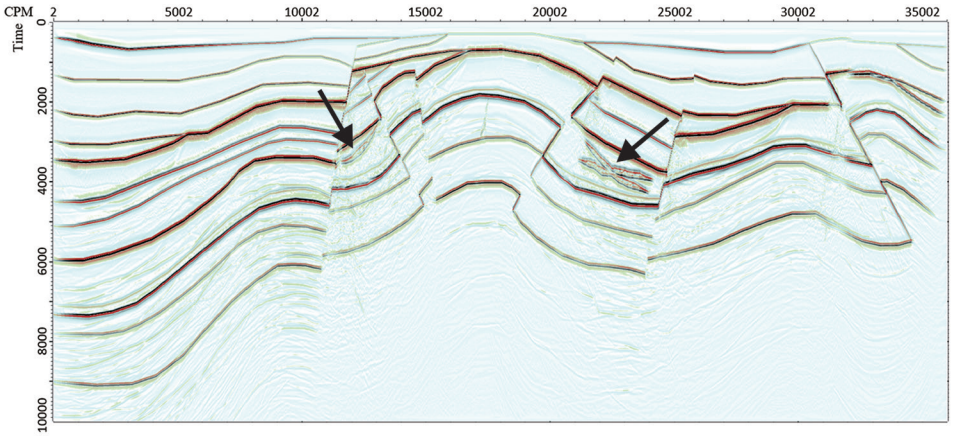

Figure 12. Pre-stack depth migration result with a maximum offset of 6000 m (bin size: 2.5 m; fold: 150)
Abbreviation: CPM: Common middle point.

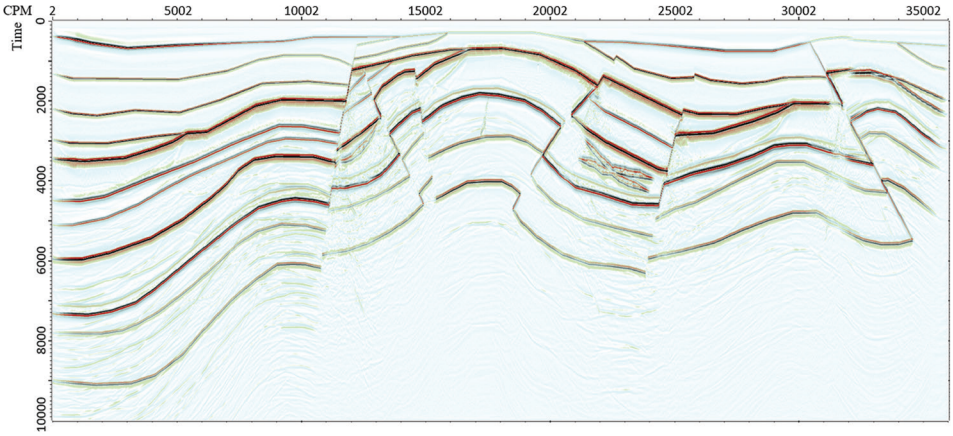

Figure 13. Pre-stack depth migration result with a maximum offset of 5000 m (bin size: 2.5 m; fold: 150)
Abbreviation: CPM: Common middle point.

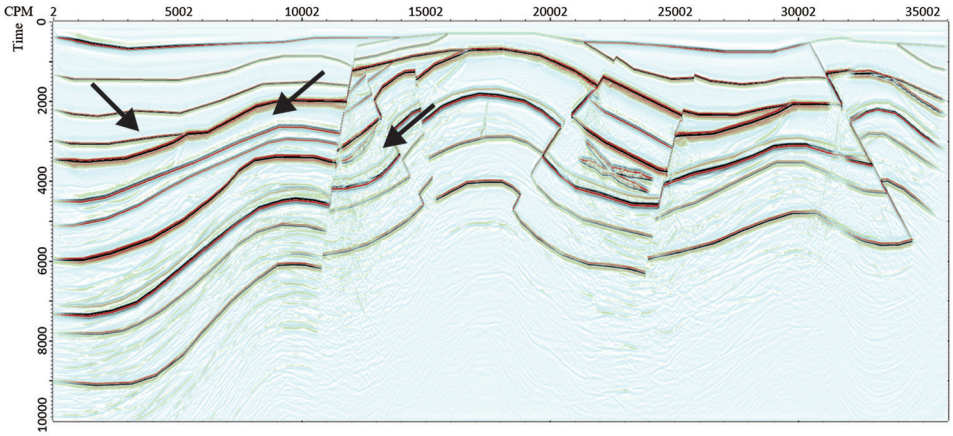

Figure 14. Pre-stack depth migration result with trace spacing of 5 m (bin size: 2.5 m; fold: 200)
Abbreviation: CPM: Common middle point.

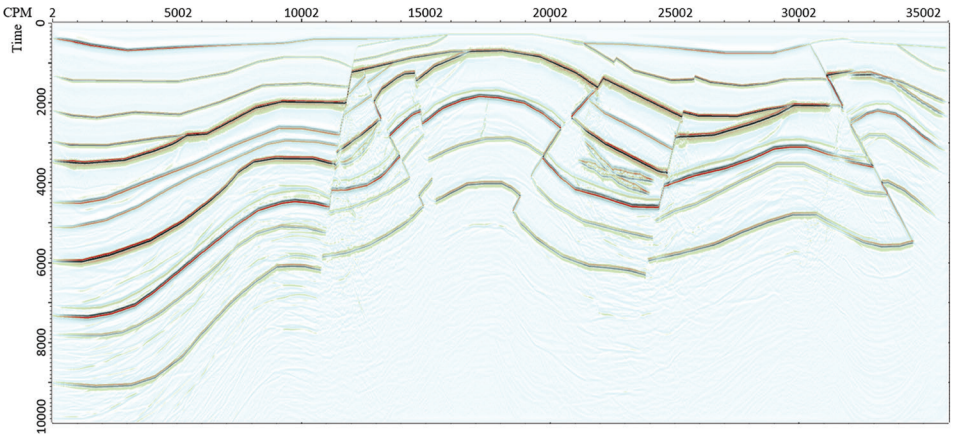

Figure 15. Pre-stack depth migration result with trace spacing of 10 m (bin size: 5 m; fold: 200)
Abbreviation: CPM: Common middle point.

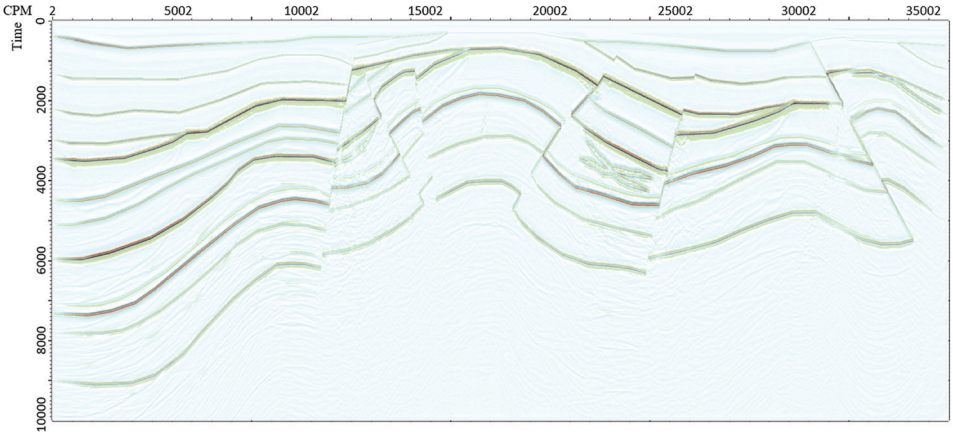

Figure 16. Pre-stack depth migration result with trace spacing of 20 m (bin size: 10 m; fold: 200)
Abbreviation: CPM: Common middle point.

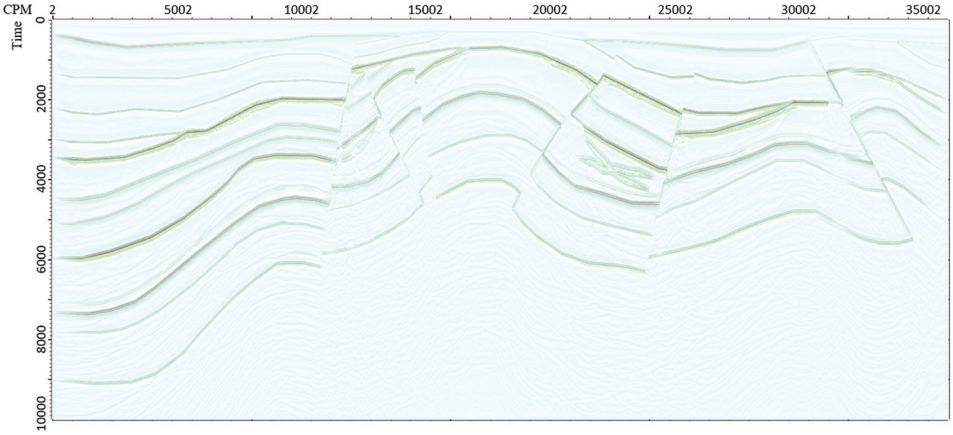

Figure 17. Pre-stack depth migration result with trace spacing of 40 m (bin size: 20 m; fold: 200)
Abbreviation: CPM: Common middle point.

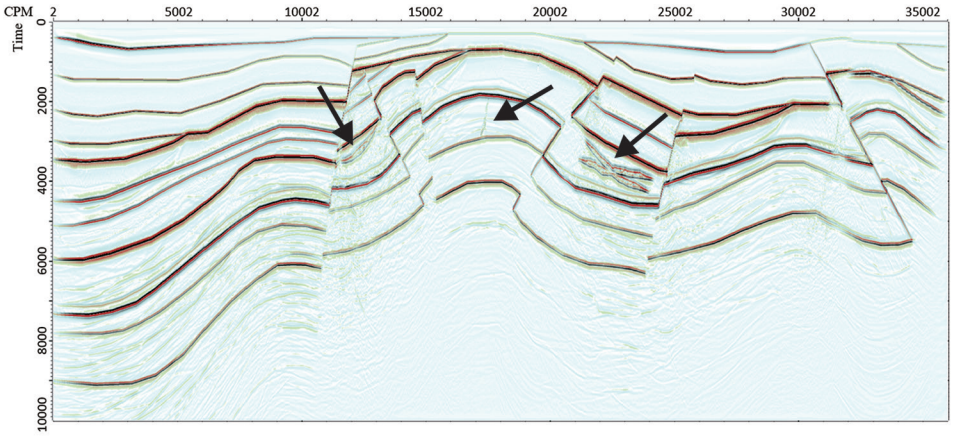

Figure 18. Pre-stack depth migration result with a maximum shot interval of 40 m (bin size: 2.5 m; fold: 200)
Abbreviation: CPM: Common middle point.

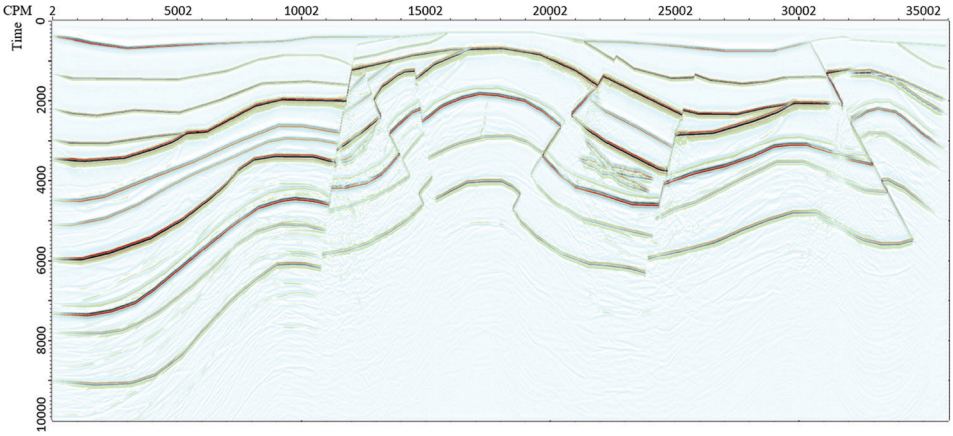

Figure 19. Pre-stack depth migration result with a maximum shot interval of 80 m (bin size: 2.5 m; fold: 100)
Abbreviation: CPM: Common middle point.

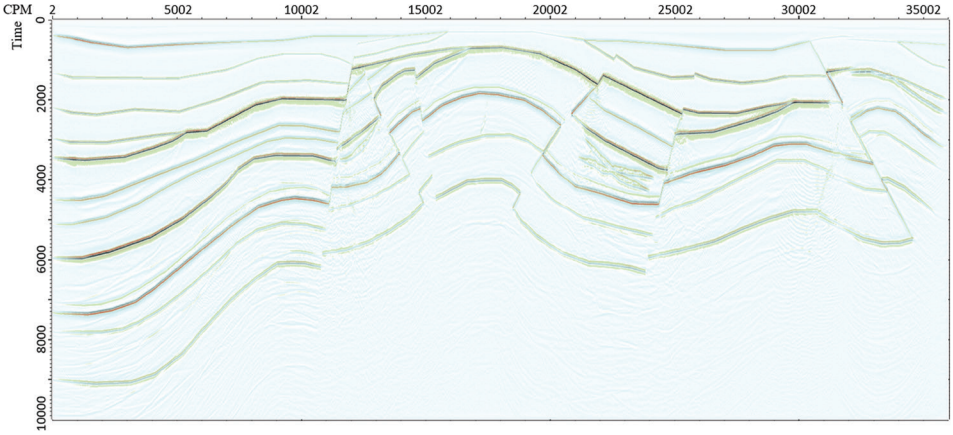

Figure 20. Pre-stack depth migration result with a maximum shot interval of 160 m (bin size: 2.5 m; fold: 50)
Abbreviation: CPM: Common middle point.

Figures 18-20 display the PSDM results for shot intervals of 40 m, 80 m, and 160 m, respectively. Comparing these outcomes demonstrates that the 40 m shot interval provides a clear advantage in imaging fracture zones (indicated by the arrows in Figure 18).

5. Discussion

This study focuses on forward modeling analysis to investigate seismic acquisition strategies for soft-structure fracture zones within deep geothermal reservoirs. However, the analysis in this study is primarily based on numerical simulations and does not yet incorporate measured observational data. Although the geological model was constructed to closely reflect actual geological conditions, discrepancies may still exist between the simulation results and real seismic observations. Such discrepancies could arise from geological complexities, uncertainties in seismic wave propagation, and noise interference in real-world data. In further studies, we aim to implement more advanced wavefield numerical simulation techniques, such as full waveform modeling and spectral element methods, to enhance the accuracy of seismic forward modeling.

Furthermore, this work centers on the influence of acquisition survey parameters (e.g., maximum offset, trace spacing, and shot interval) on seismic migration results, without evaluating the impact of different migration techniques, which can significantly affect imaging quality. Various migration approaches (e.g., Kirchhoff migration and reverse-time migration) may offer differing levels of effectiveness when applied to complex geological structures, including fracture zones. Therefore, the absence of comparative analysis on migration methods may limit our ability to fully interpret seismic imaging results. In future research, we plan to examine the performance of different migration techniques and their effects on fracture imaging in complex geological conditions.

In addition, the presence of fracture networks in soft-structure zones introduces challenges such as seismic attenuation and anisotropy, both of which directly impact data quality and interpretability. Attenuation, primarily caused by scattering losses from stochastic fractures and fluid-induced viscoelastic dissipation, can reduce high-frequency content, particularly when fractures are hosted within high-velocity layers, necessitating finer bin sizes to maintain resolution. Meanwhile, fracture-induced anisotropy may require acquisition designs with multi-azimuth coverage and long offsets to capture anisotropy signatures. While the proposed acquisition parameters (40 m shot interval and 5 m bin size) strike a balance between cost and imaging accuracy, they should be complemented by anisotropic velocity modeling to optimize target illumination, an aspect warranting further investigation.

6. Conclusion

This study investigates the seismic acquisition design for soft-structure fracture zones within deep geothermal reservoirs through forward modeling analysis. By constructing a detailed 2D elastic model incorporating stochastic fracture media, based on the geological profile from the Baoying area of China, we successfully simulated seismic wave propagation with high fidelity. High-order finite-difference methods were employed to mitigate spatial and temporal numerical dispersion, enhancing the accuracy of seismic wave simulations. The comparison between simulated records with and without fracture zones revealed significant differences, particularly when the fractures were located within high-velocity layers. Further analysis of pre-stack depth migration profiles indicated that a maximum offset exceeding 7000 m, a trace spacing (bin size) of 5 m (or 10 m as a cost-effective alternative), and a shot interval of 40 m can provide optimal imaging accuracy for fracture zones. These findings are crucial for improving seismic imaging and interpretation of soft structures within fracture zones, thus enhancing the seismic exploration of deep geothermal reservoirs. Overall, this work provides quantitative guidelines for selecting seismic simulation and acquisition parameters in geothermal exploration under complex geological settings.

Acknowledgments

None.

Funding

This study was funded by the Jiangsu Province Carbon Peak Neutral Technology Innovation Project in China (BE2022034).

Conflict of interest

The authors declare no conflicts of interest.

Author contributions

Conceptualization: Guoqiang Fu, Zhe Men, Fei Gong, Ping Che
Formal analysis: Zhiyu Tan, Qiang Guo
Investigation: Zhe Men, Ping Che
Methodology: Guoqiang Fu, Fei Gong
Writing–original draft: Guoqiang Fu, Qiang Guo
Writing–review & editing: Zhiyu Tan, Xiaoge Wu, Fan Xiao, Jingyi Lei

Availability of data

Data are not available due to restrictions related to the confidentiality of the project.

References

1. Chopra S, Sharma RK., Bredesen K, Ha T, Marfurt KJ. Seismic characterization of a Triassic-Jurassic deep geothermal sandstone reservoir, onshore Denmark, using unsupervised machine learning techniques. *Interpretation*. 2021;9(4):T1097-T1106.

   doi: 10.1190/INT-2021-0091.1

2. He K, Huang R, Xu Y, Hu S, Wei P. Crustal structures beneath the Northern Jiangsu Basin and its surrounding areas: Implications for geothermal prospecting. *J Geophys Eng*. 2022;19(3):316-325.

   doi: 10.1093/jge/gxac018

3. Tian B, Lei X, Jiang H, Xu C, Song M. Multi-method geophysical mapping of a geothermal reservoir and buried channel in langfang, northern part of china. *J Environ Eng Geophys*. 2022;27(1):1-11.

   doi: 10.32389/jeeg20-068

4. Wang X, Wang G, Gan H, Zhang Y, Gao Z. Constraints of hydrochemical and geological controls in deep-circulation geothermal systems: Insights from Chengde, Dehua, and Tashkorgan geothermal fields in China. *Geothermics*. 2025;127:103265.

   doi: 10.1016/j.geothermics.2025.103265

5. Aleardi M, Mazzotti A. A feasibility study on the expected seismic AVA signatures of deep fractured geothermal reservoirs in an intrusive basement. *J Geophys Eng*.2014;11(6):065008.

   doi: 10.1088/1742-2132/11/6/065008

6. Dyer BC, Schanz U, Ladner F, Häring MO, Spillman T. Microseismic imaging of a geothermal reservoir stimulation. *Leading Edge*. 2008;27(7):856-869.

   doi: 10.1190/1.2954024

7. Bredesen K, Dalgaard E, Mathiesen A, Rasmussen R, Balling N. Seismic characterization of geothermal sedimentary reservoirs: A field example from the Copenhagen area, Denmark. *Interpretation*. 2020;8(2):T275-T291.

   doi: 10.1190/INT-2019-0184.1

8. Fu G, Peng S, Wang R, *et al*. Seismic prediction and evaluation techniques for hot dry rock exploration and development. *J Geophys Eng*. 2022;19(4):694-705.

   doi: 10.1093/jge/gxac042

9. Samrock F, Grayver A, Dambly MLT, Müller MR, Saar MO. Geophysically guided well siting at the Aluto-Langano geothermal reservoir. *Geophysics*. 2023;88(5):WB105-WB114.

   doi: 10.1190/geo2022-0617.1

10. Zheng, Y., Wang, Y. High-resolution reflection seismic imaging to reveal subsurface geologic structures of a deep geothermal reservoir. *Geophysics*. 2023;88(5):WB37-WB43.

    doi: 10.1190/geo2022-0494.1

11. Darisma D, Mukuhira Y, Okamoto K, *et al*. Building the fracture network model for the Okuaizu geothermal field based on microseismic data analysis. *Earth Planets Space*. 2024;76(1):107.

    doi: 10.1186/s40623-024-02049-w

12. Tian A, Fu G, Tang J, Wang D. Numerical simulation of the transport and sealing law of temporary plugging particles in complex fractures of carbonate-type thermal storage. *Energies*. 2024;17(13):3283.

    doi: 10.3390/en17133283

13. Aydın H, Camcı U, Akın S. An experimental investigation of hydraulic fracturing mechanisms in menderes metamorphic rocks: Prospects for enhanced geothermal systems. *Geothermics*. 2025;130:103328.

    doi: 10.1016/j.geothermics.2025.103328

14. Mu S, Zhao L, Zhang A. Numerical simulation of geothermal extraction for interaction between irregular curve fractures and heterogeneous reservoirs. *Rock Mech Rock Eng*. 2025;58(3):2953-2970.

    doi: 10.1007/s00603-024-04339-x

15. Civilini F, Pancha A, Savage MK, Sewell S, Townend J. Inferring shear-velocity structure of the upper 200 m using cultural ambient noise at the Ngatamariki geothermal field, Central North Island, New Zealand. *Interpretation*. 2016;4(3):SJ87-SJ101.

    doi: 10.1190/int-2015-0204.1

16. Nakata N, Bi Z, Qiu H, Liu CN, Nakata R. ML-aided induced seismicity processing and interpretation for enhanced geothermal systems. *Leading Edge*. 2025;44(4):265-275.

    doi: 10.1190/tle44040265.1

17. Jianfeng Z, Tielin L. Elastic wave modelling in 3D heterogeneous media: 3D grid method. *Geophys J Int*. 2002;150(3):780-799.

    doi: 10.1046/j.1365-246X.2002.01743.x

18. Vlastos S, Liu E, Main IG, Li XY. Numerical simulation of wave propagation in media with discrete distributions of fractures: Effects of fracture sizes and spatial distributions. *Geophys J Int*. 2003;152(3):649-668.

    doi: 10.1046/j.1365-246X.2003.01876.x

19. Hoffman BT, Chang WM. Modeling hydraulic fractures in finite difference simulators: Application to tight gas sands in Montana. *J Pet Sci Eng*. 2009;69(1-2):107-116.

    doi: 10.1016/j.petrol.2009.08.007

20. Yang D, Song G, Hua B, Calandra H. Simulation of acoustic wavefields in heterogeneous media: A robust method for automatic suppression of numerical dispersion. *Geophysics*. 2010;75(3):T99-T110.

    doi: 10.1190/1.3428483

21. Liu Y, Sen MK. An implicit staggered-grid finite-difference method for seismic modelling. *Geophys J Int*. 2009;179(1):459-474.

    doi: 10.1111/j.1365-246X.2009.04305.x

22. Virieux J, Calandra H, Plessix R. A review of the spectral, pseudo-spectral, finite-difference and finite-element modelling techniques for geophysical imaging. *Geophys Prospect*. 2011;59(5):794-813.

    doi: 10.1111/j.1365-2478.2011.00967.x

23. Hedayatrasa S, Bui TQ, Zhang C, Lim CW. Numerical modeling of wave propagation in functionally graded materials using time-domain spectral Chebyshev elements. *J Comput Phys*. 2014;258:381-404.

    doi: 10.1016/j.jcp.2013.10.037

24. Lan HQ, Zhang ZJ. Seismic wavefield modeling in media with fluid-filled fractures and surface topography. *Appl Geophys*. 2012;9(3):301-312.

    doi: 10.1007/s11770-012-0341-5

25. Ren ZM, Dai X, Bao QZ. Source wavefield reconstruction based on an implicit staggered-grid finite-difference operator for seismic imaging. *Pet Sci*. 2022;19(5):2095-2106.

    doi: 10.1016/j.petsci.2022.05.008

26. Carcione JM. Seismic modeling in viscoelastic media. *Geophysics*. 1993;58(1):110-120.

    doi: 10.1190/1.1443340

27. Wang Y, Zhao L, Quintal B, Geng J. Characterizing broad-band seismic dispersion and attenuation in carbonates with fractures and cavities: A numerical approach. *Geophys J Int*. 2025;240(3):1404-1425.

    doi: 10.1093/gji/ggae452

28. Volker AWF, Blacquière G, Berkhout AJ, Ongkiehong L. Comprehensive assessment of seismic acquisition geometries by focal beams-Part II: Practical aspects and examples. *Geophysics*. 2001;66(3):918-931.

doi: 10.1190/1.1444982

29. Strong S, Hearn S. Multi-component seismic-resolution analysis using finite-difference acquisition modelling. *Explor Geophys*. 2008;39(4):189-197.

doi: 10.1071/EG08023

30. Lubrano, Lavadera P, Kühn D, *et al*. CO_2 storage in the high Arctic: Efficient modelling of pre-stack depth-migrated seismic sections for survey planning. *Geophys Prospect*. 2018;66(6):1180-1200.

doi: 10.1111/1365-2478.12637

31. Ishiyama T, Blacquière G. 3-D shallow-water seismic survey evaluation and design using the focal-beam method: A case study offshore Abu Dhabi. *Geophys Prospect*. 2016;64(5):1215-1234.

doi: 10.1111/1365-2478.12335

32. Zhang M. Efficient 3D seismic acquisition design using compressive sensing principles. *J Seismic Explor*. 2023;32(5):427-454.

33. Tsingas C, Almubarak MS, Jeong W, Al Shuhail A, Trzesniowski Z. 3D distributed and dispersed source array acquisition and data processing. *Leading Edge*. 2020;39(6):392-400.

doi: 10.1190/tle39060392.1

34. Zhao H, Chen MY, Ni YD, *et al*. Research on optimization method for irregular seismic acquisition in curved wave domain based on simulated annealing. *Appl Geophys*. 2025;22(1):220-230.

doi: 10.1007/s11770-025-1181-4

35. Wang Y, Wang L, Hu D, *et al*. The present-day geothermal regime of the North Jiangsu basin, east china. *Geothermics*. 2020;88:101829.

doi: 10.1016/j.geothermics.2020.101829

36. Zhang L, Li S, Xu W, *et al*. Discussion on deep geothermal characteristics and exploration prospects in the Northern jiangsu basin. *Energies*. 2024;17(13):3128.

doi: 10.3390/en17133128

37. Yang L, Yan H, Liu H. Optimal implicit staggered-grid finite-difference schemes based on the sampling approximation method for seismic modelling. *Geophys Prospect*. 2016;64(3):595-610.

doi: 10.1111/1365-2478.12325

38. Peng C, Toksöz MN. An optimal absorbing boundary condition for elastic wave modeling. *Geophysics*. 1995;60(1):296-301.

doi: 10.1190/1.1443758

39. Shin C, Jang S, Min D. Improved amplitude preservation for prestack depth migration by inverse scattering theory. *Geophys Prospect*. 2001;49(5):592-606.

doi: 10.1046/j.1365-2478.2001.00279.x

40. Zhou H, Lin H, Sheng SB, Chen HM, Wang Y. High angle prestack depth migration with absorption compensation. *Appl Geophys*. 2012;9(3):293-300.

doi: 10.1007/s11770-012-0339-z

ACCSCIENCE PUBLISHING

Journal of Seismic Exploration

ARTICLE

Reconstruction and quality control of non-repeatable land time-lapse seismic data

Yongjun Wang[1], Xinglei Xu[1,2]*, and Xu Wang[3,4]

[1]Teaching and Research Office of Software Technology, School of Artificial Intelligence, Wenzhou Polytechnic, Wenzhou, Zhejiang, China

[2]Department of Information Science, School of Mathematics and Statistics, Xi'an Jiaotong University, Xi'an, Shaanxi, China

[3]Institute of Applied Mechanics, Faculty of Civil Engineering, RWTH Aachen University, Aachen, North Rhine-Westphalia, Germany

[4]Northeast Electric Power Design Institute of China Power Engineering Consulting Group, Changchun, Jilin, China

Abstract

Onshore non-repeatable time-lapse (TL) seismic exploration is a challenging yet convenient technique for enhancing production in mature oil and gas fields. Data repeatability across two or more acquisition phases is fundamental for reliable TL analysis. However, differences in acquisition geometries – from variations in geological targets, acquisition technologies, and acquisition parameters – can cause significant inconsistencies between two data vintages. Drawing on survey design parameters, this study proposes a dual-constraint method for data reconstruction and quality control, integrating common midpoint (CMP) similarity with the sum of shot-receiver geometric distances. Unlike conventional techniques, the proposed approach simultaneously controls shot and receiver position errors through a dynamic threshold, indirectly preserving offset and azimuth consistency. Compared with typical methods, it avoids cross-domain transformations and multi-parameter adjustments, offering high applicability. Applied to conventional (2004) and high-density (2008) datasets from a Chinese onshore oilfield, the method achieved data utilization rates of 77.5% and 39.8%, respectively. The reconstructed data demonstrated higher offset distribution uniformity and improved CMP fold consistency compared with the CMP-constrained receiver deviation method. This study provides a practical reference for TL studies in onshore mature oilfields.

Keywords: Onshore seismic exploration; Non-repeatable time-lapse seismic data; Pre-stack data reconstruction

***Corresponding author:**
Xinglei Xu
(xingleixu@wzpt.edu.cn)

Citation: Wang Y, Xu X, Wang X. Reconstruction and quality control of non-repeatable land time-lapse seismic data. *J Seismic Explor*. 2025;34(3):76-92.
doi: 10.36922/JSE025230010

Received: June 6, 2025

1st revised: July 20, 2025

2nd revised: August 16, 2025

Accepted: September 3, 2025

Published online: October 16, 2025

1. Introduction

Time-lapse (TL, sometimes referred to as four-dimensional) seismic technology is a methodology for studying reservoir characteristics by analyzing differences, such as fluid changes in hydrocarbon reservoirs, and in seismic responses between two or more phases under specific conditions, including reservoir properties, fluid characteristics, and seismic data quality.[1,2] This technology has advanced seismic exploration from static structural surveys and reservoir characterization (e.g., structural and lithological

properties) to dynamic monitoring of hydrocarbon reservoirs. Under favorable conditions, it enables effective dynamic reservoir management and enhances recovery rates.[3,4] However, in recent years, high-precision and high-density seismic surveys have been conducted in mature exploration areas to identify complex lithological structures and subtle traps. By leveraging legacy and newly acquired data for non-repeatable TL seismic studies, reservoir development can be guided effectively without increasing acquisition costs.[5,6] Since the 1980s,[4] applied research on TL seismic technology has been conducted in many oilfields.[7,8] Nguyen *et al.*[9] reviewed prior studies and provided an in-depth introduction to recent advancements in TL seismic data processing and interpretation, focusing on four-dimensional seismic processing workflows. Sambo *et al.*[10] and Emami[11] also provided comprehensive reviews of TL seismic studies, reaffirming its significant applications.

However, environmental factors, such as ambient noise, environmental changes, and near-surface velocity variations, along with discrepancies in field acquisition parameters (e.g., differences in geophone types and positions and source excitation methods) and divergent processing requirements (e.g., workflows, parameters, algorithms, and software), lead to poor repeatability between seismic datasets from different periods. These inconsistencies manifest as mismatches in energy, timing, phase, velocity, and frequency bandwidth, rendering legacy processing results unsuitable for direct TL seismic interpretation. Therefore, targeted data reprocessing from both periods is necessary to minimize inconsistencies and obtain the accurate TL seismic response caused by reservoir changes.[12] Seismic processing aimed at this goal is often referred to as non-repeatable TL seismic processing.[13-16]

Given that TL seismic exploration has high requirements for the repeatability of two (or multiple) phases of non-repeatable seismic data, researchers have investigated its theoretical basis, feasibility, and practical implementation. Li and Chen[17] examined the prerequisites for TL seismic by assessing its feasibility. Based on TL seismic practices, Zhang[18] discussed the key conditions necessary to complete a TL project strictly, emphasizing the substantial challenges involved. Liu *et al.*[19] highlighted that TL seismic exploration must be considered from the initial stage of design acquisition, underscoring the inherent difficulties of non-repeatable TL projects. Considering the challenges of conducting accurate TL seismic exploration, Zhou *et al.*[20] proposed the concept of pseudo-TL seismic exploration, which focuses on analyzing the response characteristics of seismic data to geological and reservoir problems rather than ensuring strict multi-phase data consistency.

Analysis shows that significant differences in wavelet characteristics—mainly energy, frequency, and phase—can arise from variations in source–receiver conditions or acquisition geometry settings, even within the same survey conducted over two (or more) periods.[21] Therefore, applying appropriate data processing techniques to improve repeatability and reduce inconsistencies—while preserving the accurate TL seismic response caused by reservoir changes—is a core and essential task in non-repeatable TL seismic data processing.[22] In general, these consistency processing steps can be grouped into three main categories:

(i) Pre-stack data reconstruction: Initial data matching and reconstruction, including binning, midpoint alignment, fold adjustment, azimuth regularization, and signal-to-noise ratio optimization.
(ii) Pre-stack consistency processing: Maintenance of pre-stack consistency through frequency, phase, velocity, and residual static correction adjustments.
(iii) Post-stack equalization: Calibration of time, amplitude, frequency, energy, and phase.

Regarding the first task, Yin *et al.*[23] employed a three-dimensional Gaussian beam forward modeling method to quantitatively analyze the impact of different acquisition geometry parameters on the received energy of reservoir bins through illumination simulation. The study demonstrated that offset and azimuth are the primary factors causing inconsistencies between two-phase datasets and emphasized that bin resetting and uniform offset and azimuth distribution within bins are critical in non-repeatable TL seismic acquisition. Jin *et al.*[24] and Lü *et al.*[25] investigated bin resetting methods, proposing the composition of common midpoint (CMP) sets in pre-stack data reconstruction and introducing offset-based seismic trace extraction combined with dynamic interpolation. Implementing this approach is straightforward but may result in loss of offset and azimuth information. Yang *et al.*[26] addressed land-based TL seismic data processing by combining the frequency–wavenumber (FK)-domain interpolation with bin resetting, aiming to achieve acquisition geometry consistency by considering line, point, offset, azimuth, and time during the interpolation process. While valuable for onshore TL seismic studies, implementing multidomain transformation and multidimensional interpolation is challenging. Rui[27] designed a data reconstruction method based on source–receiver positions and consistent incidence/reflection angles to preserve offset and azimuth information in reconstructed data. However, its implementation requires numerous adjustable parameters. In 2021, Rui[28] proposed three core technologies—common reflection point (CRP) trace spatial extraction, FK-domain interpolation, and

r–p domain reconstruction—for acquisition geometry consistency processing, an approach largely similar to Yang's method.[26]

For the second and third tasks, researchers such as Jin *et al.*,[24,29,30] Guo *et al.*,[15,31,32] Wang *et al.*,[33] Zhu *et al.*,[34] and Wang *et al.*[35] have explored key post-processing techniques for two-phase data. Liu *et al.*[36] performed consistency processing on data before pre-stack depth migration. Chen *et al.*[37] applied dual-domain near-surface Q attenuation compensation and surface-consistent Yu's wavelet deconvolution to ensure data consistency. Liu *et al.*[38] used matched filtering to address cross-source inconsistencies. Fomel and Jin[39] applied local similarity attributes to TL seismic data matching, which was further developed by Liu *et al.*[40] Chen *et al.*[41] presented case studies demonstrating the application of TL seismic in offshore reservoir monitoring and a gas field. Rui *et al.*[28] proposed a workflow integrating well data-driven pre-stack consistency processing with pre-stack/post-stack sensitivity attribute analysis, significantly improving the applicability of non-repeatable TL seismic data and yielding promising results.

Analysis reveals that most successful TL seismic projects have been conducted in offshore environments, while onshore projects remain comparatively scarce. This is primarily due to the complexity of the onshore acquisition environment, where it is challenging to maintain consistency in acquisition geometry, source wavelet, reception conditions, and surface characteristics across surveys from different periods. Previous literature[1-4,7-8,12,13,24,25,29-31,33-35,41-44] has focused on repeatable TL seismic exploration. Many studies[17,19,34,41,43-45] have primarily addressed acquisition and processing technologies for offshore TL seismic data. In contrast, few publications have discussed non-repeatable TL seismic exploration,[14-16,26,32,41] and even fewer specifically examine onshore non-repeatable TL seismic exploration.[24,26,46] Zhou *et al.*[46] and Rui *et al.*[26] investigated an onshore non-repeatable TL seismic case. However, Zhou *et al.*[46] concentrated mainly on the TL geological response, while Rui *et al.*[28] focused on the overall processing workflow, devoting limited attention to data reconstruction strategies.

Among the three primary research tasks outlined earlier—acquisition geometry reconstruction, pre-stack data consistency processing, and post-stack consistency processing—acquisition geometry reconstruction is the most fundamental in non-repeatable TL seismic surveys. Differences in acquisition geometry are the dominant source of inconsistencies[33] and directly influence the accuracy of final interpretation results. Although previous studies[23-27] have examined data reconstruction methods, there remains a scarcity of literature specifically addressing algorithms for onshore non-repeatable data reconstruction (Task 1) and monitoring geometries. Furthermore, the associated technical challenges are particularly significant.[14,16,20,26] Nonetheless, this area of research holds considerable theoretical and practical value for the exploitation and development of mature onshore oil and gas fields.[14,26]

Building on this analysis, and considering the relationship between offset, azimuth, incident angle, and reflection angle of imaging points with the spatial arrangement of shot and receiver points, this study proposes a CMP-constrained data reconstruction method combined with quality control techniques, incorporating an additional constraint based on the sum of geometric distances of shot gathers and receiver-point sets (SumDsDr). Unlike methods relying solely on midpoint alignment, this approach controls shot-point and receiver-point positional errors using a dynamic threshold. It accounts for CMP similarity while applying dual constraints on shot-point and receiver-point deviations between two-phase datasets. In effect, it considers offset similarity and indirectly incorporates azimuth similarity. This aligns with the findings of Smit and Watt,[47] who demonstrated that trace correlation within the same bin is influenced by the combined shot–receiver distance ($\Delta S + \Delta R$); smaller $\Delta S + \Delta R$ values correspond to higher trace similarity. Compared to the methods of Yang *et al.*[26] and Rui *et al.*,[27,28] the proposed approach offers a more straightforward practical implementation. Its application to onshore oilfield datasets—including conventional and high-density acquisition data—validates its effectiveness.

For clarity, several typical methods for data reconstruction are summarized in Table 1, along with their applicable scenarios, complexity, and onshore application bottlenecks.

This paper is organized as follows: Section 2 first demonstrates the significance of repeatability in TL seismic analysis through a wavelet subtraction example. It then presents the proposed data reconstruction framework, including core algorithmic principles and technical implementation. Quality control protocols and workflow diagrams are provided, followed by a comparison with a similar method. Section 3 validates the proposed approach through field applications on two representative non-repeatable datasets from a Chinese onshore oilfield. Section 4 concludes the study by outlining the practical potential and key implementation considerations of the method.

Table 1. Typical methods for data reconstruction

Methods	Core idea	Complexity	Onshore applicability	Limitations
Yang *et al.*[26]	Frequency–wavenumber-domain interpolation+bin regularization	High (multidomain transformation)	Low (poor stability in complex surface conditions)	Prone to loss of offset information
Rui[27]	Incident angle/reflection angle constraint	Medium (complex parameter tuning)	Medium (sensitive to surface undulations)	Requires numerous adjustable parameters
This paper	Common midpoint+SumDsDr dual constraints	Low (no domain transformation)	High (dynamic threshold adapts to surface conditions)	Threshold selection depends on experience

Abbreviation: SumDsDr: Sum of geometric distances of shot gathers and receiver-point sets.

2. Data reconstruction method and quality control techniques

2.1. Importance of repeatability in TL seismic exploration

The repeatability of two-phase seismic data is the foundation of TL seismic research and a critical factor in ensuring the reliability of its results. For non-repeatable two-phase seismic data, failure to perform consistency processing prevents the differential information from accurately reflecting actual fluid changes in hydrocarbon reservoirs. As shown in the seismic data processing workflow (Figures 1 and 2), discrepancies in wavelet parameters, such as phase characteristics (including single or composite phase variations), time delays, frequency attributes, and energy distribution, may generate differential anomalies unrelated to reservoir fluid changes (Figure 2). Therefore, systematic reprocessing of both datasets is essential. Technical measures must be applied to minimize the influence of inconsistencies caused by non-hydrocarbon factors, ensuring that the TL seismic response accurately represents dynamic reservoir changes.[12]

2.2. Method

2.2.1. Related works

For two-phase non-repeatable data, it is essential to analyze the characteristics of both datasets in conjunction with the geological conditions and geophysical background of the study area. Based on this analysis, a targeted acquisition geometry reset method should be adopted to maximize the utilization of the "intersection" between the two datasets. Commonly used methods include acquisition geometry thinning, shot gather extraction, bin sorting, CRP extraction, and interpolation.[19,24-25,42] Among these, the acquisition geometry thinning and shot gather extraction methods require the shot positions in both datasets to coincide, using the dataset with fewer shots as the extraction basis. However, differences in shot layout positions and the number of shot gathers between the two phases are common, making this a challenge. The bin sorting method has strict requirements for receiver layout. Due to the differences in source positions between the two datasets, significant errors can occur. The CRP extraction method offers certain theoretical advantages;[26,28] however, it involves FK-domain and τ–p-domain interpolation, which requires substantial computational resources, imposes high implementation demands, and provides insufficient accounting for offset after reconstruction. Data reconstruction methods that jointly consider offset and azimuth information, while following the principle of consistency between incident and reflection angles,[27] involve numerous adjustable parameters and relatively complex implementation procedures.

Previous studies have emphasized key factors for acquisition geometry resetting. Yin *et al.*[23] identified offset and azimuth as essential parameters for bin resetting. Yang *et al.*[26] attempted data reconstruction using five-dimensional interpolation and multidomain transformation. Rui[27] highlighted the importance of CRP, incidence points, reflection angles, and incident angles. Smit and Watt[47] demonstrated that, within the same bin, the smaller the sum of the shot distance and receiver distance for two seismic traces, the higher the correlation between them.

2.2.2. Data reconstruction method

Inspired by the literature and combining the composition principles of the same bin and CMP with the relationships among shot position, receiver position, shot-receiver distance, reflection angle, incident angle, and offset, this study extracted the core elements—namely, CMP points within the same bin, shot distance, and receiver distance. By operating on these core elements, the method aims to retain as much offset and azimuth information from the two phases of data as possible, without relying on multidomain transformations or neural network-based reconstruction models.

To illustrate the core concept, the method was applied to two datasets from an onshore mature oilfield in China: conventional acquisition data from 2004 and high-density acquisition data from 2008 (secondary development acquisition). The acquisition parameters of the two

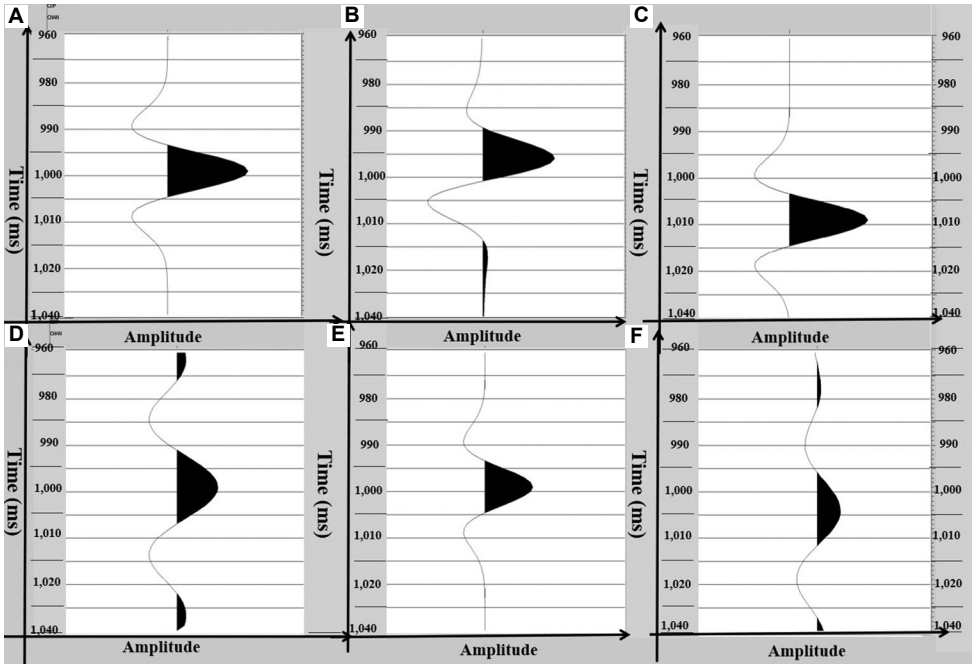

Figure 1. The original wavelet and its variations. (A) Original wavelet, (B) wavelet phase shift, (C) time shift, (D) frequency variation, (E) amplitude variation, and (F) hybrid factors. Time range: 800–1,030 ms for each plot.

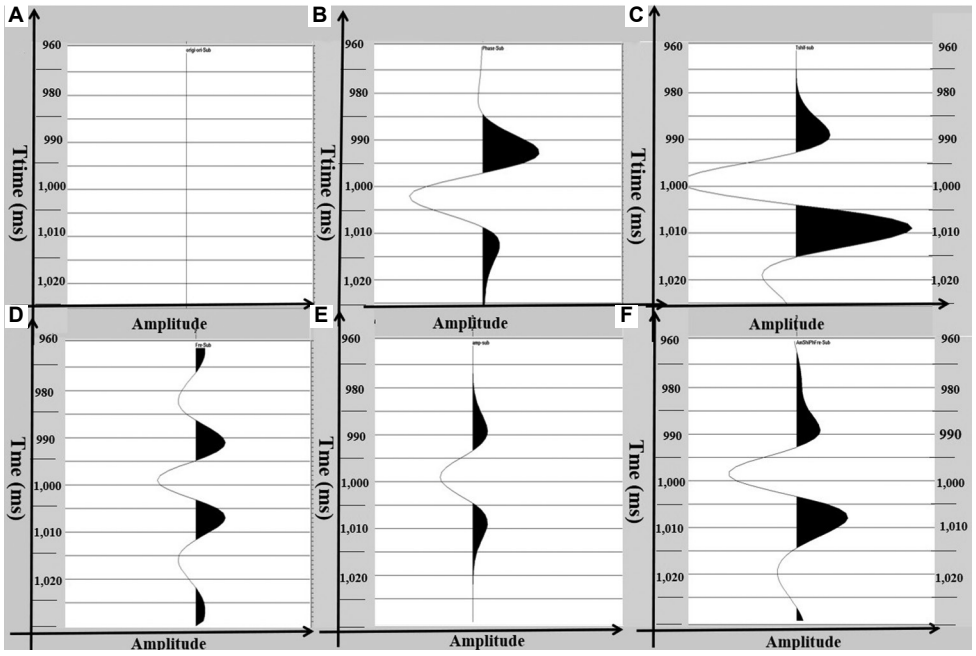

Figure 2. Subtracted results of the wavelets corresponding to Figure 1A-C. (A) Original, (B) phase shift, (C) time shift, (D) frequency variation, (E) amplitude variation, and (F) hybrid factors. Time range: 800–1,030 ms for each plot.

datasets are listed in Table 2. Table 2 shows that, aside from the receiver channel spacing of 50 m receiver spacing and 128 channels per layout in both surveys, there are substantial differences in other acquisition parameters. These include variations in source depths, explosive charges, non-coincident shots, and receiver positions, which result in inconsistent source wavelets between the two phases. In addition, the 2004 acquisition used a large-bin (25 m × 25 m) design with relatively uniform fold coverage, whereas the 2008 acquisition employed a small-

Table 2. Main acquisition parameters for the two datasets

Year Geometry parameters	2004	2008
Receiver spacing	50 m	50 m
Receiver line spacing	150 m	100 m
Number of receiver lines	8	32
Channels per line/ instrument	128	128
Number of receiver channels	1,024	4,096
Source point spacing	50 m	80 m
Source line spacing	200 m	80 m
Roll distance between arrays	600 m	800 m
Explosive charge	3 kg	1–4 kg
Non-longitudinal offset	825 m	935 m
Maximum source-to-receiver offset	4,400 m	7,200 m
Source depth	15 m, 18 m	15 m–31 m
Observation system	8L×12S×128R=1,024 3,175–25–50–25–3,175	32L×10S×128=4,096 3,175–25–50–25–3,175
Bin size	25 m×25 m	10 m×10 m

bin (10 m × 10 m) design. The bin sizes of the two datasets are not integer multiples of each other, making direct bin matching infeasible. These differences significantly increase the complexity of data reconstruction and subsequent processing. Methods such as acquisition geometry thinning or bin sorting could reduce reconstruction accuracy under these conditions, highlighting the need for a more robust approach.

Acquisition discrepancies between the two seismic datasets are inherent and unavoidable. To address this, the algorithm proposed in this study aims to maximize the utilization of both datasets (e.g., shot gathers) within a defined error tolerance, while ensuring that the reconstructed non-repeatable seismic data maintain consistency in azimuth, offset, fold, and other key attributes.

The specific workflow of the algorithm is illustrated in Figure 3. First, a unified bin grid was established. Within each bin, the 2004 dataset (DATA1) was used as the reference. Based on the spatial distribution of central points in conventional three-dimensional surveys, a threshold for the SumDsDr was applied as the screening criterion. From the 2008 dataset (DATA2), data whose central points are identical or spatially proximate to those in DATA1 were selected, and redundant fold data in DATA2 were discarded. If, within the threshold range, particular shot gathers in DATA1 cannot be matched with corresponding data in DATA2, those unmatched shot gathers in DATA1 were excluded. This matching process automatically ensured central point correspondence and maintained fold, offset, and azimuth consistency.

The main steps of the workflow are as follows:

(i) Define a unified bin grid for datasets and set a pre-controlled distance threshold.

(ii) Within each bin, use the 2004 dataset (DATA1) as the reference to extract seismic traces from the 2008 dataset (DATA2) that match the midpoint positions in DATA1.

(iii) Handle unmatched data: Discard redundant fold data in DATA2 that exceeds the threshold; if particular shot gathers in DATA1 have no matching data in DATA2 within the threshold, discard those unmatched shot gathers from DATA1.

(iv) Automatic alignment: The algorithm ensures midpoint position correspondence and consistency in fold, offset, and azimuth.

Algorithm 1: Data reconstruction algorithm

Given distance threshold SumDsDr and bin size (e.g., 25 m × 25 m)
For each bin i in the survey area:
1 Extract shots and receivers of DATA1 (2004) and DATA2 (2008) within bin i
2 **For** each shot j in DATA1 within bin i:
3 Calculate DS (distance between shot j and DATA2 shots)
4 Calculate DR (distance between receivers of shot j and DATA2 receivers)
5 **If** DS + DR < SumDsDr:
6 Retain matched shots (j in DATA1) and corresponding DATA2 data
7 **Else:**
8 Discard unmatched data in DATA1
9 Discard redundant DATA2 data exceeding the threshold
Output reconstructed DATA1 and DATA2

2.2.3. Parameter setting

In the algorithm, DS denotes the shot-point distance, DR denotes the receiver-point distance, and DS + DR represents the sum of the two. SumDsDr is the threshold for reconstructed data in TL seismic processing; its value determines the allowable adjacent distance between the two datasets during reconstruction.

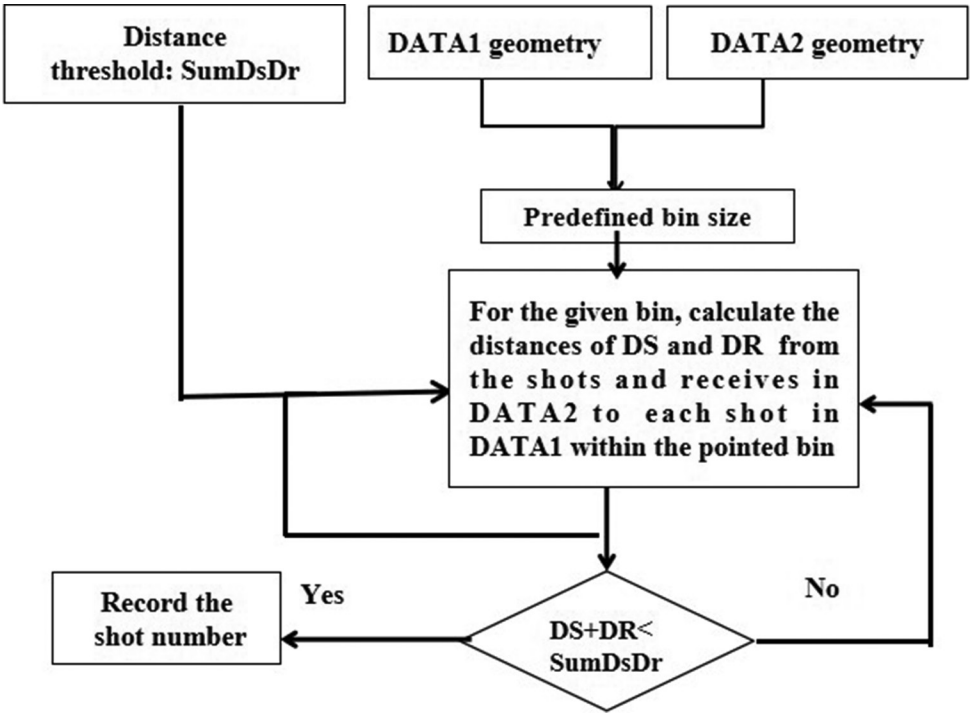

Figure 3. Flowchart of non-repeatable time-lapse reconstruction algorithm for two-phase data
Abbreviations: DS: Distance of shot gathers; DR: Distance of receiver-point sets; SumDsDr: Sum of geometric distances of shot gathers and receiver-point sets.

According to Smit and Watt,[47] smaller DS + DR values correspond to higher trace correlation similarity. Therefore, variations in DS, DR, and SumDsDr will affect the size and accuracy of the matched data between DATA1 and DATA2, ultimately impacting the fold, offset, and azimuth of the reconstructed data. As illustrated in Figure 4, when using parameter Set 1 (DS < 150 m, DR < 150 m, SumDsDr = 150 m), more original 2008 data were retained (i.e., fewer shots are discarded) compared with parameter Set 2. Consequently, the CMP fold of the 2008 data reconstructed with parameter Set 1 was slightly higher than that obtained using parameter Set 2 (Figure 4, where DS = 0, DR = 150 m, and SumDsDr = 150 m). However, the fold of the reconstructed 2008 data using parameter Set 2 was overall more uniform.

In practice, the value of SumDsDr must be determined experimentally for each dataset. Tests indicate that 150 m serves as a reasonable upper limit for both DS and DR. When SumDsDr exceeded 150 m, no additional improvement in reconstructed data consistency was observed (Figure 5). Therefore, 150 m was adopted as the experimental parameter in all subsequent examples in this study.

For the 2004 and 2008 seismic datasets, considering both their characteristics and the precision requirements of TL seismic processing, DS and DR were each set to 150 m. The statistical characteristics of the sorting and reconstruction results for the two datasets are shown in Figure 5. In the figure, the X-axis represents the preset error threshold, and the Y-axis represents the percentage of sorted gathers relative to the total original gathers under the corresponding error conditions.

Figure 5 shows that the sum of the shot-point and receiver-point errors for the two datasets is mainly distributed in the 40–120 m range. Due to inherent differences in the acquisition geometries, such as shot line spacing, shot-point spacing, receiver line spacing, and receiver-point spacing, the proportion of post-sorting receiver-point errors in the range of 10–30 m was nearly 50%, while those in the range of 40–60 m accounted for about 40%. Shot-point errors were concentrated in the range of 10–100 m. The effective utilization rate of the 2004 dataset reached 77.5%, while that of the 2008 dataset was 39.8%. It should be noted that 39.8% refers to the utilization rate of the number of shots in the 2008 dataset, calculated based on Equation I:

$$\text{Data utilization rate (\%)} = (\text{Number of shots retained after reconstruction}/\text{Total number of shots}) \times 100\% \quad \text{(I)}$$

The 2008 dataset represents high-density acquisition, with each shot containing more channels than the 2004 dataset.

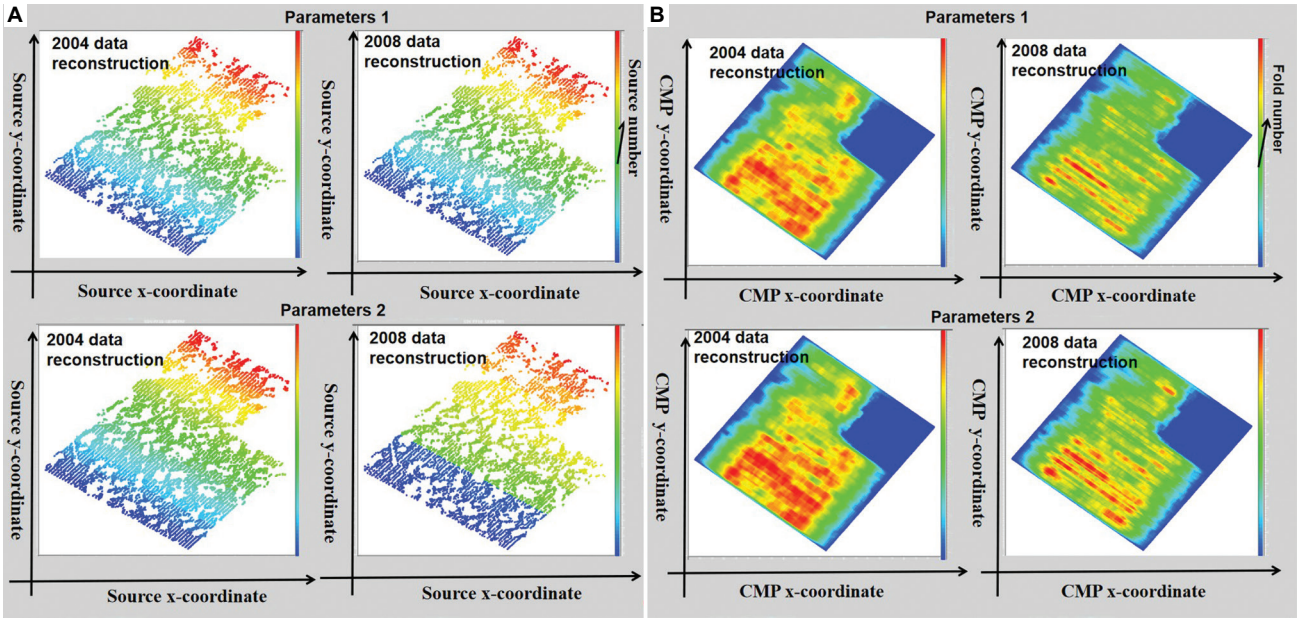

Figure 4. Shot-point distribution (A) and CMP fold (B) after data reconstruction with different DS, DR, and SumDsDr thresholds for the two datasets
Abbreviations: CMP: Common midpoint; DS: Distance of shot gathers; DR: Distance of receiver-point sets; SumDsDr: Sum of geometric distances of shot gathers and receiver-point sets.

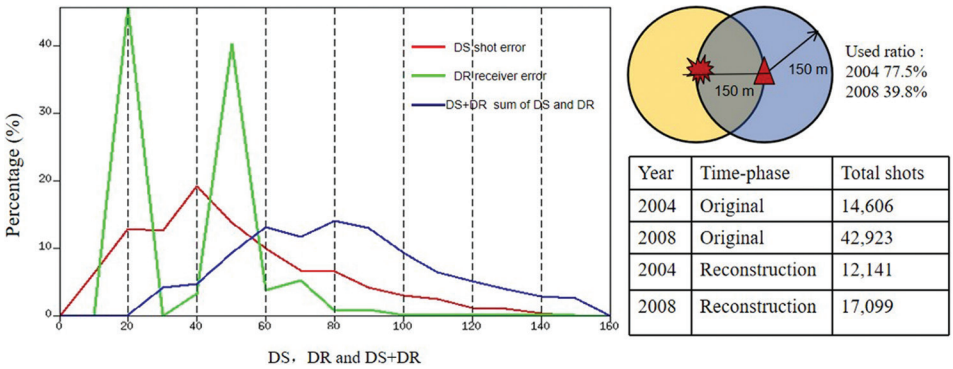

Year	Time-phase	Total shots
2004	Original	14,606
2008	Original	42,923
2004	Reconstruction	12,141
2008	Reconstruction	17,099

Figure 5. Utilization statistics of the original data in the reconstructed datasets. DS = DR = 150 m, showing the retained ratio for both datasets
Abbreviations: DS: Distance of shot gathers; DR: Distance of receiver-point sets.

During data reconstruction, maximizing original data retention must be balanced with maintaining consistency in key information such as offset and azimuth (as supported by the theory in Yin *et al.*[23]). Therefore, using DS + DR as the upper error limit for reconstructed data meets the precision requirements for acquisition geometry resetting in TL seismic exploration, ensuring an optimal balance between data volume and reconstruction quality. This is further illustrated in the following subsection.

2.3. Quality control study during the data reconstruction

As data reconstruction fundamentally depends on the acquisition geometries of both surveys, key quality control metrics include correspondence of source–receiver pairs before and after reconstruction, shot position proximity, consistency in offset and azimuth distributions, fold consistency within individual bins, overall fold distribution after reconstruction, and comparative analysis of initial migration sections.

Figure 6 compares the acquisition geometries, spatial coverage, and key characteristics of the two surveys. The 2008 survey employed high-density acquisition with smaller bins and multiple receiver spreads, whereas the 2004 survey used a sparser shot distribution with fewer receiver spreads. Differences in acquisition parameters, such as shot line spacing, shot-point spacing, and receiver line spacing, resulted in low repeatability of shot and

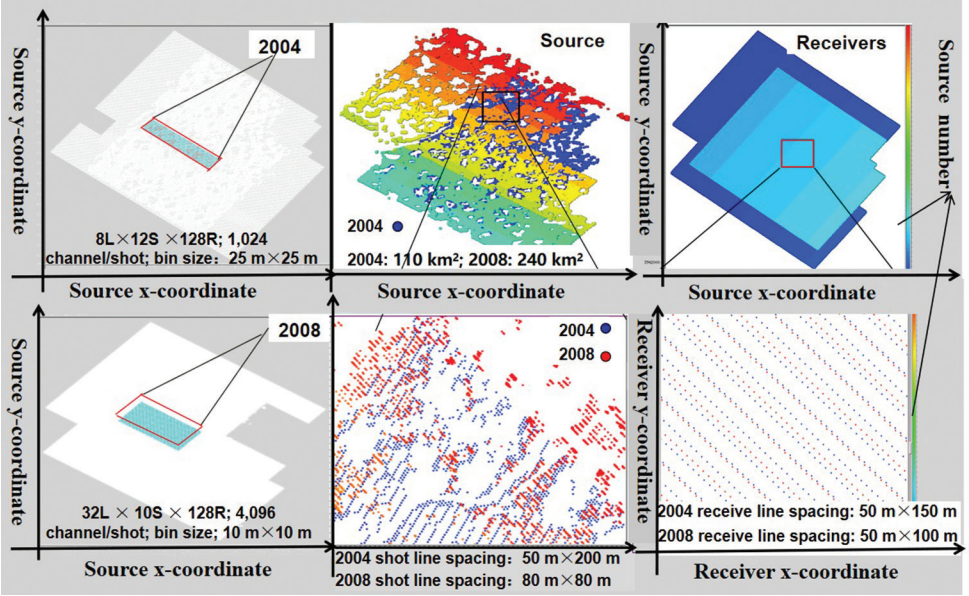

Figure 6. Comparison of shot and receiver geometries before data reconstruction for the two datasets

receiver positions between the datasets. Although the 2008 dataset covers a larger area, the 2004 data extends further in the upper-right corner. These acquisition disparities significantly increased the complexity of TL data reconstruction during the preliminary research phase.

Figure 7A shows zoomed-in views of shot-point distributions before and after matching, while Figure 7B shows zoomed-in receiver-point distributions for the same area. The figures indicate that the repeatability of shot-point distributions between the surveys is extremely low due to differences in receiver line spacing, shot-point spacing, and shot line spacing. The 2004 shot points are more regularly distributed, while overlaps in receiver points occur only occasionally; most positions differ between the datasets. Based on the preset threshold, the sorting process removed mismatched shot points from both datasets, retaining only shot and receiver points that meet the error requirements within the same bin.

Figure 8 compares CMP distributions before and after reconstruction, using the 2004 bin size standard (25 m × 25 m). Differences in the initial bin design rules for the two acquisition periods mean that resetting the bins alone could not resolve the uneven fold distribution in the 2008 data (Figure 8B). The fold maps obtained after bin resetting with the proposed reconstruction scheme (Figures 8C and D) showed substantial improvement in uniformity among adjacent bins. As illustrated in Figure 9, the fold values of the two datasets within the same area were largely consistent, and spatial uniformity was significantly enhanced in the post-reconstruction sections.

It should be noted that the scales of Figure 8A (25 m × 25 m grid) and Figure 8B (10 m × 10 m grid) are different, although the grid sizes may appear similar visually. After binning with the same bin size, however, the scales of Figure 8C and D were highly comparable. Figure 9 presents the CMP fold maps of the two-phase data before and after reconstruction. Figure 9A and B represent the entire survey areas, while Figure 9C and D show the matched portions of the reconstructed datasets. To more clearly highlight the reconstruction effect, Figure 9C and D are presented after simple normalization of the reconstructed two-phase data.

Figures 10 and 11 show the azimuth and offset distributions before and after data reconstruction. These plots demonstrate that the reconstructed datasets exhibited improved alignment in azimuth and offset ranges, resulting in significantly better consistency of maximum and minimum offset distributions.

2.4. Comparison with other methods

As reviewed in the literature, similar reconstruction methods often suffer from high implementation complexity or poor reproducibility. For example, the method by Yang *et al.*[26] requires data extraction and FK-domain transformation for reconstruction. In contrast, the method by Rui[27] necessitates the extraction of incident angles, reflection angles, and azimuths at CRP points. Some approaches also have limited applicability and are restricted to marine data or repeatable TL datasets. This study compares the proposed method only with the "common CMP point + DR constraint" method

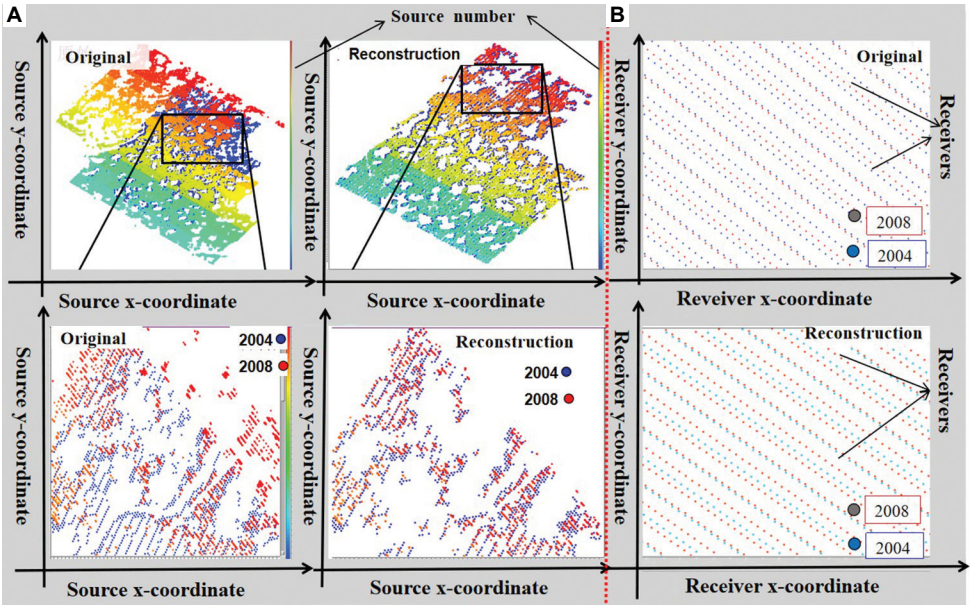

Figure 7. Shot (A) and receiver (B) point distributions before and after data reconstruction

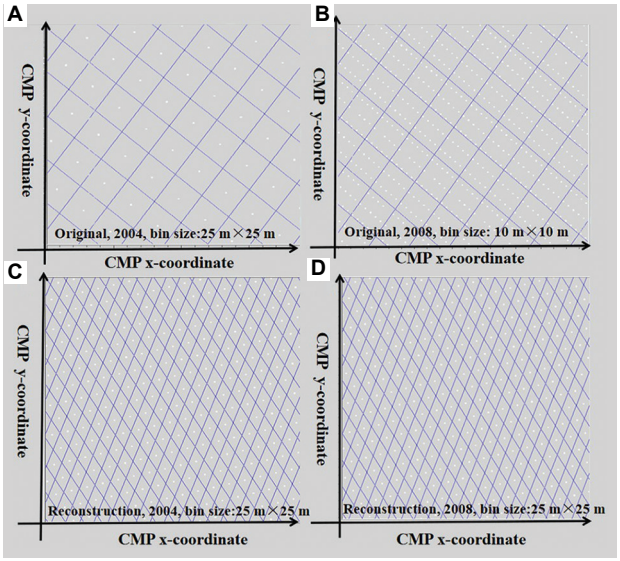

Figure 8. Common midpoint (CMP) bin. (A and B) Before and (C and D) after bin regularization.

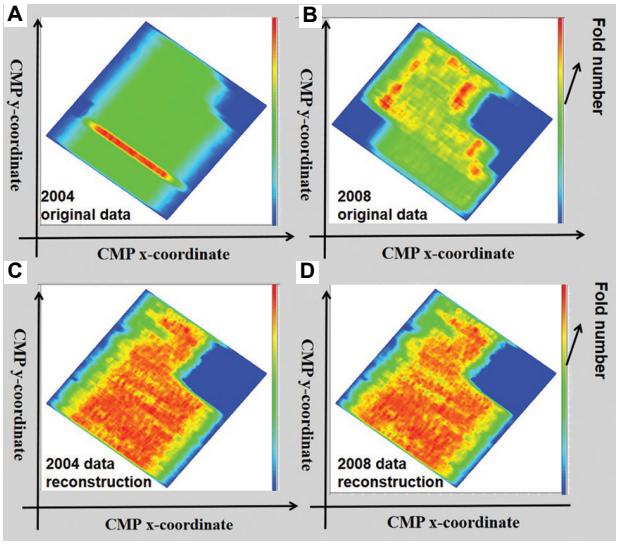

Figure 9. Common midpoint (CMP) fold maps before (A and B) and after (C and D) data reconstruction showing the matched parts of the two-phase datasets

(abbreviated as the DR method). In the DR method, reconstruction is performed under the constraint that the receiver-point error DR ≤ V (where V is a given value, 150 m in this study).

The experimental results are presented in Figure 12. Compared with the CMP + DR method, the DS + DR dual-constraint method proposed in this paper produced reconstructed datasets with more uniform offset distribution, higher CMP fold for both datasets, and higher utilization rate of original data. The DR method yielded utilization rates of 70.4% for the 2004 dataset and 38% for the 2008 dataset, which are lower than the 77.5% and 39.8%, respectively. Consequently, the consistency between the reconstructed 2004 and 2008 datasets improved, consistent with the trends shown in Figure 5.

In summary, for onshore oilfield acquisition data with significant differences in acquisition geometries between survey periods, the TL seismic data reconstruction method presented here balances data utilization and matching

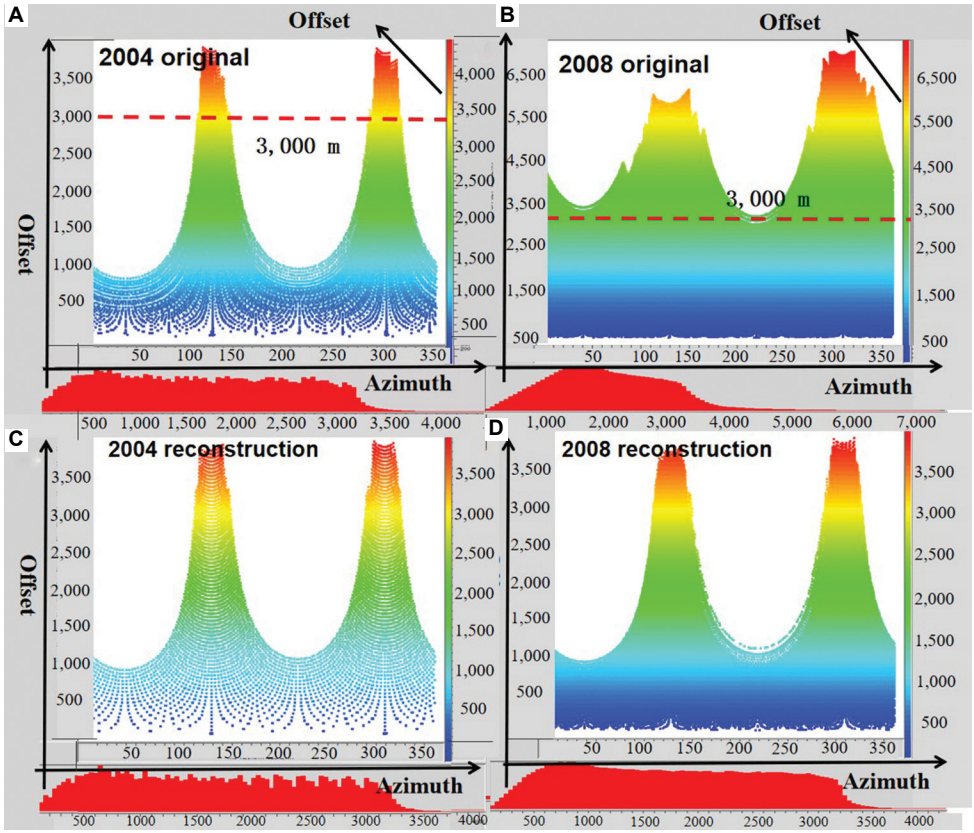

Figure 10. Azimuth distributions before and after data reconstruction for dual-phase datasets. (A) 2024 original: maximum offset: 4,400 m; minimum offset: 50 m; focus: 100–3,300 m. (B) 2024 original: maximum offset: 7,200 m; minimum offset: 25 m; focus: 100–4,200 m. (C) 2024 reconstruction: maximum offset: 4,300 m; minimum offset: 50 m; focus: 100–3,300 m. (D) 2024 reconstruction: maximum offset: 4,300 m; minimum offset: 50 m; focus: 100–3,300 m.

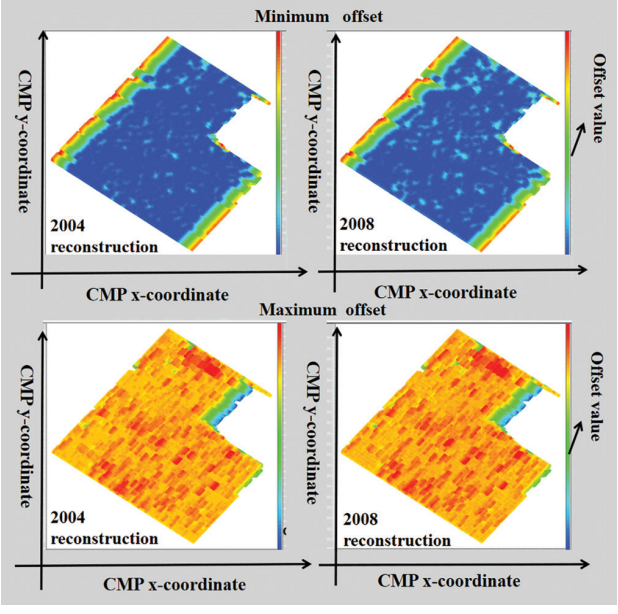

Figure 11. Offset distributions before and after data reconstruction for dual-phase datasets
Abbreviation: CMP: Common midpoint.

accuracy by adjusting thresholds. Indirectly incorporating the consistency of offset and azimuth distributions into the reconstruction process accounted more comprehensively for the impact of offset distribution differences on TL analysis than traditional methods. Our method yielded higher-quality reconstructed data compared to reconstruction approaches that consider only DR. It is also more practical for applications than other popular but complex methods, such as neural networks, compressed sensing theory, or interpolation-based reconstruction in various domains. For reconstructed two-phase datasets meeting specific conditions, shot-point distribution, receiver-point distribution, fold, azimuth, offset, and their distributions within the acquisition geometry served as key indicators for measuring repeatability. The figures presented in this study can be used as visual monitoring tools and for exporting monitoring metrics. It should be emphasized that the reconstruction algorithm provides only the foundational basis for the dataset. Even after reconstruction, the two-phase data may still exhibit inconsistencies in time, energy, waveform, frequency,

and phase. To fully meet the requirements for subsequent TL seismic interpretation, pre-stack consistency processing and post-stack mutual equalization techniques must be applied.

3. Application effects

To evaluate the practical efficacy of the proposed algorithm, the stacked profiles of the two datasets before

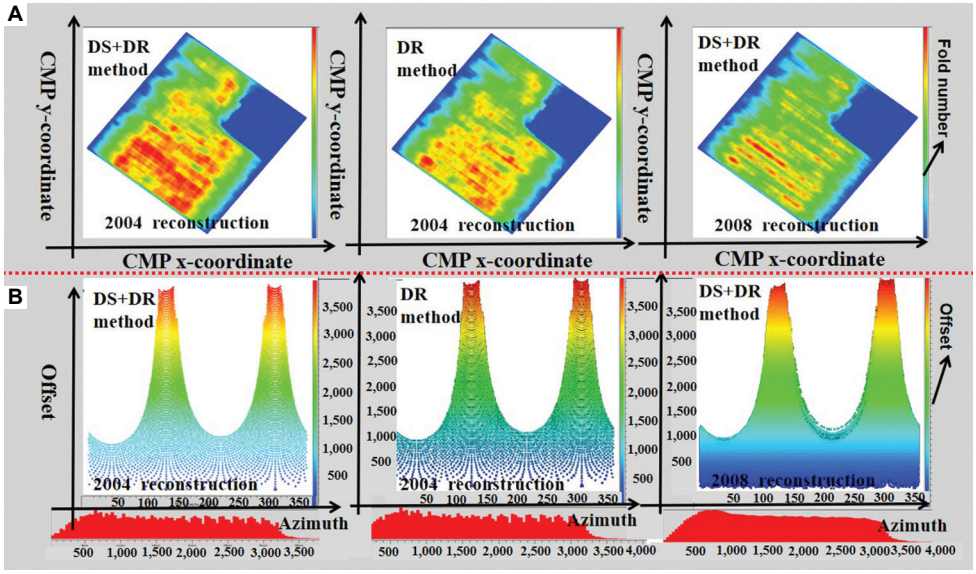

Figure 12. Comparison of DS + DR and DR methods. Common depth point fold (A) and azimuth versus offset (B).
Abbreviations: DS: Distance of shot gathers; DR: Distance of receiver-point sets.

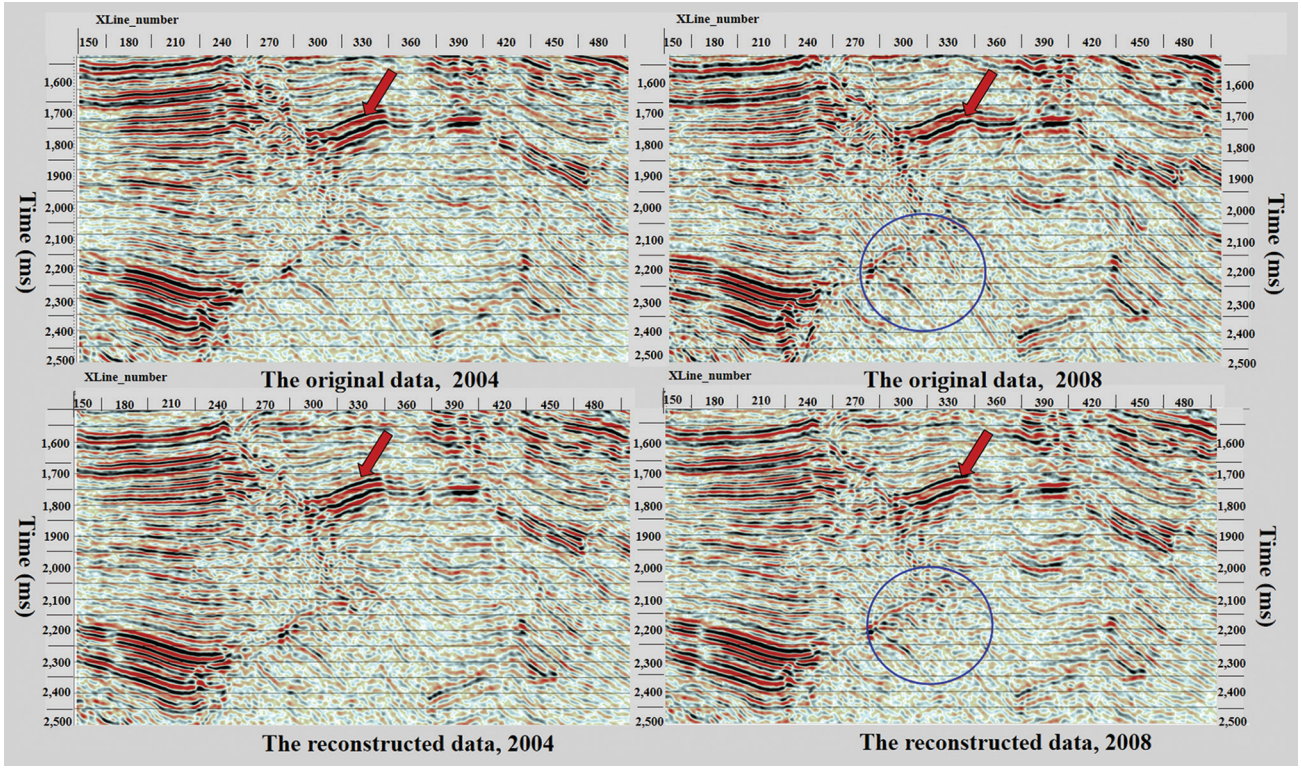

Figure 13. Stacked sections before and after data reconstruction. Blue circles and red arrows indicate areas used to assess reconstruction effectiveness.

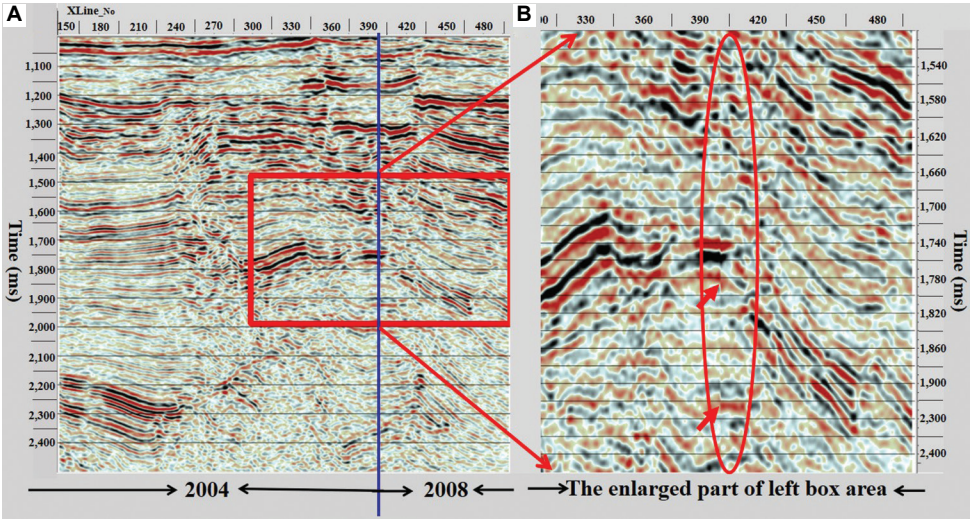

Figure 14. Merged, reconstructed, and stacked sections of dual-phase data. (A) Original. (B) Enlarged view. The blue line marks the boundary between the 2004 and 2008 datasets.

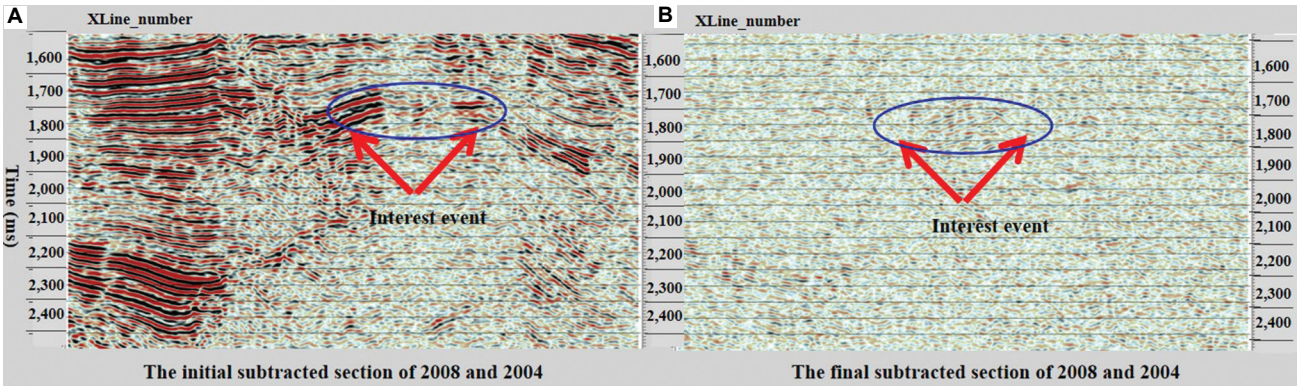

Figure 15. Subtracted seismic section. (A) Initial and (B) final.

and after reconstruction were compared. To ensure objectivity, pre-reconstruction and post-reconstruction data were processed using an identical pre-stack workflow, and results from the same longitudinal survey line were selected for analysis (Figures 13-15).

Figure 13 presents the initial stacked sections of the two datasets before and after reconstruction, while Figure 14 displays the spliced comparison of stacked profiles from the two reconstructed datasets at the same CMP location, along with the differential results obtained by directly subtracting the reconstructed data (Figure 15A). As shown in Figure 13, the reconstructed datasets exhibited substantial consistency in the positions of major structural events, overall frequency content, and wave group characteristics. Compared to the pre-reconstruction state, the proposed algorithm effectively removed shot gathers that compromised inter-dataset consistency. Although slight energy attenuation was observed for certain events in the reconstructed section, the overall consistency between the two datasets was significantly enhanced.

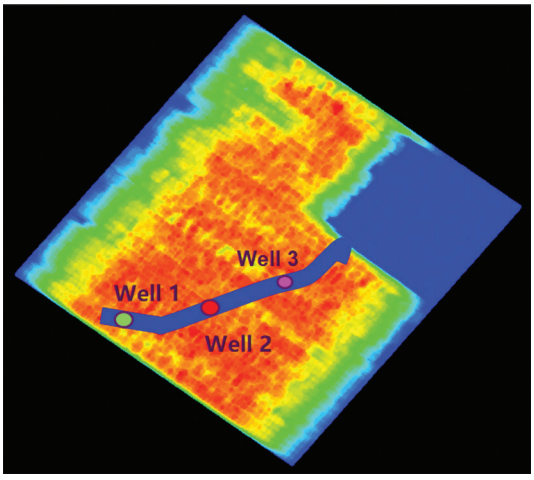

Figure 16. Seismic line crossing wells 1–3

From the spliced comparison and local magnifications of the two datasets (Figures 14A and B), minor time shifts remain, but they were negligible in magnitude. The subtraction results in Figure 15A reveal residual inconsistencies, including occasional false structures and non-seismic artifacts, indicating that the proposed method effectively mitigated significant inconsistencies between the datasets. Building on this, further pre-stack and post-stack consistency processing is recommended to suppress interference from non-reservoir fluid factors. This ensures that the differential results reflect actual TL changes in reservoir fluids, providing a solid foundation for residual oil interpretation and prediction. Figure 15 illustrates this, where the initial subtraction section (Figure 15A) and the final result after further processing (Figure 15B) can be used for TL interpretation, as noted in Figure 16.

To further illustrate the study results, a seismic survey line passing through production oil and gas wells 1–3 within the study area was selected (Figure 16). The consistency between the two-phase reconstructed data, their subtraction section (for fluid monitoring), and the production well data is shown in Figure 17.

Figure 17 shows that after processing, the subtraction section exhibited high correspondence with the production wells along the survey line. Strong seismic response events in the subtraction section aligned well with the lithological change depths in the three production wells. This correspondence reliably reflects the monitored fluid response, providing valuable data support for oil and gas production decision-making.

4. Discussion

Research on onshore non-repeatable TL seismic is highly challenging yet holds significant practical importance for developing and producing mature oil and gas fields. However, the proposed method depends on the manual selection of the SumDsDr threshold. In regions with pronounced surface undulations, the utilization rate may decline further due to significant deviations in shot or receiver positions, underscoring the need to develop an adaptive threshold algorithm in future work.

The dual-constraint reconstruction method presented in this study effectively balances data utilization and consistency in onshore oilfields with substantial differences in acquisition geometries, providing a valuable reference for preprocessing non-repeatable TL seismic data. Nevertheless, its applicability requires further verification under varying surface conditions.

An important direction for subsequent research is to objectively quantify consistency evaluation indicators for reconstructed data. Potential metrics include offset distribution indices, azimuth distribution ranges, fold uniformity, and correlation coefficients between the datasets before and after reconstruction. Establishing such

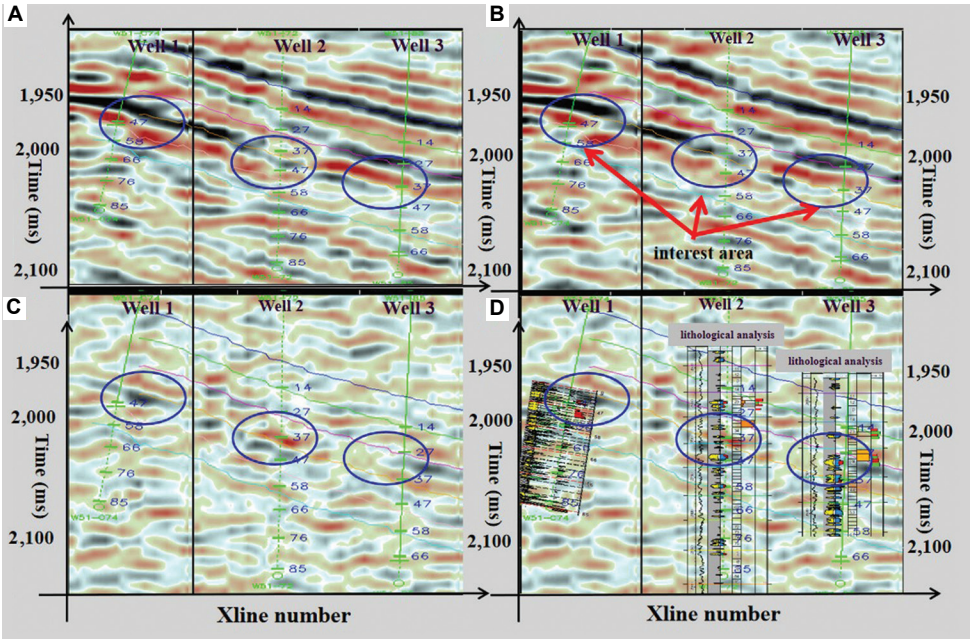

Figure 17. Seismic stack section crossing wells 1–3, corresponding to Figure 15. Green line: well logging curves and stratigraphic divisions; blue circles: areas of interest. (A) Reconstructed data of 2004; (B) reconstructed data of 2008; (C) subtraction section of 2008 and 2004; and (D) subtraction section with lithological analysis.

quantitative measures would enhance the reliability and comparability of reconstruction results.

5. Conclusion

The dual-constraint method for data reconstruction in this study can significantly reduce the inconsistency between the two onshore non-repeatable datasets. It can be used as the first step in fulfilling essential work for TL seismic exploration. The easy-to-execute yet straightforward strategy provides a practical reference for TL studies in onshore mature oilfields.

Acknowledgments

The authors sincerely thank the leaders and colleagues of the project team from the Reservoir Center of BGP, CNPC (China National Petroleum Corporation), including Ling Yun, Guo Xiangyu, Wang Guizhong, Gao Jun, Zhang Libin, Cao Sheng, and Zou Zhen, for their technical support and guidance. The authors also appreciate the data and support from Zhongyuan Oilfield, which made this research possible.

Funding

This work was supported by the Key Scientific Research Project (Grant No. WZY2025007) and Research Project on Teaching Development and Teaching Reform (Grant No. WZYzd202519) of Wenzhou Polytechnic, China; the Zhejiang Province Vocational Education "14th Five-Year Plan" Teaching Reform Project, China (Grant No. jg20240086); and the Wenzhou Significant Science and Technology Innovation Project, China (Grant No. ZG2022012).

Conflict of interest

The authors declare that they have no competing interests.

Author contributions

Conceptualization: Yongjun Wang
Formal analysis: Xinglei Xu
Investigation: Xinglei Xu, Xu Wang
Methodology: Yongjun Wang, Xinglei Xu
Validation: Xinglei Xu, Xu Wang
Visualization: Xu Wang
Writing–original draft: Yongjun Wang
Writing–review and *editing:* Xu Wang

Availability of data

The data can be obtained from the Exploration and Development Research Institute of Henan Oilfield through a request (subject to approval), and the original algorithms and codes can be obtained on request to BGP, CNPC.

References

1. Wang Z. Feasibility of time-lapse seismic reservoir monitoring: The physical basis. *Leading Edge*. 1997;16(9):1327-1329.

   doi: 10.1190/1.1437796

2. Guerin G, He W, Anderson RN, *et al.* 4D seismic: The fourth dimension in reservoir management Part 5-Reservoir simulation as a tool to validate and constrain 4-D seismic analysis. *World Oil*. 1997;218(9):75-79.

3. Nur A, Tosaya C, Thanh DV. Seismic Monitoring of Thermal Enhanced oil Recovery Processes. In: *Expanded Abstracts of the 54th Annual International SEG Meeting*. SEG; 1984. p. 337-340.

   doi: 10.1190/1.1894015

4. Greaves RJ, Fulp TJ. Three-dimensional seismic monitoring of an enhanced oil recovery process. *Geophysics*. 1987;52(9):1175-1187.

   doi: 10.1190/1.1442381

5. Efnik MS, Taib SH, Islami N. Using time-lapse 4D seismic to monitor saturation changes in carbonate reservoirs. *J Pet Explor Prod Technol*. 2016;88(6):736-742.

   doi: 10.1007/s12594-016-0541-3

6. Xin KL. Application of 4D seismic technology in SAGD steam chamber monitoring. *Pet Geophys Prospect*. 2019;54(4):882-890.

   doi: 10.13810/j.cnki.issn.1000-7210.2019.04.020

7. Lumley DE. Time-lapse seismic reservoir monitoring. *Geophysics*. 2001;66(1):50-53.

   doi: 10.1190/1.1444921

8. Jenkins SD, Waite MW, Bee MF. Time-lapse monitoring of the Duri steamflood: A pilot and case study. *Leading Edge*. 1997;16(9):1267-1273.

   doi: 10.1190/1.1437778

9. Nguyen PKT, Nam MJ, Park C, Park C. A review on time-lapse seismic data processing and interpretation. *Geosci J*. 2015;19(2):375-392.

   doi: 10.1007/s12303-014-0054-2

10. Sambo C, Iferobia CC, Babasafari AA, Rezaei S, Akanni OA. The role of time lapse (4D) seismic technology as reservoir monitoring and surveillance tool: A comprehensive review. *J Nat Gas Sci Eng*. 2020;80:103312.

    doi: 10.1016/j.jngse.2020.103312

11. Emami Niri M. 3D and 4D seismic data integration in static and dynamic reservoir modeling: A review. *J Pet Sci Eng*. 2018;167:514-529.

    doi: 10.22078/jpst.2017.2320.1407

12. Zhuang H, Xu Y. 4D seismic data processing and its key

techniques. *Prog Geophys*. 1999;14(2):33-43.

13. Yang Q, Zhong W. 4D seismic technique in oil and gas field development. *Geophys Prospect Pet*. 1999;38(3):50-57.
14. Wu D, Li Z, Jiang B, Huang X, Li F, Chen X. The problems for land non-repeated time-lapse seismic data processing and its countermeasures. *Pet Geophys Prospect*. 2015;54(4):427-434.

    doi: 10.3969/j.issn.1000-1441.2015.04.009
15. Guo N, Shang X, Liu X, Wang S. Key techniques for non-repeated time-lapse seismic data processing technology. *Pet Geophys Prospect*. 2011;46(4):581-592.

    doi: 10.1007/s12182-011-0118-0
16. Ling Y, Huang X, Gao J, Lin J, Sun D. Case study of non-repeatable acquisition in time-lapse seismic exploration. *Geophys Prospect Pet*. 2007;46(3):231-248.

    doi: 10.3969/j.issn.1000-1441.2007.03.003
17. Li J, Chen X. Feasibility analysis and evaluation technology of time-lapse seismic reservoir monitoring. *Geophys Prospect Pet*. 2012;51(2):125-132.

    doi: 10.3969/j.issn.1000-1441.2012.02.003
18. Zhang A. Research on key techniques of time-lapse seismic feasibility demonstration. *Petrochem Technol*. 2024;31(2):204-206.

    doi: 10.3969/j.issn.1006-0235.2024.02.070
19. Liu W, Deng H, Zhang L, Huang F, Li F, Chen X. Feasibility study of time-lapse seismic acquisition timing: A case study in the L gas field. *Geophys Prospect Pet*. 2022;61(3):490-498.

    doi: 10.3969/j.issn.1000-1441.2022.03.011
20. Zhou X, Xia T, Zhang Z, Liu X. Application of pseudo-time-lapse seismic to residual oil analysis in the middle and late stages of oilfield development. *Geophys Prospect Pet*. 2024;63(2):449-458.

    doi: 10.12431/issn.1000-1441.2024.63.02.016
21. Yang W. 3D Processing and Interpretation Integration Group. Study on analysis and monitoring methods of 3D seismic data. *Pet Geophys Prospect*. 2002;(5):433-440.

    doi: 10.3321/j.issn:1000-7210.2002.05.001
22. Rosa DR, Schiozer DJ, Davolio A. Evaluating the impact of 4D seismic data artefacts in data assimilation. *Pet Geosci*. 2023;29(3):603-614.

    doi: 10.1144/petgeo2022-069
23. Yin C, Ge ZJ, Rui Y, Zhao S, Cui Q. Feasibility study on time-lapse seismic reservoir monitoring with non-uniform acquisition. *J Southwest Pet Univ Nat Sci Ed*. 2014;36(1):170-180.

    doi: 10.11885/j.issn.1674-5086.2013.10.28.01
24. Jin L, Chen X, Liu Q. Quality control method of time-lapse seismic cross-equalization processing with correlation parameters. *Nat Gas Ind*. 2005;25(11):33.

    doi: 10.3321/j.issn:1000-0976.2005.11.011
25. Lü X, Chen X, Diao S. An approach to time-lapse seismic rebinning and its realization. *Prog Explor Geophys*. 2004;27(3):117-181.
26. Yang H, Li D, Zhang H, Yang J, Ma N. Key Technology of Time-Lapse Processing on Land. In: *Proceedings of the 2020 International Field Exploration and Development Conference*. Chengdu China; 2020. p. 7.

    doi: 10.26914/c.cnkihy.2020.042217
27. Rui YJ. Key techniques for time-lapse seismic processing with non-uniform onshore acquisition. *Geophys Geochem Explor*. 2016;40(4):778-782.

    doi: 10.11720/wtyht.2016.4.22
28. Rui YJ, Shang XM. Exploration and practice of non-uniform time-lapse seismic key technology in Shengli Oilfield. *Geophys Geochem Explor*. 2021;45(6):1439-1447.

    doi: 10.11720/wtyht.2021.1219
29. Jin L, Chen X. Hybrid factor processing method of cross-equalization for time-lapse seismic. *Pet Geophys Prospect*. 2005;40(4):400-406.

    doi: 10.3321/j.issn:1000-7210.2005.04.011
30. Jin L, Chen X. Effects of time-lapse seismic non-repeatability and verification of cross-equalization processing. *Prog Explor Geophys*. 2003;26(1):45-48.
31. Guo N, Meng Y, Yang W, Li H. Repeatability measurement and consistency analysis methods for time-lapse seismic data. *Comput Techn Geophys Geochem Explor*. 2012;34(2):186-192.

    doi: 10.3969/j.issn.1001-1749.2012.02.014
32. Guo N, Wu G, Shang X. Application of cross-equalization method in non-repeatable time-lapse seismic data processing. *Pet Geophys Prospect*. 2011;50(6):600-606.

    doi: 10.3969/j.issn.1000-1441.2011.06.010
33. Wang Y, Shen G, Xu H, Fu J, Shan L. Key Technology Applications of Non-Uniform Time-Lapse Seismic. In: *Proceedings of the SPG/SEG Beijing 2016 International Geophysical Conference*. Beijing China; 2016. p. 382-385. Available from: https://d.wanfangdata.com.cn/conference/ChtDb25mZXJlbmNlTmV3UzIwMj U4MjAxMDQxNTUSBzk1NjY3ODYaCDU4bGw1dmFq [Last accessed on 30 May 2025].
34. Zhu Z, Wang X, He Y, Sang S, Li L, Liu Z, *et al*. Research and application of key marine time-lapse seismic technologies. *China Offshore Oil and Gas*. 2018;30(4):76-85.

    doi: 10.11935/j.issn.1673-1506.2018.04.009
35. Wang D, Liu J, Qiu B, Yan H. Quality control technology of ocean time-lapse seismic data processing. *Chin J Eng Geophys*. 2018;15(3):253-260.
36. Liu W, Lei X, Sui B, Li Y, Chen F, Liu Z, *et al*. Research on

non-repeatable time-lapse seismic matching processing based on OBC and streamer data. *Prog Geophys*. 2025:1-13.

37. Chen CQ, Dai HT, Gao Q, Chen J, Luo W, Wang Z. A processing method for seismic data consistency under complex surface conditions and its applications. *Geophys Geochem Explor.* 2023;47(4):954-964.

    doi: 10.11720/wtyht.2023.1162

38. Liu L, Chen S, Wang YL, Xiao Y, Yue H. Research on the application of mixed source data matching processing technology in 3D seismic exploration of coal field. *Prog Geophys*. 2024;39(5):1951-1962.

    doi: 10.6038/pg2024HH0498

39. Fomel S, Jin L. Time-lapse image registration using the local similarity attribute. *Geophysics*. 2009;74(2):A7-A11.

    doi: 10.1190/1.2793090

40. Liu X, Chen X, Bai M, Chen Y. Time-lapse image registration by high-resolution time-shift scan. *Geophysics*. 2021;86(3):M49-M58.

    doi: 10.1190/geo2020-0459.1

41. Chen X, Yang X, Xiao P, Lv W, Zhang X, Duan R. Application of time-lapse seismic technology in deepwater turbidite reservoir monitoring: A case study of the deep water fan a oilfield in West Africa. *Geophys Prospect Pet*. 2023;62(3):538-547.

    doi: 10.12431/issn.1000-1441.2023.62.03.015

42. Dong FS, Fu LY, Quan HY, Dong K. Matched multi-trace geometry repeatability for time lapse seismic. *Chin J Geophys*. 2016;59(8):3056-3067.

    doi: 10.6038/cjg20160828

43. Wu Y, Ling Y, Zhang Y, Guo X. Case study of towed streamer time-lapse seismic acquisition design in offshore areas. *Pet Geophys Prospect*. 2016;51(1):1-12.

    doi: 10.13810/j.cnki.issn.1000-7210.2016.01.001

44. Li X, Hu G, Fan T, *et al*. The application conditions and prospects of time-lapse seismic technology in offshore oilfield. *China Offshore Oil Gas*. 2015;27(6):48-52.

    doi: 10.11935/j.issn.1673-1506.2015.06.008

45. Zhou J, Xie Y, Chen Z, Wang S. Application of time-lapse seismic in offshore gas fields in China. *Prog Explor Geophys*. 2011;46(2):285-292.

46. Zhou J, Zhang L, Liu W, Hu L, Wang Q. Application of time-lapse seismic gas reservoir monitoring in the Yacheng 13-1 gas field. *Geophys Prospect Pet*. 2020;59(4):637-646.

    doi: 10.3969/j.issn.1000-1441.2020.04.014

47. Smit JA, Brain J, Watt K. Repeatability Monitoring During Marine 4D Streamer Acquisition. In: *Extended Abstracts of the 67th EAGE Conference and Exhibition*. EAGE; 2005. p. C015.

    doi: 10.3997/2214-4609-pdb.1.C015

RETRACTION NOTE

DOI: 10.36922/jse.corr090225
Published online: October 16, 2025

Zhang Y, Huang J, Mao Q. Finite-difference reverse-time migration based on anisotropic pure qp wave equation in TTI media. *Journal of Seismic Exploration*. 2024;33(1):21–40.

This article is retracted at the request of the authors and with the approval of the Editor-in-Chief of *Journal of Seismic Exploration*. The article was originally published while the journal was still under the management of the former publisher, prior to its acquisition by AccScience Publishing.

The reason for this retraction is that the same article was inadvertently published twice due to an editorial oversight in the former publisher's workflow: first in Volume 33 Issue 1 (2024) and again in Volume 33 Issue 6 (2024). To correct this error and ensure the integrity of the scholarly record, the version published in Volume 33, Issue 1 is hereby retracted. The version published in Volume 33 Issue 6 remains the version of record and should be cited accordingly.

All authors are aware of this issue and agree to this retraction.

Our Journals

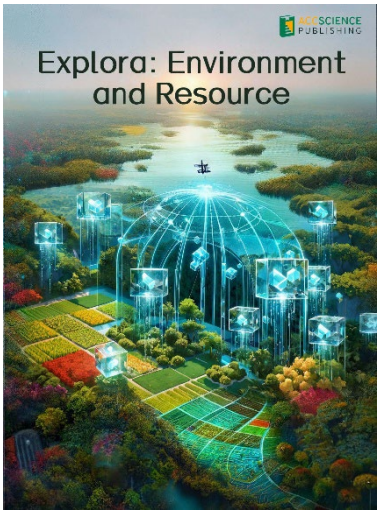

Explora: Environment and Resource (EER) is an international and multidisciplinary journal covering all aspects of the environmental impacts of socio-economic development. It is concerned with the complex interactions among society, development, and the environment, aiming to explore ways and means of achieving sustainability in all human activities related to development.

EER covers subject areas, including but not limited to the following:

- Water reclamation, wastewater treatment and waste management for eco-environment sustainability
- Innovative nanotechnology, catalysis, photocatalysis and nano materials for decontamination practices and renewable energy resources.
- Climate change-related sustainable resource and environment quality analysis
- Microorganisms and plants-oriented low-carbon processes and strategies for clean energy, water and resource management

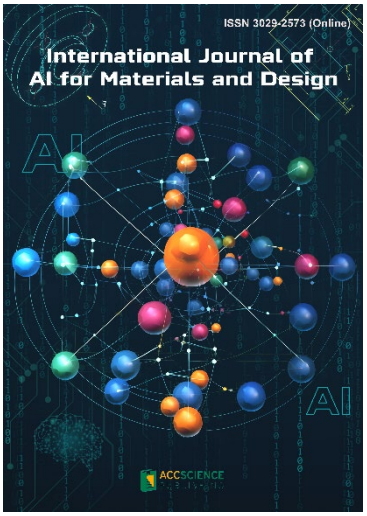

International Journal of AI for Materials and Design is an international, peer-reviewed open-access journal that aims to bridge the cutting-edge research between AI and materials, AI and design. In recent years, the tremendous progress in AI is leading a radical shift of AI research from a mainly academic endeavor to a much broader field with increasing industrial and governmental investments. The maturation of AI technology brings about a step change in the scientific research of various domains, especially in the world of materials and design. Machine learning (ML) algorithms enable researchers to analyze extensive datasets on material properties and accurately predict their behavior in different conditions. This subsequently impact the industry to leverage on big data and advanced analytics to build scientific strategies, scale operational performance of processes and drive innovation. In addition, AI and ML are uniquely positioned to enable advanced manufacturing technologies across the value chain of different industries. Integration of multiple and complementary AI techniques, such as ML, search, reasoning, planning, and knowledge representation, will further accelerate advances in scientific discoveries, engineering excellence and the future of cyber-physical systems manufacturing.

International Journal of AI for Materials and Design covers the following topics: AI or machine learning for material discovery, AI for process optimization, AI and data-driven approaches for product or systems design, application of AI in advanced manufacturing processes such as additive manufacturing, IoT, sensors, robotics, cloud-based manufacturing, intelligent manufacturing for various applications, autonomous experiments, material intelligence, energy intelligence, and AI-linked decarbonization technologies.

Start a new journal

Write to us via email if you are interested to start a new journal with AccScience Publishing. Please attach your CV, professional profile page and a brief pitch proposal in your email. We shall inform you of our decision whether we are interested to collaborate in starting a new journal.

Contact: info@accscience.com

https://accscience.com/journal/JSE

Access Science Without Barriers

Contact

www.accscience.com
9 Raffles Place, Republic Plaza 1 #06-00 Singapore 048619
E-mail: editorial@accscience.com
Phone: +65 8182 1586